Radiation-induced Inflammatory Responses in Carcinogenesis and Cardiac Disease

Kay Shigemori

Thesis submitted in partial fulfilment of the requirements for the degree of Doctor of Philosophy in Oncology

University of Oxford

Green Templeton College

Trinity Term 2022



RADIATION-INDUCED INFLAMMATORY RESPONSES IN CARCINOGENESIS AND CARDIAC DISEASE

Kay Shigemori
Green Templeton College, University of Oxford
Thesis submitted for the degree of Doctor of Philosophy in Oncology

ABSTRACT

More than half of cancer patients receive radiation treatment in the course of their treatment. Recently, clinical and preclinical studies have indicated that radiation may have anti-cancer effects through the initiation of tumour-specific immune responses in addition to tumour cell-intrinsic DNA-damage. The role of the tumour microenvironment in cancer development, progression and response to therapy is increasingly being recognised. However, few pre-clinical models are available for the co-evaluation of tumour and normal tissues in response to radiation therapy. The aims of this thesis are: (1) to establish a pre-clinical mouse model which can be used to co-evaluate tumour and normal tissue responses to cancer therapies; (2) to dissect the critical biological processes in carcinogen-induced lung tumour initiation and development (with a focus on immune and stromal context); and (3) to investigate the mechanisms important in radiation-induced normal tissue responses in cardiac and lung tissues.

Using the A/J mouse model, we established a relevant model in which to study effects of radiation. In mice treated with the carcinogen, urethane, we found that radiation treatment during the expected period of tumour initiation resulted in fewer and smaller tumours compared with controls. In parallel, we observed increased occurrence of distinct lymphocyte aggregates in the mice that had fewer tumours, which we further confirmed were positive for markers including CD3, CD19, CD103, MHCII, CXCL13 and B220. Results from treatment with a STING agonist (DMXAA) at tumour initiation were complex, revealing a decrease in tumour numbers, but an increase in tumour burden. In established lung tumours, T-cell exclusion was observed 7 days after irradiation, along with indications of chronic inflammation occurring in the lung parenchyma. Investigation of late radiation-induced pathological events in the heart revealed an increase in fibrosis in the pericardium and perivasculature in addition to discernible changes in electrical conduction including increases in QTc and P-R intervals and variability in heart rate. Unexpectedly, we observed sustained DDR in cardiac cells that lasted up to 7 days after irradiation.

In conclusion, our data introduce the A/J mouse as a novel model for studying both late cardiac toxicity and anti-tumour effects following radiation using both physiological and pathological endpoints. Our results also suggest that a potential ‘vulnerable state’ may exist prior to neoplastic cell transformation after carcinogen treatment of lung cells, that might be targeted to prevent the future development of tumours. These vulnerabilities may lie the altered cell division processes or acute immune responses that are impacted by radiation. Furthermore, STING agonism may add a selection pressure during tumourigenesis, potentially resulting in the more immune-resilient clones surviving and proliferating. The relationship between the persistent DDR observed after irradiation of cardiac tissue and the late electrophysiological and pathological effects warrants further investigation.

ACKNOWLEDGEMENTS

Here in this thesis, I would like to celebrate my DPhil journey - a period of four years at Oxford that will mark an important and memorable chapter in my life. All of this would not have been possible had it not been for the love and support from my family, friends, mentors and colleagues.

First and foremost, I would like to thank my three supervisors who have provided me with their support and guidance scientifically and otherwise, and each of whom I have been fortunate to establish relationships with as my mentors. I would like to express my deep appreciation to Dr. Eileen Parkes, for her scientific and career guidance, and her generosity in the research setting and beyond. I consider myself fortunate to have met someone I can look up to as a leader and scientist. The interactions we had outside of research too - the 'kudos' on Strava and sláinte at the formal dinner at Green Templeton College, to list a few - are ones I will remember. My deep appreciation also goes to Professor Anderson Ryan, for his guidance and mentorship for research and career throughout the four years of my DPhil. The scientific discussions that happened in 3-D at Costa Coffee or in 2-D on Teams with Misty (your favourite animal in your house) snoring in the background were all equally valuable to me, but perhaps, the most important of all lessons are the life advices and little bits of British culture that you taught me! Thank you, Andy, for being a kind and

patient supervisor, and the source of immense knowledge and wisdom. I would also like to thank Professor Maria Hawkins for the guidance she provided me in my research project, especially during the first and second years of my DPhil.

I would like to thank members of the Parkes group. In particular, I would like to thank Su Phyu, for the scientific support and moral support with laughter every day and the Mohinga soup on harder days; Yizhou Wang, for being a great lab 'parasite' (a synonym for great bench mate), and a student of impromptu Japanese classes in between western blot incubations; and Bruno Beernaert, for not only the wizardry bioinformatic analyses you whipped up in just a few days for the project (you don't know how thankful I am of those beautiful Illustrator plots!) but also for checking in during writing period to make sure I'm still, *Stayin' Alive*. My thanks also go out to Matthew Jackson, Jamie Kwon, Rebecca Sipthorpe, Tong Liu and Kathy Chan for the scientific support and friendships during the last two years of my DPhil and the memories inside and outside of lab that I will never forget. I would also like to thank members of the Ryan group, with special thanks to Yanyan Jiang, Jennifer Martin and Steve Stribbling for their help with the animal work and scientific input for projects. Those days we worked together in the basement animal house inhaling evaporating formalin are fixed in memory. In addition, I would like to thank Callum Beach, Fariha Mahfooz and Letitia Harris for their support during my time in the Ryan lab. For scientific contributions to the work in this thesis, I would like to thank all collaborators at Suzhou University and the Translational Histopathology Laboratory (University of Oxford), and support staff of the Biomedical Science Unit, Imaging Core, Microscopy and Flow Cytometry Core at the Department of Oncology, University of Oxford.

My College Advisor, Professor Anna Gloyn requires a special mention for the support she provided during one of the hardest periods of my DPhil – thank you, for being the strong supporter and calm voice during the toughest moments.

I would also like to thank the Oncology Student Committee for the support during my time as a Representative (couldn't have done it without you all); the Oxford University Personalised Medicine Society Committee for the stimulating discussions on the future of medicine; the Peer Supporters Community for showing me the warmth and kindness people can share during a tough period like COVID; and the community at Green Templeton College, for providing a truly warm and welcoming place to be a part of throughout the four years.

My best memories during my DPhil have been with my dearest friends Hira Javid, Tayyaba Komal, Maryam Alkadhimi, Shahd Fouad and Yi Chun Wang. I thank all of them for their support during the difficult moments of my DPhil journey, the precious memories (many full of laughter and list too long to fit here), and the friendships that will last beyond my years here. The journey would not have been the same without the love and support from you all.

The flatmates whom I have lived with for three years on Stable Close – Juan Ruiz, Michael Weinberger, and Malin Hedlund – have been a large part of my experience at Oxford and are whom I've formed close friendships with. The walks in the woods and hills (mud or no mud), midnight jam-making and pub nights at the Fishes are all an unforgettable part of my years at Oxford. Thank you for the laughter, friendship and support.

I would also like to thank my mentors whom I have known from the beginning of my scientific career. In particular, I would like to thank David Weinstock, for offering

generous help and taking concern for my studies and career; Mark Murakami, for your mentorship and generosity in scientific/ career advice and beyond – the chat we had during your wet and cold visit to London played a part in a turning point in my DPhil; and Noriaki Yoshida, for the friendship and scientific support during my visits back to Japan.

The love and support from my closest friendships, which extend beyond country borders (in many ways) have been my rock throughout my DPhil. Maxine Tan - you have been one of my biggest supporters throughout these four years. These years would not have been the same without our friendship. I would also like to thank Salome Giorgadze, Saran Liukasemsarn and Baturay Aydemir for the friendships I relied on. Thank you for being there through thick and thin.

Last, but certainly not least, the years here at Oxford would not have been possible without the love and support of my family. I thank them deeply for the support they have given me. During the toughest moments of this journey, I would look over to the card on my wall with the writing: “大丈夫。あわてない あせらない 落ち着いて 肩のちからぬいて ゆっくり深呼吸。大丈夫。" My source of strength and encouragement. ありがとう。

COVID-19 Thesis Impact Statement

The D.Phil. work in this thesis was impacted by the COVID-19 pandemic and the change in supervisors during this period. No access to laboratories and animal facilities was allowed between March 2020 and August 2020 due to lockdowns and partial access (~25-50% capacity) was allowed between August 2020 and January 2021 due to social distancing measures, impacting greatly data collection for the project. These periods correspond with the 5th and 6th terms (2nd year), and 7th and 8th terms (3rd year) of the DPhil course respectively. Additionally, the termination of ongoing animal experiments that were started before lockdown, and the inability to carry out experiments for more than 6 months until September 2020 limited the scope of my project which heavily relied on *in vivo* experiments that would be carried out across 9 months. Two changes in supervision occurred during the course of the DPhil, with the second change occurring during the pandemic in the 7-8th term (3rd year) of the coursework and requiring adjustments to new laboratory space/ equipment/ team and animal project licences. In particular, the data collection for Chapter 5 to investigate the role of STING signalling in tumourigenesis with STING inhibitors and STING KO models could not be carried out due to these disruptions. Projects were adjusted to generate and analyse large datasets including those from RNA sequencing, exome sequencing and multiplex immunofluorescence.

TABLE OF CONTENTS

Table of Contents

Radiation-induced Inflammatory Responses in Carcinogenesis and Cardiac Disease 1

Abstract 3

Acknowledgements 5

COVID-19 Thesis Impact Statement 9

Table of Contents 10

Abbreviations 17

Awards, Presentations and Publications 21

Awards 21

Presentations 21

Publications (from October 2018) 22

List of Figures 23

List of Tables 29

CHAPTER 1. Introduction 30

1.1 I Introduction 31

1.2 | Lung Cancer – Diagnosis and Treatment 32
Risk Factors 32
Diagnosis and screening 34
Management 34
1.3 | Tumour Biology – Hallmarks of Cancer and Lung Tumourigenesis 36
Hallmarks of Cancer 36
Tobacco-induced carcinogenesis in lung cancer 38
Immune evasion 40
1.4 | Cancer and its Microenvironment 42
The Immune Microenvironment 43
1.5 | Radiation Treatment for Cancer Therapy 49
Principles of radiotherapy 49
DNA damage and the DNA damage response 51
1.6 | Radiation-induced Immune Responses 53
Cytoplasmic nucleic acid sensing – the cGAS-STING pathway 55
Radiation and priming of immune cells 57
1.7 | Radiation-Induced Cardiac Disease 59
Radiation-induced cardiac toxicity in cancer therapy 59
1.8 | The Co-evaluation of Tumour Biology and Normal Tissue Biology from Cancer Therapies 62
Models to assess the tumour and its microenvironment 62
Preclinical models of radiation-induced cardiac toxicity 66
1.9 | Aims of This Thesis 67
CHAPTER 2. Materials and Methods 68
2.1 | Reagents 69

2.2 | Animal experiments and welfare 70
2.2.1 | Animal welfare 70
2.2.2 | Mouse strains 70
2.2.3 | Urethane induction of tumours 70
2.2.4 | Drug formulation and dosing schedule 71
2.2.5 | Tissue collection and sample preparation 72
2.3 | Magnetic Resonance Imaging 74
2.3.1 | MR image acquisition with cardio-respiratory gating 74
2.3.2 | MR Image analysis 74
2.4 | Electrocardiogram 75
2.4.1 | ECG data acquisition 75
2.4.2 | ECG trace analysis 76
2.5 | Irradiation 78
2.5.1 | Lead-shielded whole-thorax irradiation 78
2.5.2 | CT-guided whole-heart irradiation 79
2.6 | Immunohistochemistry 80
2.6.1 | Immunohistochemistry slide preparation 80
2.6.2 | Haematoxylin and Eosin 80
2.6.3 | Masson’s Trichrome staining 80
2.6.4 | Chromogenic detection and counterstaining 80
2.6.5 | Brightfield image slide scanning 81
2.6.6 | Infiltration analysis on HALO image analysis software 81
2.7 | Fibrosis Scoring and Quantification 82
2.7.1 | Fibrosis in the lung: Modified Ashcroft scoring 82
2.7.2 | Fibrosis in the heart 83
2.8 | Microscopy 84

2.8.1 I Second harmonic generation microscopy imaging 84

2.9 I Multiplex immunofluorescence 86

2.9.1 I Multiplex Immunofluorescence 86

2.9.2 I Image analysis 87

2.9.3 I Defining Tertiary Lymphoid Structures 87

2.10 I Enzyme-linked Immunosorbent Assay 88

2.11 I Flow cytometry 89

2.11.1 I Lung and cardiac tissue digestion 89

2.11.2 I Flow cytometry 89

2.12 I Western blotting 91

2.13 I Whole-exome sequencing and analysis 92

2.14 I RNA sequencing and functional analyses 94

2.15 I Statistical analyses 97

CHAPTER 3. Lung Tumorigenesis and Radiation-induced Tissue Toxicity in An *in vivo* Model 98

3.1 I Introduction 99

Urethane-induced A/J mouse model 99

Radiation and tumour infiltrating lymphocytes 102

3.2 I Results 104

3.2.1 I Lung adenocarcinomas can be chemically induced in an A/J mouse 104

3.2.2 I Urethane-induced lung tumour cells have a higher proportion of proliferating cells than parenchymal cells and contain infiltrating macrophages and $CD3^+$ T-cells . 108

3.2.3 I Radiation elicits differential DNA damage responses and innate immune responses in lung tumours and parenchymal tissues 112

3.2.4 I Radiation induces an acute innate immune response in the lung tumour, while potentially initiating a chronic inflammatory response in the parenchyma 114

3.2.5 I Radiation induces an initial reduction in T-cells in the tumours and a latent T-cell exclusion effect..... 116

3.2.6 I Radiation treatment has a modest anti-tumour effect on established tumours and induces lung fibrosis in the A/J model 119

3.3 I Discussion 122

CHAPTER 4. Radiation-Induced Immune Responses in Lung Carcinogenesis and Modification of The Tumour Microenvironment 125

4.1 I Introduction..... 126

RT in TLS formation 126

RT in carcinogenesis..... 127

4.2 I Results 129

4.2.1 I Radiation treatment of pre-neoplastic lungs limits tumour development in carcinogen-induced A/J mice 129

4.2.2 I RT of pre-neoplastic lungs result in long-term modifications in the lung immune environment but not systemic immunity 131

4.2.3 I An increase in cell division pathways and a delayed IFN response are observed in the preneoplastic lung 133

4.2.4 I RT induces an increase in T-cells in tertiary lymphoid structures in the carcinogen-exposed lung 138

4.2.5 I RT downregulates cell division and induces an acute inflammatory response in the preneoplastic lung 142

4.3 I Discussion 150

CHAPTER 5. STING in Lung Tumourigenesis and Long-Term Immunity 154

5.1 | Introduction 155

5.2 | Results 158

5.2.1 | Urethane pre-treatment sequesters IFN- β levels and T-cell infiltration stimulated by DMXAA 158

5.2.2 | Intervention with a STING agonist during tumour initiation increases tumour burden 162

5.2.3 | STING agonist treatment of pre-neoplastic tissue results in a long-term increase in lymphocytes in the lung but does not increase tertiary lymphoid structures 166

5.2.4 | RT and DMXAA treatments at tumour initiation have an additive effect on limiting tumour growth 169

5.3 | Discussion 171

CHAPTER 6. Radiation-induced cardiac disease in an A/J mouse model.....174

6.1 | Introduction 175

Mouse studies of radiation-induced cardiac toxicity 175

Mechanisms of resolving DNA damage in cardiac tissue – innate immune responses in the heart 176

6.2 | Results 179

6.2.1 | Establishing a pre-clinical model to understand radiation-induced cardiac effects 179

6.2.2 | Arrhythmia and ECG waveform changes in the heart following radiation treatment 183

6.2.3 | Radiation induces fibrosis in the pericardium and perivasculature 187

6.2.4 | Persistent DNA damage in cardiomyocytes is associated with cardiac fibrosis 191

6.2.5 | Stimulation of IFN increases cardiac fibrosis 195

6.2.6 | Macrophage infiltration and M2 macrophage polarisation in cardiac tissue after radiation treatment 197

6.2.7 | Fibroblast activation in radiation-induced cardiac fibrosis 200

6.2.8 | T-cell immunity is an unlikely contributor to cardiac fibrosis in the A/J model .. 202

6.3 | Discussion 204

CHAPTER 7. Conclusions and Discussion 208

Bibliography 217

Appendix 247

Word count: 45,000 words

ABBREVIATIONS

Abbreviation	Full term
53BP1	Tumour protein p53 binding protein 1
A/J	A/JOlaHsd
ALK	Anaplastic lymphoma kinase
ANOVA	Analysis of variance
APC	Antigen-presenting cell
APOBEC	Apolipoprotein B mRNA editing enzyme, catalytic polypeptide-like
ATM	Ataxia-telangiectasia mutated
ATR	Ataxia-telangiectasia and Rad3-related
B220	CD45R/ PTPRC, Protein tyrosine phosphatase, receptor type, C
BER	Base excision repair
BrdU	Bromodeoxyuridine
C57BL/6	C57BL/6JRccHsd
CAF	Cancer-associated fibroblasts
CC3	Cleaved caspace 3
CD103	Cluster of Differentiation 103
CD163	Cluster of Differentiation 163
CD206	Cluster of Differentiation 206
CD3	Cluster of Differentiation 3
CD31	Cluster of Differentiation 31
CD4	Cluster of Differentiation 4
CD45	Cluster of Differentiation 45
CD68	Cluster of Differentiation 68
CD8	Cluster of Differentiation 8
CD80	Cluster of Differentiation 80

CDX	Cell-line derived xenograft
cGAS	Cyclic guanosine monophosphate-adenosine monophosphate synthase
CRT	Chemoradiotherapy
CT	Computed tomography
CTLA-4	Cytotoxic T lymphocyte-associated protein 4
CXCL13	Chemokine ligand 13
CYP2E1	Cytochrome P450 2E1
DAB	3,3'-diaminobenzidine
DAMP	Damage associated molecular pattern
DC	Dendritic cell
DDR	DNA damage response
DMSO	Dimethyl sulfoxide
DNA	Deoxyribonucleic acid
DNA-PK	DNA-dependent protein kinase
DSB	Double strand break
dsDNA	Double stranded DNA
EBRT	External beam radiation therapy
ECM	Extracellular matrix
EGFR	Epidermal growth factor receptor
FDC	Follicular dendritic cell
FRC	Fibroblastic reticular cell
GEMM	Genetically engineered mouse model
Gy	Gray
H & E	Haematoxylin and eosin
H2AX	Histone H2AX
HEV	high endothelial venules
HR	Homologous recombination
HRV	Heart rate variability
i.p.	Intraperitoneal
IC_{50}	50% inhibitory concentration
ICI	Immune checkpoint inhibitors
IF	Immunofluorescence
IFN	Interferon
IgG	Immunoglobulin G
IGRT	Image-guided radiation therapy

IHC	Immunohistochemistry
IMRT	Intensity-modulated radiation therapy
IR	Ionising radiation
IRF3	Interferon regulatory factor 3
K-ras	Kirsten rat sarcoma viral oncogene homologue
KO	Knock-out
LET	Linear energy transfer
LOH	Loss of heterozygosity
LUAD	lung adenocarcinoma
Ly6G/C	Lymphocyte antigen 6 GC
MDSC	Myeloid-derived suppressor cell
MHC-I	Major histocompatibility complex class I
MHC-II	Major histocompatibility complex class II
MRI	Magnetic resonance imaging
mRNA	Messenger ribonucleic acid
MT	Masson's Trichrome
MTD	Maximum tolerated dose
mTOR	Mechanistic target of rapamycin
NC3R	National Centre for the Replacement, Refinement & Reduction of Animals in Research
NER	Nucleotide excision repair
NHEJ	Non-homologous end joining
NHS	National Health Service
NSCLC	Non-small cell lung cancer
OAR	Organ at risk
ºC	Celcius
p.o.	*Per os*, orally
p16	Protein 16
p21	Protein 21
p53	Tumour protein 53
Pas1	Pulmonary adenoma susceptibility locus 1
PBS	Phosphate buffered saline
PD	Pharmacodynamic
PD-1	Programmed cell death protein 1
PD-L1	Programmed death-ligand 1
PDX	Patient-derived xenograft

PEG	Poly(ethylene glycol)
PET	Positron emission tomography
PM	Particulate matter
PNAd	Peripheral lymph node addressin
RIHD	Radiaton-induced heart disease
RMSSD	root mean square of successive differences
ROI	Region of interest
ROS	Reactive oxygen species
RT	Radiation therapy
RT	Radiotherapy
SABR	Stereotactic ablative body radiotherapy
SARRP	Small animal radiation research platform
SASP	Senescence-associated secretory phenotype
SCID	Severe combined immunodeficiency
SCLC	Small cell lung cancer
SEM	Standard error of the mean
SLO	Secondary lymph node organ
SSB	Single-strand break
ssDNA	Single-stranded DNA
STING	Stimulator of interferon genes
TBK1	TANK-binding kinase 1
TCR	T-cell receptor
TIL	Tumour-infiltrating lymphocyte
TKI	Tyrosine kinase inhibitors
TLS	Tertiary lymphoid structure
TME	Tumour microenvironment
WES	Whole-exome sequencing

Awards, Presentations and Publications

Awards

National Cancer Research Institute Award, November 2020

Awarded top 5 abstracts submitted to the National Cancer Research Institute Annual Meeting 2020

Presentations

Radiation Research Society Conference, Virtual, October 2021

Poster Presentation

A pre-clinical model of radiation-induced cardiac disease: cardiac fibrosis and electrophysiological changes six months after X-irradiation in an A/J mouse model

National Cancer Research Institute Conference, Virtual, November 2020

Selected for National Cancer Research Institute Award and Live Oral Presentation

Radiation and DMXAA prevent tumour development in a urethane-induced lung cancer model through inflammatory response

Oxford Institute for Radiation Oncology Symposium, Oxford, June 2020

Oral Presentation

The impact of radiation on the immune responses in lung normal and tumour tissues

Oxford Institute for Radiation Oncology Symposium, Oxford, June 2019

Poster Presentation

Radiation-induced heart disease: Protecting the heart from late toxicities

Publications (from October 2018)

1. Murakami, M. A., Winter, P. S., Navia, A. W., Bilal, L. L., Strouf, H., **Shigemori, K.**, Gupta, A., ... Weinstock, D. M., Shalek, A. K. Single-cell profiling reveals programs mediating oncogenic kinase-independence and mi-nimal residual disease in BCR-ABL-rearranged acute lymphoblastic leukemia. *Cancer Research* (in review).
2. Jiang, Y., Martin, J., Alkadhimi, M., **Shigemori, K.**, Kinchesh, P., ... Ryan, A. J. (2021). Olaparib increases the therapeutic index of hemithoracic irradiation compared with hemithoracic irradiation alone in a mouse lung cancer model. *British Journal of Cancer*.
3. Yoshida, N., **Shigemori, K.**, Cordero, N. A., ... Weinstock, D. M. (2020) Genomic landscape of young ATLL patients identifies frequent targetable CD28 fusions. *Blood*. **(Editors' Choice)**
4. Beheshti, A., Stevenson, K., Vanderburg, C., Ravi, D., McDonald, J. T., Christie, A. L., **Shigemori, K.**, Jester, H., Weinstock, D. M., Evens, A. M., (2019) Identification of Circulating Serum Multi-MicroRNA Signatures in Human DLBCL Models. *Scientific Reports*.
5. Loss, C., Liu, Y., Kolb, K.E., Christie, A. L., Scoyk, A. V., Prakadan, S. M., **Shigemori, K.**, Stevenson, K. E., ... Weinstock, D. M. (2019). Mechanisms of lymphoma clearance induced by high-dose alkylating agents. *Cancer Discovery*.
6. Koch, R., Christie, A. L., Crombie, J. L., Palmer, A. C., Plana, D., **Shigemori, K**., Morrow, S. N., ... Weinstock, D. M. (2019). Biomarker-driven strategy for MCL1 inhibition in T-cell lymphomas. *Blood*.
7. Lee, D., Zheng, X., **Shigemori, K.,** Krasniak, C. ... Ahmad, S. T. (2019). Expression of mutant CHMP2B linked to neurodegeneration in humans disrupts circadian rhythms in Drosophila. *FASEB*.
8. Ng, S. Y., Yoshida, N., Christie, A. L., Murakami, M. A., **Shigemori, K**., Morrow, S. N., ... Weinstock D. M., Koch, R. (2018). Preclinical models of T-cell lymphoma define targetable vulnerabilities. *Nature Communications*.

LIST OF FIGURES

Figure 1.1. Updated Hallmarks of Cancer. 37

Figure 1.2. Mutations found in NSCLC....39

Figure 1.3. The tumour microenvironment. 42

Figure 1.4.Tertiary lymphoid structure cell composition, location, maturation states, and molecular characteristics. 46

Figure 1.5. The therapeutic window of radiotherapy. 50

Figure 1.6. Radiation-induced DNA damage....51

Figure 1.7. DNA repair mechanisms. Schematic outlining mutagenic sources, DNA lesions and repair mechanisms. 53

Figure 1.8. The cGAS-STING pathway. 56

Figure 1.9. Radiation-induced normal tissue toxicities. 60

Table 1.1. A summary of the advantages and disadvantages of preclinical mouse models. 66

Table 2.1. List of drugs, respective vehicles and dosing schedules used in the in vivo experiments in this thesis. 71

Figure 2.1. Perfusion and isolation of the mouse heart. 72

Figure 2.2. ECG leads. 75

Figure 2.3. ECG waveform segmentation. 76

Figure 2.4. Lead shielding of the mouse for thoracic irradiation. Lead 78

Figure 2.5. Guidelines for fibrosis scoring on the Ashcroft scale. 82

Figure 2.6. HALO AI tissue segmentation of heart structures. 83

Figure 2.6. Collagen fibre analysis on ct-FIRE. 85

Table 2.2. Antibody panels for flow cytometry 90

Figure 3.1. Urethane induces lung adenocarcinomas in A/J mice. 105

Figure 3.2. Lung tumour induction increased with higher concentration or frequency of carcinogen dose. 106

Figure 3.3. Lung tumours increase in numbers and tumour burden weeks after urethane treatment. 107

Figure 3.4. Urethane-induced lung tumours have a low rate of proliferation. 110

Figure 3.5. Established urethane-induced lung tumours contain infiltrating macrophages and $CD3^+$ T-cells. 111

Figure 3.6. Increase in DNA-damage response 2 hours after 15 Gy thorax irradiation. 113

Figure 3.7. M2 macrophages increase in lung normal tissue after RT. 115

Figure 3.8. T-cells depleted 24 hours after RT and recovered back to baseline 7 days after RT. 117

Figure 3.9. CD8 and CD4 T-cell exclusion at the tumour-parenchyma border 7 days post-RT 118

Figure 3.10. RT reduces lung tumour counts and tumour burden. 120

Figure 3.11. RT induces fibrosis in the lung 6 months after treatment.....121

Figure 4.1. RT-intervention during lung tumourigenesis in A/J mice significantly reduces tumour counts and tumour burden. 130

Figure 4.2. RT intervention during tumour initiation creates a long-term inflammatory state in the lung.....132

Figure 4.4. DNA damage response and STING upregulated in the preneoplastic lung. 137

Figure 4.6. RT induces an increase in B-cells in the lung parenchyma. 141

Figure 4.7. Studying the early events following RT of pre-neoplastic lungs.....142

Figure 4.8. RT of the preneoplastic lung stimulates immune responses and suppresses cell division and chromosomal segregation.....144

Figure 4.9. Nuclear division, chromosomal segregation and cell division pathways are upregulated in urethane and downregulated in urethane + RT condition. 146

Figure 4.10. RT of the pre-neoplastic lung increases CD4+ and CD8+ T-cells and decreases neutrophils, macrophages and MDSCs in the lung. 148

Figure 4.11. RT of the pre-neoplastic lung induces no change in IFN-β and TNF-α concentration in the plasma. 149

Figure 5.1. Mechanisms of tumour-suppressive action of cGAS-STING. 156

Figure 5.2. Studying the early events in the lung following DMXAA treatment during tumour initiation. 159

Figure 5.3. DMXAA treatment stimulates T-cell infiltration in the lung with minimal impact on neutrophil, macrophage and MDSC populations in the lung. 161

Figure 5.4. Intervention of lung tumourigenesis with a STING agonist. 162

Figure 5.5. DMXAA treatment during lung tumourigenesis reduces tumour counts and increases tumour burden.....163

Figure 5.6. DMXAA treatment during tumourigenesis results in tumours that are histologically different from urethane-treated control. 164

Figure 5.7. DMXAA treatment during tumourigenesis increases resident leukocytes in the lung but has little impact on the number of tertiary lymphoid organs. 167

Figure 5.8. DMXAA treatment stimulates an increase in B-cells and $CD8^+$ T-cells in the lung.....168

Figure 5.9. RT + DMXAA treatment during tumourigenesis has an additive anti-tumourigenic impact on lung tumour growth. 170

Table 6.1. Summary of clinical and pathophysiological phenotypes of late radiation-induced cardiac effects in A/J mice. 180

Figure 6.1. Heart and thoracic heart irradiation of A/J mice. 181

Figure 6.2. Hypertrophic cardiomyopathy and sudden death were observed in radiation-treated A/J mice. 182

Figure 6.3. Cardiac RT is associated with an increase in heart rate variability. 185

Figure 6.4. Cardiac RT Increases QTc and decreases PR interval. 186

Figure 6.5. Cardiac irradiation above 13 Gy can induce pericardial and perivascular fibrosis 6 months after treatment in an A/J mouse model. 188

Figure 6.6. SHIM analysis of collagen fibres in the pericardium indicates that radiation does not induce a change in length, width or straightness of collagen fibres. 190

Figure 6.7. Persistent DNA-damage response in the heart contributes to radiation-induced cardiac fibrosis. 192

Figure 6.8. Treatment with DDR modulators increases pericardial fibrosis six months after treatment. 194

Figure 6.9. Stimulation of IFN increases perivascular fibrosis. 196

Figure 6.10. Analysis of immune cell infiltration and fibroblast activation with flow cytometry. 198

Figure 6.11. Macrophages infiltrate cardiac tissue post-RT and polarise toward an M2-like population. 199

Figure 6.12. Cardiac fibroblasts are not activated 7 days after RT but potentially six months after RT.....201

Figure 6.13. No change in CD3+ T-cell populations in cardiac tissue 7 days after RT and no change in cardiac fibrosis after anti-PD-L1 antibody treatment. 203

Figure 7.1. The 'vulnerable state' of preneoplastic pulmonary cells. 210

Figure 7.2. Radiation-induced cardiac toxicity in the A/J mouse model. 213

Appendix 1. Equipment, machines and their manufacturers. 248

Appendix 2. Specifications for MR image acquisition settings. 252

Appendix 3. Physical set-up of irradiation rigs. (.....253

Appendix 4. Variation in radiation dose received in positions A-B on mouse rig and depth. 254

Appendix 5. Flow cytometry gating strategies. 255

Appendix 6. Script for *DESeq2* for differential gene expression analysis. 256

Appendix 7. Representative histology images of papillary, solid, and mixed tumours. 262

Appendix 8. Tracking lung tumour growth in the A/J mouse with MRI. 263

Appendix 9. Categories of immune infiltration based on histological characteristics of tumour-infiltrating T lymphocytes. 264

Appendix 10. Lung tumour and normal cells demonstrate different DNA damage response kinetics after RT. 265

Appendix 11. Plasma IFN-β and TNF-α levels 24 hours to 7 days after 15 Gy thorax RT. 266

Appendix 12. 10 mg/ kg and 15 mg/ kg doses of DMXAA were well-tolerated with 13 Gy thorax RT. 267

LIST OF TABLES

Table 1.1. A summary of the advantages and disadvantages of preclinical mouse models. 66

Table 2.1. List of drugs, respective vehicles and dosing schedules used in the in vivo experiments in this thesis. 71

Table 2.2. Antibody panels for flow cytometry. List of antibodies used for lymphoid, myeloid, fibroblast and macrophage polarisation analyses by flow cytometry. 90

Table 6.1. Summary of clinical and pathophysiological phenotypes of late radiation-induced cardiac effects in A/J mice. 180

CHAPTER 1. INTRODUCTION

1.1 | INTRODUCTION

Radiation therapy is a powerful tool. In the clinical setting, more than half of cancer patients will receive radiotherapy during their treatment (Najafi et al., 2021), often with a curative intent. Research into radiotherapy is focused on improving anti-tumour effectiveness while minimising normal tissue toxicity. Understanding the biology underpinning immunobiological responses to radiotherapy is critical to advancing our understanding of the role of radiation in shaping immune responses and how this could be exploited for future therapeutic gain. These important clinical and biological questions are therefore the focus of this work.

In the past decade, immunotherapy has been introduced into the clinic as a new mode of cancer therapy along with surgery, radiotherapy and chemotherapy, and has been used in combination with other modes of treatment including radiotherapy. In the era of immunotherapy, research on radiotherapy has developed from the observation that radiation induces immune responses, with excitement for its potential capacity to generate an "*in situ* vaccination" effect. There is growing interest in the field to understand the radiation-induced immune events for its potential for enhanced anti-cancer effects in combination with immunotherapies. In addition to studying the anti-cancer effects of radiation and immune modulators, there is also a need to understand the impact radiation has on the normal tissues surrounding the tumour; for both the long-term adverse effects it may induce, and for the impact it may have on modulating the microenvironment around the tumour. We will therefore assess the impacts of radiation and other cancer therapies in tumours and adjacent and non-adjacent normal tissues in a carcinogen-induced lung adenocarcinoma mouse model.

1.2 | LUNG CANCER – DIAGNOSIS AND TREATMENT

Lung cancer is one of the most frequently diagnosed cancers and the leading cause of cancer-related deaths worldwide with an estimated 2.2 million new cases and 1.79 million deaths per year, accounting for 18% of cancer-related deaths (*Global Cancer Observatory: cancer today*; Thai et al., 2021). Tobacco smoking remains a major risk factor for lung cancer (*American Cancer Society. Cancer Facts and Figures 2015.*). Due to absence of clinical symptoms and effective screening programmes, most lung cancers are diagnosed at advanced stages. Consequently, despite promising advances in clinical management, lung cancer mortality remains high, with over half of patients diagnosed with lung cancer resulting in death within one year, and a 5-year survival rate of 22.9% (*National Cancer Institute. SEER Cancer Statistics Review, 2012-2018*).

Lung cancer is broadly classified as non-small cell lung cancer (NSCLC) or small cell lung cancer (SCLC), which account for 85% and 15% of total diagnoses respectively (Thai et al., 2021). NSCLC is further classified into three histological subtypes, with adenocarcinomas being the most common subtype (40%), followed by squamous cell carcinoma (25%) and large cell carcinoma (10%) (Noguchi et al., 1995; "Non-Small Cell Lung Cancer Treatment," 2002; Travis et al., 2015).

Risk Factors

Smoking is the leading risk factor for lung cancer development, accounting for approximately 80% of lung cancer deaths. An increase in lung cancer cases followed tobacco manufacturing and consumption in the 1900s (Doll & Hill, 1950). Increases in

the number of years or the number of packs smoked per day is correlated with an increase in risk for lung cancer (National Center for Chronic Disease et al., 2014).

However, despite this prominent risk factor, 10-25% of lung cancer cases occur in non-smokers[1]. Other risk factors such as second-hand smoking, increased exposure to radon (S. Darby et al., 2005) and occupational exposure (e.g. asbestos, arsenic compounds, beryllium or beryllium oxide) (Spyratos et al., 2013) may contribute to disease occurrence in non-smoker patients. Air pollution has also been significantly associated with an increase in lung cancer (Raaschou-Nielsen et al., 2013); every 10 $\mu g/m^3$ elevation in fine particulate air pollution is associated with an 8% increase in lung cancer mortality (Pope Iii, 2002). A breaking abstract at a recent ESMO conference reports that an increase in particulate matter 2.5 levels was associated with an increased risk of NSCLC harbouring EGFR mutations (a mutation observed more frequently in non-smokers) (Swanton et al., 2022).

Genetic susceptibility has also been thought to increase the risk of lung cancer development, particularly in patients who develop the disease under the age of 50 (Matakidou et al., 2005). An epidemiological study showed that the familial history of lung cancer was associated with a 1.5-fold increase in risk in developing the same disease (Coté et al., 2012). Furthermore, smokers who were carriers of *TP53* germline mutations were three times more likely to develop lung cancers than non-smokers (Hwang et al., 2003). Recently, it has been found that germline exon 20 T790M mutations of EGFR (Gazdar et al., 2014), and mutations in the transmembrane domain

[1] Non-smokers: defined as individuals who have smoked fewer than 100 cigarettes in their lifetime.

of HER2 (Yamamoto et al., 2014) may be oncogenic and cause hereditary and sporadic lung adenocarcinomas.

Diagnosis and screening

For the diagnosis of lung cancers with clinical presentation in the clinic, the Tumour-Node-Metastasis (TNM) classification system forms the basis for staging (Goldstraw et al., 2016). An array of imaging technologies is available to allow for the lung cancer detection, however, current methods for early detection and diagnosis remains limited due to our lack of molecular understanding of early lung cancer development.

In the UK, guidelines from the National Institute for Health and Care Excellence recommend a chest X-ray if lung cancer is suspected from a display of symptoms (National Institute for Health and Care Excellence, 2020). This exam is typically followed by computed tomography (CT) to confirm the presence of a tumour (National Health Service, 2019; National Institute for Health and Care Excellence, 2020). Additional testing can include a positron emission tomography (PET) scan, a bronchoscopy, or an endobronchial ultrasound along with a biopsy of the primary tumour and suspected lymph nodes (National Health Service, 2019). If the tumour is suspected to have metastasised, a PET scan, magnetic resonance imaging (MRI) scan, bone scan, or abdominal ultrasound can also be used (Cancer Research UK, 2019a).

Management

NSCLC is a heterogeneous disease and requires accurate assessment and staging of the cancer to choose the appropriate treatment for each patient. Tumours are generally classified into three treatment categories: resectable, locally advanced

or advanced. NSCLC treatment options include surgery, chemotherapy, and radiotherapy, which can be combined with immunotherapy or targeted approaches including treatment with anti-angiogenic monoclonal antibodies or tyrosine kinase inhibitors (TKI) if the tumour harbours specific mutations.

With the emergence of immune checkpoint inhibitors (ICIs) in the past decade, harnessing the body's immune system to target tumours has become possible. Currently, ICIs include antibodies against programmed cell death protein 1 (PD-1), programmed cell death 1 ligand 1 (PD-L1), and cytotoxic T lymphocyte-associated protein 4 (CTLA4). Although some patients (between 20-40%) show dramatic and durable responses, the majority do not benefit from ICIs. Reasons underpinning these diverse outcomes are yet to be understood, and the search for alternative treatment modalities that could stimulate the immune system, and the possibility of combination approaches for improved anti-tumour response has driven research interest in this area.

1.3 | Tumour Biology – Hallmarks of Cancer and Lung Tumourigenesis

This section provides an overview of tumour biology, with a particular focus on the initial stages of cancer development (neoplastic transformation) and mechanisms of immune evasion. Carcinogenesis will be summarised here in the context of tobacco-induced lung cancers.

Hallmarks of Cancer

The evolution of cancer from normal cells to neoplasia and malignancy is a multi-step process, where cancers acquire the functional capabilities unique to cancers as they progress. The 'functional capabilities' of cancer are laid out as the "Hallmarks of Cancer", proposing 14 hallmarks in the recently revised version by Hanahan (Hanahan, 2022). The hallmarks of cancer include: sustained proliferative signalling, evasion of growth suppression, resistance to cell death, replicative immortality, angiogenesis, invasion and metastasis, reprogramming of cell metabolism, and evasion of immune destruction (Hanahan & Robert, 2011; Hanahan & Weinberg, 2000); the newly proposed hallmarks in the 2022 revision include phenotypic plasticity, epigenetic reprogramming, polymorphic microbiomes and cell senescence (Hanahan, 2022) (**Figure 1.1**). The acquisition of these hallmarks – enabling the preneoplastic cells to transform into a neoplastic cell and continue to adopt more functional traits - is driven initially by genomic instability and the generation of genomic diversity (Hanahan, 2022; Hanahan & Robert, 2011). The pathogenesis of cancer is complex with heterogeneity and dynamic temporal changes contributing to this complexity. Not only do cancers differ from patient to patient and tumour to tumour within the same patient

(intertumour heterogeneity) but there is also a diversity of cells that make up the cancer cells and stromal components within individual tumours (intratumoural or clonal heterogeneity). In particular, the intratumoral heterogeneity poses a challenge in tackling cancer as the diverse subpopulation of cells can generate variable responses to therapeutic agents (Pribluda et al., 2015). Additionally, single-cell RNA sequencing studies in lung cancer demonstrate this complexity by showing that clones have multiple developmental lineages which can dynamically inter-converge with one another to drive heterogeneity (Drapkin & Minna, 2020; Marjanovic et al., 2020), with many other studies reporting similar complexities in the evolutionary process of cancers (Bailey et al., 2021; Jamal-Hanjani et al., 2017; McGranahan & Swanton, 2017; Vendramin et al., 2021).

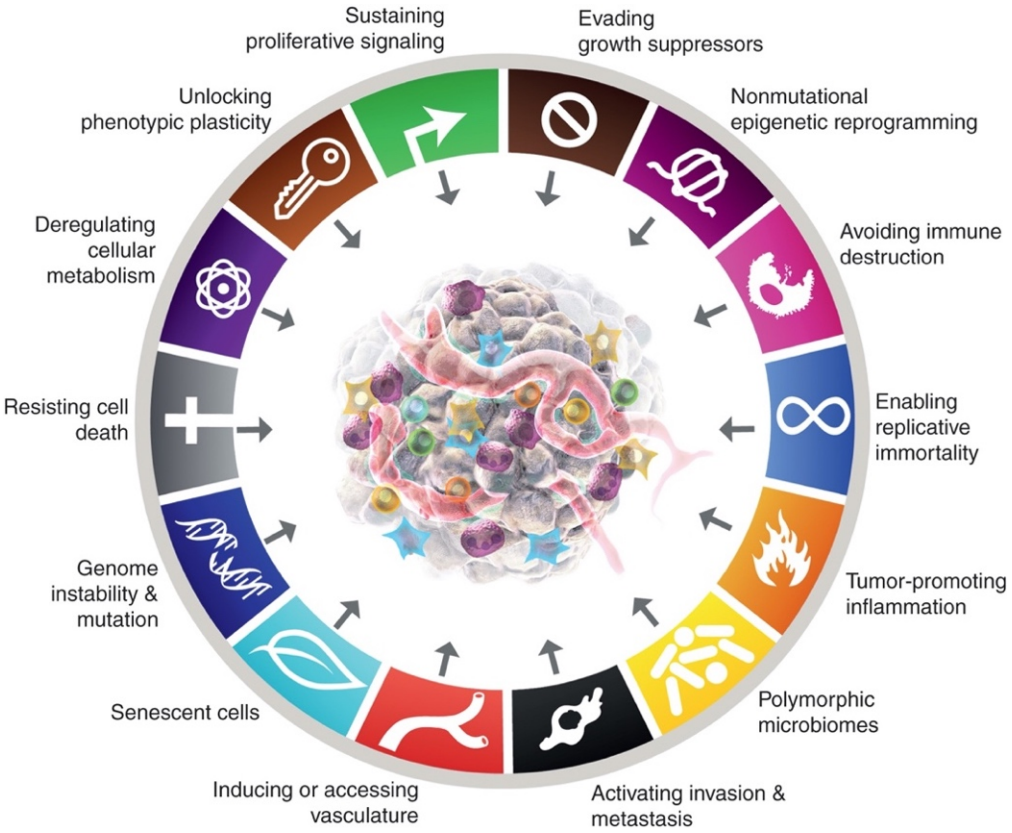


Figure 1.1. Updated Hallmarks of Cancer. The canonical and prospective new additions to the "Hallmarks of Cancer". Proposed additional hallmarks are: "unlocking phenotypic plasticity," "nonmutational epigenetic reprogramming," "polymorphic microbiomes," and "senescent cells." Figure adapted from (Hanahan, 2022)

Tobacco-induced carcinogenesis in lung cancer

Tobacco smoke is made up of more than 7000 chemicals, including over 70 that are known to cause cancer. These cancer-causing chemicals are referred to as carcinogens. Some of the most toxic chemicals in tobacco smoke are: benzo[a]pyrene (BaP), 4-(methylnitrosamino)-1-(3-pyridyl)-1-butanone (NNK), 4-aminobiphenyl and urethane (Centers for Disease et al., 2010). Most carcinogens from tobacco products require metabolic action before they can react with DNA, however some are able to act directly on DNA. The metabolic activation generally requires conversion of the compound by the cytochrome P540 enzyme. The reaction of the activated carcinogen with the DNA results in DNA adducts, which can be removed by DNA repair mechanisms, but are mutagenic when they escape DNA repair and the adducts persist through DNA replication (Hecht, 2003). DNA adducts from cigarette smoking result most frequently in G>T and G>A mutations (Loechler et al., 1984; Seo et al., 2000; Singer & Essigmann, 1991).

Lung tumours are heterogeneous and have a diverse profile of genetic abnormalities. The most common mutations are found in TP53 (46%), KRAS (33%), STK11 (17%), EGFR (14%), BRAF (10%), SETD2 (9%), and PIK3CA (7%) ("Comprehensive molecular profiling of lung adenocarcinoma," 2014) (**Figure 1.2**). Driver mutations such as EGFR or ALK occur early in tumour progression and are present in all tumour cells (termed ‘truncal’ or ‘trunk’ mutations). By contrast, branch mutations are confined to specific subclones within one tumour, leading to intratumoural heterogeneity and potentially causing resistance to cancer therapies. The branch subclones can have high levels of mutations, such as those caused by the

apolipoprotein B mRNA editing enzyme, catalytic polypeptide-like (APOBEC) family of enzymes (Jamal-Hanjani et al., 2017; Yoshida et al., 2020).

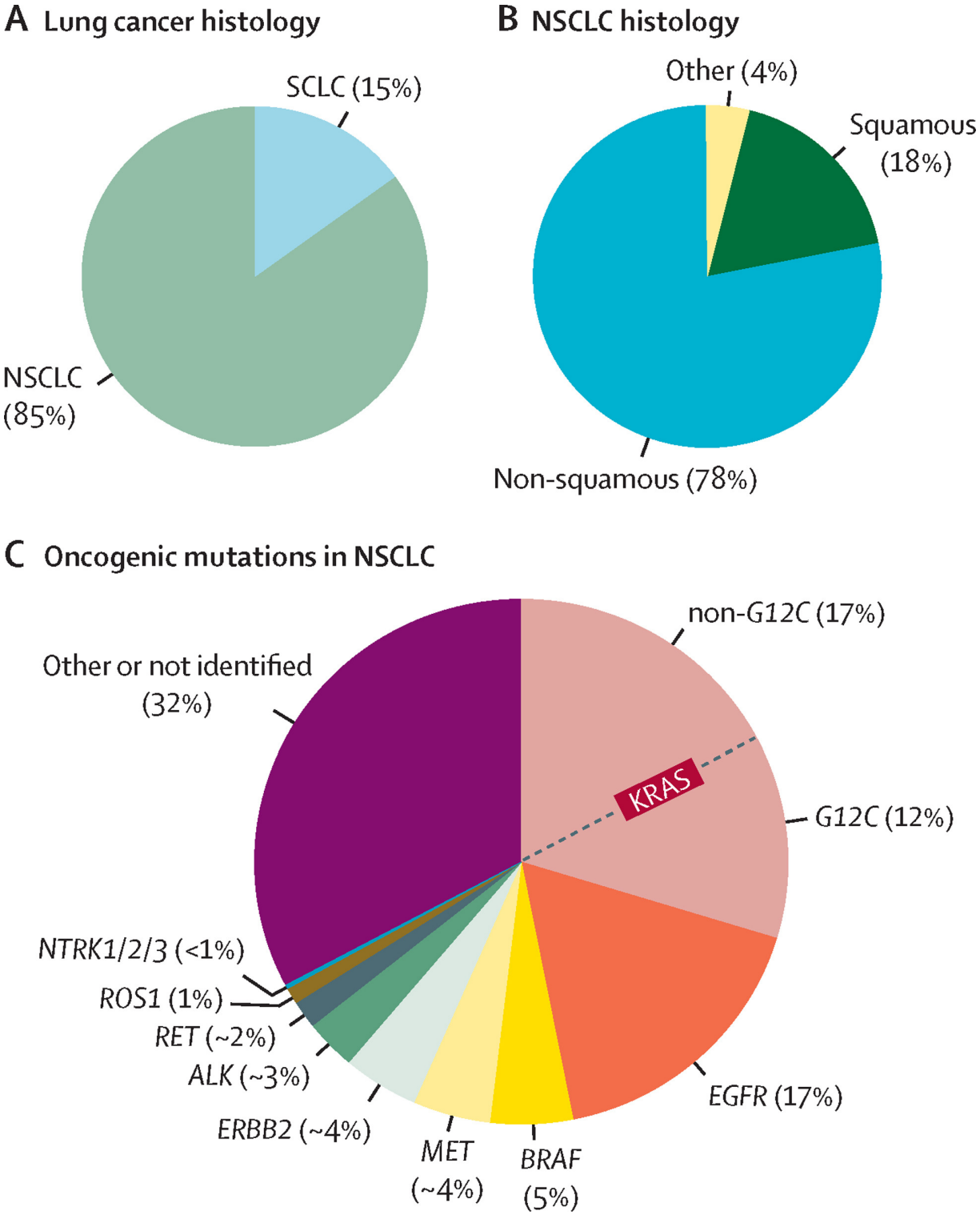


Figure 1.2. Mutations found in NSCLC. *KRAS*, *EGFR*, *BRAF*, and *MET* are the most commonly identified mutations in non-small cell lung cancers. Figure adapted from (Thai et al., 2021).

Immune evasion

Cancers undergo an evolutionary process of genetic diversification and selective pressures. The immune system can recognise antigens on the surface of the tumour cell, and therefore apply a selection pressure for clones that can evade detection by the immune system or withstand the immune response.

The immune system, through interactions with neoplastic cells throughout its evolutionary process, can shape the characteristics of the emerging tumours. Depending on the context of the immune environment and the nature of the tumour-immune interactions, the immune system can either promote or suppress tumour growth. The process whereby the immune system constrains or promotes tumour development is termed cancer immunoediting (Dunn et al., 2004; Schreiber et al., 2011). Cancer immunoediting consists of three phases: elimination (i.e., cancer immunosurveillance), equilibrium, and escape. During the elimination phase, the innate and adaptive cells cooperate to detect and kill the early tumours before they become clinically apparent. The tumour subclones that survive the elimination phase enter the equilibrium phase, whereby the immune cells can hold the tumour cells in a state of dormancy. Finally, in the escape phase, the tumours become capable of inducing immunosuppression through the production of cytokines and growth factors and recruitment of immunosuppressive cells (Dunn et al., 2004; Schreiber et al., 2011).

A wide-scale genomic, transcriptomic and pathologic analyses of samples collected from 88 patients with early-stage lung cancer (“Tracking Non-Small-Cell Lung Cancer Evolution through Therapy” (TRACERx) clinical study) found several key mechanisms through which the tumours evaded the immune system, with the majority of tumours harbouring at least one of these mechanisms of immune evasion. These

included: HLA loss or downregulation of expression (Garrido et al., 2017; McGranahan et al., 2017; Tran et al., 2016), defects in antigen presentation such as loss of B2M (Drake et al., 2006) and elimination of neoantigens through copy number loss (Anagnostou et al., 2017). Furthermore, the studies revealed that the mechanism of immune evasion depended on the tumour immune infiltration landscape. Tumours considered “immune cold” were high in copy-number loss of clonal neoantigens and decreased in immunoediting as the tumour evolved, whereas “immune hot” tumours exhibited HLA loss of heterozygosity (LOH) or a decrease in neoantigens (Rosenthal et al., 2021).

1.4 | CANCER AND ITS MICROENVIRONMENT

Cancers are complex, composed not just of tumour cells, but also non-tumour components such as immune cells, fibroblasts, blood vessels, extracellular matrix (ECM) and an extracellular milieu of chemokines and cytokines. The non-tumour cell compartment around the tumour is referred to as the tumour microenvironment (TME) (**Figure 1.3**). The TME consists of a sophisticated network of interactions and crosstalk between cancer cells and the cellular and non-cellular components. These interactions have been recognised to play an important role in tumorigenesis and cancer progression (Hanahan & Coussens, 2012). An overview of the immune and fibroblast components that make up the tumour microenvironment is shown in **Figure 1.3**.

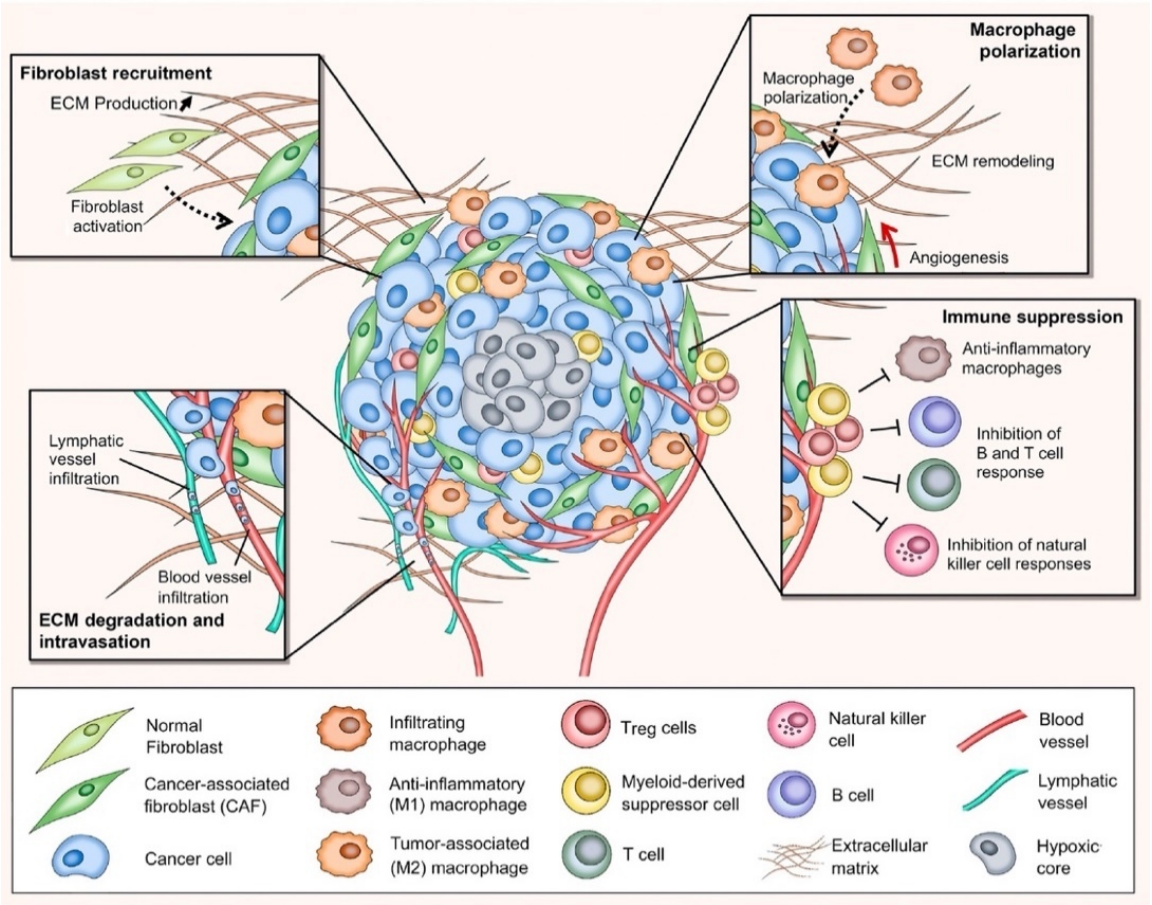


Figure 1.3. The tumour microenvironment. The TME consists of immune cells, fibroblasts, blood vessels, extracellular matrix (ECM) and chemokines and cytokines. Figure adapted from (Rodrigues et al., 2021).

The Immune Microenvironment

Tumour-infiltrating lymphocytes

Recent studies have shed light on the complex interactions between cancers and the immune cells in the TME, highlighting the importance of these interactions in cancer prognosis and outcome of treatments with ICIs (Bates et al., 2006; Clemente et al., 1996; Galon et al., 2006; Johnson et al., 2000). The characteristics of the immune microenvironment differs between patients, consisting of varying populations of T-cells, B-cells, dendritic cells (DCs), natural killer (NK) cells, myeloid-derived suppressor cells (MDSCs), neutrophils and macrophages. It is recognised that infiltrating immune cells play a dual role in cancer: they can either suppress tumour growth through increased immunological surveillance (Berraondo et al., 2016; Burnet, 1970), or facilitate tumour growth through immunosuppression (Schreiber et al., 2011), depending on their composition and density. Specifically, cytotoxic T-cells and helper T-cells are generally associated with a positive prognosis for cancers, while regulatory T-cells (T_{regs}) and MDSCs are thought to be key players in inhibiting anti-tumour responses.

Cytotoxic T-cells can produce a strong antitumour response through the release of cytokines and cytotoxic molecules such as type I interferons (IFN), tumour-necrosis factor-α (TNF-α), perforin and granzymes. Additionally, these cells form a subset of memory populations such as central memory T (TCM), effector memory T (TEM), and tissue-resident memory cells (TRM) that can provide long-term protection after the initial insult (Martin & Badovinac, 2018). Helper T-cells promote the priming of cytotoxic T-cells through stimulation of CD40 on DCs resulting in the release of cytokines including IL-12, IL-15 and IFN-γ, increased antigen presentation, and the recruitment

of B-cells and naïve $CD8^+$ T-cells. T_{regs}, when stimulated, inhibit tumour-specific T-cell activity through the production of immunosuppressive cytokines IL-10 and TGF-β, and by expression of inhibitory co-stimulatory molecules CTLA-4, PD-1, and PD-L1. MDSCs are myeloid progenitor cells and immature myeloid cells capable of inhibiting lymphocyte function by stimulating T_{regs} and producing cytokines such as TGF-β.

Tumour associated macrophages (TAMs) are also thought to be important players in the tumour microenvironment and are typically categorised into two large subtypes: proinflammatory, classically activated M1 macrophages or anti-inflammatory, alternatively activated M2 macrophages (Noy & Pollard, 2014; Pan et al., 2020). M1 macrophages play a role in anti-tumour immunity and the removal of pathogens. M2 macrophages, on the other hand, play a large role in anti-inflammatory responses, wound-healing and tissue remodelling, and in cancers promote the growth and metastasis of tumours. M1 and M2 macrophages display a high level of plasticity and can be converted into one type or the other depending on the surrounding environment or stimulation through therapeutic means (Noy & Pollard, 2014; Pan et al., 2020). Standardisation of the classification of these macrophage subtypes have remained challenging due to a lack of highly specific markers (Jayasingam et al., 2020), however characteristically M1 macrophages have been shown to express high levels of MHC II, CD68, CD80, and CD86, as well as Th1 cell-attracting chemokines, including CXCL9 and CXCL12, and M2 macrophages have been shown to express high levels of markers including CD206, CD163, CD209, FIZZ1,and Ym1/2 (Biswas & Mantovani, 2010).

Recent studies have revealed that not only the presence of TILs, but that the spatial organisation of TILs in relation to tumours, vasculature and with other

lymphocytes can also play a role in anti-cancer immunity (Asrir et al., 2022; Fridman et al., 2012; Lopez de Rodas et al., 2022; Tsakiroglou et al., 2020). In particular, the observation of highly organised structures containing B-cells, T-cells and stromal components have been described as tertiary lymphoid structures (TLSs) and have gained attention in recent years for their potential role in mediating anti-cancer immune responses.

Tertiary lymphoid structures

Tertiary lymphoid structures (TLSs) are ectopic lymphoid organs that develop in non-lymphoid tissues at sites of chronic inflammation including tumours. These structures are also found under other pathological conditions including autoimmunity, infection and allograft rejection. Studies have found correlations between the presence of TLSs and favourable prognosis in various types of cancers (Dieu-Nosjean et al., 2014; Pitzalis et al., 2014; van de Pavert & Mebius, 2010). However, few reports have shown that it may have a negative prognosis in some cancer settings (Kang et al., 2021). The potential for TLSs to be a positive prognostic factor has generated interest in understanding the role of TLSs in cancers. The development of the cancer-associated TLSs and the significance of these structures in cancer are not yet well-understood and is currently an active field of investigation.

TLSs can resemble some characteristics of secondary lymph node organs (SLOs). These structures have distinct T-cell and B-cell compartments, follicular dendritic cells (FDCs), fibroblastic reticular cells (FRCs) and high endothelial venules (HEVs) (Pitzalis et al., 2014). These structures form in response to chronic inflammatory cues and can exhibit plasticity (can be present transiently), as compared to the SLOs where development is genetically pre-programmed (Drayton et al., 2006).

The TLSs can have varying levels of organisation, from aggregates of lymphocytes to sophisticated and compartmentalised structures that are reminiscent of SLOs. The heterogeneity in TLS architecture may reflect the different maturation states or transitional developmental stages (Schumacher & Thommen, 2022) (**Figure 1.4**).

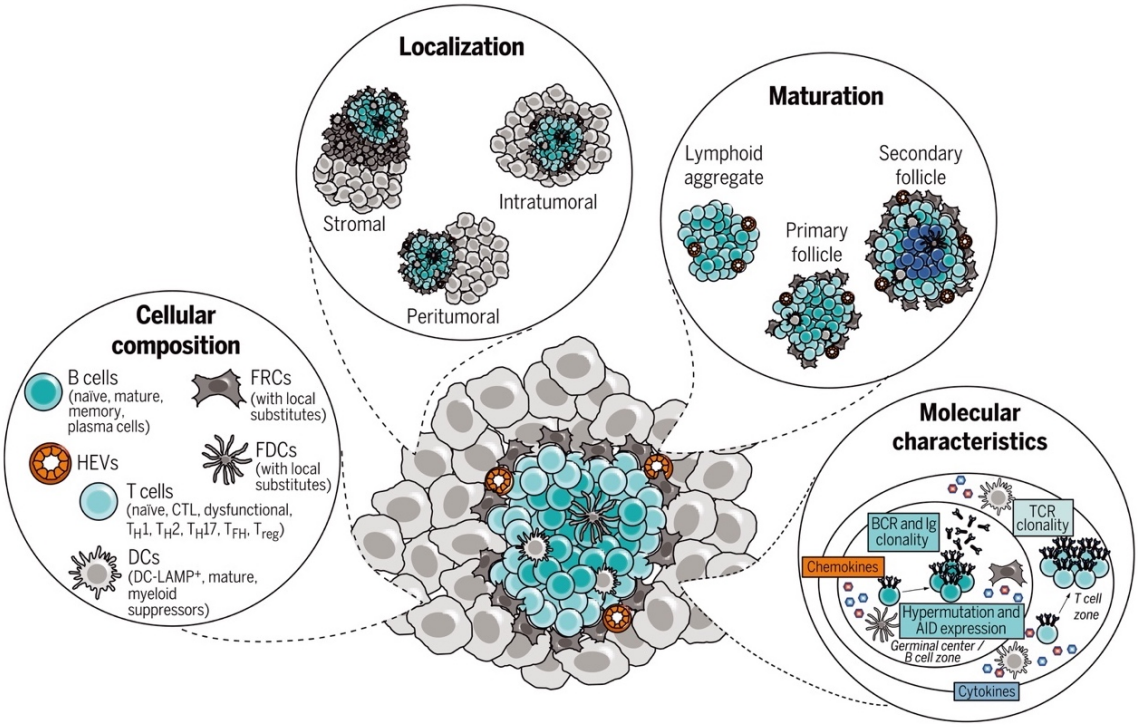


Figure 1.4.Tertiary lymphoid structure cell composition, location, maturation states, and molecular characteristics. Summary figure adapted from (Schumacher & Thommen, 2022).

Tumour TLSs are largely associated with favourable clinical outcomes for many cancers. One of the first studies to report this association was a retrospective study of NSCLC patients, where they correlated TLSs with increased overall, disease-specific and disease-free survival (Dieu 2008). Similar correlations were reported from studies of lung cancers (de Chaisemartin 2011, Goc 2014), breast cancer (Martinet 2011) and melanoma (Martinet 2012). However, there are also studies correlating TLS and poor prognosis in colorectal cancer (Bento 2015), hepatocellular carcinoma and primary breast carcinoma patients (Figenschau 2015). Interestingly, the cellular composition,

organisation and localisation of the TLSs may dictate whether the structures are advantageous or deleterious for disease outcomes. High densities of DC-LAMP$^+$ mature DCs have been associated with long-term survival for NSCLC patients (Dieu 2008), and high B-cell densities have been correlated with a positive outcome for triple-negative breast cancer patients (Germain 2014). In contrast, recruitment of T_{regs} and/or MDSCs to TLSs have been associated with the promotion of tumour growth (Shields 2010) or increased risk of disease relapse and death (Gobert 2009). Furthermore, T_{regs} in the TLS were found to be actively suppressing anti-tumour immune responses in a lung adenocarcinoma model (Joshi 2015).

The majority of current data linking TLS to cancer control in patients and mice have been correlative. It is, therefore, not fully understood whether TLSs are mere bystanders or are active participants in tumour development and anti-tumour responses to cancer therapies. Although still debated, there is mounting evidence that suggests that TLSs have the potential to initiate or participate in a local immune response to control or exacerbate the disease (as shown above). It is thought that tumour-specific TLSs may support anti-tumour immune responses in the following ways: (i) *Speed*: The priming of T and B cells at the tissue site may shorten the time to generate immune responses because it bypasses the trafficking of DCs and lymphocytes to and from SLOs. (ii) *Efficiency*: The formation of a local lymphoid niche may foster the induction of stronger or broader immune responses because lymphocytes may be more likely to encounter cognate antigens. (iii) *Control*: The direct exposure of TLS-associated immune cells to the inflamed tissue milieu may enable the fine-tuning of immune responses toward specific output signals. (iv) *Survival*: Lymphocyte homeostasis and survival could be promoted by survival factors that are

secreted by TLS-associated cell populations or by repeated APC encounter by effector T cells (Schumacher & Thommen, 2022).

However, unknowns remain regarding the exact mechanisms underlying the development of TLSs and how they control or exacerbate cancers. Current interests lay in the possibility of stimulating tumour antigen-specific lymphocyte infiltration to the TLS to increase anti-tumour immune response – i.e. the induction of tumour-specific TLSs.

1.5 | Radiation Treatment for Cancer Therapy

Principles of radiotherapy

Radiotherapy (RT) is a vital component of current cancer management strategies, with more than half of cancer patients receiving RT over the course of their treatment. RT can be utilised as a sole treatment or in combination with other therapies such as surgical resection, chemotherapy, and in recent years with immunotherapies and targeted therapies in multimodality regimens.

The primary objective of radiotherapy is to eliminate the cancer cells (potentially curative radiotherapy) or to slow their growth or to alleviate disease-related symptoms (palliative radiotherapy) by damaging their DNA. Conventional RT broadly consists of two modalities: external beam RT (EBRT) and brachytherapy. EBRT utilizes X-ray or particle beams. Typically in EBRT, a linear accelerator (LINAC) generates a source of X-rays positioned at a distance from the patient that can be targeted as beams aimed at the tumours. Brachytherapy utilizes radiation emanating from radioactive sources implanted inside the patient's body in proximity to the tumour. (*Radiation Therapy to Treat Cancer*).

RT, however, can also come with long-lasting adverse effects. Therefore, minimising normal tissue damage while achieving tumour control is a consideration that is made during treatment planning. The difference between the tumour tissue and normal tissue responses to radiation is also known as the "therapeutic window" (**Figure 1.5**), and the development of novel radiation sensitisers and other cancer therapies may aim to increase the window for optimal anti-tumour efficacy with minimal normal tissue toxicity. Following this principle, techniques of radiation therapy and diagnostic

imaging have advanced over the decades, enabling more localized and precise dose deposition within tumours and greater sparing of adjacent normal tissues. These include intensity-modulated radiation therapy (IMRT), image-guided radiation therapy (IGRT), integration of MRI and PET imaging into CT-based treatment planning, and advanced motion management strategies during treatment. Another way in which radiation oncologists have tried to achieve selective radiosensitisation of cells is by applying the 5 Rs: Repair, Repopulation, Redistribution, Reoxygenation, and Radiosensitivity. These concepts are particularly relevant for the application of fractionated delivery of RT.

Despite advances in technologies of RT, normal tissue toxicities have remained one of the limitations to optimal dose delivery for tumour control in the clinic. Consideration of normal tissue toxicities may be further complicated by the availability and use of immunotherapies and targeted therapies in the clinic.

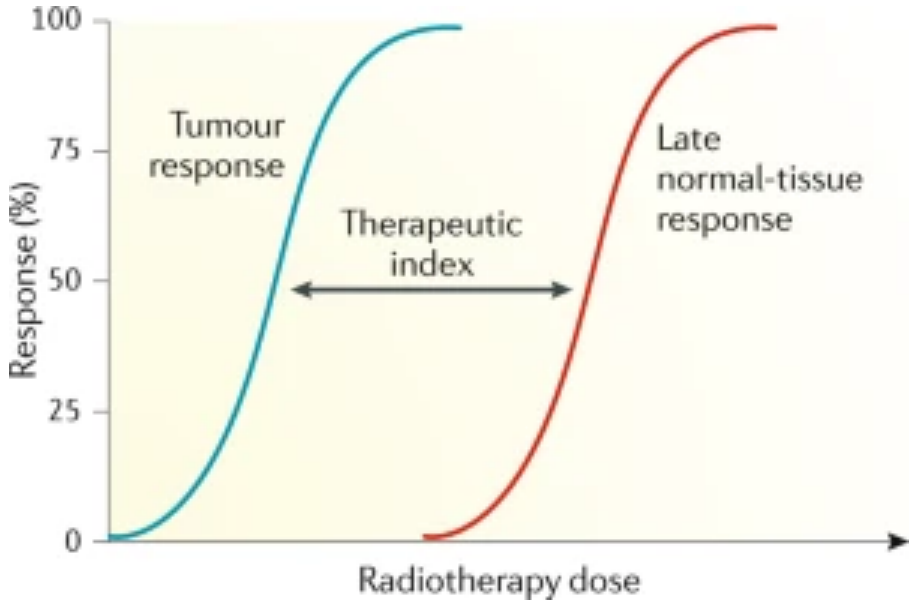


Figure 1.5. The therapeutic window of radiotherapy. The ratio between the effects on tumour tissue and the effects on normal tissues is called the therapeutic index. The therapeutic index can be explained as the sigmoidal relationships between the dose and effects on normal tissues and tumours. Figure adapted from (De Ruysscher et al., 2019b)

DNA damage and the DNA damage response

Radiation can control the growth of rapidly dividing cancer cells. It does this by indirectly or directly damaging the cells with energy emitted by ionizing radiation (IR) (Hall & Giaccia, 2012). IR can induce direct damage to deoxyribonucleic acid (DNA) or indirect damage through the generation of free radicals such as reactive oxygen species (ROS) that can interact with DNA molecules (Santivasi and Xia, 2014).

The DNA damage induced by IR falls into three main categories : base damage, single-strand breaks (SSBs), or double strand breaks (DSBs) (**Figure 1.6**) (Lomax et al., 2013). Low linear energy transfer (LET) radiation such as photons, causes primarily oxidative damage at single sites, resulting in base damage, while high LET radiation such as alpha particles causes clustered ionising events and can directly result in DSBs (Lomax et al., 2013). Among the damage resulting from IR, DNA DSBs are considered to be the most lethal form of damage.

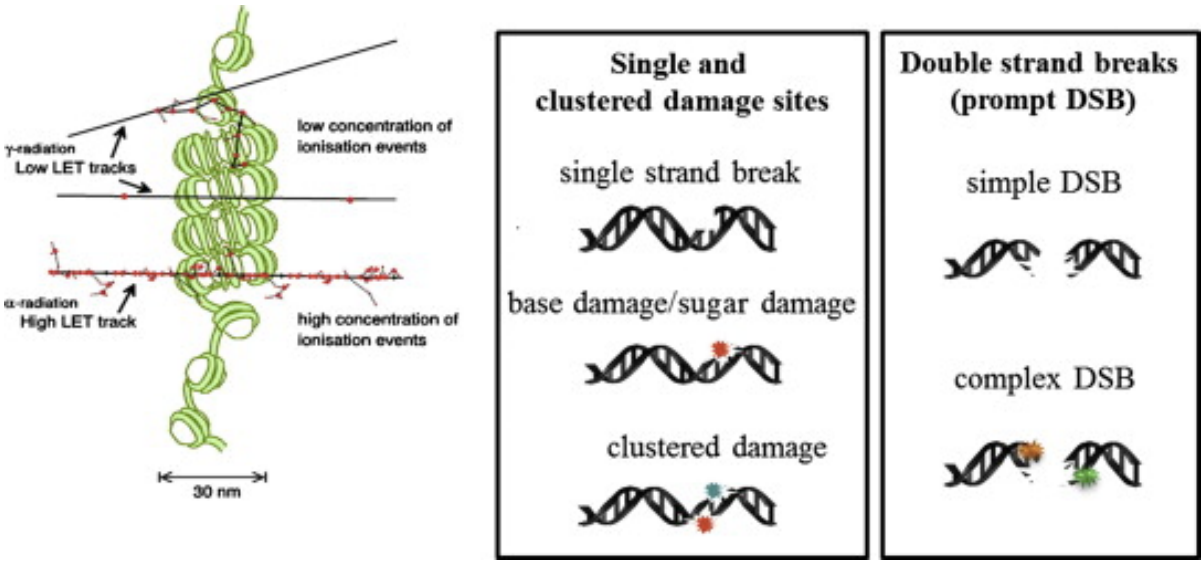


Figure 1.6. Radiation-induced DNA damage. Schematic of the types of DNA lesions induced by low or high LET tracks from radiation. Figure adapted from (Lomax et al., 2013).

In the event of a base or nucleotide damage, base excision repair (BER) or nucleotide excision repair (NER) mechanisms are activated. SSBs are repaired

through repaired through base excision repair (BER) or nucleotide excision repair (NER), and DSBs are repaired through homologous recombination (HR) or non-homologous end joining (NHEJ) (**Figure 1.6**). NHEJ is considered to be an 'error-prone' mechanism, as it can result in the loss of genetic material, whilst BER, NER and HR are considered to be 'error-free', as they use complementary strands or sister chromatids as templates for repair (Jackson & Bartek, 2009). The repair mechanism is largely defined by the type of DNA lesion, however, factors such as stage of the cell cycle can have an influence. As HR requires proximity to a sister chromatid, it does not occur during G0/G1 or early S phases (Jackson & Bartek, 2009). The possible fates of the cell following DNA damage include: (i) recovery following DNA damage repair, or (ii) cell death or (iii) cell senescence upon incomplete or unrepaired DNA damage. Cells are most sensitive to radiation when they are undergoing mitosis; on the other hand, cells in G0 or late S phase are the most radioresistant. As cancer cells undergo cell divisions at a faster rate than surrounding normal cells, this creates a vulnerability for the cancer cells for cell elimination (Lomax et al., 2013).

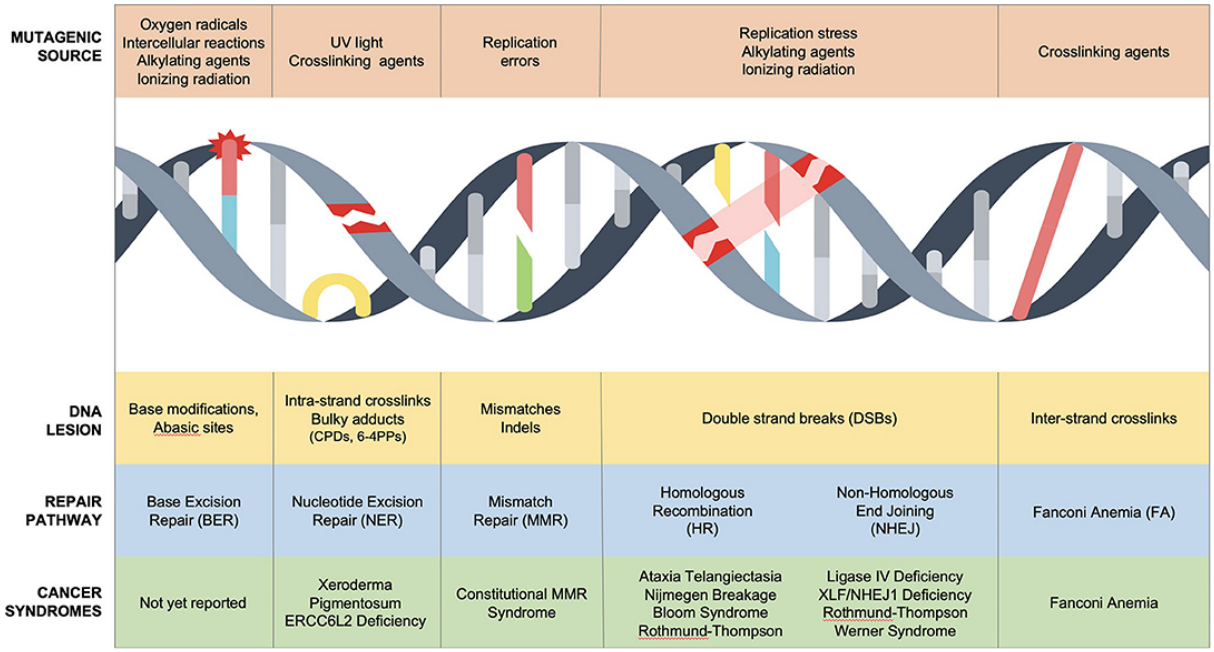


Figure 1.7. DNA repair mechanisms. Schematic outlining mutagenic sources, DNA lesions and repair mechanisms. Figure adapted from **(**Sharma et al., 2020**)**.

1.6 | Radiation-induced Immune Responses

It is believed that the anti-tumour effects of radiation is dependent primarily on DNA-damage-mediated tumour cell-autonomous cell death (mechanisms described in **1.5**). Recent clinical reports have suggested, however, that radiation can also generate an anti-tumour response through the activation of the immune system. Clinical observations have been made of the shrinkage of tumours that fall outside the field of radiation (Dovedi et al., 2017; Golden et al., 2015; Golden et al., 2013; Postow et al., 2012), and the inferior tumour responses to RT in immunocompromised patients (Tseng et al., 2018). Radiotherapy has been increasingly viewed as a promising combination with ICIs. The PACIFIC trial[2] demonstrated an increased overall survival with durvalumab after chemoradiotherapy in NCSLC patients (Antonia et al., 2018;

[2] PACIFIC trial: A randomised phase III clinical trial of durvalumab (anti-PD-L1 antibody) and chemoradiotherapy on stage III locally advanced NSCLC patients.

Scott J. Antonia et al., 2017). Another study attributed improved patient outcome to CTLA-4 blockade and radiotherapy to the induction of anti-tumour T-cell responses from the combination therapy (where otherwise anti-CTLA-4 alone had failed to demonstrate efficacy) (Formenti et al., 2018). In particular, there is optimism in the field for the potential for RT to generate an "*in situ* vaccination" effect, which comes from the hope that RT of the tumour can become a source of tumour-specific antigens to immunise the host. It is thought that RT can modulate the immunogenicity of tumours by triggering the release of pro-inflammatory or anti-inflammatory signals, enhancing neoantigen expression, and increasing the infiltration of immunostimulatory/ immunosuppressive cells into the tumour. Additionally, radiation can have profound immunomodulatory effects both through direct impact on the tumour and indirect means through modification of the TME, including fibroblasts, blood vessels, and immune cells (Barker et al., 2015; Jiang et al., 2016; McLaughlin et al., 2020; Menon et al., 2019).

However, despite growing optimism for the potential of RT as an immunostimulatory agent, studies also suggest a complex relationship between RT and the immune system. While some immunotherapy/ radiation clinical trials (mentioned above) demonstrate a synergistic effect of immunotherapy and RT, a phase II randomised clinical trial in 2020 comparing survival and disease advancement between pembrolizumab and RT and standard of care cetuximab-RT in locally advanced head and neck squamous cell carcinoma patients failed to demonstrate any benefit of pembrolizumab over cetuximab when combined with RT (Bourhis et al., 2020; Tao et al., 2023). It was thought that the lack of beneficial outcome may have been due to the lack of an adjuvant component such as the case for the PACIFIC trial, or

the need for a stratification of patients according to PD-L1 status or the potential detrimental effects of 50 Gy radiation treatment for T-cell priming; however these remain speculations. Furthermore, there is growing evidence that support that RT can have immunostimulatory *or* immunosuppressive effects (Weichselbaum et al., 2017) depending on the characteristics of the individual tumours, their microenvironment, and the nature of the delivered radiation (dose and energy levels). The potential for RT to become a double-edged sword depending on biological responses it elicits in the tumour or the microenvironment highlights the need to understand these complex mechanisms.

Cytoplasmic nucleic acid sensing – the cGAS-STING pathway

Irradiation of a cell can result in the occurrence of double stranded DNA (dsDNA) in the cytosol (Deng, Liang, Xu, et al., 2014; Durante & Formenti, 2018), with micronuclei[3] formation and rupture as one of the main mechanisms (Harding et al., 2017; Mackenzie et al., 2017). Having evolved as an anti-viral defence mechanism, ectopic occurrence of dsDNA in the cytosol is 'sensed' by cyclic guanosine monophosphate-adenosine monophosphate synthase (cGAS), and can activate the interferon (IFN) pathway through a cascade of events including the translocation of the stimulator of IFN genes (STING) from the endoplasmic reticulum (ER) to the Golgi, phosphorylation of TANK-binding kinase 1 (TBK1), recruitment of interferon regulatory factor 3 (IRF3) and phosphorylation of IRF3 (Kwon & Bakhoum, 2020) (**Figure 1.9**).

[3] Micronuclei (MN): extra-nuclear bodies that contain genetic material which arise form cell cycle progression through mitosis in cells with DNA damage. MN can form as a result of an accumulation of DNA damage and defects in cell repair machinery. These structures are prone to rupture and when ruptured, release their genomic content into the cytosol.

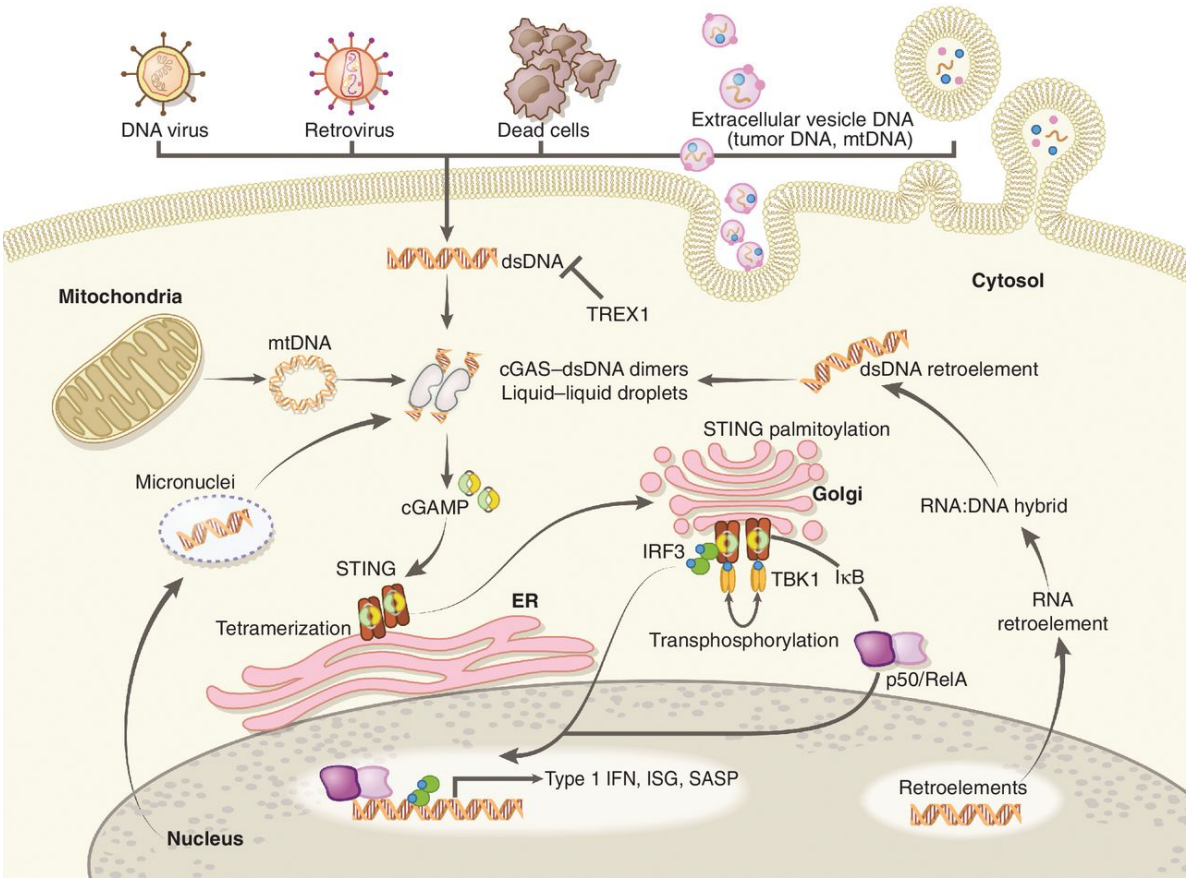


Figure 1.8. The cGAS-STING pathway. The virally-induced immune mechanism is activated by the sensing of cytosolic DNA. The canonical pathway of STING activation occurs through cGAMP signalling, STING translocation to the Golgi and subsequent activation of TBK1 and IRF3, ultimately resulting in the release of type I IFN. Figure adapted from (Kwon & Bakhoum, 2020)

The release of dsDNA into the cytosol following DNA damage and the subsequent activation of the cGAS-STING pathway can lead to immune surveillance, cell-intrinsic senescence, or chronic inflammatory signalling. The immunostimulatory events occur through the increase in type I IFN signalling, the activation of dendritic cells (DCs) and priming of tumour-specific $CD8^+$ T-cells (Deng, Liang, Xu, et al., 2014). The differential responses of immunostimulation or immunosuppression are thought to be dependent on the chronicity or acuity of IFN signalling (Wilkins et al., 2019).

Radiation and priming of immune cells

Tumour cell immunogenicity can result in the stimulation of adaptive immune responses through three main aspects of immune stimulation, namely: antigenicity, adjuvanticity and reactogenicity. 'Antigenicity' refers to the ability of tumour cells to present tumour peptides on the surface of the cell. 'Adjuvanticity' is the ability to attract and activate T-cells through the production of adjuvant molecules such as cytokines like type I IFN. Lastly, 'reactogenicity' refers to the ability of tumour cells to stimulate T-cell killing mechanisms by binding to co-stimulatory molecules on the surface of the T-cell (Chabanon et al., 2021).

One of the main mechanisms by which IR stimulates an immune response is via the generation of ROS and genotoxic damage. These genotoxic stressors can result in regulated cell death, which is referred to as immunogenic cell death (ICD). ICD can be accompanied by the release of an array of damage-associated molecular patterns (DAMPs), including calreticulin, ATP, annexin A1 (ANXA1) high-mobility group box 1 (HMGB1) and type I IFN.(Garg et al., 2010; Yatim et al., 2017). The cell death and cell lysis can result in the release or surface presentation of tumour-specific neoantigens. Accompanied by the adjuvanticity generated by DAMPs, ICD can initiate adaptive immune responses through increased antigen presentation by dendritic cells (DCs) in the environment and subsequent priming of T-cells.

Radiation increases major histocompatibility complex class I (MHC-I) expression on the surface of tumour cells (Garnett et al., 2004; Reits et al., 2006; Sharabi et al., 2015; Sharma et al., 2011), which presents antigens required for the activation of cytotoxic $CD8^+$ T-cells. It has been shown that the addition of DNA-damage response (DDR) inhibitors to RT can further increase MHC-I expression on

the surface of tumour cells (Dillon et al., 2019). Additionally, RT is also capable of increasing the intracellular peptide pool, which can result in changes to the peptide profiles presented on MHC-I (Reits et al., 2006). In a study with a mouse breast carcinoma model, an increase in $CD8^+$ T-cells reactive to the AH1 antigen (a known MHC-I peptide) was observed in response to radiation and anti-CTLA-4 treatment (Rudqvist et al., 2018). Additionally, colorectal cancer patients treated with RT saw an increase in surviving-reactive T-cells in peripheral blood (Schaue et al., 2008).

Interestingly, it has been observed that RT may also be associated with an expansion of the T-cell receptor (TCR) repertoire. In a mouse study of a breast carcinoma model in which rejection by CD8 T cells occurs in mice treated with RT and anti-CTLA-4 in combination, but not as monotherapy, they observed that RT increased the diversity of the TCR repertoire of the intratumoural T-cells (Rudqvist et al., 2018). Similarly, in a study where CTLA-4 and RT combination was used on a metastatic melanoma mouse model, it was found that anti-CTLA4 promoted the expansion of T cells while RT shaped the TCR repertoire of the expanded clones (Twyman-Saint Victor et al., 2015). In addition to increased MHC-I presentation and $CD8^+$ TCR repertoire expansion, cross-presentation of tumour antigens to DCs is required for the RT-induced immune response (Martinek et al., 2019; Sharabi et al., 2015). Together, these studies indicate the varying roles of RT in inducing immune response in cancer. However, the effects of the radiation-induced effects on normal tissue components are less well-characterised.

1.7 | RADIATION-INDUCED CARDIAC DISEASE

Radiation-induced cardiac toxicity in cancer therapy

Increasing radiation doses to improve tumour control can be limited by normal tissue toxicities. Despite technological advances in radiation, long-term adverse effects from RT continue to pose a problem in cancer patients. Normal tissue toxicities of RT in thoracic malignancies including lung cancer include: acute and late toxicities in the oesophagus, lungs and heart (**Figure 1.9**). Pulmonary tissues in particular, are radiosensitive and are therefore susceptible to radiation-induced acute events such pneumonitis and late events such as pulmonary fibrosis (Ding et al., 2013; Simone, 2017). Historically, the heart was thought to be radioresistant and therefore was not typically avoided in radiation dose planning in cancer patients. However, in the 1960s, reports began to emerge detailing cardiotoxic pathologies observed in patients treated with radiotherapy to the heart, in some cases leading to sudden death years after treatment (Cutter et al., 2015; Darby et al., 2003; Darby et al., 2013; McGale et al., 2011). Cardiotoxic events have been reported in 8% of cancer patients that receive RT to the heart (2 – 5 fold higher than the normal population) and pathologies include: pericarditis, ischemic heart disease, conduction abnormalities causing arrhythmias, myocardial fibrosis, valvular abnormalities (Clarke et al., 2005; Cutter et al., 2015; Darby et al., 2013; Taunk et al., 2015; Taylor et al., 2017) and early mortality (Darby et al., 2003; S. C. Darby et al., 2005; Harris et al., 2006; Tukenova et al., 2010). Additionally, in a study of breast cancer patients receiving radiotherapy, a dose-dependent increase in major coronary events of 7.4% per Gy was reported (Darby et al., 2013), which findings were supported by other clinical studies including a study of

Hodgkin's lymphoma patients (Haque et al., 2018; Jacobse et al., 2019; van Nimwegen et al., 2016; Vivekanandan et al., 2017; Yegya-Raman et al., 2018). These results taken together, highlight the need to protect cardiac tissue as far as possible from radiation exposure. Although technologies to deliver radiation to target tissues while minimising the dose to non-target tissues have developed in recent years, modern clinical trials show that the risks of RICT remain relevant in the clinic (Boero et al., 2016; Saiki et al., 2017). Additionally, with improvements in cancer therapy, cancer patients are living longer, and addressing the problem of late normal tissue toxicities from cancer therapies is increasingly important.

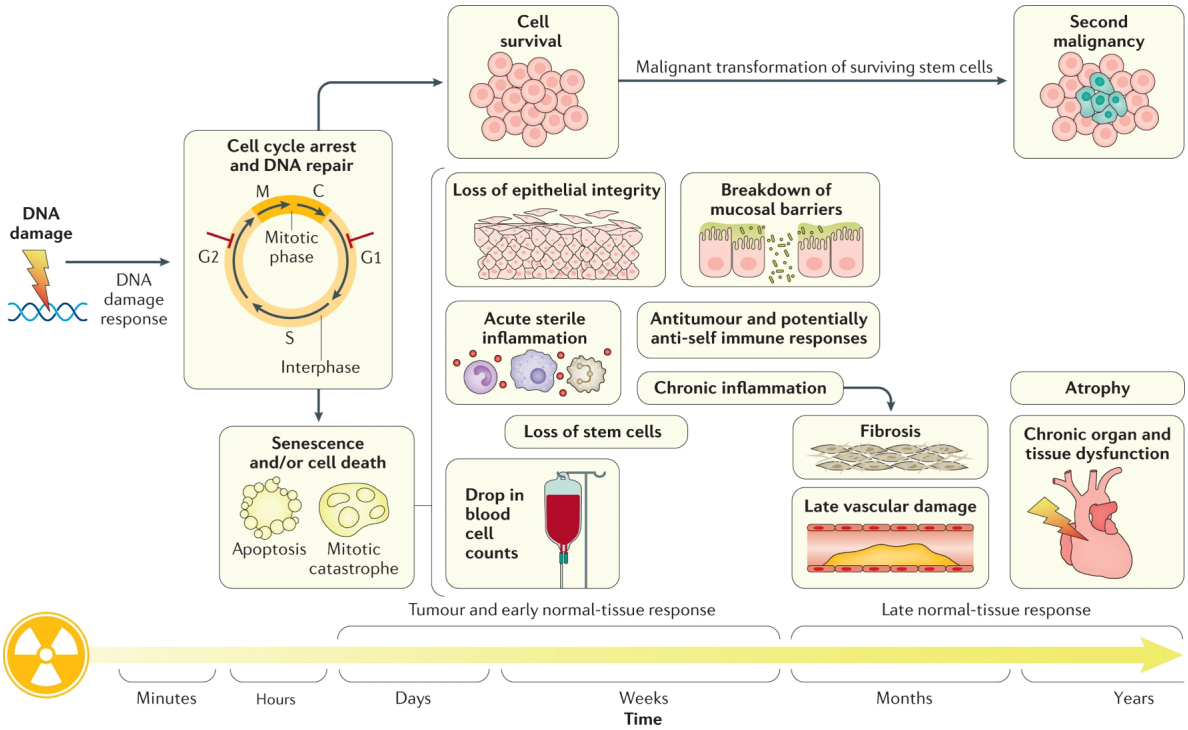


Figure 1.9. Radiation-induced normal tissue toxicities. Schematic summary of radiation-induced cellular events and subsequent pathological events including fibrosis and cardiac organ dysfunction. Figure adapted from (De Ruysscher et al., 2019a)

In recent years, more studies are reporting cardiotoxic effects of immunotherapies including immune checkpoint inhibitors (ICI) and chimeric antigen receptor (CAR) T-cell therapies (Agostinetto et al., 2021; Salem et al., 2018; Stein-Merlob et al., 2021), with some reporting cardiotoxic events of immunotherapies in

combination with RT (Myers & Lu, 2017) suggesting immunological contributions to radiation-induced late tissue cardiotoxicity.

Therefore, understanding the biological mechanisms that cause RICT is crucial in reducing the risk of long-term effects from cancer treatments. Especially as cancer immunotherapies drugs become increasingly available and are a part of standard therapy for cancer treatment (and sometimes combined with RT), there is a need to understand the radiation-induced immune events occurring in the heart.

1.8 | The Co-evaluation of Tumour Biology and Normal Tissue Biology from Cancer Therapies

Models to assess the tumour and its microenvironment

As established in previous sections, there is a need to evaluate both tumour and normal tissue biology and their responses to cancer therapies. The interactions between cancers and their microenvironment are complex and occur from the early stages of tumourigenesis to shape both the biology of the tumour and the TME over time. Additionally, the importance of evaluating cancer therapies not only for their anti-cancer properties, but adverse events on normal tissue have become increasingly recognised. Pre-clinical models provide important tools that allow us to study the biology of tumour development along with the efficacy of cancer treatments and mechanisms of resistance. This section will provide an overview of preclinical models with the following key considerations: (i) the modelling of the cancer evolutionary process in its organ environment; and (ii) the ability to evaluate early and late organ toxicities from cancer therapies.

Preclinical models provide important tools that allow us to study the biology of tumour development along with the efficacy of cancer treatments and mechanisms of resistance. Currently, *in vitro* (2-D and 3-D cell culture, *ex vivo* cultures and organ-on-a-chip) and *in vivo* (see below) models are broadly the two types of preclinical models used in cancer research. Cell line models are inexpensive and allow for genetic manipulation and perturbations with cancer treatments for the understanding of the biology of cancers on a cellular level. However, are limited in their capability to mimic

the complexity of the cellular components that make up the tumours and their microenvironment. Organoid or 3-D cell cultures, cell co-culture and *ex vivo* cultures can model some aspects of the complexity of tumour biology by providing extracellular matrices or introducing other cellular components that make up the microenvironment (Herbst et al., 2018; Hynds et al., 2021). However, these are still limited in their capacity to model tumour evolution and processes such as cancer immunoediting.

Animal models, on the other hand, provide the opportunity to better mimic the complexities of human cancers in their organ environment (stromal and immune microenvironment), 3-D architecture and genetically diverse cellular make-up. A variety of animal models have been used for cancer research; among these, models using *mus musculus*, the laboratory mouse, are most commonly used for the study of cancer biology. The mouse is an appropriate biological model for the understanding of human diseases due to (i) their high degree of homology with the human genome; (ii) similarity in their physiological functions and organs in the body; (iii) and their shorter lifespan, which allows for the studying of disease development and progression over a shorter period (Mendes et al., 2020). There are some differences with humans, however, such as the differences in the cancer immune biology (Ebert et al., 2016; Shrimali et al., 2017). These include the composition of the immune cells in the TME, tumour antigens, and the complexity of immune suppression (Dranoff, 2012; Gould et al., 2015; Hegde & Chen, 2020). This could be critical when considering the direct translations of findings from mouse studies into the human context. However, in the studies of the biological mechanisms of cancer development in their immunological context, the mouse model remains a highly relevant and efficient model for this purpose.

Currently, there are broadly three main approaches in mouse models used for cancer research. These are (1) Tumour implantation models (xenograft or allograft models); (2) genetically engineered mouse models (GEMMs); and (3) chemically induced cancer models.

Tumour implantation models Tumour implantation models utilise cancer cells from cell lines for cell-line-derived xenografts (CDXs) or from primary patient samples for patient-derived xenografts (PDXs). The cells can be implanted subcutaneously or orthotopically into the appropriate strain of mice (depending on the strain origin of the cell line or whether the cells are from humans) (Day et al., 2015; Mendes et al., 2020). PDXs have the advantage of modelling human cancers more closely and hence allow for experiments that can recapitulate patient population-based responses in mice for cancer therapeutic studies (Townsend et al., 2016). However, in addition to the challenges of successful engraftment in mice, an immunocompromised host is required for this model, posing a problem for studies of tumour-immune interactions (Hynds et al., 2021).

GEMMs GEMMs are generated by inbreeding mouse strains that have been genetically manipulated to express the oncogenic alleles or deleted tumour suppressor genes. Spatial (tissue/ cell) and temporal (timing of genetic manipulation) control of mutagenesis are possible with conditional mutation systems such as Cre-LoxP and FLP-FRT. The most widely used lung cancer GEMM is the K-ras^{G12D} mutant LUAD model (Jackson et al., 2001). These models allow for experimental control over key mutations, typically by altering a select few strong oncogenes or tumour suppressor genes. GEMMs can generate rapidly developing lung cancers with multiple tumours but lack the mutational diversity seen in smoker patients (Westcott et al., 2015).

GEMMs, due to the strong genetic component that drives tumourigenesis, tumours that arise in GEMM models are not subject to the same evolutionary histories as human tumours (Hynds et al., 2021).

Carcinogen-induced models Chemically-induced cancer models for lung cancer rely on the carcinogenic actions (often through mutagenesis) of chemicals found in tobacco smoking for the generation of autochthonous and spontaneous tumour formations (usually specifically in the lungs). The most commonly used chemical is urethane, which generates predominantly *K-ras* driven lund adenocarcinoma (Hynds et al., 2021; Westcott et al., 2015). Tumours that arise in this model typically recapitulate those of early cancers and capture the diversity of mutations seen in tumours of smoking-induced lung cancer patients (Hynds et al., 2021; Westcott et al., 2015). Additionally, because the tumours arise autochthonously, the tumour cells have undergone the selective pressures applied by the organ environment and immune environment. This allows for the studies of the cancers that have been shaped by interactions with the tumour microenvironment. (Above mouse models summarised in **Table 1.1**.)

Table 1.1. A summary of the advantages and disadvantages of preclinical mouse models.

Mouse model	Advantages	Disadvantages
Patient-derived xenografts (PDXs)	- Cells are derived from patient, and the biology can be more easily translatable - Permissive to the on-going development of novel models (e.g. humanised mouse models)	- Requires implantation in an immunocompromised mouse strain - Unable to track the evolution of cancers
Genetically engineered mouse models (GEMMs)	- Control over genetic alterations - Immune competent animals - Tumours arise *in situ* microenvironment	- Strong oncogenic drive limits the study of early tumour evolution - Lacks the genomic damage by tobacco-smoking, and does not capture the mutational diversity of smoker tumours
Chemically-induced tumour models	- Mimics the high tumour mutation burden seen in tumours of smoker patients - Tumours arise *in situ* microenvironment - Immune competent animals - Mimics early stages of tumour evolution	- Can result in multi-organ carcinogenesis - Susceptibility to carcinogenesis is strain-dependent

Preclinical models of radiation-induced cardiac toxicity

RICT remains an understudied area of clinical importance. Despite the clinical need, few preclinical models are currently available to study radiation-induced cardiac effects (Schlaak et al., 2020). Studying RICT in animal models remains challenging, in part, due to the biological differences in the responses to radiation between humans and animal models such as rodent models, zebrafish models (Schlaak et al., 2020). Additionally, currently available technology in delivering radiation to the hearts (or subregions of the heart) in small mammalian models such as mice poses another difficulty in studying RICT in animals. Due to this, the biological mechanisms underlying RICT are largely not understood (Walls et al., 2022), and there is an unmet need for preclinical models for the evaluation of RICT.

1.9 | AIMS OF THIS THESIS

There is an identified need to understand the role of radiotherapy and its immune modulating effects on cancer, TME as well as other normal tissues. Understanding this important biology will provide insights into potential approaches to protect vulnerable tissues from radiation toxicity and biological understanding of radiation-induced immune responses.

Therefore, the aims of this thesis are to:

1. Characterise the A/J mouse as a model for the co-evaluation of anti-tumour effects and normal tissue toxicities of cancer therapies.
2. Investigate important mechanisms underlying lung carcinogenesis in the chemically induced lung adenocarcinoma mouse model.
3. Study the late adverse normal tissue effects in cardiac and pulmonary tissues from cancer therapies including radiation.

CHAPTER 2. MATERIALS AND METHODS

2.1 | REAGENTS

The list of chemicals and reagents used in the following methods can be found in **Appendix 1**. Equipment, machines and their manufacturers are indicated in each method.

2.2 | ANIMAL EXPERIMENTS AND WELFARE

2.2.1 | Animal welfare

Experiments were conducted in accordance to the Animals Scientific Procedures Act of 1986 (UK) (project license held by Dr. Anderson Ryan PIL number: 30/3395). The protocol was approved by the Committee on the Ethics of Animal Experiments of the University of Oxford. Mice were housed in individual ventilated cages (n = 6 per cage) in a room with 12h-light 12h-dark cycle maintained at 22°C and 50% humidity. Mice were fed a certified rodent diet and given filtered water ad libitum. Autoclaved bedding material and cage enrichment were provided in the cages. The health of the mice was monitored daily, and weights were collected twice weekly. In the event of more than 10% body weight loss for 2 consecutive days, or greater than 15% weight loss in one day or clinical signs, mice were euthanised. Animals were allocated to treatment groups with matched mean starting weights. Euthanasia was performed by an overdose of pentobarbital and death was confirmed by cessation of blood circulation.

2.2.2 | Mouse strains

A/JOlaHsd (A/J) mice used in this project were purchased from Envigo (UK, #049), C57BL/6 mice were purchased from Charles River (UK, #632) and were acclimatised for 7 days before the start of each experiment.

2.2.3 | Urethane induction of tumours

Urethane (5% urethane/ PBS, 0.1mL/10g body weight) or PBS (0.1mL/10g body weight) was injected intraperitoneally (i.p.) in 6–10 week-old female mice. Mice were

monitored for spontaneous tumours with live MR imaging and were culled no longer than 39 weeks after urethane treatment was given to the mice or when they developed clinical signs such as 15% loss in body weight. Control animals were given PBS (0.1mL/10g body weight, i.p.).

2.2.4 | Drug formulation and dosing schedule

The compounds, respective vehicles and dosing schedule in the mice for *in vivo* experiments are listed in Table 2.1.

Table 2.1. List of drugs, respective vehicles and dosing schedules used in the in vivo experiments in this thesis.

Chemical	Company	Vehicle	in vivo dosing schedule
Urethane	Sigma-Aldrich, U2857	PBS	single or two doses of 5% weight/volume (w/v), i.p.
AZ31	Provided by AstraZeneca	2.5% DMSO, 10 % captisol, water	50mg/ kg per dose (10 doses across two weeks), p.o.
AZ64	Provided by AstraZeneca	0.1% tween 80, 0.5% HPMC, water	50mg/ kg per dose (10 doses across two weeks), p.o.
AZD6738	Provided by AstraZeneca	2.5% DMSO, 40% PEG, water	50mg/ kg per dose (10 doses across two weeks), p.o.
Anti-PD-L1 (clone 10F.9G2)	Bioxcell, BE0101	PBS	single dose at 10mg/ kg, i.p.
DMXAA (Vadimesan)	Selleckchem, S1537	5% DMSO, 5% NaHCO3, water	single dose at 10-20 mg/ kg, i.p.
H-151	Selleckchem, S6652	0.1% Tween 80, PBS	daily dose at 10 mg/ kg, i.p. for up to two weeks

2.2.5 | Tissue collection and sample preparation

Lung, heart tissue and serum collection

Heart, lungs, and peripheral blood were collected from the mice at the study endpoint after euthanasia by an overdose of pentobarbital. Heart and lung samples were rinsed with cold HBSS and placed in formaldehyde for fixation or collagenase for tissue digestion, or RNAlater for downstream analyses. In experiments that required single-cell isolated heart samples, perfusion of the heart was performed as detailed by Aronoff et al. (2018) prior to sample collection (**Figure 2.1**) (Aronoff et al., 2018; Pinto et al., 2013). 50 ml ice-cold HBSS was injected into the right ventricle of the heart at a 5 ml/ min rate for 3 min for complete perfusion of the heart. Peripheral blood was collected by cardiac puncture and serum was isolated after centrifugation of peripheral blood at 1.5 x10^3 relative centrifugal force (rcf), and stored at -20°C.

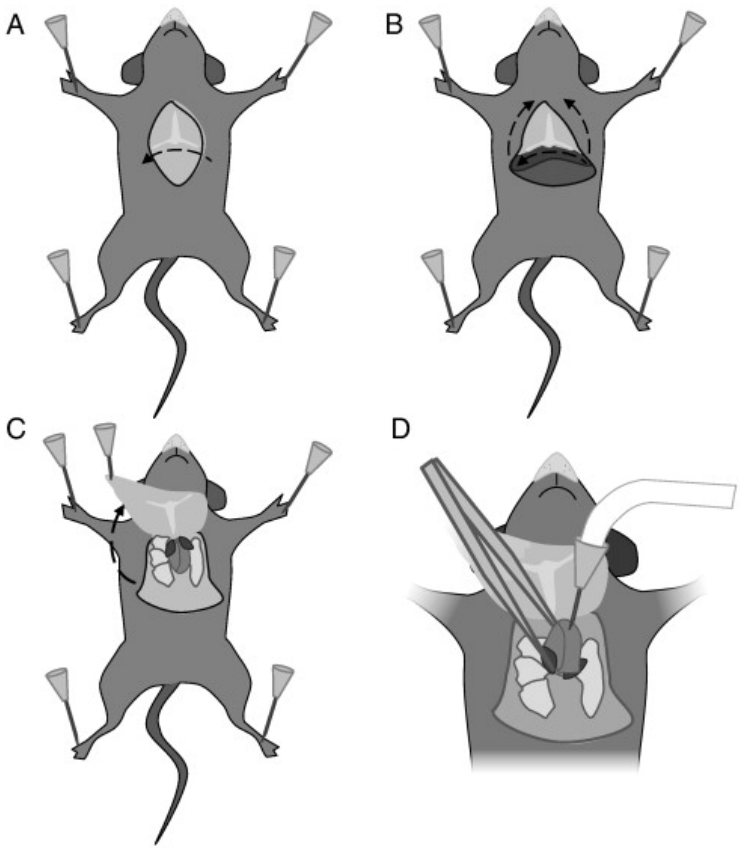


Figure 2.1. Perfusion and isolation of the mouse heart. Schematic illustrating the procedures for cardiac tissue perfusion and isolation. **(A)** An incision is made below

the lower costal bone and diaphragm to open the peritoneal cavity. **(B)** The diaphragm is cut open while holding the septum in place. The anterior chest wall is cut from the anterior thorax towards the head. **(C)** The diaphragm and anterior thoracic wall are pinned to allow access to the thoracic cavity. **(D)** For perfusion, incisions are made in the left and right atria syringe containing cold HBSS is inserted at the apex of the heart into the left ventricle. HBSS is injected into the heart for 5 minutes at a flow rate of approximately 5 ml/ min. Figure adapted from Pinto et al. (2013).

Histology sample preparation

Tissues collected from the mice were fixed in 10% neutral buffered formalin for 24 hours at 4 °C and stored in 70% ethanol. Fixed hearts were sectioned along the longitudinal or transverse plane and fixed lungs were assessed for superficial tumours before tissue processing. Tissues were placed in ethanol, xylene and paraffin wax with a Spin Tissue Processor (Thermo Fisher Scientific, STP-120), and embedded in paraffin on a HistoStar™ Embedding Workstation (Thermo Fisher Scientific, A81000003).

2.3 | MAGNETIC RESONANCE IMAGING

2.3.1 | MR image acquisition with cardio-respiratory gating

Cardio-respiratory gated bSSFP (balanced Steady-State Free Precession) magnetic resonance imaging (MRI) was used to image lungs and heart in live mice. Cardio-respiratory gating methods were developed for MR imaging in collaboration with the Imaging Scientific Research Facility at the Department of Oncology, University of Oxford and details of the imaging settings are specified in Gomes et al., 2019 and **Appendix 2** (Gomes et al., 2019). The 7.0 T (310mm horizontal bore Varian Nuclear Magnetic Resonance Spectrometer, Varian Inc.) was used to perform MRI. Mice were anaesthetised using isoflurane (2-4%) and placed onto a pre-heated cradle in the MRI machine in a head-first supine position, during which time the mice were monitored for their temperature with an optical rectal probe, breathing with a pressure-sensing balloon, and heart rates with ECG measured by needle probes inserted subcutaneously under the skin of the upper abdomen. Mice were maintained at 37°C, respiration rate was monitored and maintained at 40–60 breaths/mins. MRI of the thoracic region of the mouse was captured at an isotropic resolution of 200 µm.

2.3.2 | MR Image analysis

3D MR images of the lung and heart were segmented and reconstructed using a semi-automatic segmentation on ITK-SNAP software (v 3.6.0) (Yushkevich et al., 2006). Automatic segmentation was used for lung volume and tumours were segmented manually. Lung, tumour and heart volumes were measured from the reconstructed images.

2.4 | ELECTROCARDIOGRAM

2.4.1 | ECG data acquisition

Mice were anaesthetised using isoflurane (2-4%) and body temperature was maintained at 37°C and respiration rate was monitored and maintained at 40–60 breaths/mins during the course of data collection. Needle electrodes were inserted subcutaneously under the skin of the upper abdomen of the mice to collect lead I surface electrocardiogram (ECG) traces (**Figure 2.2**). Traces were acquired with PowerLab (ADInstruments, UK) under a controlled isoflurane dose (2-4%) and stable breathing for a duration of 5-10 minutes. ECG readings were acquired 22 and 26 weeks after thorax or heart irradiation.

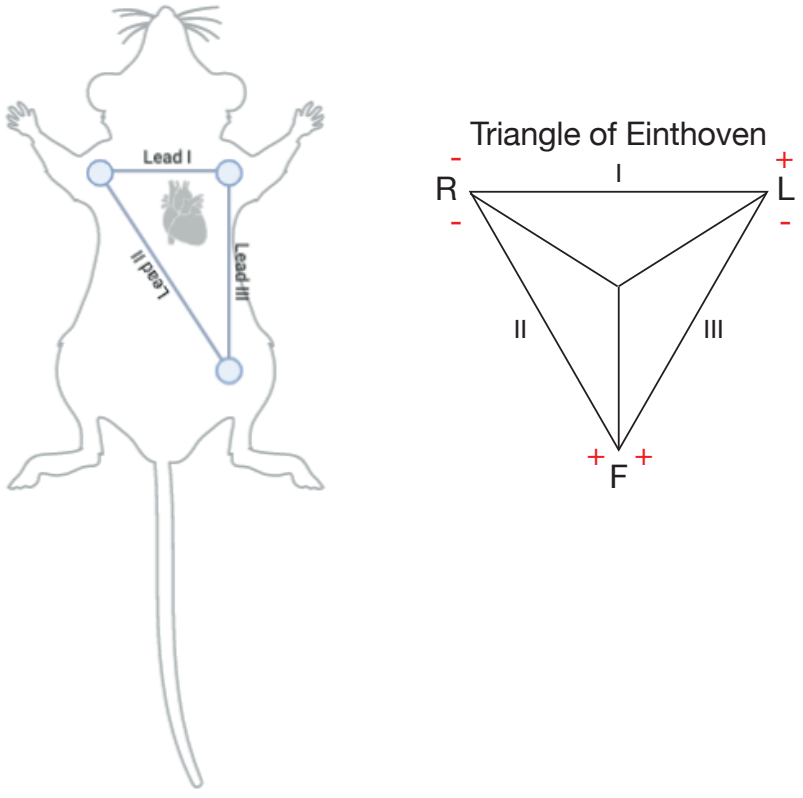


Figure 2.2. ECG leads. Schematic figure of possible positions of ECG probes and ECG leads that can be collected. Subcutaneous needle probes were inserted under the skin of the upper abdomen to acquire lead I ECG traces.

2.4.2 | ECG trace analysis

ECG traces were analysed for R-R intervals and waveform segmentation using LabChart 8 (v8.1.13).

ECG waveform segmentation and analyses

An ROI consisting of 100-300 consecutive heartbeats were selected on each ECG trace. Traces with an isoelectric noise < 0.1 mV and < 8 mV activity, and R-R intervals < 0.2 seconds and a form factor < 125 were excluded from the analysis. An ECG analysis module (LabChart 8, ADInstruments) was applied with mouse ECG trace settings (4 beats averaging; pre-P baseline of 10ms, maximum PR of 50 ms and maximum RT of 40 ms) for segmentation of ECG waveforms to identify P-wave, QRS complex and T-waves as shown in **Figure 2.3**.

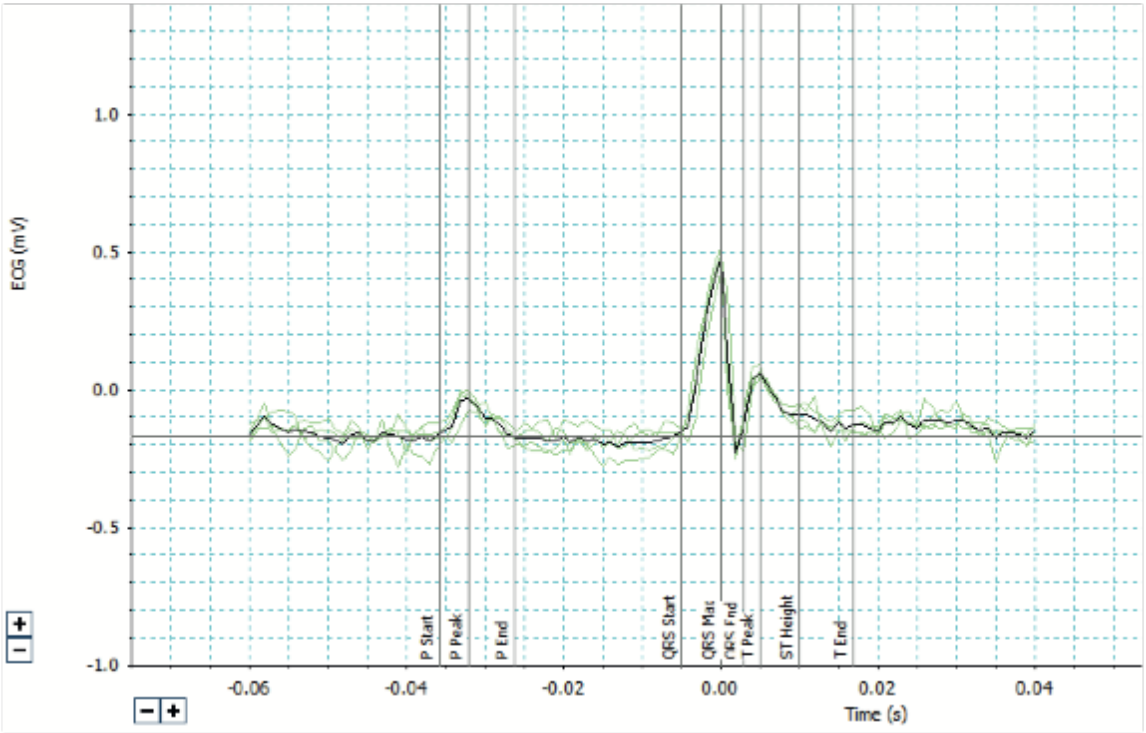


Figure 2.3. ECG waveform segmentation. P-wave, QRS complex and T-waves were identified on an automatic segmentation algorithm on LabChart8 for each heartbeat.

Assessment of Heart Rate Variability

Heart rate variability (HRV) was assessed as the root mean square of successive differences (RMSSD) between heartbeats. R-R interval values were obtained from analyses carried out with the ECG analysis module with settings specified as above, and RMSSD was calculated with the formulae below for each individual.

$$RMSSD = \sqrt{\frac{1}{N-1}\sum_{i=1}^{N}(RR_{i+1} - RR_i)^2}$$

2.5 | IRRADIATION

2.5.1 | Lead-shielded whole-thorax irradiation

Mice were anaesthetised with isoflurane (2-4%) and placed in 6mm-thick lead-shielded cradle in a supine position to expose the thorax to X-ray irradiation (**Figure 2.4**). X-rays were delivered using a Gulmay medical RS320 irradiation system (Gulmay Medical, Ltd, Camberly, UK) at a dose rate of 2.02 Gy/min (300 kV, 10 mA). The physical set-up of irradiation rigs is indicated in **Appendix 3** and the range of radiation dose received on the ventral surface of the mouse, at the isocentre and at on the dorsal surface of the mouse is indicated in **Appendix 4**.

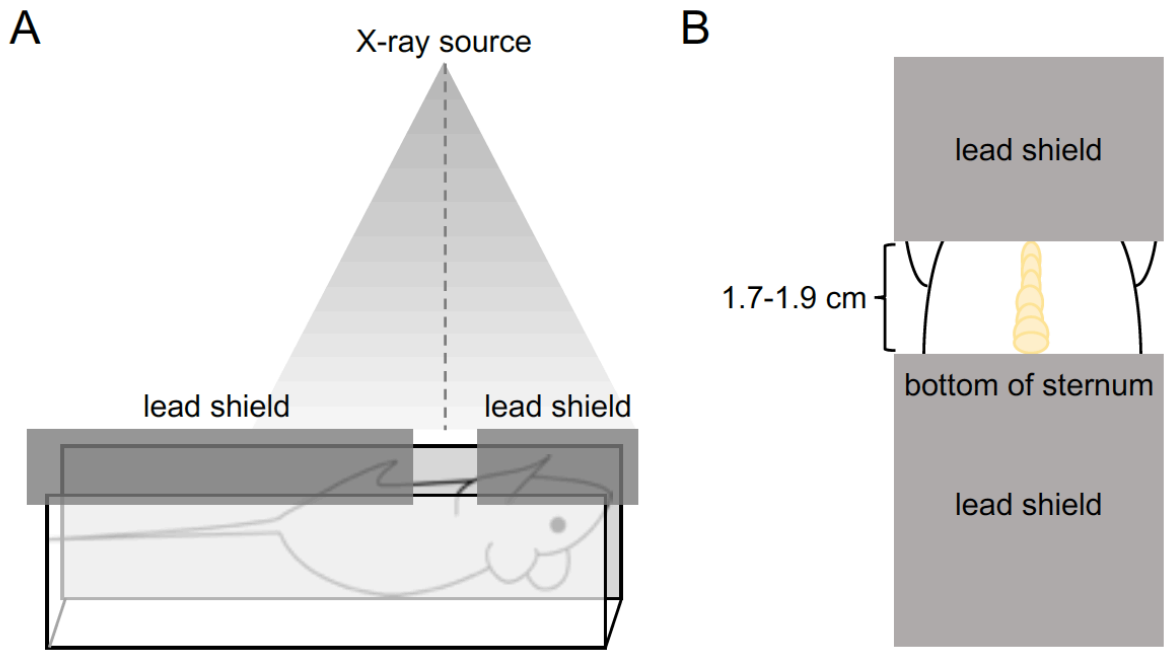


Figure 2.4. Lead shielding of the mouse for thoracic irradiation. Lead shields are indicated in dark grey boxes, and X-ray beam is indicated in light grey. Thoracic irradiation set up viewed from the side **(A)**, and the top **(B)**. Figure adapted from Martin (DPhil Thesis, 2021).

2.5.2 | CT-guided whole-heart irradiation

Mice were anaesthetised (2-4%) and placed on a mouse bed for 360° image acquisition with computer tomography (CT) using an image-contouring step with a CT2MD system. Radiation beam size and position were calculated using the Small Animal RadioTherapy (SmART) Plan treatment system and an X-ray was delivered with an arc beam on the X-Rad225Cx small animal irradiator (Precision Xray, North Branford CT) at 10-400 cGy/min (225kV, 13 mA). Dose planning and irradiation were performed using machines and facilities at Suzhou University (Suzhou, China) by researchers at SuZhou University and Crown Bioscience (Suzhou, China).

2.6 | IMMUNOHISTOCHEMISTRY

2.6.1 | Immunohistochemistry slide preparation

4 µm-thick sections were prepared from formalin-fixed paraffin-embedded tissues for all subsequent immunohistochemistry methods. A single-central section of the lung or a central transverse section of the heart were used unless otherwise specified.

2.6.2 | Haematoxylin and Eosin

Lung and heart sections were stained with haematoxylin and eosin (H&E) for general histological assessment of tissues. Haematoxylin Harris's (351945S, Sigma-Aldrich) and eosin (HT110132, Sigma-Aldrich) was used for this method and carried out per the manufacturer's instructions.

2.6.3 | Masson's Trichrome staining

Lung and heart sections were stained with Masson's Trichrome (MT) for the detection of collagen. Samples were stained using a Trichrome Stains (Masson) Kit (#HT15, Sigma-Aldrich, UK) according to the manufacturer's instructions.

2.6.4 | Chromogenic detection and counterstaining

Dual-stain chromogenic immunohistochemistry (IHC) was performed for the assessment of specific protein expression in a tissue section. Antigen retrieval was performed with citrate buffer (pH 6.0) on 4 µm-thick tissues, followed by chromogenic IHC staining using Dako EnVision+ G2 Doublestain System (K4003 and K3468, Agilent) and counterstaining with Gill's haematoxylin (GHS132, Sigma-Aldrich) according to the

manufacturer's instructions. The list of primary antibodies can be found in **Appendix 1**.

2.6.5 | Brightfield image slide scanning

Slides were scanned using the brightfield Aperio ScanScope CS (Leica) with a 20x/ 0.75 Plan Apo objective at a resolution of 0.25 μm/ pixel.

2.6.6 | Infiltration analysis on HALO image analysis software

The invasive 'tumour boundary' was manually annotated on chromogenic IHC images stained for immune cell markers according to H & E-stained images for tumour tissue identification. The HALO digital analysis platform (Indica Labs, v 2.3) was used for the infiltration analysis. Object locations were identified for all positive events (DAB+ brown staining) using HALO. An infiltration analysis was carried out using the object data whereby positive cells were counted within the 'invasive margin', which was defined as 200 μm inside and 200 μm outside of the tumor as identified with a rainbow markup.

2.7 | FIBROSIS SCORING AND QUANTIFICATION

2.7.1 | Fibrosis in the lung: Modified Ashcroft scoring

Lung fibrosis was assessed on central lung slices stained with Masson's Trichrome. The grade of lung fibrosis was scored using a modified Ashcroft scale (Hübner et al., 2008) (**Figure 2.5**), whereby lung fibrosis was scored on the extent of the most severe fibrosis.

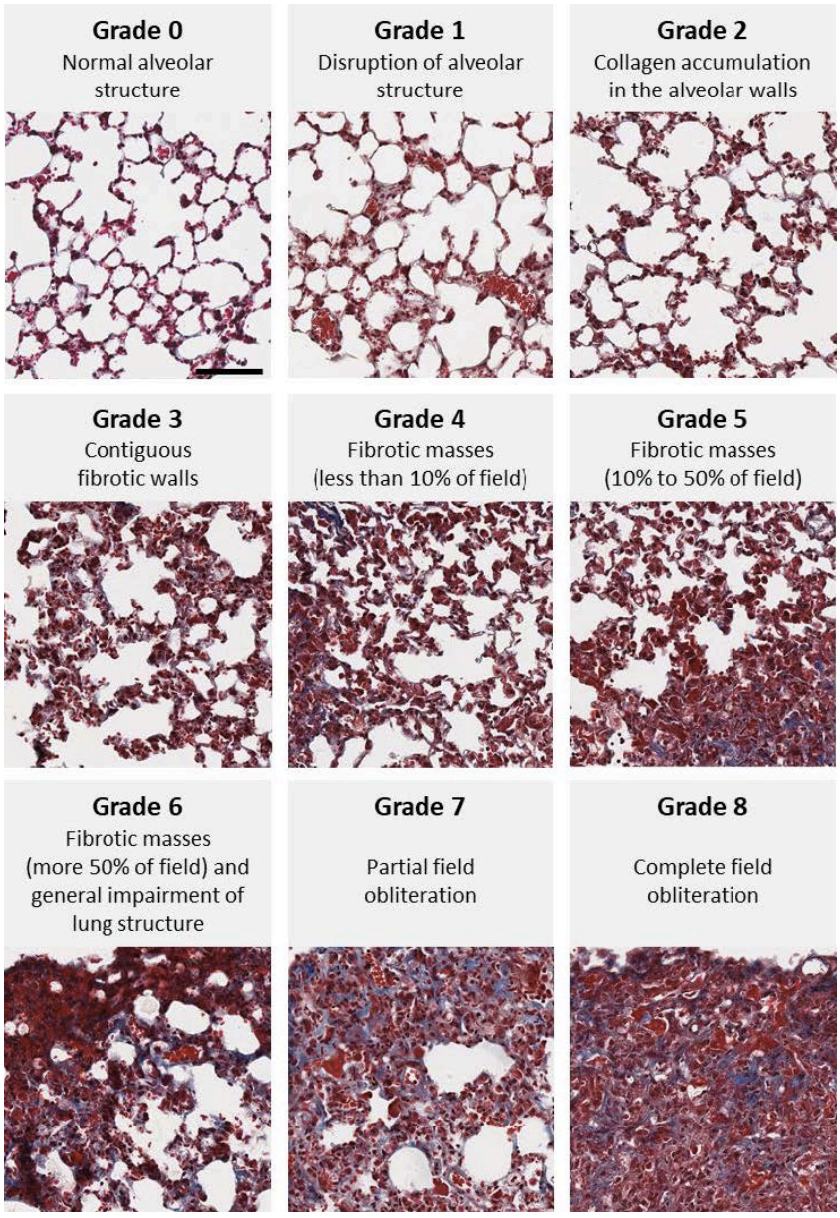


Figure 2.5. Guidelines for fibrosis scoring on the Ashcroft scale. Scale bar: 80 µm. Figure adapted from Lourenco (DPhil Thesis, 2017).

2.7.2 | Fibrosis in the heart

Pericardial fibrosis (Percent fibrotic pericardium)

Cardiac fibrosis was assessed on central transverse sections of the heart stained with Masson's Trichrome. The grade of pericardial fibrosis was quantified as the percent "thickened" (defined as > 5 μm collagen layer in the pericardium) pericardium of the total perimeter of the pericardium.

AI-based tissue segmentation on HALO

Collagen thickening around the perivasculature was quantified by the area of collagen tissue per mm of a blood vessel. The miniNet AI algorithm (HALO Image Analysis Platform Software, Indica Labs) was used to identify collagen tissue, myocardial tissue and glass on Masson's Trichrome-stained images of cross-sections of the heart. The AI was trained by at least 15 manually annotated regions of collagen, myocardium and glass. The calculated total area of collagen was used for quantification. Tissue segmentation was completed as shown in a representative image in **Figure 2.6**.

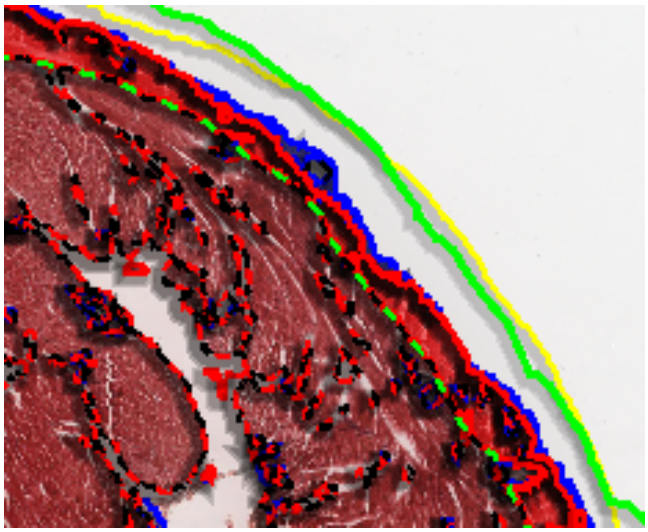


Figure 2.6. HALO AI tissue segmentation of heart structures. AI-based segmentation of collagen tissue is indicated in blue and myocardial tissue is indicated in red.

2.8 | MICROSCOPY

2.8.1 | Second harmonic generation microscopy imaging

Second-harmonic imaging microscopy

Second-harmonic imaging microscopy (SHIM) is a two-photon excitation fluorescence method that can be used to visualise non-centrosymmetric molecular structures including collagen, myosin, tubulin, and carbohydrate structures, and was used for the assessment of collagen fibres in the heart. 4 µm-thick longitudinal heart sections were stained with haematoxylin and eosin using standard methods and mounted with DPX. One whole-tissue image and three to five ROIs were imaged (including the pericardium in the field) per sample on the Zeiss 880 NLO confocal microscope using the Mai Tai Ti: Sapphire oscillator (Spectra-Physics, California, USA). SHIM Images were captured with an excitation wavelength of 890 nm, a pulse length of approximately 100 fs (check) and an emission filter centred at 445 nm and 10x objective.

SHIM image analysis with ct-FIRE

Microscopy images acquired on the Zeiss 880 microscope were deconvoluted on the ImageJ software. Pericardial regions were manually labelled on individual images and an algorithm-based image analysis tool on ct-FIRE software (https://loci.wisc.edu/software/ctfire) was used to analyse collagen fibre length, width, straightness and angles.

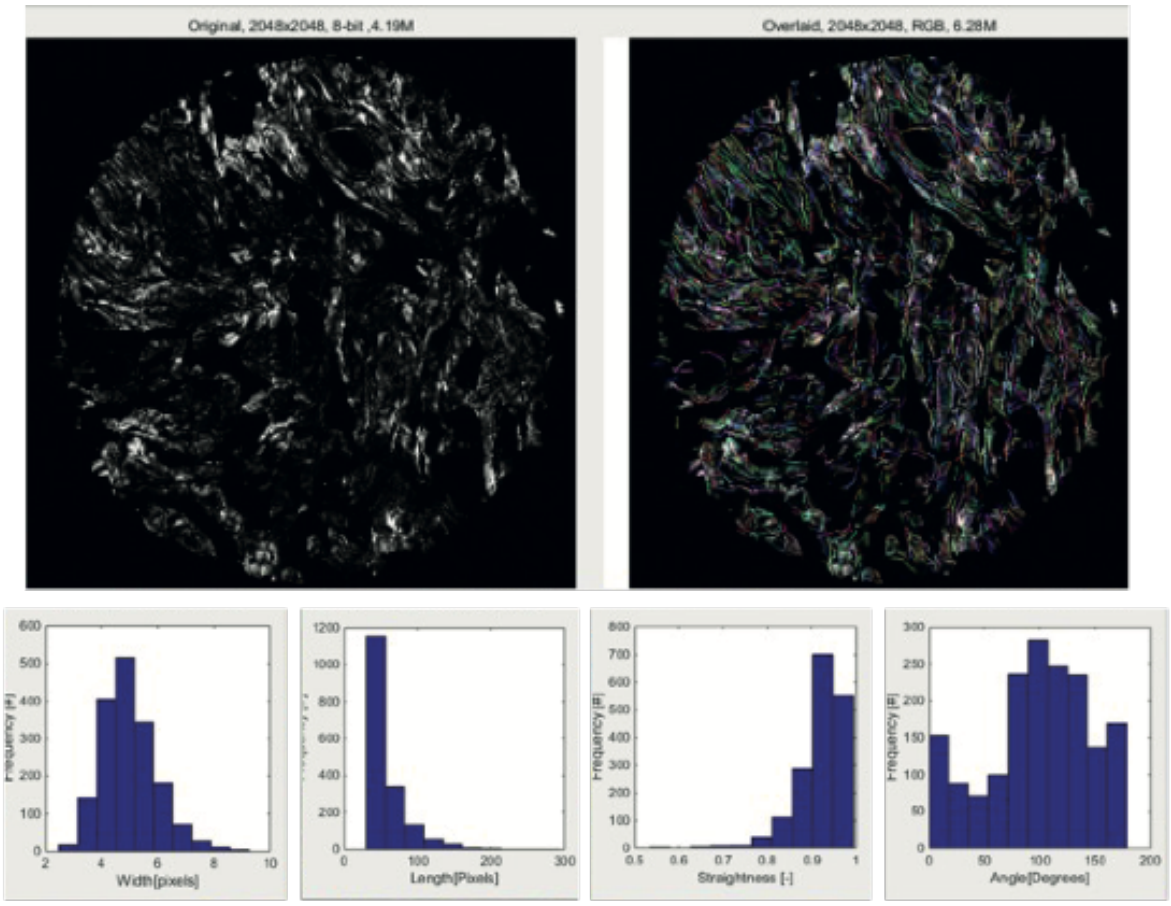


Figure 2.6. Collagen fibre analysis on ct-FIRE. Top panel: Sample images of deconvoluted SHIM image (left) and collagen fibre analysis processed by cf-FIRE (right). Bottom panel: Histograms automatically generated with software analysis, plotting width, length, straightness and angle of collagen.

2.9 | MULTIPLEX IMMUNOFLUORESCENCE

The experiment was done in collaboration with the Translational Histopathology Laboratory (THL) services in the Department of Oncology, University of Oxford and carried out by methods established at the THL services.

2.9.1 | Multiplex Immunofluorescence

Mouse sample preparation

Mouse lung tissues were collected and prepared in formalin-fixed paraffin-embedded (FFPE) block as described in **2.2.5**.

7-colour multiplex IF

Formalin-fixed paraffin-embedded (FFPE) samples were sectioned at 4 μm thickness onto TOMO+ IHC slides. Samples were baked overnight at 60°C. Multiplex (MP) immunofluorescence (IF) staining was carried out on FFPE sections using the OPAL™ protocol (AKOYA Biosciences) on the Leica BOND RXm autostainer (Leica, Microsystems). Six consecutive staining cycles were performed using the following primary Antibody-Opal fluorophore pairings; 1) CD4, clone EPR19514 (Abcam, Cat# ab183685) – Opal 480, 2) PNAd, clone Meca-79 (BioLegend, Cat# 120801) – Opal 520, 3) CD103, clone EPR22590-27 (Abcam, Cat# ab224202) – Opal 570, 4) CD19, clone D4V4B (Cell Signalling, Cat# 90176T) – Opal 690, 5) FoxP3, clone D608R (Cell Signalling, Cat# 126553) – Opal 620, 6) CD8, clone D4W2Z (Cell Signalling, Cat# 98941) – Opal 780. Primary antibodies were incubated for 30 minutes and detected using the BOND™ Polymer Refine Detection System (DS9800, Leica Biosystems) as per the manufacturer's instructions, substituting the DAB for the Opal fluorophores,

with a 10-minute incubation time and without the haematoxylin step. Antigen retrieval at 100°C for 20 minutes, as per standard Leica protocol, with Epitope Retrieval (ER) Solution 2 (AR9640, Leica Biosystems), was performed before each primary antibody was applied. Sections were then incubated for 10 minutes with spectral DAPI (FP1490, Akoya Biosciences) and the slides were mounted with VECTASHIELD® Vibrance™ Antifade Mounting Medium (H-1700-10, Vector Laboratories). Whole slide multispectral images (MSIs) were obtained on the AKOYA Biosciences Vectra® Polaris™ (scanned at 40x magnification). Batch analysis (spectral unmixing) of selected areas (all tissue) within each whole slide MSI was performed with the inForm 2.4.11 software. Finally, batch analysed MSIs were fused in HALO (Indica Labs, v 2.3), to produce a spectrally unmixed reconstructed whole tissue image, ready for analysis.

2.9.2 | Image analysis

Analysis was carried out on the HALO digital pathology platform (Indica Labs, v2.3). Tumour and tertiary lymphoid structure regions were delineated (pragmatic definitions and delineation of TLS regions are described in **2.9.3**) on individual images. CD4 T-cells ($CD4^+$), CD8 T-cells ($CD8^+$), regulatory T-cells ($CD4^+$ $FoxP3^+$), B-cells ($CD19^+$), dendritic cells ($CD103^+$), memory CD8 T-cells ($CD8^+$ $CD103^+$), and high endothelial venules (HEVs) ($PNAd^+$) were quantified.

2.9.3 | Defining Tertiary Lymphoid Structures

Regions with aggregates of > 50 cells in a 1×10^4 μm^2 area on multiplex IF images that contained both B-cell and T-cell populations were defined as tertiary lymphoid structures.

2.10 | ENZYME-LINKED IMMUNOSORBENT ASSAY

Plasma samples were collected from mice as detailed in **2.2.5** and stored at -20°C. Cytokines were evaluated from plasma samples using the Mouse IFN-β Quantikine® ELISA kits (R&D Systems, MIFNB0) and the mouse TNF-α Quantikine® ELISA kits (R&D Systems, MTA00B) according to the manufacturer's instructions.

Absorbance values were obtained at 450 nm and 540 nm wavelength on the Omega spectrophotometer (POLARstar Omega spectrophotometer, BMG Labtech). Final values were calculated by subtraction of the absorbance at 540 nm from the absorbance at 450 nm. A standard curve was plotted, and the equation derived from this standard curve was used to calculate the concentration of cytokines.

2.11 | FLOW CYTOMETRY

2.11.1 | Lung and cardiac tissue digestion

Lung and cardiac tissues were collected from mice as described in **2.2.5 I** (with perfusion) and transported in ice-cold Hanks Balanced Salt Solution (HBSS). Methods for cardiac tissue isolation and digestion were modified from methods described by Pinto et al. (2013) (Pinto et al., 2013). Atria were removed and tissues were minced with surgical scissors and passed through an 18 G needle. Lung tissues were minced and passed through an 18 G needle in a similar fashion to the heart tissue. Chemical digestion was performed with collagenase/ DNase solution at 37°C for 30 minutes with agitation. Cells were passed through a 50 μm cell strainer and red blood cells were lysed for flow cytometry analysis directly or viably frozen in 10% DMSO/ FBS for later analyses.

2.11.2 | Flow cytometry

Flow cytometry was performed on single-cell isolated lung and cardiac cells. Mouse cells were suspended in 2% FBS/ PBS blocked with Mouse FcγIII (CD16) and FcγII (CD32) antibody (BD Biosciences, 553141) and stained with antibodies for surface markers and/ or intracellular markers after fixation and permeabilisation (eBioscience) performed as per manufacturer's instructions with antibodies specified in **Table 2.2**. Flow cytometry was performed on the Attune NxT Flow Cytometer with the Invitrogen Attune Cytometric Software (Invitrogen, UK) or the CytoFLEX Flow Cytometer, and CytExpert software (Beckman Coulter, Indianapolis US). Analysis was carried out on FlowJo (v10.6.1, BD Bioscience). Gating strategies for flow analyses are detailed in Di**Appendix 5**.

Table 2.2. Antibody panels for flow cytometry. List of antibodies used for lymphoid, myeloid, fibroblast and macrophage polarisation analyses by flow cytometry.

Lymphoid panel
LD Green
CD45 PE
NK1.1 PerCP-Cy5.5
CD8 PE-Cy7
CD4 APC
CD3 APC-Cy7
PD-1 BV421

Myeloid panel
L/D Green
iNOS PE
CD206 PerCP-Cy5.5
CD11b PE-Cy7
Ly6G APC
Ly6C APC-Cy7
F4/80 BV421
Gr1 BV510
CD11c BV605

Cardiac fibroblast panel
αSMA AF405
Collagen I AF488
PDGFR-α/CD140a PE-Cy5
TGF-β RII AF700
Live/Dead stain eF780

Macrophage polarisation panel
L/D Green
CD45 APC-Cy7
F480 BV421
CD11b AF700
CD80 PE
CD206 APC

2.12 | WESTERN BLOTTING

Protein extraction from mouse lung tissue

Mouse lung samples were collected as described in **2.2.5** and snap frozen for storage at -80°C. Lysis buffer (20 mM Tris pH 7.5, 137 mM NaCl, 50 mM NaF, 10 % glycerol, 1% NP-40, 0.1% SDS, 1mM Na3VO4 and 1 tablet of protease inhibitor/25mL of buffer) and tissues were mixed in a 1:2 ratio of tissue to buffer (e.g. for 50 mg of tissue, 100 uL of lysis buffer was added). Samples were minced with surgical scissors and physically mashed with a pestle. Samples were then sonicated with the Bioruptor® Plus (Diagenode). Samples were centrifuged and the supernatant was collected for storage at -20°C.

Western Blotting

The BioRad system was used for western blotting. Experiments were carried out using equipment from BioRad and the method was carried out according to the manufacturer's instructions. Laemmli sample buffer (Sigma-Aldrich, S3401) was used to prepare the protein sample, and pre-cast 4-15% polyacrylamide gradient gels (Mini-PROTEAN® Precast gels or Criterion™ TGX gels, BioRad) and running buffer (BioRad, 1610732) were used for gel electrophoresis run at 100V. Transferring of the protein from the gel to a nitrocellulose membrane (0.45 μm pores; Bio-Rad, 162-0115) was performed with a transfer buffer (BioRad, 1610734) and an electrical current of 10 mA in a cold room. Membranes were washed with TBS-T and blocked with 3% BSA/ TBS-T for 1 hour and probed with primary antibodies at 4°C overnight. After incubation with primary antibodies, membranes were washed with TBS-T and probed with dye-conjugated secondary antibodies (IRDye 800CW, LI-COR, 926-32211 or IRDye680RD,

LI-COR, 926-68071) for detection with the LI-COR Odyssey 9120 western blot detection system (LI-COR Biosciences, UK). Images were acquired and analysed on ImageStudio (v5.2.5, LI-COR Biosciences).

2.13 | WHOLE-EXOME SEQUENCING AND ANALYSIS

Whole-exome sequencing

Mouse lungs were treated with RNAlater for 24 hours before storage at -80°C. Lung tumours were resected from mice and stored individually for DNA extraction and genomic DNA library preparation at Source BioScience (Nottingham, UK). The DNA was extracted using the DNeasy Blood & Tissue Kit and quantified using the Qubit dsDNA Broad Range assay and qualified using the NanoDrop Spectrophotometer. DNA libraries were prepared in accordance with the Nextera Flex for Enrichment with RNA Probes Demonstrated Protocol, and enrichment of genomic DNA library was carried out using the SureSelectXT Mouse All Exon kit (Agilent, 5190-4641). The library pool was validated using the Agilent BioAnalyser 2100. Sequencing was carried out on the NovaSeq 6000 S4 flow cell lane, 150 bp paired-end read mode. A yield of 2500M read pairs in total was obtained for an average of ~65M read pairs per sample. Somatic variant calling was performed at the Bioinformatics Core Facility, Source BioScience. Steps for data processing are specified below.

Data processing

Adapter and Quality Trimming

Raw FASTQ files were adapter- and quality- (Q30) trimmed using bbduk (bbmap Version 38.86).

Mapping, Deduplicating, Sorting and Indexing Trimmed Reads

Trimmed FASTQ files from runs 1, 2 and 3 were aligned (or mapped) to the reference genome using BWA-mem (version 0.7.17-r1188) and combined using Picard's MergeSamFiles. Duplicate reads were then marked and removed (deduplicated) to enable accurate quantification of variants. The resulting BAM files were sorted by coordinate and indexed for visualisation with common genome browser software. Genome coverage was assessed using Picard's CollectHsMetrics tool.

Somatic Variant Calling

Variant calling was performed using Strelka (Strelka v 2.9.10) to identify somatic single nucleotide variations (SNVs) and Manta (Manta v1.6.0) to identify somatic short insertions and deletions (INDELs), within the target regions. Strelka starts with a preliminary step to estimate regional statistics from the input alignments, including the sequence depth distribution. All input samples are jointly analysed to identify candidate alleles, realign all input reads, analyse reads to make model-specific variant inferences, then compute properties of each variant used to apply filters or empirically recalibrate confidence that each variant represents a somatic variant in the input sample(s). For somatic variant calling, it is a recommended best practice to provide INDEL candidates from the Manta SV and INDEL caller. In addition to the default flags, Exome/Targeted sequencing flags were given (--exome and --callRegions). As two control samples were provided, these were merged and used as the reference ("NORMAL") sample for each analysis.

2.14 | RNA SEQUENCING AND FUNCTIONAL ANALYSES

RNA sequencing

Total RNA was isolated from mouse lung tissues pre-treated with RNAlater using the RNAeasy Mini kit (Qiagen). RNA was quantified using the Qubit RNA Broad Range assay and qualified using the RNA 6000 Nano assay on the Agilent BioAnalyzer and NanoDrop Spectrophotometer. Poly-A mRNAs were prepared using the Illumina Stranded mRNA Prep Ligation/ TruSeq Stranded mRNA Sample Preparation protocol and RNA libraries were validated on the Agilent BioAnalyzer 2100 and Qubit Hight Sensitivity for assessment of size distribution and library concentration. RNA sequencing was carried out on the NovaSeq 6000 flow cell lane, 150 bp paired-end read mode at the Genomics Core Facility, Source BioScience (Nottingham, UK). Gene expression profiles were processed at the Bioinformatics Core Facility, Source BioScience. Raw read counts were normalised into transcripts per million mapped reads (TPM). Steps for data processing are specified below.

Data processing and differential expression analysis

Adapter Trimming

Raw FASTQ files were adapter-trimmed using bbduk (bbmap v38.89).

Quantification of Gene Expression and Gene Annotation

Gene expression was quantified using the tool Salmon (Patro et al., 2017). Relative transcript abundance was determined by performing a quasi-alignment to trimmed FASTQ files using Salmon 1.4.0, to count and generate transcripts per million (TPM). Technical replicate pairs were merged for this analysis.

Differential Gene Expression Analysis

The *tximport* R package (v. 1.18.0) (Soneson et al., 2016) was used to summarise *Salmon* transcript-level abundance estimates at the gene level. The resulting gene-level counts were corrected for library size using the *DESeq2* (v. 1.30.1) (Love et al., 2014) *'median-of-ratios'* normalisation procedure and lowly expressed genes – with a cumulative sum below 10 transcripts across all treatment groups – were omitted. Gene expression counts were variance-stabilised using the *DESeq2 'regularised log'* (rlog) transformation prior to performing hierarchical clustering and principal component analyses (PCA). Differential expression analyses were carried out with *DESeq2* using the default Wald test for significance testing and the Benjamini-Hochberg (BH) method for multiple test correction. Genes with absolute binary logarithm fold-changes (FC) > 1 and BH-adjusted p-values ≤ 0.05 were considered significantly differentially expressed. Script for *DESeq2* is detailed in **Appendix 6**.

Overrepresentation analyses

The *clusterProfiler* R package (v. 3.14.3) (Wu et al., 2021) and *g:Profiler* (2019 update) (Raudvere et al., 2019) web server were used to analyse pathway enrichment among differentially expressed genes. Probabilities of Gene Ontology (GO) term overrepresentation were computed based on hypergeometric testing with Benjamini-Hochberg false discovery rate (FDR) correction. The statistical domain scope for overrepresentation analyses was limited to the ~16,000 genes captured within the RNA-seq experiment. The high level of redundancy among lists of statistically enriched functional categories was reduced based on semantic similarity metrics using the *simplify()* function of the *clusterProfiler* package or the REVIGO webtool (Supek et al., 2011), for clusterProfiler and g:Profiler analysis outputs, respectively.

Gene set enrichment analyses

Differential expression analyses outputs were used to perform pre-ranked gene set enrichment analyses (*'GSEAPreranked'*) using the product of the fold-change sign with the negative decimal logarithm of the BH-adjusted p-value (*i.e.* FC sign x -$\log_{10}$(BH-adj. p-value)) as the ranking metric for each gene. GSEA was performed with the Broad Institute GSEA software (v. 4.1.0) (Mootha et al., 2003; Subramanian et al., 2005) using default settings and functional annotations for GSEA analyses were obtained from the Molecular Signatures Database (MSigDB) Hallmark (Liberzon et al., 2015) and GO Biological Process (Ashburner et al., 2000) gene set collections.

2.15 | STATISTICAL ANALYSES

Data were expressed as mean ± standard error of the mean (SEM) and analysed using the GraphPad Prism software (version 9.0, GraphPad). Student's t-test was used for comparison of two groups, and one-way analysis of variance (ANOVA) with a Bonferroni correction was used on comparisons of more than two groups unless otherwise specified. Statistical significance was defined as $^{ns}p > 0.05$, $*p < 0.05$, $**p < 0.01$, $***p < 0.001$, $****p < 0.0001$.

CHAPTER 3. LUNG TUMORIGENESIS AND RADIATION-INDUCED TISSUE TOXICITY IN AN *IN VIVO* MODEL

3.1 | INTRODUCTION

The dose of radiation given for cancer treatment can be limited due to considerations for adverse events in normal tissues. Therefore, widening the therapeutic window of radiotherapy (RT) remains an important question for cancer treatment. Despite the need to evaluate both anti-tumour efficacies and normal tissue toxicities induced by cancer therapies including RT, most currently available preclinical mouse models cannot assess both tissues in parallel. In order to address these limitations, our laboratory has used a carcinogen-induced lung cancer model in the A/J mouse strain, which has biological features associated with human disease and treatment side effects. In this mouse model, lung tumours are initiated in the A/J mouse model by injection of urethane (ethyl carbamate), a known carcinogen commonly found in tobacco smoke (U.S. Food and Drug Administration, 2012; Forkert, 2010; Li & Hecht, 2022).

Urethane-induced A/J mouse model

Urethane is the ethyl ester of carbamic acid ($NH_2COOC_2H_5$) and when administered in mice, result in higher incidences and the earlier formation of pulmonary adenomas that arise autochthonously (Field & Lang, 1988). Urethane can induce mutagenic events such as chromosomal breaks/ rearrangements and changes in nucleotide/ base sequences (Auerbach, 1967). The chemical is absorbed into all tissues in the body, and the mutagenic action takes place more rapidly and most frequently in the pulmonary tissue, giving rise to pulmonary tumours within 6 months after urethane treatment (Field & Lang, 1988) with a latency period of a year for tumour

development in other tissues (Chen et al., 1994; Mostofi & Larsen, 1951; White et al., 1970).

The susceptibility of mice to urethane-induced pulmonary tumours is strain-specific, with higher incidences of pulmonary tumours in A/J mice in a comparative study of urethane-induced tumorigenicity with CD-1 and C57BL/6 mice (Forkert, 2010; Titis & Forkert, 2001). The organ- and strain-specificity of mutagenesis from urethane treatment is thought to be due to (i) the presence of a susceptibility locus around the *K-ras* gene on chromosome 6 in the A/J mice and (ii) the higher expression of enzymes that convert urethane into a metabolite with higher mutagenic potency, vinyl carbamate epoxide, in the lung tissue and the A/J strain (see below).

Studies of lung tumour induction with urethane in the A/J mice revealed a major lung tumour susceptibility locus (pulmonary adenoma susceptibility locus 1, *Pas1*) on a distal region of chromosome 6, a region including *K-ras-2*, and its association with lung tumour development (Gariboldi et al., 1993). Additionally, investigations into the A/J mouse strain as a lung cancer model uncovered a 37-base pair deletion in an intron of *K-ras*, which correlated with a higher susceptibility to urethane tumour induction and a higher mRNA expression of the 4A isoform of the *K-ras* gene, suggesting the region may act as a quantitative trait locus (Chen et al., 1994; Dassano et al., 2014; To et al., 2006). Similarly, the resistance to urethane-induced tumour induction in mouse strains such as C57BL/6 and C3H/He may be explained by the presence of the 37-base pair region in the *K-ras* intron which is absent in the A/J mouse and the lower expression of *K-ras* 4A (Chen et al., 1994; Dassano et al., 2014). The *Pas1* locus and tumour susceptibility phenotype have also been associated with altered mRNA expression of numerous genes within the mitogen-activated protein kinase (MAPK) and

phosphatidylinositol 3-kinase (PI3K) pathways in lung tumours, further supporting K-ras as the upstream effector of tumour susceptibility (Cotroneo et al., 2016).

The susceptibility of mouse pulmonary tissue to urethane-induced tumourigenesis could also be due to the tissue-specific activity of an enzyme, P450 2E1 (CYP2E1), which metabolises urethane into more potent mutagens including vinyl carbamate and vinyl carbamate epoxide (Dahl et al., 1978; Forkert, 2010; Titis & Forkert, 2001). Vinyl carbamate epoxide reacts with DNA to form base adducts, the mutagenic capacity of which has been directly measured in the mouse lung tissue (Hernandez & Forkert, 2007; Titis & Forkert, 2001). Base substitutions at codon 61 of *K-ras* were observed in nearly half of the tumours that were directly induced by the administration of vinyl carbamate epoxide (Borrego et al., 2018; Malkinson, 1992; Titis & Forkert, 2001). A comparative study of A/J, CD-1, and C57BL/6 mice uncovered that A/J mice had a 40% and 10% higher rate of CYP2E1 activity than in the C57BL/6 mice and CD-1 mice (Forkert, 2010).

The tumours that arise from urethane treatment predominantly harbour *K-ras* and *p53* mutations (Horio et al., 1996; Westcott et al., 2015), and are histologically categorised as adenomas and adenocarcinomas (Forkert, 2010; Gunning et al., 1991; Mostofi & Larsen, 1951; Westcott et al., 2015). Additionally, an exome-sequencing study of genetically-driven (*K-ras*^{LA2} mutant mouse model) and carcinogen-driven lung cancer models (MNU or urethane-initiated) revealed a highly complex mutational spectra in tumours that arise in the carcinogen-driven lung cancer models compared with those in the genetically driven lung cancer model (Westcott et al., 2015). The genetic (*K-ras* and *p53* mutants), histological and mutational (high TMB) characteristics of the urethane-driven cancer model make the model relevant for the

studies of early stage lung tumours in smokers, as lung tumours in smokers are known to have a high abundance of *K-ras* and *p53* mutations, and have a high mutational burden (Zappa & Mousa, 2016).

Furthermore, A/J mice have also been shown to develop relevant pathophysiological adverse events to cancer therapies such as radiation treatment. Previous studies using the A/J mice reported pneumonitis and pleural effusions from a dose of 15 Gy or 18 Gy to the thorax (Jackson et al., 2011; Paun et al., 2017). Additionally, studies in our laboratory have revealed that the A/J mice develop oesophagitis 7-10 days (Martin, 2020) and pulmonary fibrosis 4-6 months following 5 x 5 Gy fractionated or 13 Gy single dose RT to the thorax (Lourenco, 2017) (**Figure 3.1**). The development of inflammation-induced toxic events such as oesophagitis and pneumonitis suggests the mouse model's potential use for the evaluation of early immune events following treatment with cancer therapies and other inflammation-driven late toxicities from cancer therapies.

Radiation and tumour infiltrating lymphocytes

A growing body of evidence suggests that radiation can induce an immune response that can have an impact on tumour development (Formenti & Demaria, 2013; Frey et al., 2012; Weichselbaum et al., 2012). The immunomodulatory effects of radiation appear complex, however, with some evidence pointing to its role in tumour promotion (Weichselbaum et al., 2017) and others pointing to its anti-tumour effects (Dovedi et al., 2017; Golden et al., 2015; Golden et al., 2013; Postow et al., 2012). The role of tumour-infiltrating lymphocytes stimulated by radiation and their subsequent effects on tumour growth largely depends on the type of immune cells that are recruited to the tumour; these include DCs, macrophages, cytotoxic T-cells, T_{regs}, and MDSCs

(Demaria & Formenti, 2012; Deng, Liang, Burnette, et al., 2014; McBride et al., 2004; Schaue et al., 2012). Among these, tumour-infiltrating T-lymphocytes have been found to be associated with beneficial clinical outcome for a number of solid tumours including head and neck, breast, ovarian, prostatic, renal, colorectal, and lung cancers (Fridman et al., 2012). Several studies have reported $CD3^+$ and $CD8^+$ TILs to be correlated with clinical benefit, and regulatory T-cells (T_{reg}) to be correlated with a worse prognosis for NSCLC patients (Balermpas et al., 2014; Fridman et al., 2012; Gooden et al., 2011). On the other hand, the interplay between radiation, tumour-associated macrophages (TAMs; classified into M1 which have anti-tumour properties and M2, which have tumour-promoting properties) and tumour development is not yet fully understood, with conflicting evidence for TAMs playing a role in tumour promotion (Medrek et al., 2012) *and* in tumour elimination (Meng et al., 2010). Further studies are required to elucidate the role of radiation on modulating the immune microenvironment around the tumours, and impact this has on cancer development.

Together, the urethane-induced A/J mouse model is a candidate model in which evaluations of both lung tumour development and normal tissue responses to cancer treatments can be performed. There is also a need to understand how radiation modulates the tumour immune microenvironment. Therefore, the aims of the chapter are to (1) characterise tumour development in the A/J model and evaluate RT-induced normal tissue toxicities for potential therapeutic window studies; and (2) assess the early events (with an immunological focus) in lung normal and tumour tissues following radiation.

3.2 | RESULTS

3.2.1 | Lung adenocarcinomas can be chemically induced in an A/J mouse

To first investigate the A/J model as a model for the study of lung cancer development, 6–8-week-old mice were injected with urethane (1 x 5%, 2 x 5% or 1 x 10% of body weight), intraperitoneally (i.p.) and assessed for tumour growth in the lung (**Figure 3.1a**) and other organs. In the two-dose condition, the second dose of urethane was administered 6 days after the first dose.

All urethane-treated mice developed visible nodules on the surface of the lungs (**Figure 3.1b**), and distinguishable microscopic tumours on sectioned lungs 26 weeks after treatment (**Figure 3.1c**). No other organs developed visibly detectable tumours. The lung nodules were histologically characterised as tumours of solid and mixed phenotypes[4] (**Figure 3.1c**). In addition, the induction of lung tumours was confirmed to be specific to urethane- treatment as demonstrated by the lack of superficial tumours in PBS-treated A/J mice ($p < 0.0001$) (**Figure 3.2a, b**). Furthermore, results demonstrated that the number of lung tumours formed was dependent on the number of doses (1 x 5% compared to 2 x 5%, $p < 0.001$) and the total dosage of urethane administered per dose (5% compared to 10%, $p < 0.05$) (**Figure 3.2a, b**). These results suggest that the number of DNA lesions caused by the carcinogen (indicated by dose-dependence) *and* the number of initiation events (i.e. the two-step process of

[4] Tumour classification defined by Westcott et al. (2015i.e.) and detailed in **Appendix 7**.

carcinogenesis, and indicated by dependence on the number of doses) may each play a role in the formation of lung tumours in the A/J mouse model.

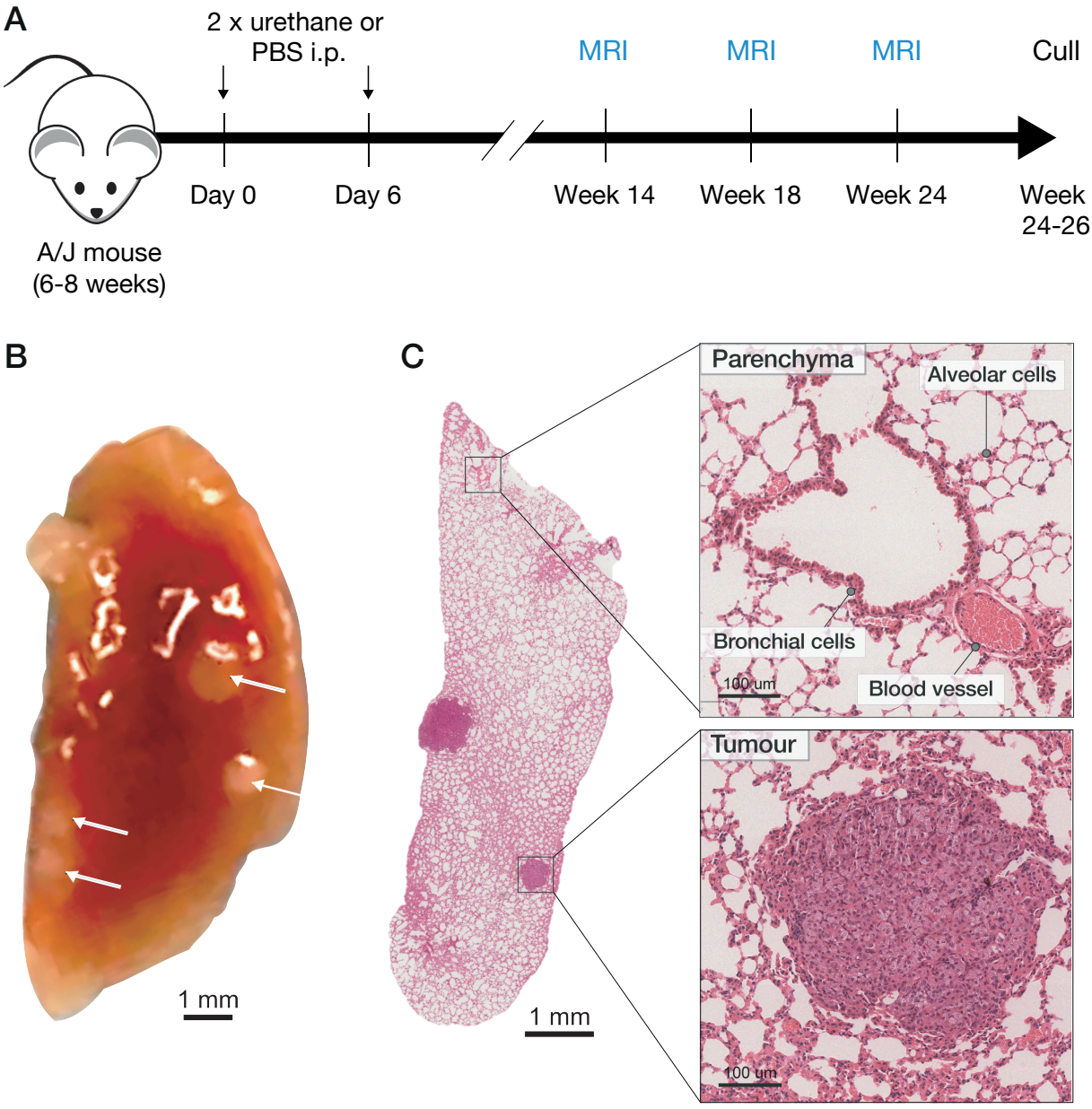


Figure 3.1. Urethane induces lung adenocarcinomas in A/J mice. (A) Schematic representation of an *in vivo* experiment of lung tumour induction with a carcinogen in the A/J mice. Mice were treated with urethane (1 × 5%, 2 × 5% or 1 × 10% of body weight) or PBS i.p. on day 0 and day 6 and culled 24-26 weeks after treatment for assessment of lung tumour growth (n = 3-5 per treatment group). Lungs were collected for analysis. **(B)** Representative image of a lung lobe collected from a mouse 24 weeks after urethane treatment. Scale bar: 1 mm. **(C)** Representative image of a cross-section of a lung lobe stained with H & E (left). Enlarged images show the lung parenchyma and lung tumour (right) collected from a mouse 26 weeks after urethane treatment. Scale bar: 1 mm (left) and 100 μm (right).

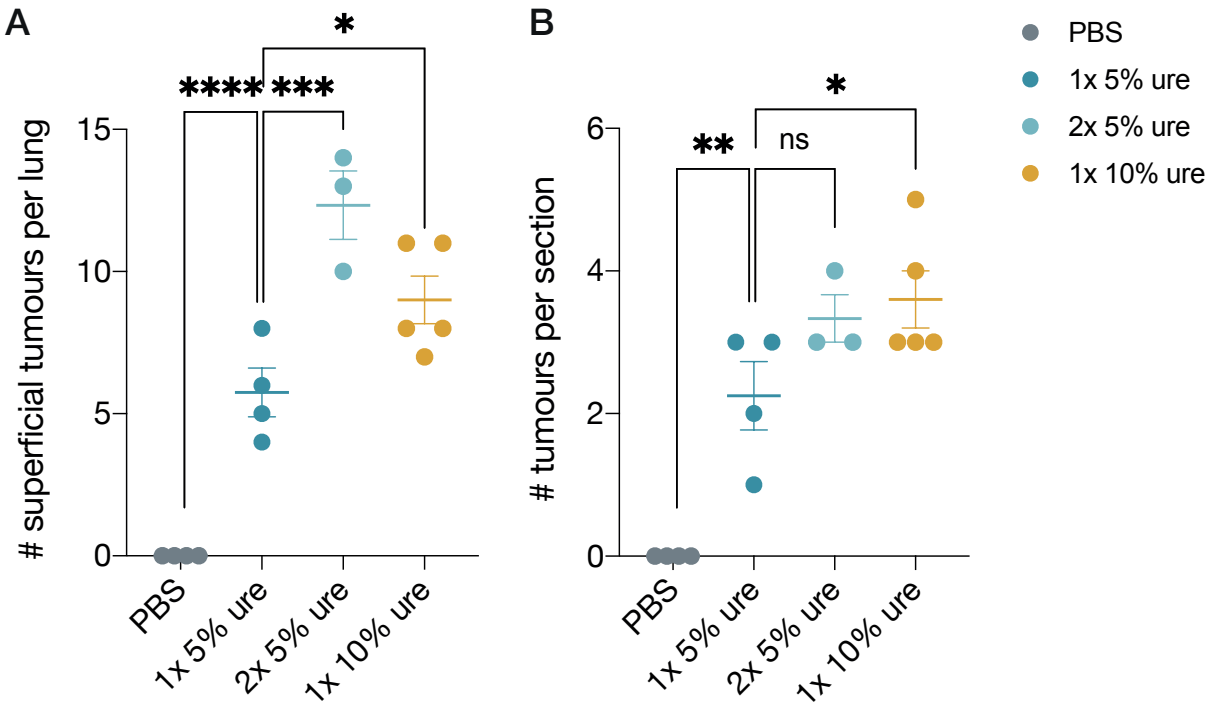


Figure 3.2. Lung tumour induction increased with higher concentration or frequency of carcinogen dose. (A) The number of tumours counted on the surface of the left lung, **(B)** number of tumours counted per lung section from PBS-, or urethane-(1 × 5%, 2 × 5% or 1 × 10%) treated mice. n = 3-5 per treatment group. Results are mean ± SEM, analysed by a one-way ANOVA test. $^{ns}p > 0.05$, $^{*}p < 0.05$, $^{**}p < 0.01$, $^{***}p < 0.001$, $^{****}p < 0.0001$.

To identify the timepoints in which we can evaluate the stages of early lung tumour development, the lung tumours of the mice were quantified at 0 days, 3 days, 4 weeks, 18 weeks, 24 weeks and 32 weeks after a 5% dose of urethane treatment (**Figure 3.3a**). Superficial lung tumours were visible and quantifiable 18 weeks after treatment and beyond ($p < 0.01$) (**Figure 3.3b**). The data also demonstrated that lung tumour development could be tracked over time after urethane administration (0 days compared to 32 weeks, $p < 0.0001$) (**Figure 3.3b**). Assessments of tumour numbers and tumour volume on magnetic resonance imaging (MRI) confirmed the measurability of lung tumours 18 weeks after treatment, and the ability to follow lung tumour growth over time (**Appendix 9**). These data together suggest that both tumour numbers *and* tumour burden increase over time from a one-time initiation event with urethane.

In the following experiments, a dose of 5% urethane was used for tumour induction and the assessment of lung tumours was carried out after a minimum of 18 months after treatment.

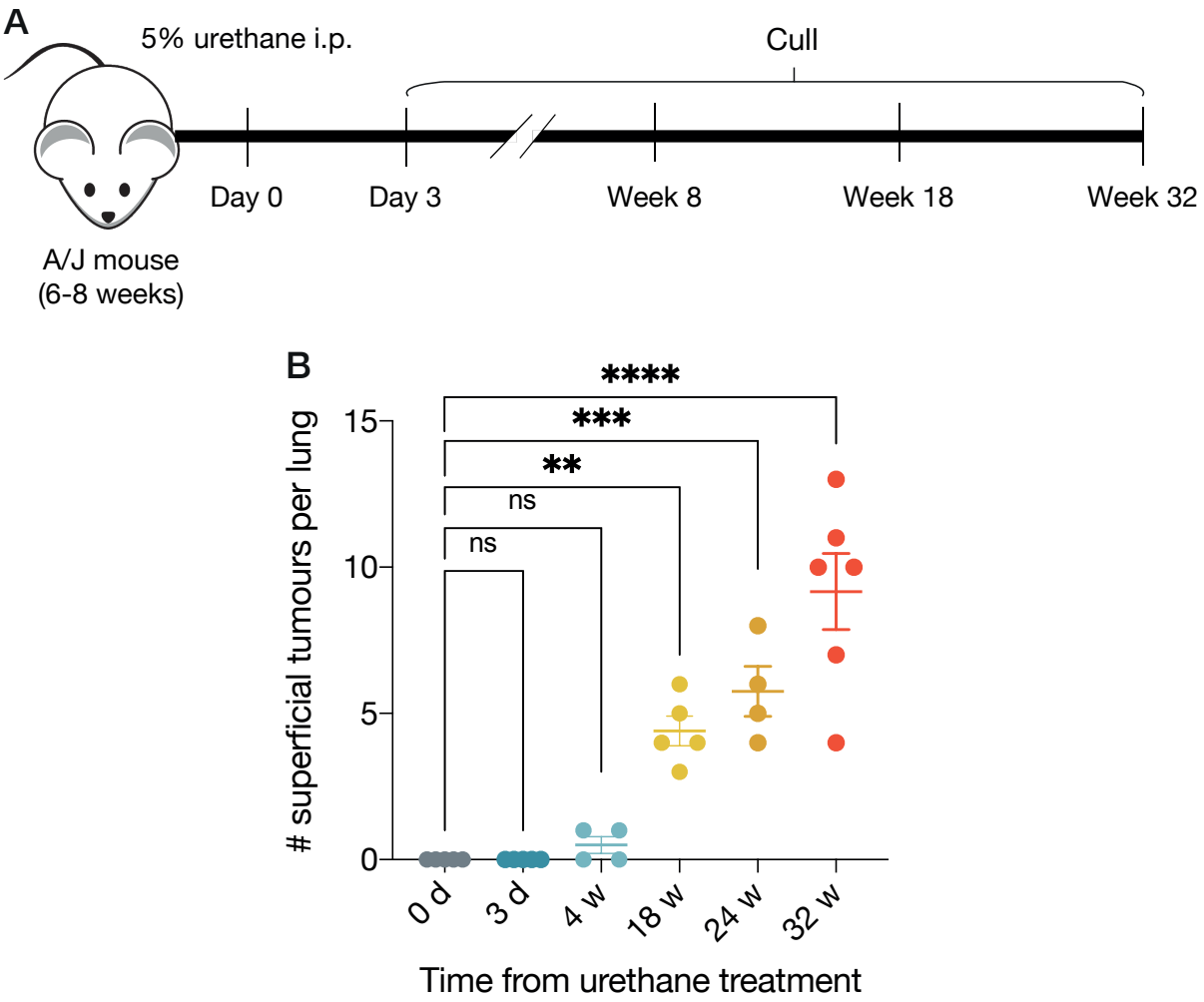


Figure 3.3. Lung tumours increase in numbers and tumour burden weeks after urethane treatment. (A) The number of nodules counted on the surface of the left lung, **(B)** the number of tumours per lung section from mice euthanised 0 days, 3 days, 4 weeks, 18 weeks, 24 weeks, and 32 weeks after urethane treatment. n = 4-6 per group. Results are mean ± SEM, analysed by a one-way ANOVA test. $^{ns}p > 0.05$, $*p < 0.05$, $**p < 0.01$, $***p < 0.001$, $****p < 0.0001$.

3.2.2 | Urethane-induced lung tumour cells have a higher proportion of proliferating cells than parenchymal cells and contain infiltrating macrophages and CD3$^+$ T-cells

To establish the baseline characteristics of the urethane-induced lung tumours, a histological assessment of lung tumour tissue and normal tissues of the mice was performed 18 weeks after urethane treatment. Proliferation (Ki67), apoptosis (cleaved caspase 3, CC3) and infiltrating immune cells (CD45$^+$ lymphocytes, CD68$^+$ macrophages, CD3$^+$ T-cells and CD8$^+$ cytotoxic T-cells) were evaluated by IHC. As expected, Ki67 staining indicated that lung tumours had a higher proportion of proliferating cells compared to parenchymal cells (**Figure 3.4**). IHC staining for CC3 showed that there is little to no cell death in the tumour or parenchymal cells of the lung (**Figure 3.4**). The low rate of apoptosis, however, might require confirmation with other assessment methods such as terminal deoxynucleotidyl transferase dUTP nick end labelling (TUNEL) assays as the quality of CC3 staining could not be confirmed with positive controls.

Tumour infiltrating lymphocytes (TILs), in particular, CD68$^+$ macrophages and CD3$^+$ T-cells were observed in the lung tumours. CD8$^+$ cytotoxic T-cells, however, were not found frequently within the tumours (**Figure 3.5**). According to a T-cell-based classification of immune 'hot'/ 'intermediate'/ 'cold' tumours as defined by Galon and Bruni (2019) (Galon & Bruni, 2019) (detailed in **Appendix 11**), the urethane-induced lung tumours could be classified as an 'intermediate' immune phenotype, as they contain CD3$^+$ T-cells, but not many CD8$^+$ T-cells within the tumour tissues.

The ‘intermediate’ phenotype for TILs might be explained by the known high mutational burden of lung tumours in the urethane A/J mouse (Westcott et al., 2015), potentially inducing some tumour immunogenicity. However, at the same time, in order to become established, tumours could have undergone some processes of immunoediting, creating a more complex picture of the immunogenic landscape of the tumour. The understanding of TAMs in these tumours might benefit from a further understanding of the type of macrophages that occupy the tissue, i.e. if they are M2 or M1 macrophages, which we further investigates in later sections of the Chapter.

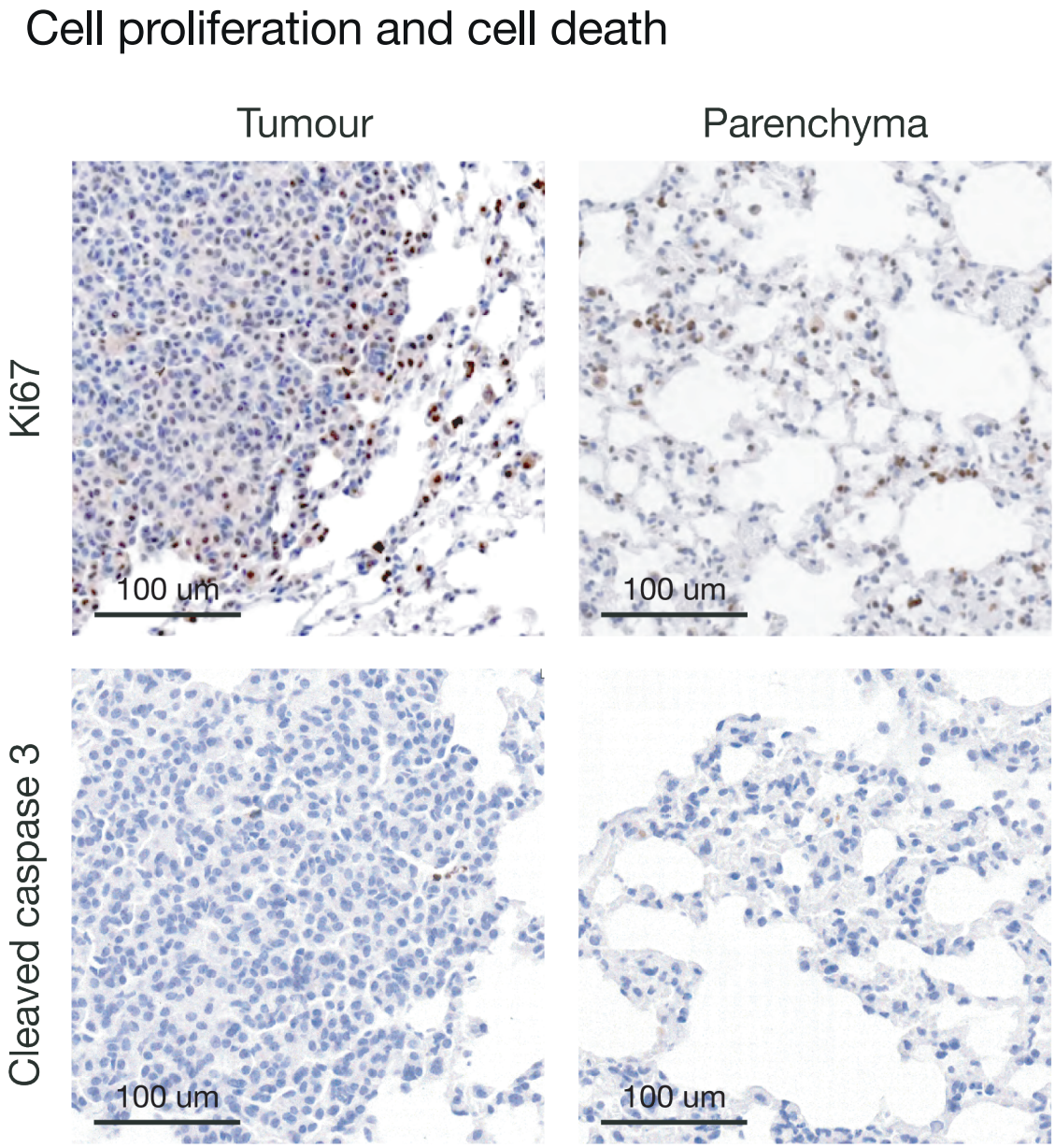


Figure 3.4. Urethane-induced lung tumours have a low rate of proliferation. Representative IHC images of Ki67 positive cells and cleaved caspase 3 (CC3) positive cells in the lung tumour and lung parenchyma. Scale bar: 100 μm.

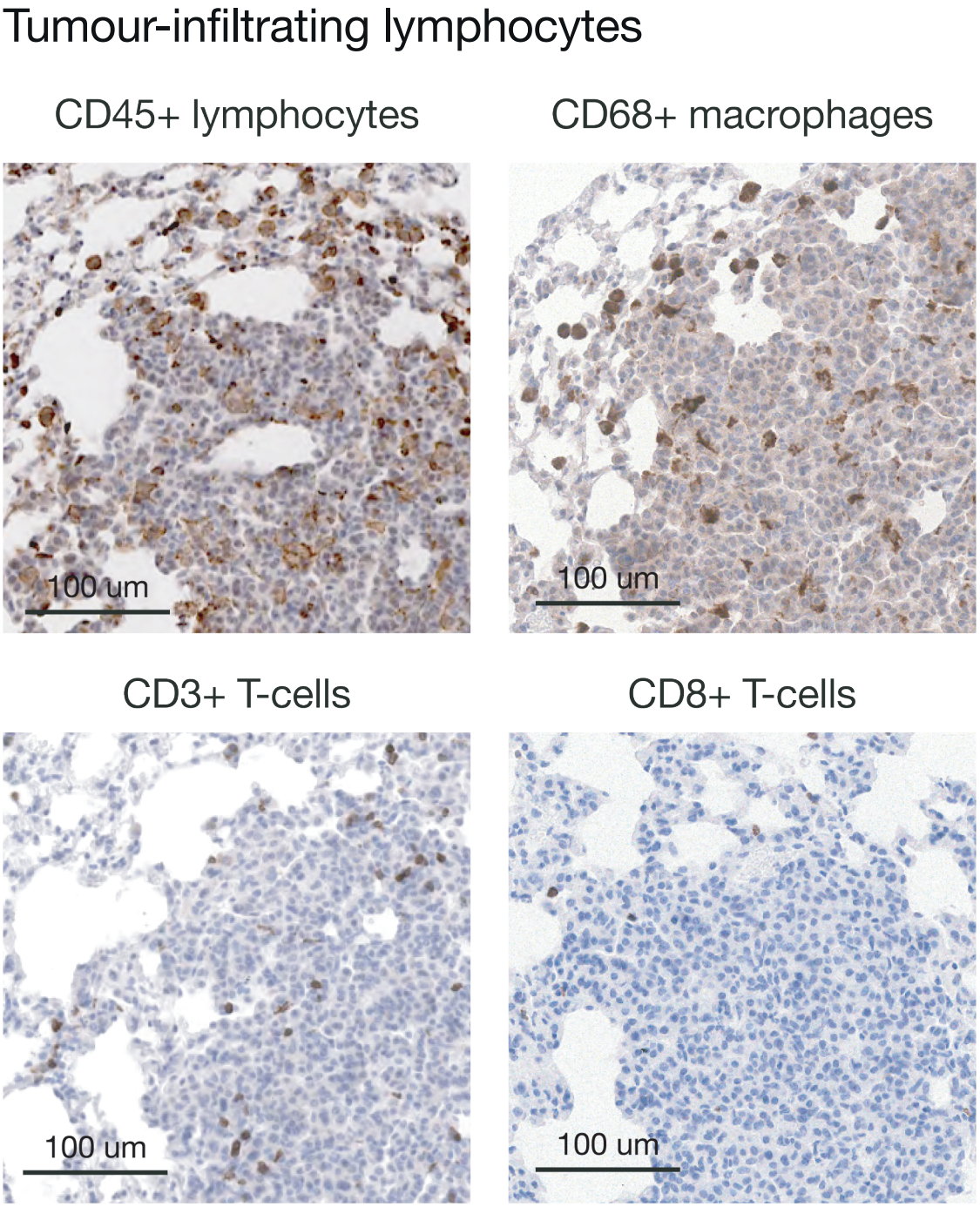


Figure 3.5. Established urethane-induced lung tumours contain infiltrating macrophages and CD3⁺ T-cells. Representative IHC images of CD45⁺ lymphocytes, CD68⁺ macrophages, CD3⁺ T-cells and CD8⁺ T-cells in lung tumour. Scale bar: 100 μm.

3.2.3 | Radiation elicits differential DNA damage responses and innate immune responses in lung tumours and parenchymal tissues

In order to compare the early responses of the tumours and normal tissues to radiation, DNA damage response (DDR) and immune events were assessed after 15 Gy thorax RT of mice with established lung tumours (18 weeks post 5% urethane i.p.) (**Figure 3.6a**).

IHC analysis for markers of DDR (γ-H2AX and 53BP1) revealed differential kinetics to RT in lung tumours versus normal cells following RT. A greater increase in γ-H2AX and 53BP1 foci occurred in lung tumour cells compared to parenchymal cells 2 hours after RT (**Figure 3.6b**). Quantification of γ-H2AX and 53BP1 foci positive nuclei in tumour and parenchymal tissues 2 hours to 7 days after RT further revealed that the differential responses are not limited to the acute responses (hours after insult) following RT, but that the tumour and parenchymal tissues can differ in their DDR up to 7 days after RT (**Appendix 10**). Specifically, γ-H2AX and 53BP1 foci levels in tumours rapidly returned to baseline levels 24 hours and 7 days after RT, whereas, the parenchyma demonstrated a more gradual decline in DDR responses 24 hours to 7 days after RT (53BP1 2 hours versus 7 days, ns) (**Appendix 10**).

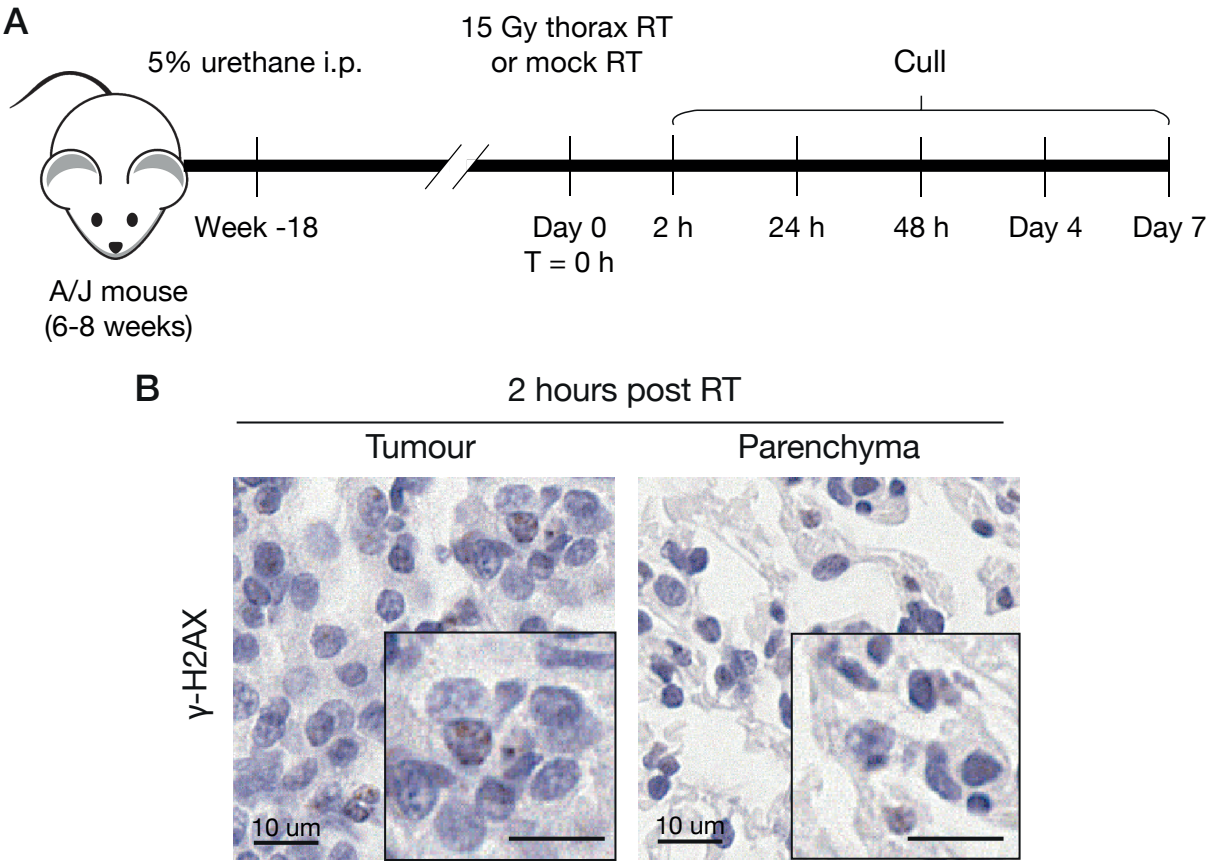


Figure 3.6. Increase in DNA-damage response 2 hours after 15 Gy thorax irradiation. (A) Schematic representation of irradiation experiment on lung tumour-bearing mice. Mice were treated with one dose of urethane (5%, i.p.) and treated with a dose of 13 Gy thoracic RT 18 weeks after urethane treatment. Mice were culled 2 hours, 24 hours, 4 days and 7 days post-RT for the assessment of cellular and molecular events in the lung. n = 4 per group. **(B)** Representative IHC images of lung tumour and parenchymal cells with γ-H2AX foci 2 hours after 15 Gy thorax RT. Scale bars: 10 μm.

3.2.4 | Radiation induces an acute innate immune response in the lung tumour, while potentially initiating a chronic inflammatory response in the parenchyma

Changes in macrophage responses ($CD68^+$ and $CD163^+$ macrophages) after RT were studied in tumour and parenchymal tissues with IHC. Results indicated that while $CD68^+$ macrophages increased 24 hours after RT ($p < 0.0001$) and decreased back to baseline level 7 days after RT (ns) in tumour tissue, the macrophages displayed steady increase across 7 days in the parenchyma ($p < 0.01$) (**Figure 3.7a**). Moreover, $CD163^+$ M2 macrophages were found to follow a generally similar trend to the $CD68^+$ macrophages, demonstrating a transient increase in the tumours and a gradual increase in the parenchyma (mock RT versus 7 days, $p < 0.01$) (**Figure 3.7b**).

These results are noteworthy, as they suggest that an acute immune response is initiated in the tumour tissues while a chronic innate immune response may be occurring in the parenchyma. Although a possibility, we are not yet certain if the differential DDR responses between tissue types observed in **3.2.3**. play a role in the innate immune responses observed here.

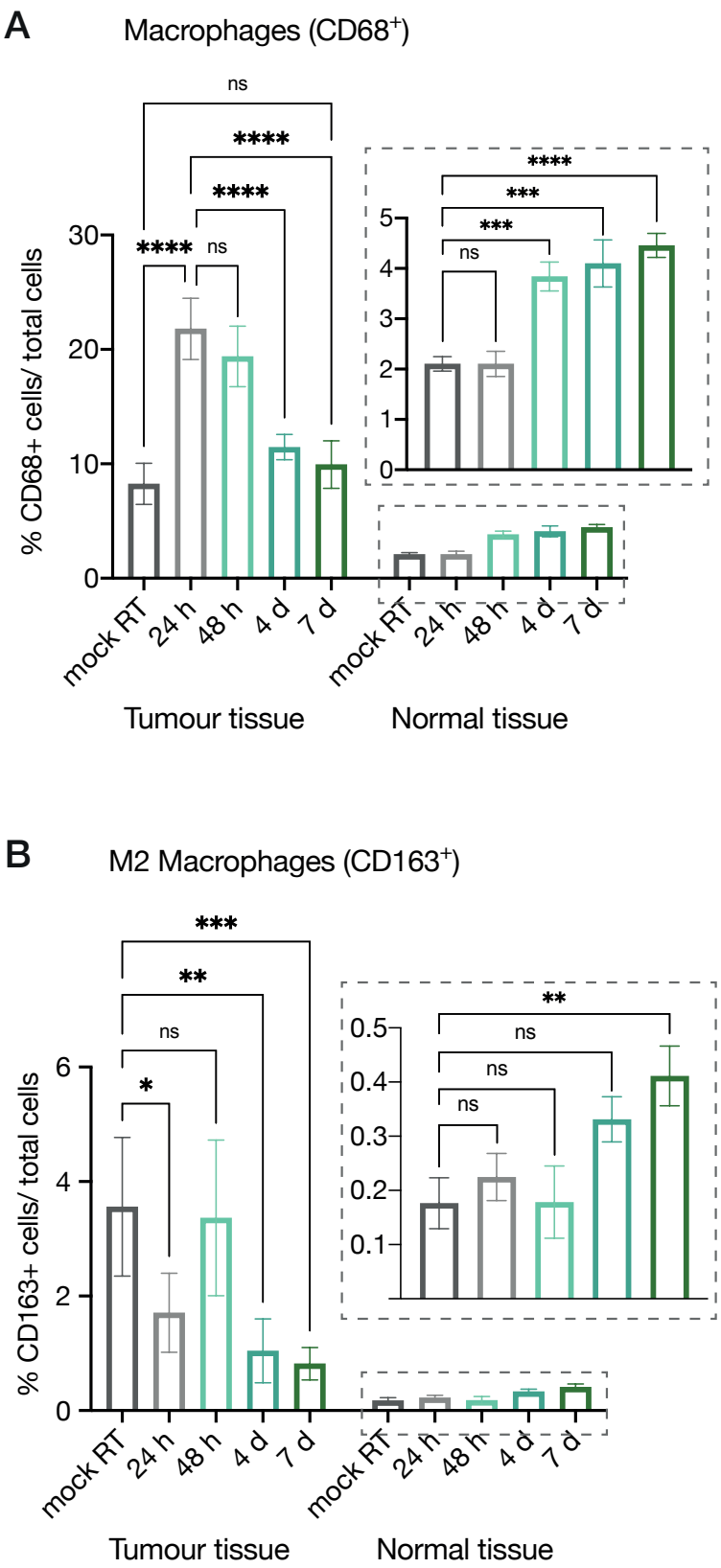


Figure 3.7. M2 macrophages increase in lung normal tissue after RT. (A) Quantification of macrophages ($CD68^+$), **(B)** M2 macrophages ($CD163^+$) on IHC images of lungs collected 0 hours to 7 days after RT. 3-5 tumour regions and 9 normal tissue regions were analysed per group. Results are mean ± SEM, analysed by one-way ANOVA tests for each tissue type. $^{ns}p > 0.05$, $^{*}p < 0.05$, $^{**}p < 0.01$, $^{***}p < 0.001$, $^{****}p < 0.0001$.

3.2.5 | Radiation induces an initial reduction in T-cells in the tumours and a latent T-cell exclusion effect

T-cell responses after RT were evaluated in parallel to the innate immune responses evaluated in **3.2.4**. An assessment of the T-cell population ($CD3^+$) with IHC revealed that the tumour and normal tissues both demonstrated an initial decrease in T-cells 24 hours after RT ($p < 0.05$ and $p < 0.001$ respectively), and recovery back to non-irradiated levels 7 days after RT (**Figure 3.8a**). Interestingly, an assessment of the spatial distribution of the cells revealed that $CD3^+$ T-cells tended to cluster around the tumour-parenchyma border 7 days after irradiation, while before treatment, the $CD3^+$ T-cells were distributed more evenly throughout the tumour tissue (**Figure 3.8b**).

To further investigate this phenotype, the lungs were studied for $CD4^+$ helper T-cells, $CD8^+$ cytotoxic T-cells and with IHC and analysis was performed for cell infiltration events with digital pathology software [5]. Results confirmed that the distributions of both $CD4^+$ and $CD8^+$ T-cell populations are relatively even between -200 μm and +200 μm of the tumour border of the untreated mice. However, 7 days after RT, higher densities of both T-cell populations ($CD4^+$ T-cells and $CD8^+$ T-cells) were observed closer to the tumour border, being most frequent between -40 μm and +40 μm of the tumour border at 0 μm (**Figure 3.9**).

[5] HALO image analysis software was used, and the methods for the image analysis are detailed in **Chapter 2**, **section 2.2.7**

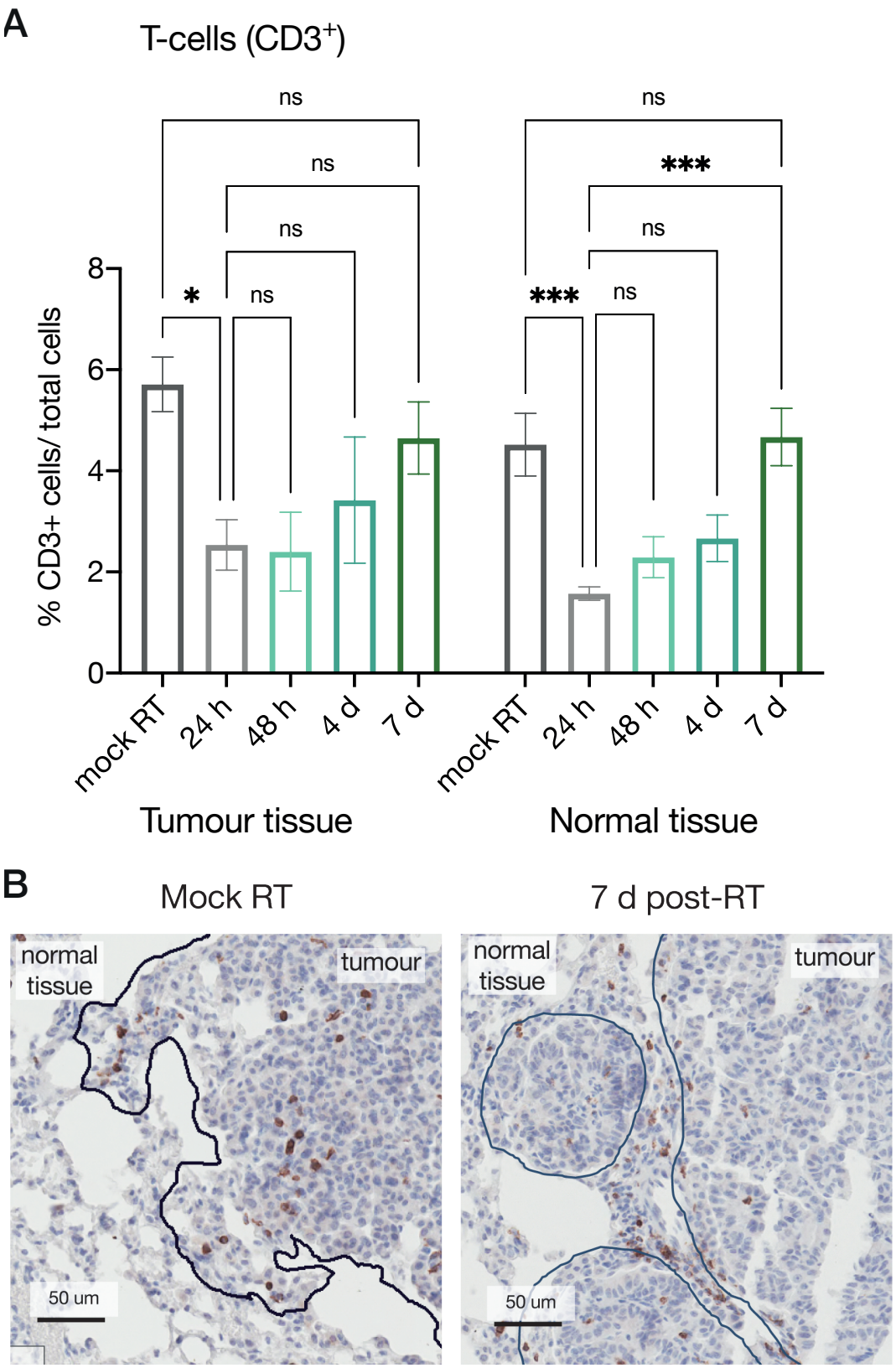


Figure 3.8. T-cells depleted 24 hours after RT and recovered back to baseline 7 days after RT. (A) Quantification of T-cells (CD3+) in IHC images of lungs collected 0 hours to 7 days after RT. 5-10 ROIs were selected for analysis. Results are mean ± SEM, analysed by a two-way ANOVA test. $^{ns}p > 0.05$, $^{*}p < 0.05$, $^{**}p < 0.01$, $^{***}p < 0.001$, $^{****}p < 0.0001$. **(B)** Representative IHC images of tumour-parenchyma border in lungs post mock or 13 Gy RT stained for CD3. Scale bar: 50 μm.

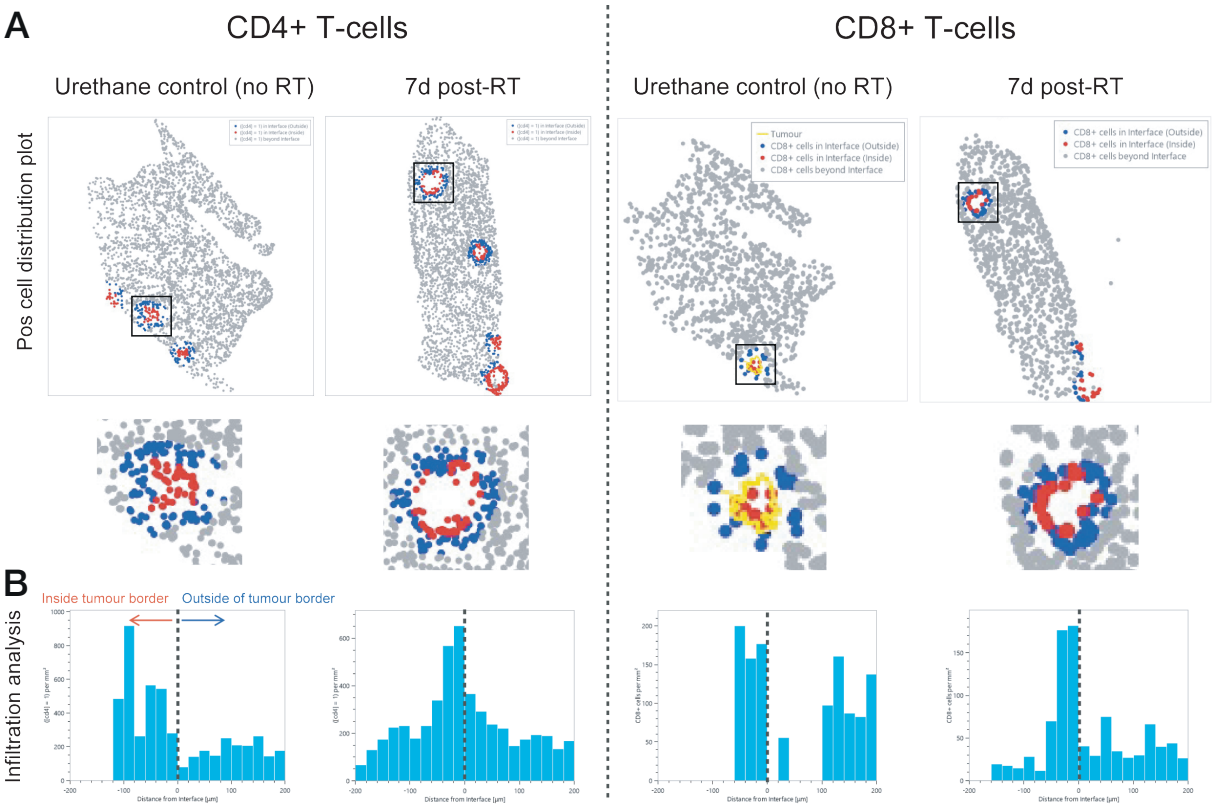


Figure 3.9. CD8 and CD4 T-cell exclusion at the tumour-parenchyma border 7 days post-RT. (A) Dot plot of positive events on their x, y coordinates from an analysis of CD4 or CD8-stained IHC images of RT/ mock RT-treated lung sections. The interface was drawn along the tumour borders. Red dots indicate positive events identified ≤ 200 µm inside the interface, blue dots indicate positive events identified ≤ 200 µm outside the interface, and grey dots indicate positive events identified outside the interface. **(B)** The density of positive cells around the interface is plotted against the distance from the interface. The dotted line indicates the interface (0 µm).

3.2.6 | Radiation treatment has a modest anti-tumour effect on established tumours and induces lung fibrosis in the A/J model

To investigate the anti-tumour and normal tissue effects of thorax RT in the mouse model, lung tumours and tissue toxicities (fibrosis and organ weight) were evaluated after 13 Gy thorax RT was given 8 or18 weeks after urethane treatment of A/J mice (**Figure 3.10a**).

The evaluation of anti-tumour efficacy of radiation on the lung tumours in the A/J model demonstrated fewer surface tumours when RT was given 8 weeks after urethane ($p = 0.153$) whist there was no difference in tumour numbers when given RT was given 18 weeks after urethane (ns) (**Figure 3.10b**). The lack of anti-tumour efficacy seen at 18 weeks could indicate that the tumours may have already developed a resistance to genotoxic insults like RT (through tumour-cell intrinsic resistant mechanisms or the development of a microenvironment that encourages resistance) or that the radiation dose/ fractionation schedules may not have been sufficient.

Lung fibrosis and organ weights were assessed to study radiation-induced lung toxicities. Fibrosis was assessed by Masson's Trichrome staining of lungs 24 weeks after 13 Gy thoracic RT. An abundance of collagen and disrupted alveolar structures/ fibrotic masses were observed throughout the irradiated lung tissue (**Figure 3.11a**). Additionally, lipid-laden, foamy macrophages were visible in the irradiated lung (**Figure 3.11a**). Quantification of collagen in the fibrotic lungs revealed a significant increase in fibrosis 24 weeks after RT ($p < 0.05$) (**Figure 3.11b**). Organ weights were measured as an additional indicator of treatment-induced toxic effects. This demonstrated an increase in weight with RT compared to the mock RT controls ($p < 0.001$) (**Figure 3.11c**).

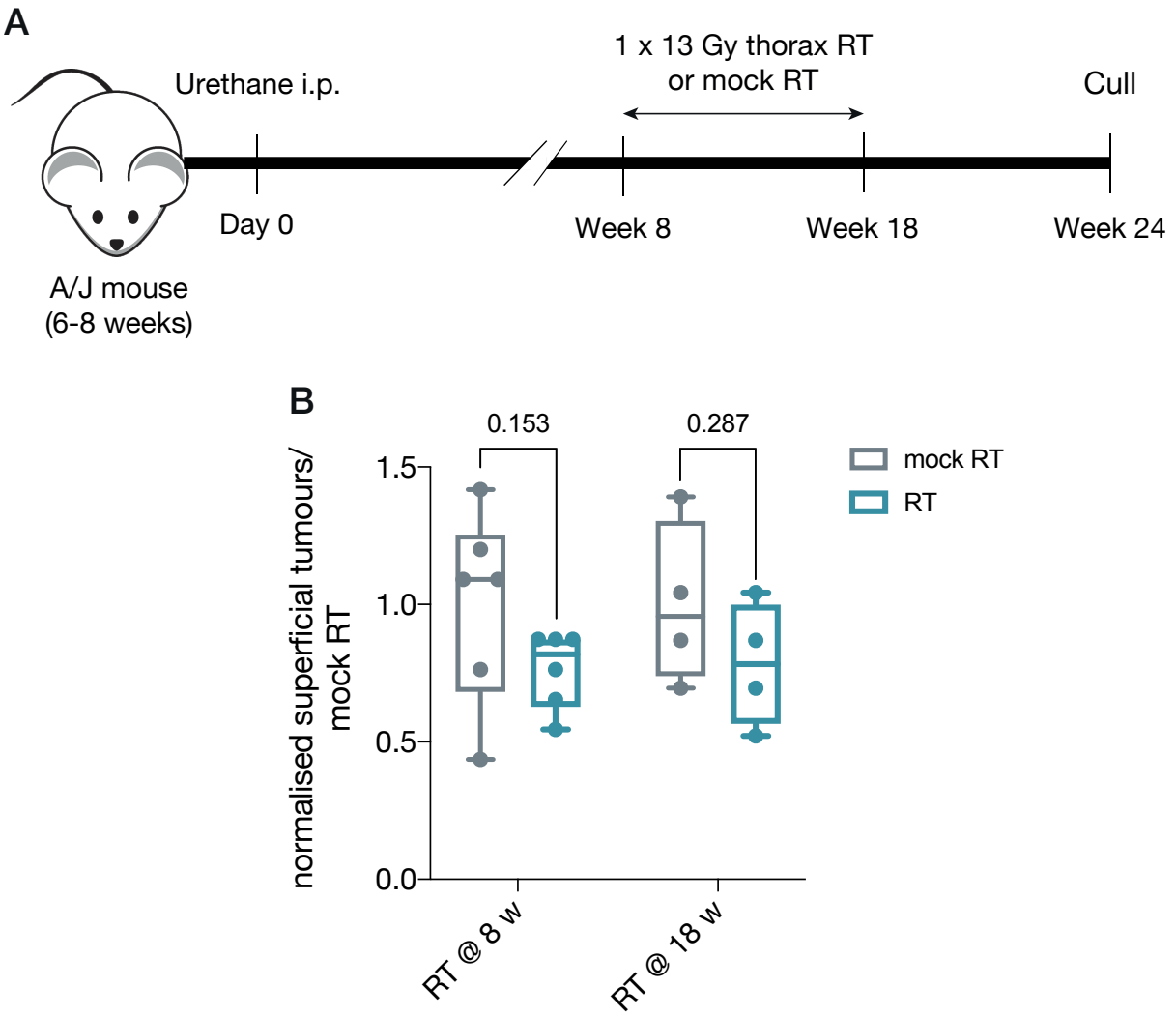


Figure 3.10. RT reduces lung tumour counts and tumour burden. (A) Schematic representation of irradiation experiment on lung tumour-bearing mice. Mice were treated with one dose of urethane (5%, i.p.) and treated with a dose of 13 Gy thoracic RT 8 weeks after urethane treatment. Mice were culled 24 weeks after RT for the assessment of lung tumours and normal tissue toxicities. **(B)** Normalised superficial tumour counts to the mean of mock RT control. Results are mean ± SEM, analysed by an unpaired Student's t-test. $^{ns}p > 0.05$, $*p < 0.05$, $**p < 0.01$, $***p < 0.001$, $****p < 0.0001$.

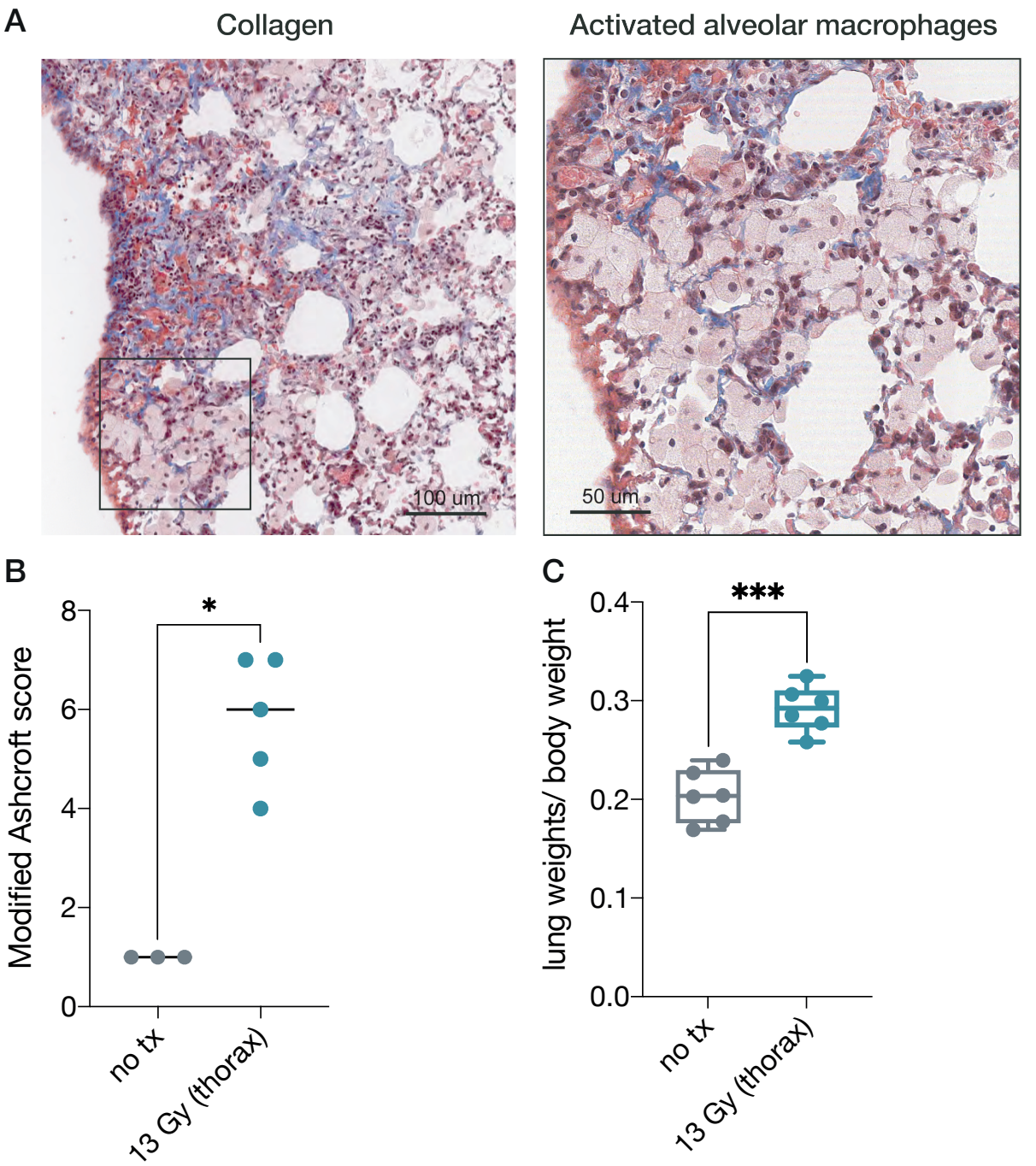


Figure 3.11. RT induces fibrosis in the lung 6 months after treatment. (A) Representative images of lung sections from mock RT and 13 Gy RT-treated mice stained with Masson's Trichrome. Left: an image of collagen structures. Scale bar: 100 μm. Right: an image of activated alveolar macrophages. Scale bar: 50 μm. **(B)** Quantification of lung fibrosis with a modified Ashcroft score. Results are mean, analysed by a Mann-Whitney test. **(C)** Lung weights at the study endpoint were normalised by whole-body weight. Results are mean ± SEM, analysed by an unpaired Student's t-test. $^{ns}p > 0.05$, *$p < 0.05$, **$p < 0.01$, ***$p < 0.001$, ****$p < 0.0001$.

3.3 | DISCUSSION

In this chapter, we characterised lung tumourigenesis and lung tissue in the carcinogen-induced A/J mouse model and confirmed its suitability as a model for the co-evaluation of anti-tumour and normal tissue effects of cancer therapies as demonstrated for RT. Additionally, distinctive radiation-induced immunological events in the lung tumour and parenchymal tissues were identified in the mouse model (described below).

Administration of urethane (one or two doses) in the A/J mouse strain resulted in the development of autochthonous lung adenomas and adenocarcinomas over the course of weeks to months. Results from this chapter confirmed the reproducibility of the model with respect to: (i) tumour development - 100% of mice injected with urethane develop lung tumours; and (ii) quantification of lung tumour development (tumour numbers and tumour burden). Moreover, the characterisation of established lung tumours in the A/J mouse model demonstrates its relevance as a model of early-stage lung cancer with tumours of moderate immunological activity. Additionally, intervention with cancer therapies including radiation (reported in this chapter) and other compounds (reported in previous studies in our laboratory; Jiang et al. (2021); Lourenco (2017); Martin (2020)) result in a reduction in lung tumour counts and size. In parallel, the development of lung fibrosis months following RT in the mouse model demonstrates that the evaluation of late normal tissue responses to cancer therapies is also possible. Lung, oesophageal and skin toxicities from RT have previously been evaluated in the A/J mouse model by investigators in our laboratory, however, the RT-induced toxic events in the heart have not yet been explored. This will be explored in

detail in **Chapter 6**, where the late RT-induced cardiotoxic events and early events following radiation will be evaluated.

Interestingly, we observed distinctive innate and adaptive immune responses following RT in the lung adenocarcinoma model. First, we observed key differences in the patterns of innate immune responses in the lung tumour and parenchyma after radiation; a transient increase in macrophages (at 24 hours) was observed in tumour tissue, whilst a gradual increase in macrophages across 7 days was observed in the lung parenchyma. A similar pattern in response was seen in M2 macrophages in tumours versus parenchyma. This suggests that while an acute innate immune response occurs in the tumour, a chronic innate immune response could be stimulated in the lung parenchyma. In parallel, we observed T-cell exclusion occurring at the tumour border days after RT. RT induced an initial reduction in T-cells (at 24 hours), followed by a recovery in the cell population back to baseline levels (pre-RT level) 4-7 days after RT in tumour and parenchyma similarly. This may suggest that: (a) T-cells repopulate the irradiated lung from circulation or that (b) T-cells that survive the RT insult proliferate locally in the lung. Given that the time taken for T-cells to return to baseline level matches the time required for T-cell response to pathogen exposure (Janeway, 2001), and that we did not observe distinct T-cell clustering, the more likely explanation may be T-cell repopulation. Additionally, we found that T-cells were accumulating at the tumour-parenchyma border (also pathologically described as the “invasive margin” (Hendry et al., 2017)). This phenomenon has been described as T-cell exclusion and has been thought to be an indication of immune privilege (Joyce & Fearon, 2015). Furthermore, studies implicate that stromal cells of the tumour microenvironment (TME), including activated cancer-associated fibroblasts (CAFs),

myeloid cells including myeloid-derived suppressor cells (MDSCs) and tumour-associated macrophages (TAMs) may mediate the exclusion of T cells from infiltrating into the tumours (Bayne et al., 2012; Feig et al., 2013; Garcia et al., 2014; Lesokhin et al., 2012; Strachan et al., 2013). Previous studies have suggested that T-cell exclusion occurs through (i) the alteration of proinflammatory chemokines in the TME including those secreted by suppressive myeloid cells (Molon et al., 2011); (ii) the expression of FasL in tumour vasculature (Motz et al., 2014); (iii) and the secretion of ECM components by activated cancer-associated fibroblasts (CAFs) (Koppensteiner et al., 2022; Paolo et al., 2012; Provenzano et al., 2006; Sahai et al., 2020; Salmon & Donnadieu, 2012). Interestingly, our results have indicated both an existing population of macrophages within the tumour at baseline (prior to any treatment), and an increase in macrophages (particularly in $CD163^+$ M2 macrophages) in the parenchyma following radiation. It is known that the activation of M2 macrophages can promote fibroblast proliferation and ECM deposition (Barbazan & Matic Vignjevic, 2019; Giraldo et al., 2019; Monteran & Erez, 2019). Although further evaluation of events such as ECM accumulation and the analyses of the location of where the “chronic” immune responses occur in relation to the tumour may be required, we could hypothesise that the chronic inflammatory response in the parenchyma may be taking part in generating a physical barrier for the T-cells to infiltrate into the tumour through the activation of fibroblasts and the accumulation of ECM. The importance of assessing lymphocyte infiltration into solid tumours for prognosis has been highlighted, with a higher “immunoscore” found to be correlated with improved patient prognosis (Curiel et al., 2004; Galon et al., 2006). The mechanisms of T-cell exclusion post-RT and whether overcoming this improves the anti-tumour response elicited by RT warrants exploration in future studies and may have important clinical implications.

CHAPTER 4. RADIATION-INDUCED IMMUNE RESPONSES IN LUNG CARCINOGENESIS AND MODIFICATION OF THE TUMOUR MICROENVIRONMENT

4.1 | INTRODUCTION

RT in TLS formation

Harnessing anti-tumour immune responses is an important area of interest in the current age of immunotherapy. In this effort, TLS has become a focal point of research and is gathering excitement because of emerging evidence demonstrating correlations with positive prognosis for cancer (Dieu-Nosjean et al., 2016; Sautès-Fridman et al., 2016) and response to immunotherapies (Cabrita et al., 2020; Beth A. Helmink et al., 2020; Petitprez et al., 2020). It is thought that TLSs have potential anti-cancer benefits as they may act as a local source for immune cells for a more rapid, efficient and controlled anti-cancer immune response (Schumacher & Thommen, 2022). However, despite the potential importance of TLSs in anti-cancer responses and therapies, little is understood about the formation of these structures (Schumacher & Thommen, 2022), and few studies have demonstrated *de novo* TLS organogenesis. Studies demonstrating TLS induction thus far, have been clinical studies of cancer vaccine treatments in HPV 16–positive cervical cancer (Maldonado et al., 2014) and pancreatic adenocarcinoma (Lutz et al., 2014).

Additionally, the role of radiation in the formation or modulation of TLSs is poorly characterised. A study by Boivin et al. (2018) demonstrates an acute and transient depletion of existing TLSs in a *Kras* $^{Lox\text{-}STOP\text{-}LOX\text{-}G12D/WT}$*; p53* $^{Flox/Flox}$ (KP) lung adenocarcinoma mouse model following RT, however, does not indicate TLS organogenesis or correlate TLS presence with anti-tumour effects (Boivin et al., 2018). As RT is a cornerstone of lung adenocarcinoma treatment, investigating interactions between RT and TLS composition is clinically relevant and requires further research.

RT in carcinogenesis

It has been thought that radiation of normal tissue increases the risk of cancer formations as seen in numerous epidemiological studies of human populations exposed to radiation from medical, occupational and accidental sources; historical cases which include increased cases of cancers observed from atomic bomb survivors in Hiroshima and Nagasaki (Ozasa et al., 2012), and the fallout from Chernobyl nuclear reactor (Williams, 2008). These studies have shown radiation to be a 'universal carcinogen', in that it can induce cancers in most tissue types, in most species and across all ages (Little, 2000). This is in contrast to chemical carcinogens that tend to be tissue-specific in their actions, and the universal nature of the carcinogenic action of radiation is largely thought to be due to its physical ability to penetrate cells and deposit energy in a random fashion (Little, 2000). For cancer treatments, radiation is used for its cell-killing properties on established solid tumours or cancer cells in circulation that have undergone malignant transformation. However, few studies have reported the impact of radiation on cells that are on the cusp of normal cell to neoplastic cell transformation.

Interestingly, preliminary experiments carried out in our laboratory indicated that radiation treatment during tumour initiation may be capable of preventing future tumour formation in the carcinogen-induced lung adenocarcinoma mouse model. This was a surprising finding as it was initially hypothesised that radiation would encourage lung tumour growth given its carcinogenic properties in non-cancerous tissues. We found this serendipitous finding worthy of further investigation as it may provide opportunities to gain insight into important biological mechanisms of neoplastic cell transformation. Furthermore, provided the recent findings by Swanton and colleagues that air pollution

increases lung cancer risk, the biological findings from a study on preneoplastic cells may have importance in considerations for cancer preventative interventions (Swanton et al., 2022).

Additionally, findings from **Chapter 3** indicated that RT induces an immunological response in the A/J model. Therefore, we investigated the impacts of RT on the preneoplastic lesions with an immunological focus.

The aims for this chapter are as follows: (1) investigate the ability of RT to limit tumour growth when administered following injection of urethane; (2) investigate the local and systemic (if any) alterations induced by RT intervention during tumourigenesis; and (3) identify potential pathways that can be targeted for the intervention of tumorigenesis.

4.2 | RESULTS

4.2.1 | Radiation treatment of pre-neoplastic lungs limits tumour development in carcinogen-induced A/J mice

To first confirm the preliminary findings of RT impact on tumourigenesis in our laboratory, an *in vivo* experiment was carried out, whereby mice were treated with RT during tumour initiation. A/J mice were treated with urethane (5%, i.p.) to induce the development of lung tumours. On the third day of urethane induction, the mice received 13 Gy whole thorax-radiation treatment (RT) and were euthanised after five months for the assessment of lung tumours (**Figure 4.1a**). RT induced a 61.9% reduction in surface lung tumour numbers compared to the mock RT control group ($p < 0.01$) (**Figure 4.1b**). Microscopic analysis of lung tumours confirmed the reduction in tumour numbers with RT ($p < 0.05$) compared to the mock RT group (**Figure 4.1c**). Additionally, a reduction in lung tumour size was observed with RT compared to mock RT upon quantification of tumour area per histology section; this demonstrated a 69.5% reduction in tumour burden ($p = 0.0732$) in the urethane + RT group compared to the mock-irradiated controls (**Figure 4.1d**).

These results confirm initial results that intervention of a carcinogen-induced tumour initiation with radiation limited the future development of tumours, both in total tumour numbers and tumour burden.

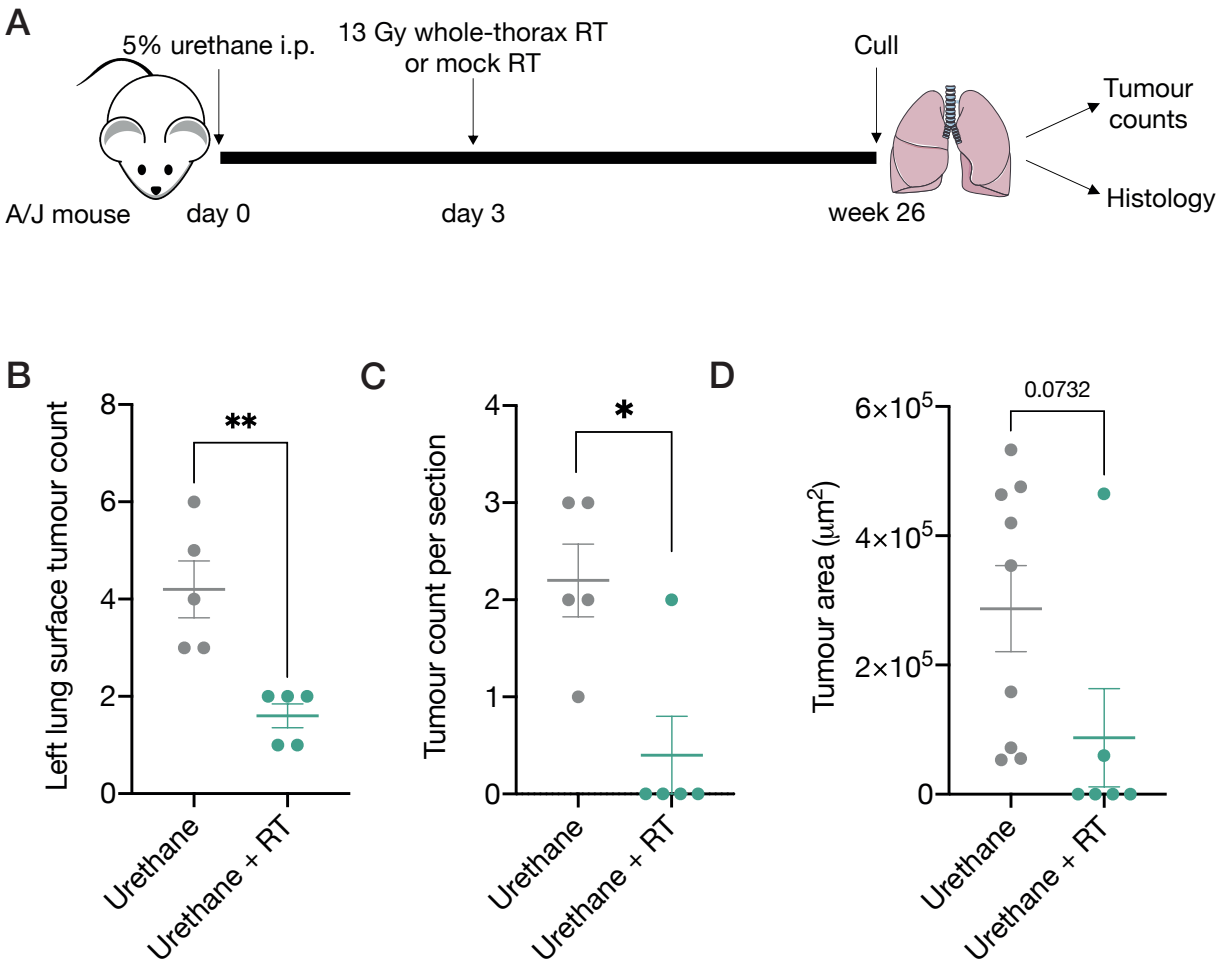


Figure 4.1. RT-intervention during lung tumourigenesis in A/J mice significantly reduces tumour counts and tumour burden. (A) Schematic representation of *in vivo* experiment design. A/J mice were treated with urethane and given mock RT (n = 5) or 13 Gy RT (n = 5) to the thorax 3 days after urethane treatment. Mice were euthanised 26 weeks after the start of the experiment for evaluation of lung tumours. **(B)** The number of tumours counted on the surface of the lung of urethane- and urethane + RT-treated mice. **(C)** The number of tumours identified per lung section stained with H&E of urethane-treated and urethane + RT treated mice. **(D)** Area of all tumours per lung section from urethane or urethane + RT-treated mice. Sections in which no tumours were identified were recorded as 0 μm^2. Results are mean ± SEM, analysed by an unpaired student's t-test. $^{ns}p > 0.05$, $^{*}p < 0.05$, $^{**}p < 0.01$, $^{***}p < 0.001$, $^{****}p < 0.0001$.

4.2.2 | RT of pre-neoplastic lungs result in long-term modifications in the lung immune environment but not systemic immunity

In parallel to the observations of reduced tumour growth made in **4.2.1.**, tight aggregates of cells (distinguishable from tumour cell phenotypes) were observed in the lungs of urethane + RT mice (**Figure 4.2a**). Given a histological appearance consistent with lymphocytes, $CD45^+$ staining was performed and confirmed that the cell aggregates observed consist of $CD45^+$ leukocytes (**Figure 4.2b**). This suggested that RT intervention following chemical carcinogenesis resulted in a long-term change in the lung immune environment. A higher number of $CD45^+$ cells were identified in urethane + RT mice compared to the urethane-treated control ($p < 0.01$) (**Figure 4.2c**).

Additionally, 'leukocyte aggregates'[6] were quantified per lung section per treatment group. Indeed, higher numbers of $CD45^+$ cell aggregates were present in the lungs of urethane + RT treated mice compared to the urethane control ($p < 0.0001$) and the RT control ($p < 0.01$). (**Figure 4.2d**). These data suggest that, in our model, radiotherapy following carcinogenic insult promoted a long-term change in the environment of the preneoplastic lesion and resulted in the formation of organised lymphoid structures.

[6] 'Leukocyte aggregates' were identified as tight aggregates of 50 or more CD45+ cells within a 1×10^4 μm^2 area.

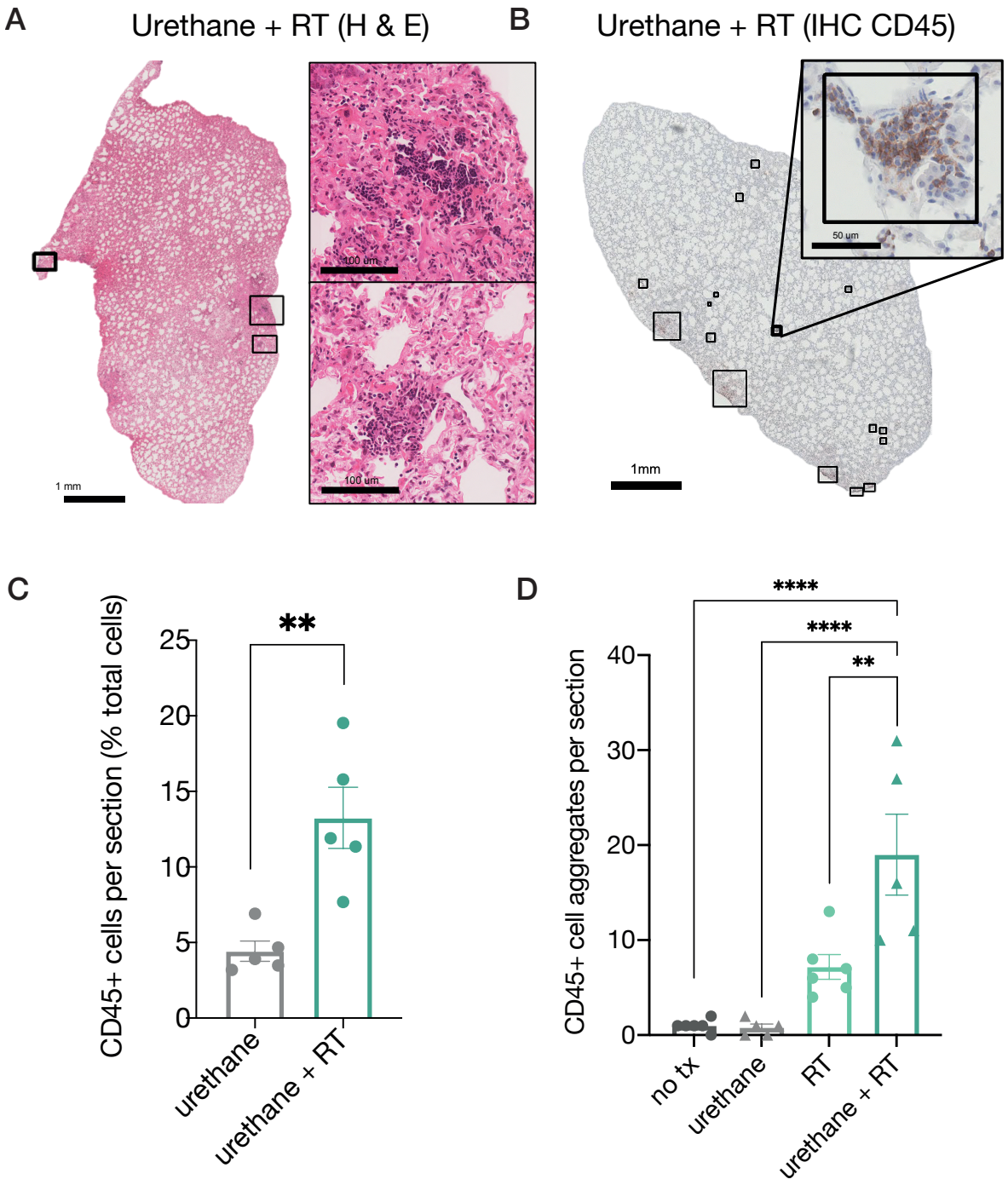


Figure 4.2. RT intervention during tumour initiation creates a long-term inflammatory state in the lung. (A) Representative H & E image of a lung section from a mouse treated with urethane + RT. Enlarged images show cell aggregates. **(B)** Representative IHC image of a lung section stained for CD45 from a urethane + RT treated lung 6 months after treatments. **(C)** Quantification of individual CD45⁺ cells per section per mouse. Analysed by student's t-test. **(D)** Quantification of CD45⁺ Lymphocyte aggregates per lung section per mouse. Results are mean ± SEM, analysed by one-way ANOVA $^{ns}p > 0.05$, *$p < 0.05$, **$p < 0.01$, ***$p < 0.001$, ****$p < 0.0001$.

4.2.3 | An increase in cell division pathways and a delayed IFN response are observed in the preneoplastic lung

To investigate the biological mechanisms occurring in the carcinogen-exposed preneoplastic lung, lungs were collected from mice treated with urethane 24 hours, 48 hours, 3 days and 10 days after a dose of urethane (5%, i.p.) for transcriptomic and protein analyses. RNA-sequencing of lungs isolated from mice 3 days and 10 days after urethane treatment revealed significant upregulation in DNA synthesis and cell cycle regulation pathways (E2F targets, mitotic spindle and G2M checkpoint), DNA repair and apoptosis (p53 pathway, apoptosis, and DNA repair) and immune regulation (IFN-α, IFN-γ, inflammatory response) compared to the urethane-naïve mice (**Figure 4.3**). Specifically, genes of E2F targets (required for cell cycle progression and proliferation), mitotic spindle (involved in chromosomal segregation), p53 pathway (important for the regulation of cell cycle arrest, apoptosis, and DNA repair processes), apoptosis (programmed cell death) and mTOR signalling (regulates cell growth and metabolism) are significantly upregulated in both 3 day and 10-day post-urethane conditions. However, this upregulations is more pronounced in the 10 day condition (**Figure 4.3**).

The upregulation of genes involved in pathways of cell division and cell cycle progression indicates that urethane is likely initiating cell proliferation of the lung cells. At the same time, we observe an increase in activity in pathways controlling cell death (**Figure 4.3**). This points to the possibility that the lung, in trying to cope with the genotoxic stress from urethane, could be eliminating some cells in that process. Of note, there is a marked increase in IFN-α and IFN-γ signalling (cytokines involved in type I and type II IFN pathways, respectively) 10 days after urethane treatment (**Figure**

4.3). While an acute infection and upregulation of IFN is found to be beneficial for DC activation and priming of T-cells, chronic infection with sustained IFN production has been shown to induce a suppressive phenotype (Teijaro et al., 2013; Wilson et al., 2013). The delayed upregulation in IFN responses after urethane induction points to the onset of chronic inflammation in the carcinogen-exposed lung. Interestingly, downregulation of genes involved in allograft rejection was also observed 3 days after urethane treatment (**Figure 4.3**). This potentially indicates that the preneoplastic cells in the lung are undergoing immunoediting, whereby there it actively downregulates the immune system that is involved in non-self antigen (Ingulli, 2010) as soon as 3 days after urethane injection.

We expanded on findings from transcriptomic analysis with IHC analysis of proteins involved in DNA repair mechanisms (γ-H2AX, p-p53) and STING in lung samples collected 0 hours, 24 hours and 72 hours after urethane treatment. An increase in and sustained level of γ-H2AX foci positive nuclei (0 hours versus 24 hours, $p < 0.05$) and p-p53 expression (0 hours versus 24 hours, $p < 0.001$) were seen in the lung tissue 24 hours and 72 hours after urethane administration (**Figure 4.4**). These results confirmed that urethane is initiating a heightened level of DNA damage that requires the subsequent activation of repair mechanisms. Interestingly, we also observed an increase in STING expression in the lung 72 hours after urethane treatment ($p < 0.05$) (**Figure 4.4**). More analysis is required to understand which cells (i.e. immune cells or preneoplastic lung cells) STING expression increased in or whether the expression was localised to the perinuclear region. However, literature indicates that increased STING expression in cancers is associated with immune cell

infiltration of myeloid cells including macrophages and DCs (Gan et al., 2022; Raaby Gammelgaard et al., 2020), which coincides with findings from our transcriptomic data.

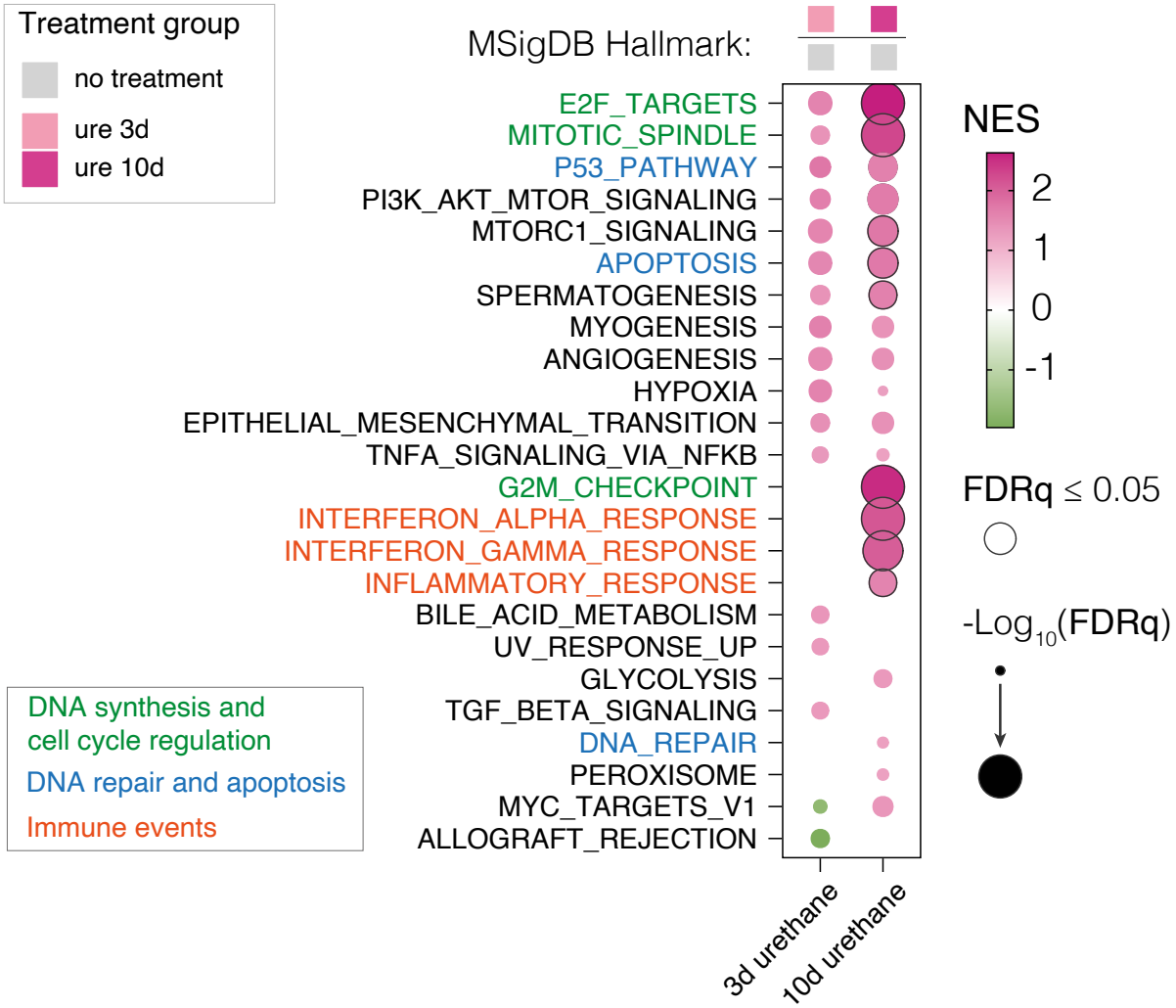


Figure 4.3. Upregulation of cell cycle regulation, DNA repair and immune response and downregulation of genes involved in allograft rejection in the preneoplastic lung. Functional enrichment analysis (based on MSigDB Hallmark annotation) of significantly upregulated and downregulated genes in lung tissues of urethane-treated mice. n = 3 per group. Only biological process terms that are significantly (BH-adj. $p \leq 0.05$) overrepresented are highlighted in the figure.

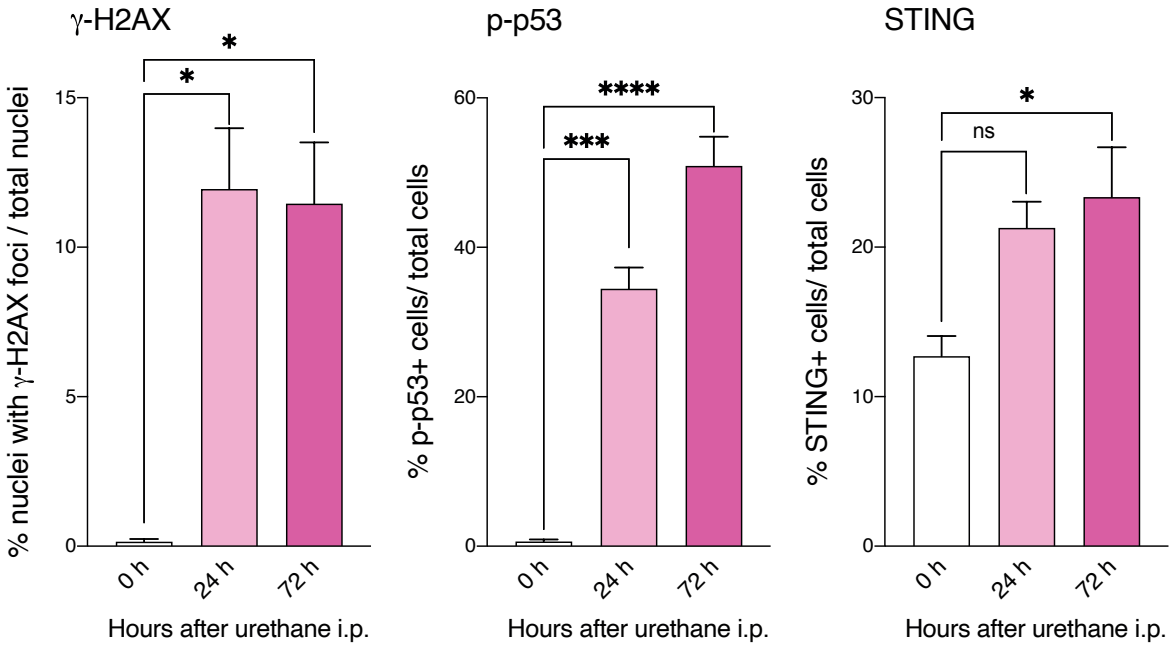


Figure 4.4. DNA damage response and STING upregulated in the preneoplastic lung. Quantification of γ-H2AX positive nuclei, and cells positive for p-p53 and STING proteins from IHC images of lungs collected 0 hours, 24 hours or 72 hours after urethane treatment. n = 3 per group; analyses on 3 ROIs were averaged for each data point. Results are mean ± SEM, analysed by a one-way ANOVA test. nsp > 0.05, *p < 0.05, **p < 0.01, ***p < 0.001, ****p < 0.0001.

4.2.4 | RT induces an increase in T-cells in tertiary lymphoid structures in the carcinogen-exposed lung

To investigate if the CD45$^+$ lymphocyte aggregates we observed in **4.2.3** resemble tertiary lymphoid structures (TLSs), we performed further IHC evaluation on lungs of urethane + RT treated mice for immune cells and chemokines that are key components of TLSs including T-cells (CD3$^+$), B-cells (CD19$^+$), mature B-cells (B220$^+$), antigen-presenting cells (MHCII) and CXCL13 chemokines[7].

Results revealed that the lymphoid aggregates contained all the above cells and chemokines important for TLS, except PNAd$^+$ HEVs (**Figure 4.5a**). As TLSs can have varying levels of maturity, the lack of HEVs may indicate that the TLSs that we observe in the urethane + RT mouse lungs are not fully matured. Further evaluation of the location of the immune cell aggregates in proximity to other structures in the lung revealed that aggregates occurred more frequently in close proximity to blood vessels within the lung (**Figure 4.5a**). We were unable to assess the proximity of the structures to tumours, however, as the urethane + RT treated lungs had reduced tumour numbers and tumours were rarely identified in histology sections.

Preliminary evaluation of the composition of the TLSs with chromogenic IHC reveals that (i) generally B-cells (CD19$^+$) occurred around the central region of the structures whilst T-cells (CD3$^+$) occupied the outer region of the structures and (ii) that the densities of B-cells and T-cells can vary between different TLSs (**Figure 4.6**). The variation in T-cell and B-cell densities could indicate the varying levels of TLS maturity.

[7] CXCL13: a chemokine thought to be important for the development of TLSs. (Ukita et al., 2022).

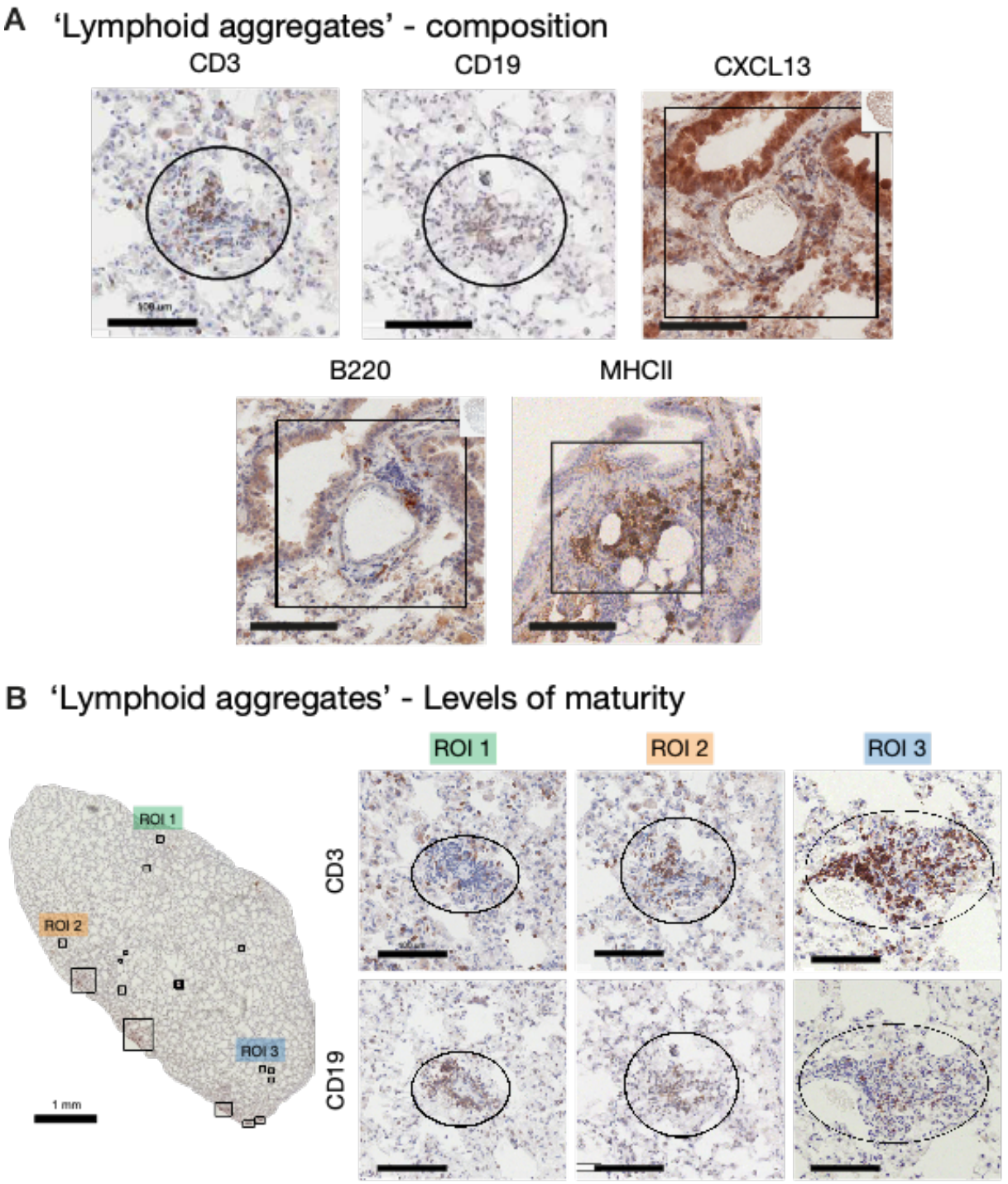


Figure 4.5. Tertiary lymphoid structures contain T-cells, B-cells, APCs and CXCL13 chemokine. (A) Representative images of immune cell aggregates stained with CD3, CD19, CXCL13, B220 and MHCII. Scale bars: 100 μm. **(B)** Representative image of a lung section treated with urethane + RT (left). Scale bar: 1mm. Three representative ROIs from CD3 and CD19-stained lung sections (right). Scale bars: 100 μm.

Following this finding, an in-depth analysis of the immune cell populations that make up the TLSs (and the lung parenchyma) was carried out with multiplex immunofluorescence (IF) to evaluate how RT impacted the immune cell compositions in the TLSs and parenchyma. Cytotoxic T-cell ($CD8^+$), helper T-cell ($CD4^+$), regulatory T-cells ($CD4^+$ $FoxP3^+$), B-cell ($CD19^+$) and dendritic cell ($CD103^+$) populations were assessed in this IF panel. Data revealed a significant increase in B-cells ($p < 0.05$) and DCs ($p < 0.05$) in the lung parenchyma in irradiated mice with the carcinogen pre-treatment compared to the mock irradiated mice (**Figure 4.6**). Interestingly, the TLSs on the other hand, demonstrated increases in helper T-cells ($p < 0.05$) and T_{regs} ($p < 0.01$) and trending increases in cytotoxic T-cells ($p = 0.179$) and B-cells ($p = 0.205$) (**Figure 4.6**). These results suggest that the long-term changes brought by radiation in the lung parenchyma and TLSs differ in nature.

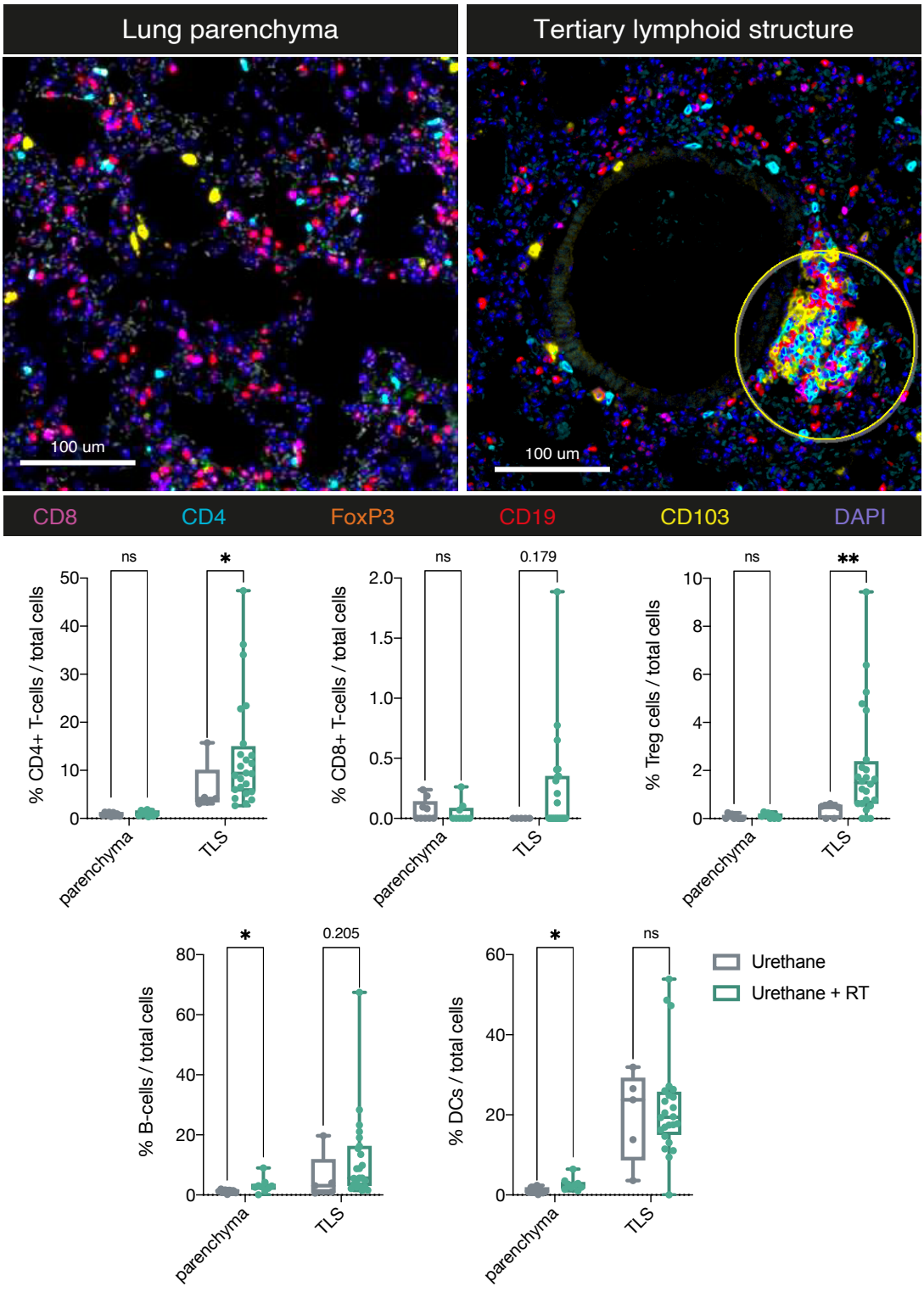


Figure 4.6. RT induces an increase in B-cells in the lung parenchyma. Top: Representative images from multiplex IF staining of lungs collected from mock RT or RT treated mice pre-treated with urethane for CD4, CD8, FoxP3, CD19 and CD103 markers; lung parenchyma (left) and TLS (right). Scale bar: 100 μm. Bottom: Quantification of CD19+ B-cells, CD4+ T-cells, CD8+ T-cells, and FoxP3+ T-cells in lung parenchyma (n = 9; 3 mice per group and 3 ROIs per mouse) and TLS (n = number of TLSs identified per group). Results are mean ± SEM, analysed by an unpaired student's t-test with Welch's correction. $^{ns}p > 0.05$, *$p < 0.05$, **$p < 0.01$, ***$p < 0.001$, ****$p < 0.0001$.

4.2.5 | RT downregulates cell division and induces an acute inflammatory response in the preneoplastic lung

To investigate the early events that occur after RT of the carcinogen-treated lung, A/J mice were treated with urethane (5%, i.p.) on day 0, and mock or thoracic RT (1 dose of 13 Gy) on day 3. Mice were euthanised at 6 hours, 24 hours and 7 days after mock RT or RT during which time which lungs were collected for subsequent RNA-sequencing or flow cytometry analyses (**Figure 4.7**).

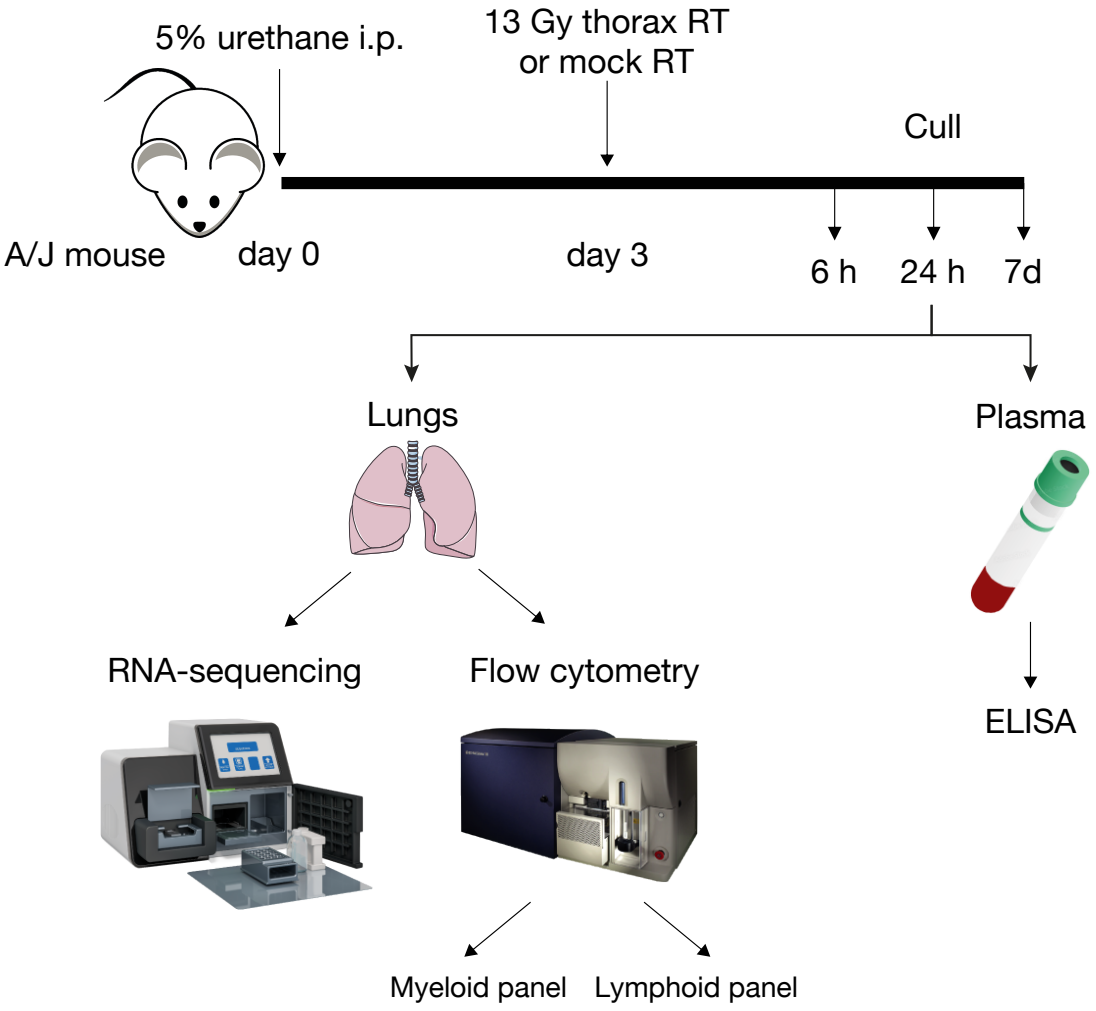


Figure 4.7. Studying the early events following RT of pre-neoplastic lungs. Schematic representation of in vivo experiment design. A/J mice were treated with urethane and given mock RT or 13 Gy thorax RT 3 days after urethane treatment. Mice were euthanised 6 hours, 24 hours and 7 days after mock or thorax RT (n = 4 per time point per treatment group) for molecular and cellular analyses of the lungs including RNA-sequencing, flow cytometry and ELISA assays.

Previously (in section **4.2.1**), we observed that the lungs of urethane-treated mice had upregulated cell division pathways and downregulated immune pathways involved in allograft rejection 3 days post-treatment. Interestingly, transcriptomic data after RT revealed that the lungs of mice pre-treated with urethane (indicated in purple squares in **Figure 4.8**) observed a distinctive downregulation of pathways involved in cell cycle and cell division (specifically, E2F targets, mitotic spindle, and G2M checkpoint) and transient IFN response (IFN-α and IFN-γ) 24 hours after treatment that were not observed in the urethane-naïve condition (**Figure 4.8**). The uniquely upregulated *and* uniquely downregulated pathways each potentially indicate important biological mechanisms that reflect 'vulnerable points' of the urethane-treated preneoplastic lungs.

We further dissected the RNA-sequencing data to investigate which genes were upregulated in the urethane, and downregulated in the urethane and RT setting. Data confirmed that there was a strong downregulation in an array of genes involved in nuclear division, chromosomal segregation and cell division pathways (**Figure 4.9a, b**). Among the list of genes, *Top2a* (DNA topoisomerase II alpha)[8], *Ccnb2* (cyclin B2)[9] and *Kif11* (kinesin family member 11)[10] were selected for graphical representation to illustrate the sequestering of these genes following radiation treatment which are

[8] *Top2a*: gene encodes a DNA topoisomerase, a nuclear enzyme involved in processes like chromatid separation, chromosome condensation, and the relief of torsional stress during DNA transcription and replication. (NCBI, 2022)

[9] *Ccnb2*: gene encodes for cyclin B2, a member of the cyclin family, and together with other B-type cyclins, is an essential component of the cell cycle regulatory machinery. (NCBI, 2022)

[10] *Kif11*: gene encodes a protein of the kinesin-like protein family. The protein family is involved in activities including positioning of the chromosome and centrosome separation during mitosis. (NCBI, 2022)

induced by urethane (**Figure 4.9c**); similar patterns which are observed in other genes listed in **Figure 4.9a.** *Top2a* in particular is an interesting candidate, not only for its biological role in chromosomal condensation and DNA replication but also because it provides a possible targetable candidate, as inhibitors of the enzyme (e.g. irinotecan, topotecan and etoposide) are clinically available. Further investigation with additional *in vivo* experiments of urethane and topoisomerase inhibitors could be considered in the future.

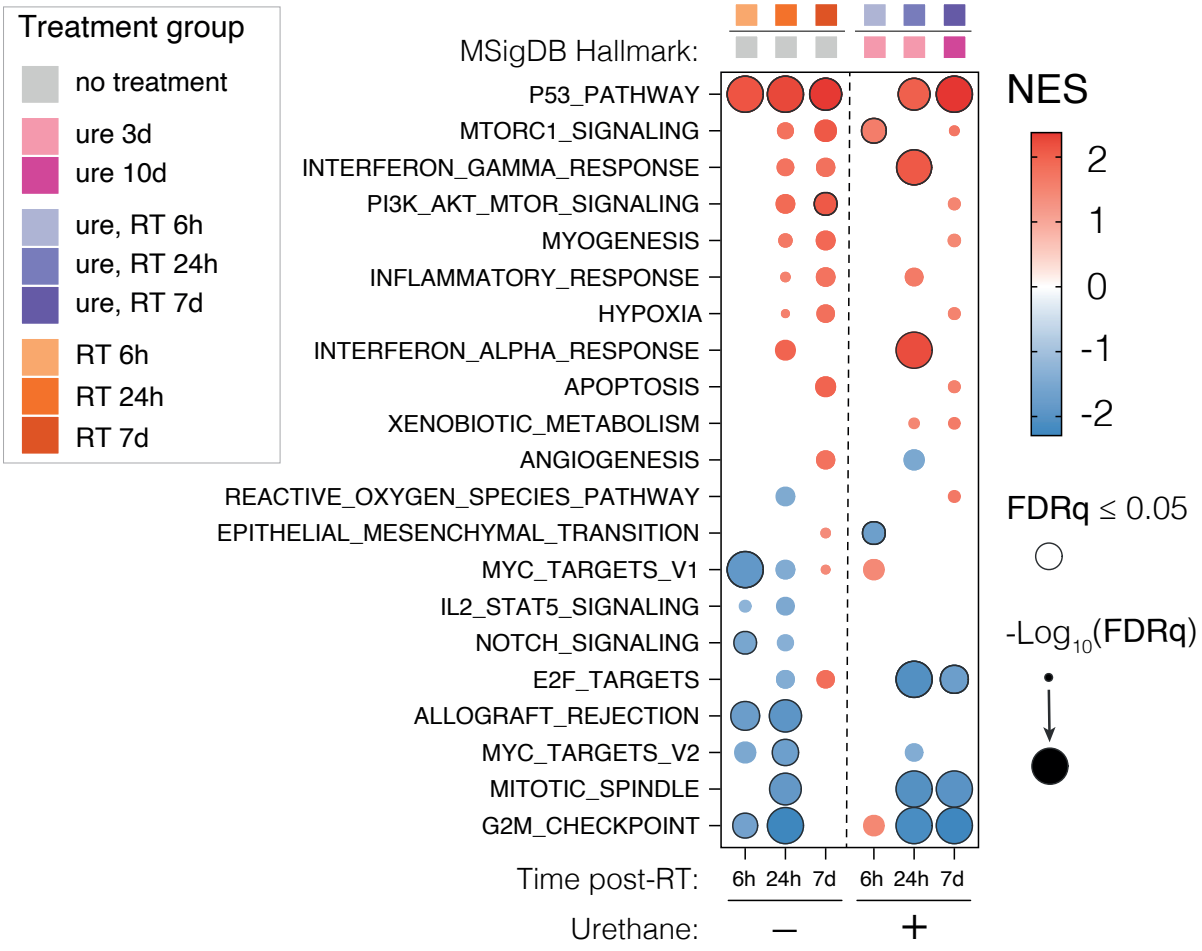
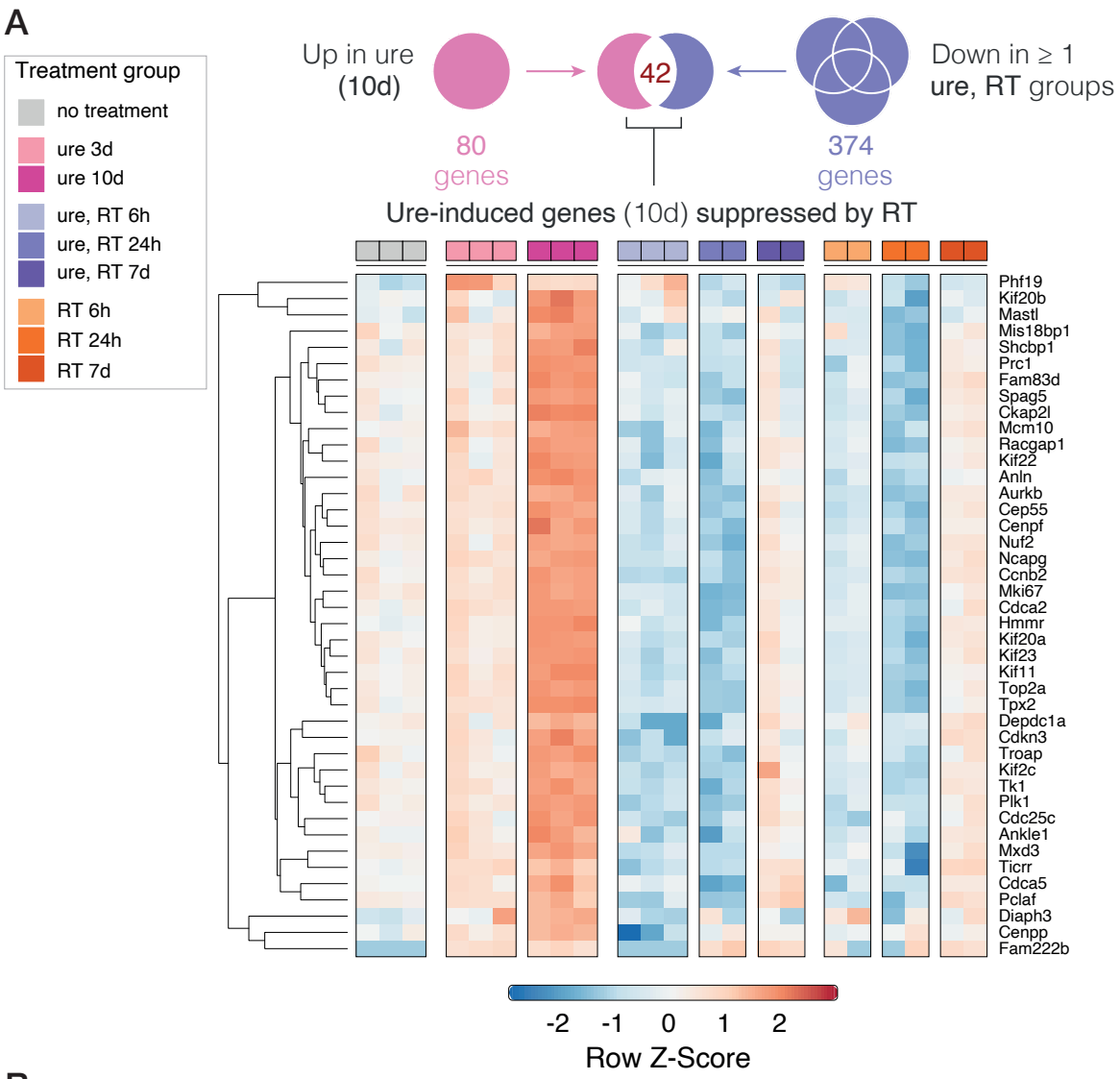
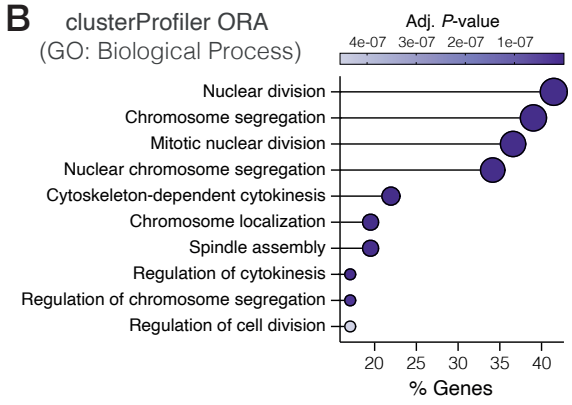


Figure 4.8. RT of the preneoplastic lung stimulates immune responses and suppresses cell division and chromosomal segregation. Functional enrichment analysis (based on MSigDB Hallmarks annotation) of significantly upregulated and downregulated genes upon RT treatment in the lung tissues of urethane pre-treated and urethane-naïve mice. Only biological process terms that are significantly (BH-adj. $p \leq 0.05$) overrepresented in at least half (3 out of 6) of group comparisons are shown in the figure.


A
Treatment group
no treatment
ure 3d
ure 10d
ure, RT 6h
ure, RT 24h
ure, RT 7d
RT 6h
RT 24h
RT 7d
Up in ure (10d)
80 genes
42
374 genes
Down in ≥ 1 ure, RT groups
Ure-induced genes (10d) suppressed by RT
Phf19
Kif20b
Mastl
Mis18bp1
Shcbp1
Prc1
Fam83d
Spag5
Ckap2l
Mcm10
Racgap1
Kif22
Anln
Aurkb
Cep55
Cenpf
Nuf2
Ncapg
Ccnb2
Mki67
Cdca2
Hmmr
Kif20a
Kif23
Kif11
Top2a
Tpx2
Depdc1a
Cdkn3
Troap
Kif2c
Tk1
Plk1
Cdc25c
Ankle1
Mxd3
Ticrr
Cdca5
Pclaf
Diaph3
Cenpp
Fam222b
-2 -1 0 1 2
Row Z-Score


B
clusterProfiler ORA
(GO: Biological Process)
Adj. P-value
4e-07 3e-07 2e-07 1e-07
Nuclear division
Chromosome segregation
Mitotic nuclear division
Nuclear chromosome segregation
Cytoskeleton-dependent cytokinesis
Chromosome localization
Spindle assembly
Regulation of cytokinesis
Regulation of chromosome segregation
Regulation of cell division
20 25 30 35 40
% Genes

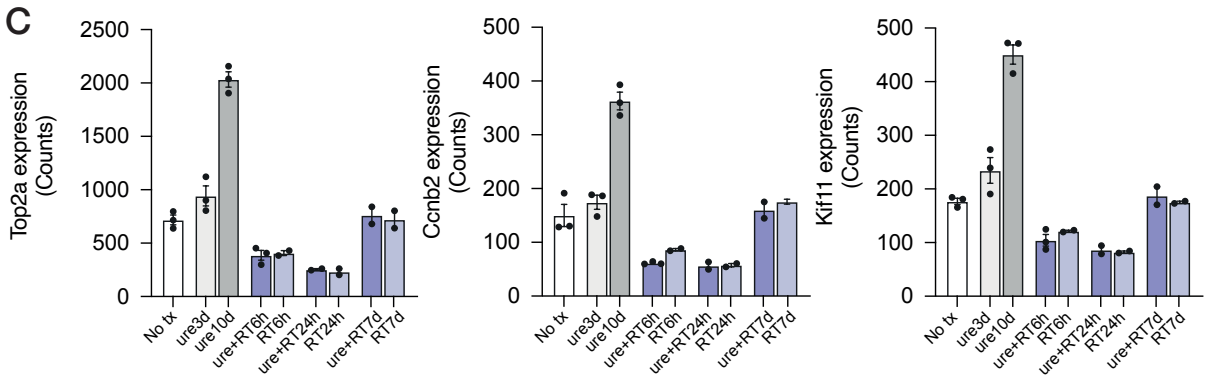

C
Top2a expression (Counts)
2500
2000
1500
1000
500
0
Ccnb2 expression (Counts)
500
400
300
200
100
0
Kif11 expression (Counts)
500
400
300
200
100
0
No tx
ure3d
ure10d
ure+RT6h
RT6h
ure+RT24h
RT24h
ure+RT7d
RT7d

Figure 4.9. Nuclear division, chromosomal segregation and cell division pathways are upregulated in urethane and downregulated in urethane + RT condition. (A) Heatmap of genes that are both significantly upregulated after 10d urethane treatment and suppressed by RT treatment in a urethane background (at either 6h, 24h or 7d post-RT). **(B)** Biological Process term overrepresentation analysis of urethane-induced genes suppressed by RT treatment. **(C)** *Top2a*, *Ccnb2* and *Kif11* gene expression in urethane, RT and urethane + RT lungs were plotted.

In both RT and urethane plus RT conditions, increases in CD4 and CD8 T-cells were observed in the lungs 7 days after thoracic RT compared to 6 hours after RT ($p < 0.05$) (**Figure 4.10a**). However, lungs from the urethane plus RT mice demonstrated a more pronounced increase in both T-cell populations compared to lungs from the mice treated with RT alone ($p < 0.05$) (**Figure 4.10a**). This suggests that there is a synergistic adaptive immune stimulation when RT is given on a urethane-treated background.

Interestingly, in contrast to the stimulation of adaptive immunity seen in the lung, a strong reduction in the neutrophil, macrophages and MDSC populations in the lungs of urethane plus RT mice compared to the RT mice was observed ($p < 0.05$) (**Figure 4.10b**). Therefore, we were able to confirm that the transcriptional changes in immune responses that we were identifying from the RNA-sequencing data were occurring on the cellular level and further characterised these events to be dominated by T-cell infiltration events.

ELISA on plasma isolated from the peripheral blood 6 hours after radiation treatment revealed that there were no significant differences in systemic IFN-β or TNF-α concentration 6 hours after thorax or mock RT (**Figure 4.11**). No differences in the cytokines were observed 24 hours nor 7 days after thorax or mock RT either (**Appendix 10**). The data suggests that the heightened immune responses that we see in the urethane plus RT setting occur locally in the lung with minimal impact on the systemic immune response.

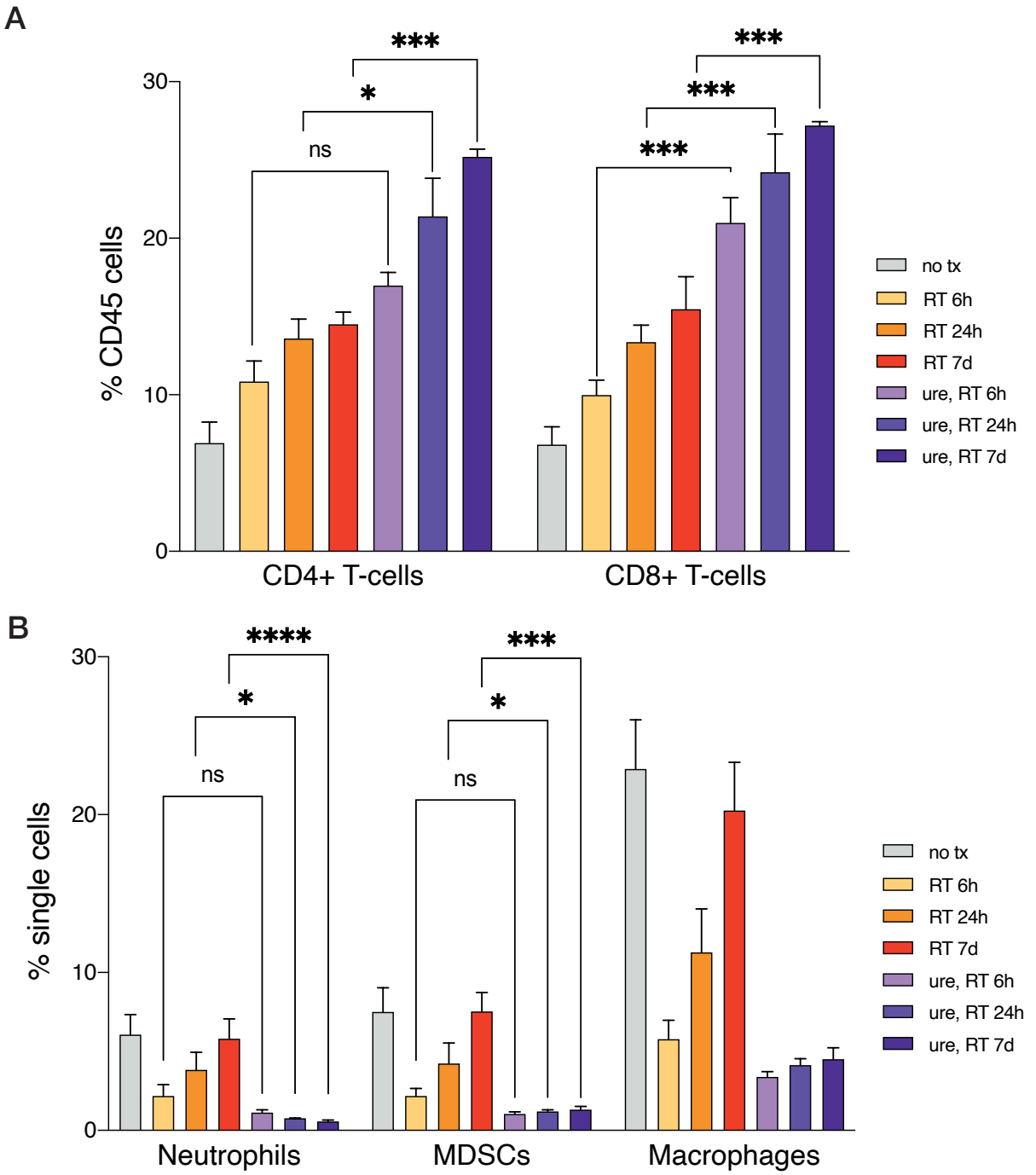


Figure 4.10. RT of the pre-neoplastic lung increases CD4⁺ and CD8⁺ T-cells and decreases neutrophils, macrophages and MDSCs in the lung. (A) CD4⁺ and CD8⁺ cells of CD45⁺ cells, and **(B)** neutrophils, macrophages and MDSCs of single cells were analysed on flow cytometry of single-cell isolated lung cells collected 6 hours, 24 hours and 24 hours after RT treatment. n = 4 per group. Results are mean ± SEM, analysed by a one-way ANOVA test. $^{ns}p > 0.05$, $^{*}p < 0.05$, $^{**}p < 0.01$, $^{***}p < 0.001$, $^{****}p < 0.0001$.

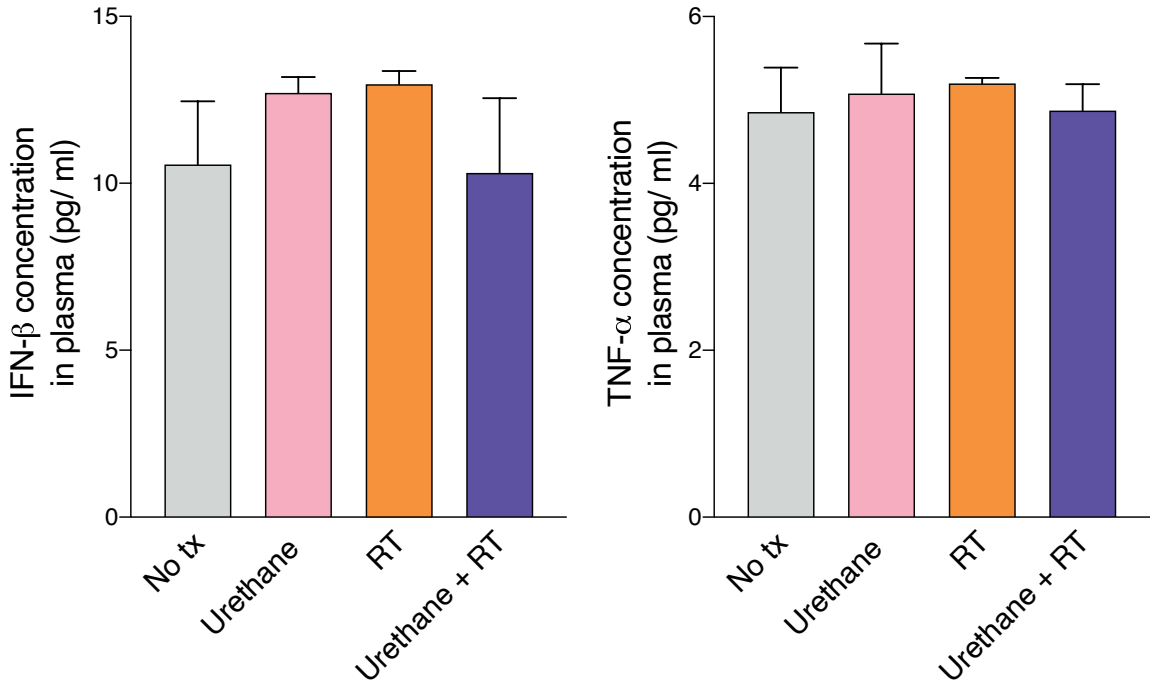


Figure 4.11. RT of the pre-neoplastic lung induces no change in IFN-β and TNF-α concentration in the plasma. IFN-β and TNF-α concentrations in the plasma collected 6 hours, 24 hours and 24 hours after RT treatment (urethane or untreated background). Results are mean ± SEM, analysed by a one-way ANOVA test. $^{ns}p > 0.05$, $^{*}p < 0.05$, $^{**}p < 0.01$, $^{***}p < 0.001$, $^{****}p < 0.0001$.

4.3 | DISCUSSION

Here, we confirmed initial findings indicating the capacity of radiation to induce a tumour-preventative effect. In addition to this, we further described a radiation-induced long-term modification of the lung immune environment, specifically in the form of increased frequencies of TLS throughout the lung tissue. Furthermore, we identified several biological processes that may be critical in generating anti-preneoplastic and immunomodulatory phenotypes, including cell cycle and division pathways and cytokine upregulation and leukocyte infiltration.

To our knowledge, this study is the first to report an induction of TLS with radiation. TLSs are thought to play an important role in immune responses in immunotherapies for cancer treatment (Colbeck et al., 2017; Qin et al., 2022; Sautes-Fridman et al., 2019). Separately, the presence of B-cells in the lung environment is thought to play an important role in cancer therapy responses as well (B. A. Helmink et al., 2020; Lauss et al., 2022; Ruffin et al., 2021; Wang et al., 2019; Wennhold et al., 2021). If the change in immune environment is introduced as a reaction to the elimination of preneoplastic cells, then an interesting question to consider is the question of whether we have generated some specific immune environment in the lung – some sort of memory of the immune response against the carcinogen exposure. We have not been able to carry out (i) an experiment whereby we introduce the same tumour cells into the mice after we generated the memory to see if they can eliminate them, nor (ii) an experiment where we re-challenge the mice to the same carcinogen, which could be potential future experiments.

There is a possibility that with radiation treatment we are pushing the stressed preneoplastic cells over a threshold where they could be either: (i) undergoing cell senescence, apoptosis/ necrosis from direct stress; (ii) recognised and eliminated by immune cells (potentially due to increased stress signalling or increased antigen presentation); or (iii) switching from a chronically inflamed environment to an acutely inflamed environment.

With regard to (i), the idea of cell death from direct stress, we can consider other settings whereby the preneoplastic cells undergo additional stress. From our transcriptomic data, we identified an array of genes involved in aspects of cell cycle regulation and mitotic cell division that were upregulated with urethane but downregulated with radiation. We cannot yet conclude if this altered state of cell cycle regulation results in a dampening of cell growth and/ or the state of cell senescence, or if these ultimately lead to increased cell death. More investigation is required in this area to confirm if these events lead to increased apoptotic events in the lung. Of note, our data in **Chapter 3** suggests that the nature of the insult/ genotoxic stressor may be critical in determining tumour promotion or tumour elimination/ prevention. Here, we described an experiment in which we introduced an additional dose of a chemical mutagen (two doses of urethane treatment 3 days apart) to the mice. In this setting, we observed the promotion of tumour growth – this was in contrast to results we observed with 13 Gy RT. On the molecular level, both the chemical carcinogen and radiation may similarly induce breaks in the DNA. However, potentially due to the physical/ chemical nature of the carcinogen and the types of DNA lesions (formation of DNA adducts with urethane, and ROS generation leading to an array of lesions including base damage, SSBs and DSBs with radiation) induced by each treatment,

different downstream pathways might be activated to lead to the different tumourigenic phenotypes.

The potential role of radiation in increasing immunosurveillance for preneoplastic cells is interesting, and in particular, we think that the possibility of radiation acting through increasing tumour (neo)antigens could be an avenue for future investigation. Numerous studies have reported that radiation can induce neoantigen presentation (Lhuillier et al., 2019; Reits et al., 2006; Sharabi et al., 2015) – also what forms the basis behind the excitement in the field for the capacity of RT in "*in situ* vaccination". Furthermore, it is known that carcinogen-induced cancers such as lung adenocarcinomas cases in smoker patients can have a high mutation burden (Altorki et al., 2019; Jamal-Hanjani et al., 2017; Tian et al., 2021) and that these tend to present more tumour-specific peptides (Anagnostou et al., 2017; Rosenthal et al., 2019). Given that the A/J lung adenocarcinoma mouse model also has a high mutation burden compared to genetically-driven cancer models such as the *K-ras*^{LA2} model (Westcott et al., 2015), the radiation-induced increase in TLSs may be stimulated through the release of (neo)antigens from genotoxic stress and immunogenic cell death mechanisms. And therefore, the immune cells that make up the TLS are likely to have immunity specifically to the preneoplastic cells. Further investigation into (neo)antigen presentation following radiation in this model is required.

The chronicity/ acuity of immune responses could also play a critical role in tumourigenesis. We observed indications of chronic inflammation from our study on the lungs of the urethane-treated mice. Specifically, we observed a delayed onset of IFN signalling 10 days after urethane was administered. The addition of radiation during this period might have instead encouraged an acute, innate immune response,

leading to an immune environment in the lung that discouraged tumour growth. There was indication that this is happening from our transcriptomic data that demonstrated that RT induced a significant but transient increase in IFN signalling (IFN-α and IFN-γ) 24 hours after treatment. The immune microenvironment is known to play an important role in the initiation and promotion of tumour growth (Hanahan & Coussens, 2012).

Studies have indicated a virally-induced innate immune signalling pathway cGAS-STING, can be upregulated after high doses of radiation (Deng, Liang, Xu, et al., 2014). Following the transcriptomic data indicating a transient increase in IFN genes after RT, we hypothesised that the STING signalling plays a role in the tumour preventative effect and TLS formation. In the following chapter, the impacts of STING modulation on tumourigenesis and long-term immunomodulation will be explored further.

CHAPTER 5. STING IN LUNG TUMOURIGENESIS AND LONG-TERM IMMUNITY

5.1 | INTRODUCTION

The cGAS-STING pathway serves as a defence mechanism against viral infections by sensing ectopic cytoplasmic double-stranded DNA and mounting an immune response through the activation of STING and subsequent stimulation of IFN responses. Given its immune-stimulatory role, it was thought that activation of cGAS-STING suppresses tumour initiation and progression through increased immune surveillance. Indeed, some studies have shown that cGAS-STING signalling can elicit an anti-tumour immune response (Harlin et al., 2009; Marcus et al., 2018). However, recent studies have revealed that cGAS-STING signalling can also act as a driver of tumourigenesis and cancer metastasis through induction of an immune-suppressive tumour microenvironment (Ahn et al., 2014; Barbie et al., 2009).

It is thought that the anti-tumour responses through activation of cGAS-STING occur through stimulation of IFN signalling and subsequent immune cell infiltration including NK cells and T-cells into the tumours (Harlin et al., 2009; Marcus et al., 2018). The activation of the STING-IRF3-IFN pathway can be stimulated through cancer cell-intrinsic cytosolic DNA accumulation (Marcus et al., 2018) or through transferring of tumour DNA to the cytosol of DCs, (Deng, Liang, Xu, et al., 2014; Diamond et al., 2011; Woo et al., 2014) or the secretion of cGAMP into the extracellular space and uptake by immune cells (Ritchie et al., 2019) (**Figure 5.1**). Acute STING-driven SASP is also a suggested mechanism, based on evidence demonstrating an association between the loss of cGAS or STING, a compromised SASP response and increased tumour growth (Dou et al., 2017; Glück et al., 2017; Ranoa et al., 2019).

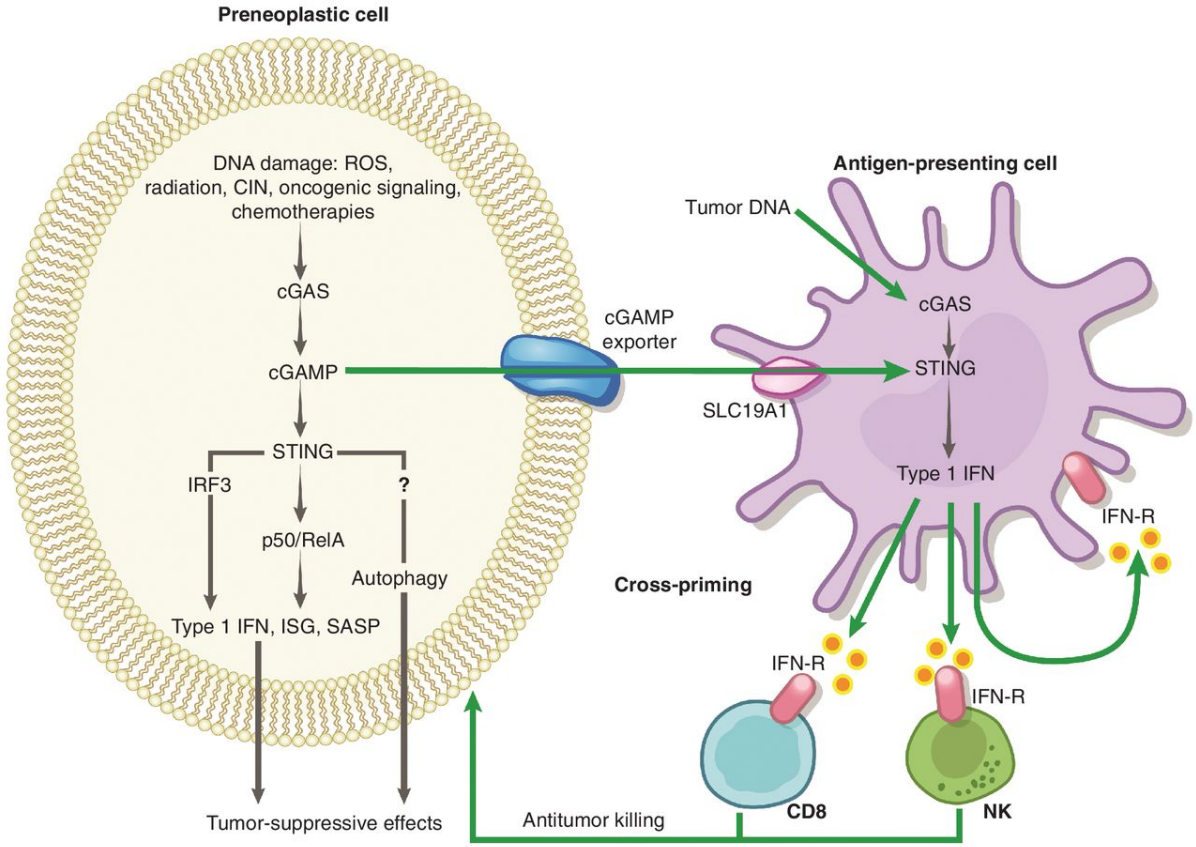


Figure 5.1. Mechanisms of tumour-suppressive action of cGAS-STING. Genotoxic stressors such as radiation, ROS and chromosomal instability can generate cytosolic DNA, which can activate the cGAS-STING pathway resulting in the upregulation of type I IFN, IFN stimulating genes and SASP. STING signalling can occur in the cancer cell in neighbouring immune cells through cGAMP- or tumour-DNA transfer-mediated crosstalk mechanisms. Figure adapted from (Kwon & Bakhoum, 2020).

On the other hand, there is growing evidence that suggests cGAS-STING could also have a role in facilitating tumourigenesis and cancer metastasis. The protumourigenic action is largely thought to be a result of chronic STING signalling and the establishment of an immune-suppressive microenvironment. These can occur through the mobilisation of myeloid suppressor cells (Liang et al., 2017), the recruitment of T_{regs} (Liang et al., 2015) and chronic SASP signalling (Coppé et al., 2008; Dou et al., 2017; Yang et al., 2017).

Further investigation is needed to uncover the dichotomous role of STING in tumourigenesis, and no studies to our knowledge have investigated the role of STING in the context of carcinogen-driven lung adenocarcinomas. In the previous chapter, we observed that radiation treatment during carcinogenesis prevented tumour development and stimulated the generation of *de novo* TLSs. Importantly, a transcriptomic analysis of lungs from carcinogen pre-treated mice revealed a transient increase in IFN signalling 24 hours following radiation treatment. This finding led us to hypothesise that the cGAS-STING pathway is involved in the anti-tumourigenic effect (and potentially the generation of TLSs) through mechanisms including increased immune surveillance. We set out to test our hypothesis in this chapter using a murine STING agonist (vadimezan, 5,6-dimethylxanthenone-4-acetic acid) with the following aims: (1) investigate the impact of STING modulation (using a STING agonist) during tumour initiation on tumour development, and (2) characterise the long-term and short-term immunomodulatory effects of STING agonism/ antagonism during tumourigenesis.

5.2 | RESULTS

5.2.1 | Urethane pre-treatment sequesters IFN- β levels and T-cell infiltration stimulated by DMXAA

First, in order to investigate the interactions between urethane and STING agonist, DMXAA (Vadimesan), early events following the two treatments were evaluated in an *in vivo* experiment. Here, A/J mice were given a dose of urethane (5%, i.p.) on day 0, followed by one dose of DMXAA (20 mg/kg, i.p.) on day 3, after which time mice were euthanised on days 3 to 10 (6 hours to 7 days after DMXAA treatment) (**Figure 5.1a**).

An assessment of cytokines in the plasma collected from urethane and urethane + DMXAA treated groups with an ELISA confirmed that DMXAA treatment significantly elevated IFN-β and TNF-α levels in the blood 6 hours after treatment compared to the vehicle control ($p < 0.05$) (**Figure 5.1b**). A similar spike in IFN-β and TNF-α levels were observed in mice pre-treated with urethane (urethane versus urethane + DMXAA, $p < 0.05$) (**Figure 5.1b**). Of note, a significantly lower level of IFN-β was observed in mice treated with urethane + DMXAA compared to the DMXAA control ($p < 0.05$) (**Figure 5.1b**), potentially indicating a counteractive effect between urethane and DMXAA in IFN-β levels.

Given the increase in STING expression in the lungs 3 days after urethane (**Figure 4.4**), it is possible that an overstimulation of IFN is occurring in the lungs, and a compensatory mechanism (a downregulation of IFN) is at play. However, further investigation is required to confirm these mechanisms.

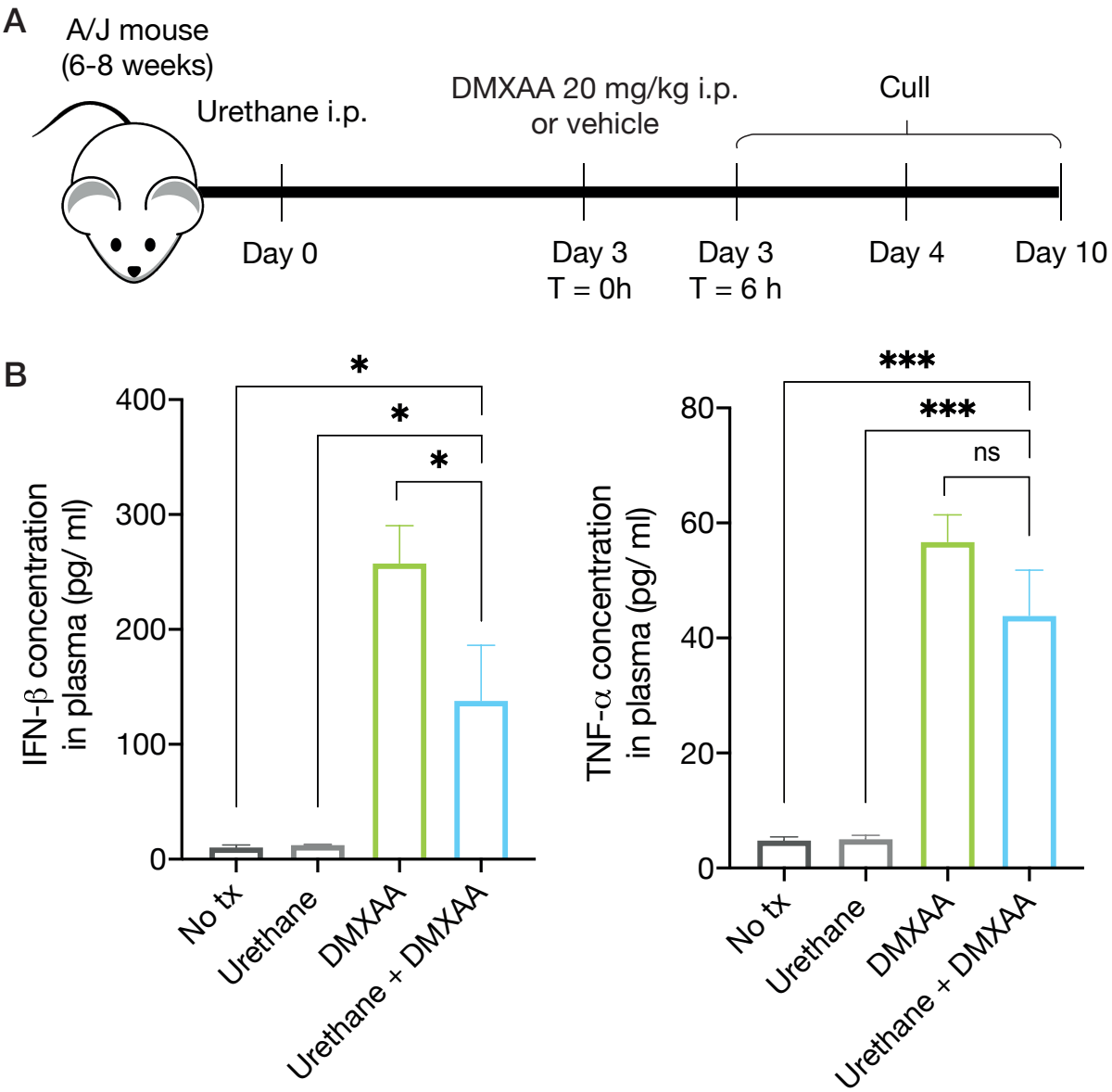


Figure 5.2. Studying the early events in the lung following DMXAA treatment during tumour initiation. (A) Schematic representation of in vivo experiments of DMXAA or H-151 intervention during carcinogenesis. A/J mice were treated with urethane i.p. on day 0 and administered vehicle and DMXAA (one dose of 20 mg/kg i.p. on day 3). Mice were euthanised on day 4 or 10 (n = 3 or 4 per time point per treatment group). **(B)** ELISA quantification of IFN-β and TNF-α in plasma collected from mice 6 hours, 24 hours and 24 hours after DMXAA treatment (with or without urethane pre-treatment). n = 4 per group. Results are mean ± SEM, analysed by a one-way ANOVA test. $^{ns}p > 0.05$, *$p < 0.05$, **$p < 0.01$, ***$p < 0.001$, ****$p < 0.0001$.

The cellular events were then investigated with flow cytometry on lung samples collected from experiments detailed in **Figure 5.1a**. Results revealed that DMXAA treatment stimulated an infiltration of $CD4^+$ and $CD8^+$ T-cells into the lungs 7 days after treatment (with or without urethane-pre-treatment) (**Figure 5.2a**). Interestingly, the data also revealed a dampening of $CD4^+$ T-cell infiltration to the lungs under urethane pre-treated conditions (DMXAA versus urethane + DMXAA, $p < 0.01$) (**Figure 5.2a**). A similar effect was observed in $CD8^+$ T-cell infiltration, however, this did not reach statistical significance (**Figure 5.2a**). On the other hand, DMXAA treatment (or urethane pre-treatment) did not have an impact on innate immune cell populations, including neutrophils ($CD11b^+$, $Ly6G^+$), macrophages ($CD11b^+$), and MDSCs ($CD11b^+$, $Gr1^+$) (**Figure 5.2b**).

The dampening of T-cell infiltration, in combination with the data demonstrating a sequestering IFN-β (in **Figure 5.1b**) both seen in the urethane pre-treatment setting, suggests that the presence of the carcinogen prior to immune stimulation creates a suppressive effect for future immune stimulation through mechanisms not yet understood. This is a phenomenon that has not yet been described in other studies and is an area that requires further investigation.

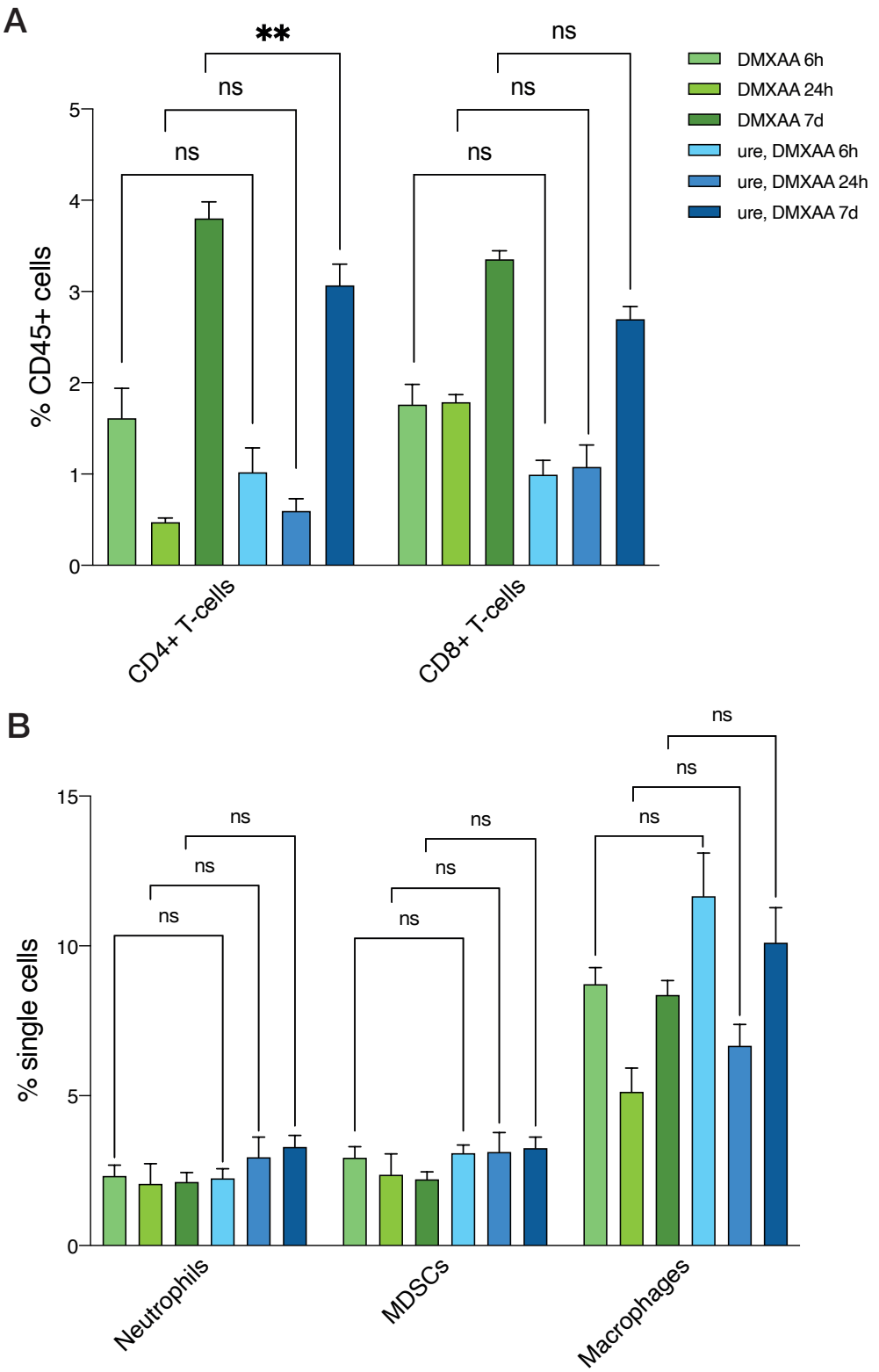


Figure 5.3. DMXAA treatment stimulates T-cell infiltration in the lung with minimal impact on neutrophil, macrophage and MDSC populations in the lung. **(A)** Percent CD4⁺ T-cells, CD8⁺ T-cells of CD45⁺ cells, and **(B)** percent neutrophils (CD11b⁺, Ly6G⁺), macrophages (CD11b⁺), and MDSCs (CD11b⁺, Gr1⁺) of single cells analysed by flow cytometry of single-cell isolated lung cells collected 6 hours, 24 hours and 7 days after DMXAA treatment (with or without urethane pre-treatment). n = 4 per group. Results are mean ± SEM, analysed by a one-way ANOVA test. $^{ns}p > 0.05$, *$p < 0.05$, **$p < 0.01$, ***$p < 0.001$, ****$p < 0.0001$.

5.2.2 | Intervention with a STING agonist during tumour initiation increases tumour burden

The impact of STING agonism on lung tumour development was then evaluated with an *in vivo* experiment. A/J mice were treated with urethane (5%, i.p.) on day 0 and DMXAA (20 mg/kg, i.p.) on day 3. Mice were euthanised 26 weeks after urethane treatment for assessments of lung tumour growth (**Figure 5.3**).

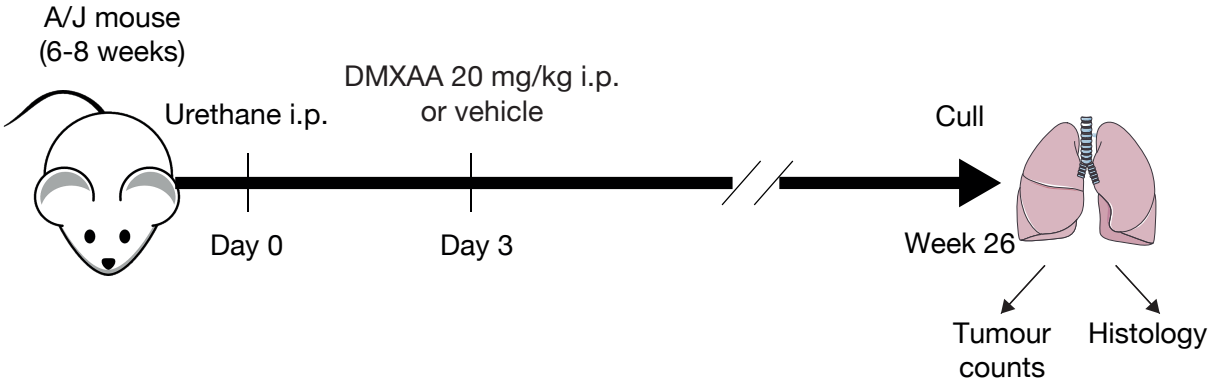


Figure 5.4. Intervention of lung tumourigenesis with a STING agonist. Schematic representation of *in vivo* experiment design of lung tumour intervention with DMXAA. A/J mice were treated with urethane and given vehicle or DMXAA (20 mg/ kg, i.p.) 3 days after urethane treatment (n = 10 per group) and euthanised 26 weeks later for the evaluation of lung tumours.

DMXAA treatment of pre-neoplastic lungs induced a reduction in lung tumour numbers (superficial tumours, $p < 0.05$) (**Figure 5.4a**), however, increased tumour burden ($p = 0.109$) (**Figure 5.4b**). Upon close examination of the lung tumours from urethane and urethane plus DMXAA-treated mice by histology, tumours from the urethane plus DMXAA treated mice had smoother, well-defined edges compared to the tumours of the urethane-treated mice had ill-defined, irregular borders with finger-like projections into normal tissue (**Figure 5.5**). The histological characteristics of the urethane and urethane plus DMXAA-treated lung tumours appeared similar otherwise, with solid tumour phenotypes (Westcott et al., 2015).

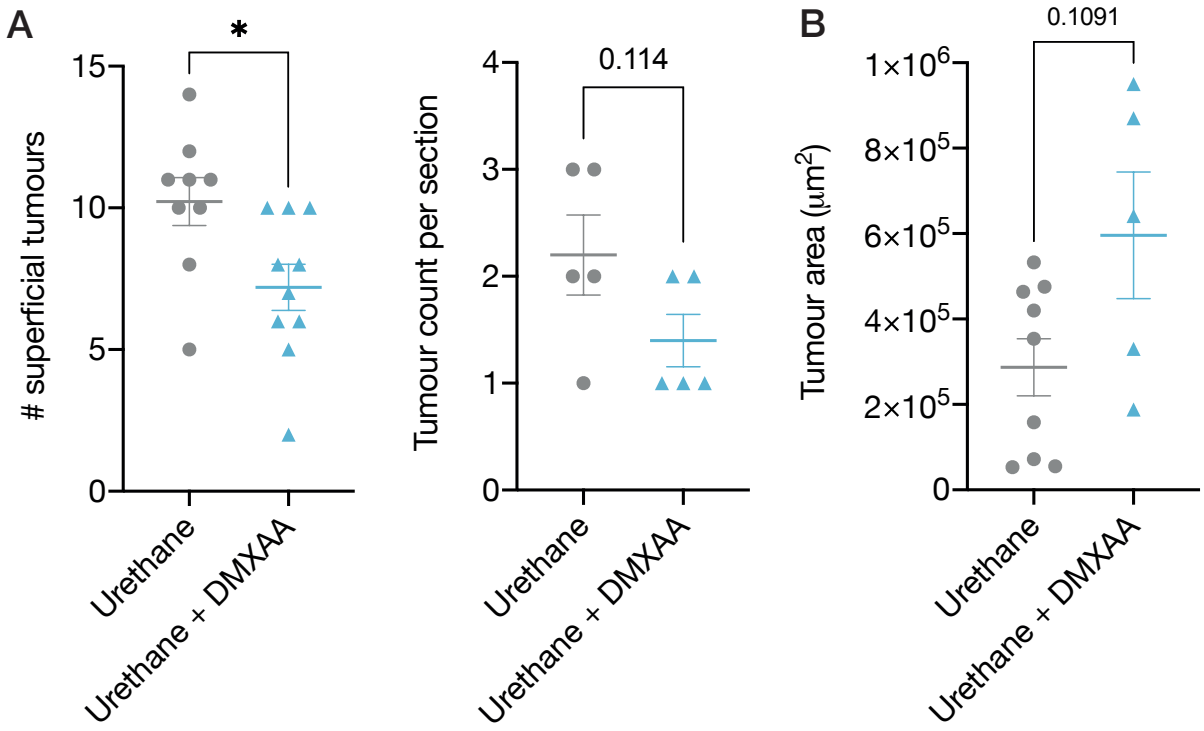


Figure 5.5. DMXAA treatment during lung tumourigenesis reduces tumour counts and increases tumour burden. (A) The number of nodules counted on the surface of lungs and **(B)** tumours counted per section of lungs from urethane-treated and urethane + DMXAA-treated mice (n = 10 per group). **(C)** Area of tumours per lung section of urethane or urethane + DMXAA-treated mice. n = 5 lung sections per group quantified. Results are mean ± SEM, analysed by unpaired student's T-test. $^{ns}p > 0.05$, $^{*}p < 0.05$, $^{**}p < 0.01$, $^{***}p < 0.001$, $^{****}p < 0.0001$.

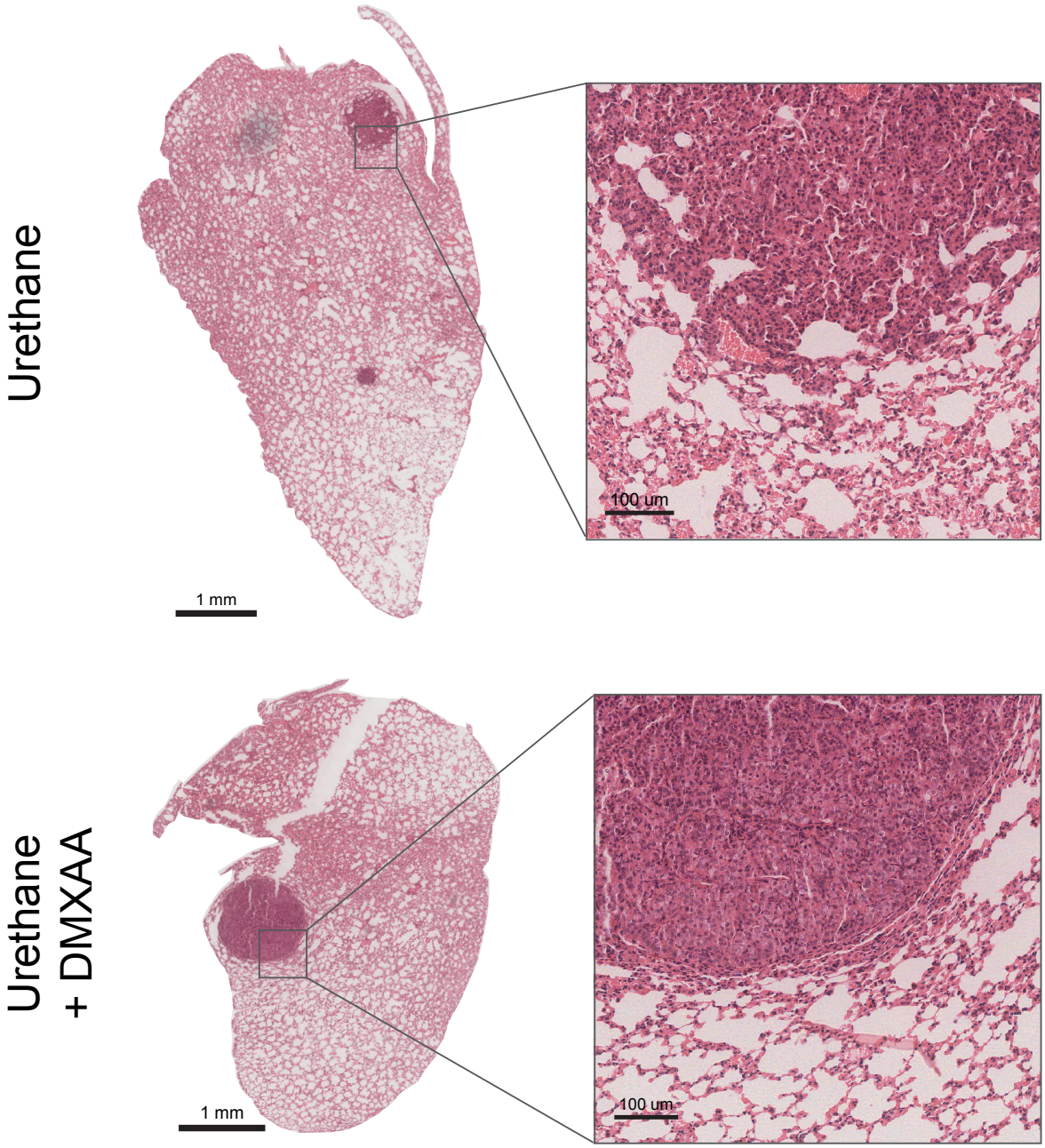


Figure 5.6. DMXAA treatment during tumourigenesis results in tumours that are histologically different from urethane-treated control. Left, representative images of lung sections from urethane or urethane + DMXAA mice. Scale bar: 1 mm. Right, representative images of tumour border. Scale bar: 100 μm.

Following the interesting observations that have not yet been described in other studies, and the questions that remain on the role of STING in tumourigenesis in the mouse model, an *in vivo* experiment with a STING inhibitor, H-151, in the urethane-induced A/J model was planned to further investigate mechanisms. However, these experiments could not be carried out due to the COVID-19 pandemic and the nature of the experiment (5-6 months tumour-growth period required for evaluation of lung tumours). Other planned experiments included studying tumourigenesis in a STING KO model.

5.2.3 | STING agonist treatment of pre-neoplastic tissue results in a long-term increase in lymphocytes in the lung but does not increase tertiary lymphoid structures

To understand if DMXAA treatment of the pre-neoplastic lung induced long-term changes to the lung environment, we evaluated the lungs of the urethane and urethane plus DMXAA treated mice by histology. Chromogenic IHC revealed that there was a long-lasting increase in $CD45^+$ immune cells residing in the urethane plus DMXAA treated lung compared to the urethane-treated controls ($p < 0.001$) (**Figure 5.7a, b**). However, in contrast to the phenotypes seen in mice that were treated with urethane plus RT in **Chapter 4** (where an increase in $CD45^+$ cell aggregates was observed, and structures were characterised as TLS), we did not observe any significant increase in $CD45^+$ cell aggregates in the urethane plus DMXAA treated mice compared to urethane control (ns) (**Figure 5.7c**).

For further characterisation of the immune microenvironment that DMXAA treatment of preneoplastic lesions induces, we analysed B-cell, T-cell ($CD4^+$ helper T-cells, $CD8^+$ cytotoxic T-cells, regulatory T-cells), dendritic cells and memory T-cells ($CD8^+$ $CD103^+$) on multiplex IF. Quantification of the immune cell populations revealed that across the lung, there was a trending increase in B-cells ($CD19^+$) ($p=0.0823$) and significant increases in $CD8^+$ T-cell ($p<0.05$) with DMXAA treatment (**Figure 5.8**). Analysis of populations within the TLSs revealed a trending increase in $CD8^+$ T-cells ($p = 0.0866$) but did not reveal any significant differences in other immune cell populations (**Figure 5.8**).

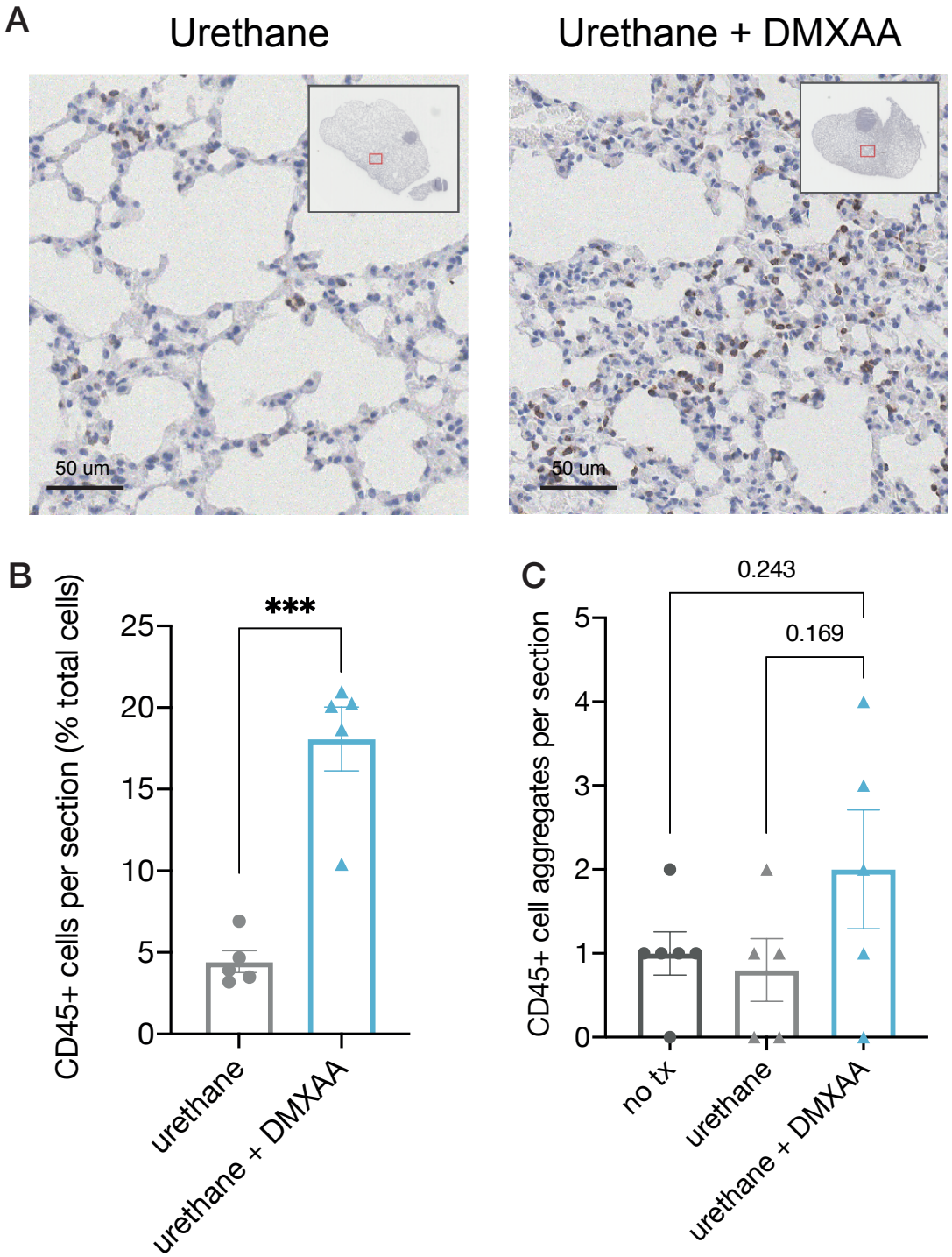


Figure 5.7. DMXAA treatment during tumourigenesis increases resident leukocytes in the lung but has little impact on the number of tertiary lymphoid organs. (A) Representative images of sections from urethane and urethane + DMXAA-treated lungs (26 weeks after treatment) stained histologically with CD45. Scale bar: 50 μm. **(B)** Quantification of $CD45^+$ lymphocyte aggregates per lung section per mouse. n = 5 per group. **(C)** The number of $CD45^+$ cell aggregates per section per mouse. n = 5 per group. Results are mean ± SEM, analysed by a one-way ANOVA test. $^{ns}p > 0.05$, $^{*}p < 0.05$, $^{**}p < 0.01$, $^{***}p < 0.001$, $^{****}p < 0.0001$.

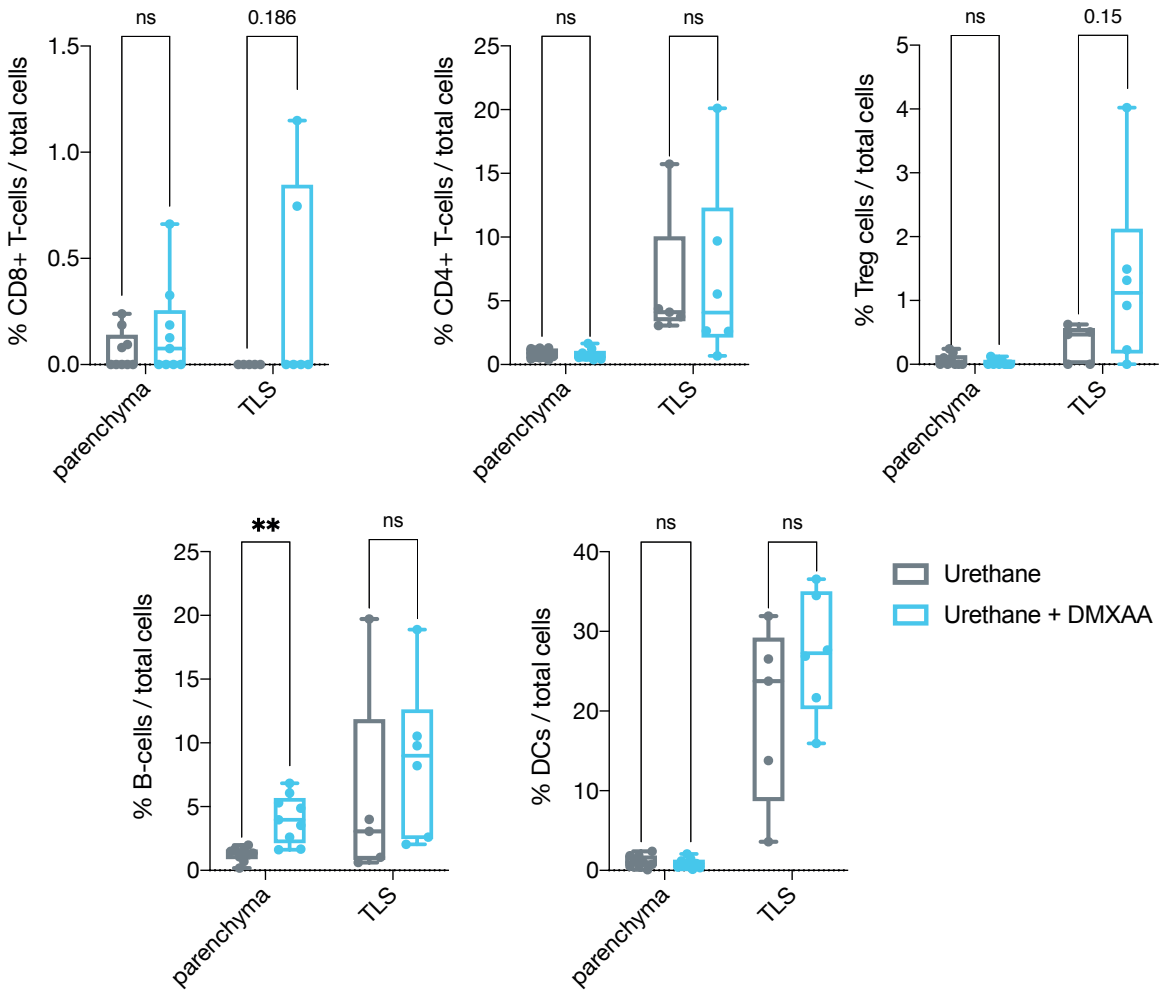


Figure 5.8. DMXAA treatment stimulates an increase in B-cells and CD8⁺ T-cells in the lung. Quantification of CD19⁺ B-cells, CD4⁺ T-cells, CD8⁺ T-cells, and FoxP3⁺ T-cells in lung parenchyma (n = 9; 3 mice per group and 3 ROIs per mouse) and TLS (n = number of TLSs identified per group). Results are mean ± SEM, analysed by an unpaired student's t-test with Welch's correction. $^{ns}p > 0.05$, *p < 0.05, **p < 0.01, ***p < 0.001, ****p < 0.0001.

5.2.4 | RT and DMXAA treatments at tumour initiation have an additive effect on limiting tumour growth

To investigate the impact of radiation treatment (RT) with DMXAA during tumourigenesis, we carried out an *in vivo* experiment whereby A/J mice were treated with urethane (5%, i.p.), followed by RT (13 Gy, thorax) and DMXAA (15 mg/ kg, i.p.)[11] treatment 3 days after urethane treatment. Mice were euthanised 26 weeks after urethane treatment for evaluation of the lung (**Figure 5.9a**).

To our surprise, the RT + DMXAA combination treatment demonstrated a synergistic tumour-preventative effect on the urethane pre-treated mice. Surface tumour counts from the combination treatment were not only significantly lower than the urethane-control ($p < 0.0001$) and urethane + DMXXA ($p < 0.001$), but also trended toward significance compared to the urethane + RT treated group ($p = 0.135$) (**Figure 5.9b**).

[11] Maximum tolerated dose of 13 Gy thorax RT and DMXAA was determined in a study whereby doses of 20 mg/ kg, 15 mg/ kg, and 10 mg/kg DMXAA were assessed together with urethane and 13 Gy thorax RT in A/J mice. Experiment design and body weights detailed in **Appendix 12**. 20 mg/ kg was not tolerated (decline in body weight; gut toxicity observed upon necropsy), however 15 mg/ kg was tolerated with urethane and 13 Gy thorax RT and used for treatment schedule in **section 5.4.4**.

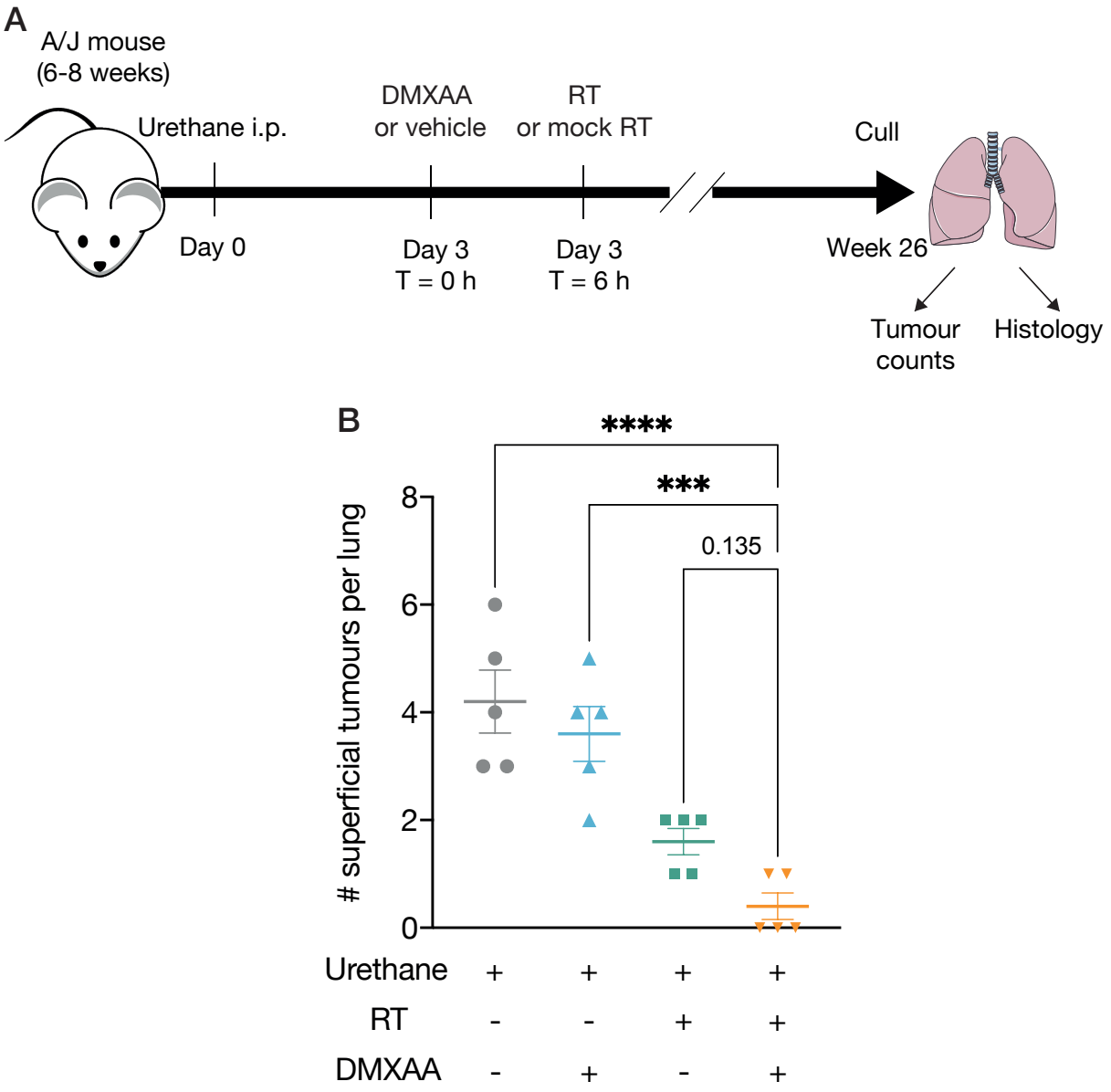


Figure 5.9. RT + DMXAA treatment during tumourigenesis has an additive anti-tumourigenic impact on lung tumour growth. (A) Schematic representation of *in vivo* experiment design of lung tumour intervention with RT and DMXAA. A/J mice were treated with urethane and given RT/ mock RT and DMXAA (15 mg/ kg, i.p.)/ vehicle 3 days after urethane treatment and euthanised 26 weeks later for the evaluation of lung tumours. n = 5 per treatment group. **(B)** Number of nodules counted on the surface lungs from: (i) urethane; (ii) urethane + DMXAA; (iii) urethane + RT; and (iv) urethane + RT + DMXAA-treated mice. n = 5 per treatment group. Results are mean ± SEM, analysed by one-way ANOVA. $^{ns}p > 0.05$, $*p < 0.05$, $**p < 0.01$, $***p < 0.001$, $****p < 0.0001$.

5.3 | DISCUSSION

Findings in this chapter allude to the complex role of STING signalling in lung carcinogenesis – a punctuated activation of STING during tumour initiation with STING agonist, DMXAA, limited the number of tumours formed, however, increased tumour burden. Initial immune responses after STING activation with DMXAA included a spike in TNF-α and IFN-β in circulation and an increase in T-cell infiltration without changes to innate immune cell populations in the lung. These STING stimulated responses in the carcinogen pre-treatment setting resulted in a long-term increase in residing immune cell populations in the lung including $CD19^+$ B-cells, $CD4^+$ helper T-cells, and $CD8^+$ cytotoxic T-cells, however, did not stimulate TLS generation.

The paradoxical finding that STING activation during tumour initiation resulted in decreased tumour numbers and increased tumour burden was unexpected and countered our initial hypothesis that STING activation would have an anti-tumourigenic effect through increased immune surveillance. Interestingly, however, the observation of the growth of fewer albeit more aggressive tumours suggests that STING activation applied a selection pressure during tumour initiation. Indeed, it has been thought that cancer cells with high levels of chromosomal instability and chronic release of cytosolic DNA and STING-mediated IFN signalling adopt strategies to inhibit this pathway to evade immune surveillance (Bakhoum, 2022; Kwon & Bakhoum, 2020). Supporting this thinking are studies demonstrating decreased expression of cGAS and STING in some late-stage tumours (Song et al., 2017; Xia, Konno, Ahn, et al., 2016; Xia, Konno, & Barber, 2016), and increased methylation in cGAS and STING promoters in a subset of tumours (Konno et al., 2018). Notably, our results in **Chapter 4** showed an increase

in STING expression 3 days after carcinogen treatment, although it was unclear if the increase in protein occurred in the preneoplastic cells by histological assessment. STING activation with DMXAA may have allowed the elimination of clones that had not yet developed resistance to STING signalling, however, encouraged the neoplastic cells that had inactivated STING signalling to persist.

In parallel, we observed that systemic STING agonism resulted in an increase in resident T-cells and B-cells in the carcinogen pre-treated lung, however without aggregate structures that resembled TLSs. Understanding whether the resident immune cells provide benefits for anti-tumour responses (or instead create a pro-tumourigenic environment) requires further investigation.

Additionally, we observed a dampening effect of DMXAA-stimulated immune responses (specifically in IFN-β levels and T-cell infiltration into the lung) in the urethane pre-treated mice. Interestingly, some evidence suggests cigarette smoking can alter immune functions (Feldman & Anderson, 2013; Mehta et al., 2008; Qiu et al., 2017), however, the direct interactions between chemical carcinogens and immune stimulating agents are not yet known. Further investigation is required in this area to validate this finding and to understand if these mechanisms have an impact on tumour development outcomes.

Findings from this study could have benefitted from additional *in vivo* experiments using a STING inhibitor such as H-151 during tumour initiation, or carcinogen-stimulation in a STING KO model. These experiments were indeed identified as critical, however, could not be carried out due to restricted laboratory access during COVID-19.

This study is one of the first to investigate the role of STING signalling in a carcinogen-induced lung adenocarcinoma mouse model. The question regarding the complexity of the role of STING in tumour initiation, particularly on its possible role in tumour clone selection is of importance - both for the biological understandings of cancer evolution, and clinical considerations in treatment planning with STING modulators that have been introduced into the clinic in recent years for cancer therapy.

CHAPTER 6. RADIATION-INDUCED CARDIAC DISEASE IN AN A/J MOUSE MODEL

6.1 | INTRODUCTION

Thus far, we have studied the impacts of radiation and other cancer therapies on tumour development. However, in our literature review (**Chapter 1**), we also found the clinical importance to evaluate the effects of cancer therapies on normal tissues in parallel, with the concern for widening the therapeutic window of cancer therapies including radiation. Furthermore, we identified an urgent need to address toxicities in the heart which are seen in a subset of cancer patients receiving thoracic radiation. There is currently a lack of understanding of the underlying mechanisms that give rise to late heart toxicities, and therefore a lack of interventions to mitigate the disease other than to minimise the dose of radiation to the organ.

Mouse studies of radiation-induced cardiac toxicity

Despite the clinical importance of studying radiation-induced cardiac toxicities (RICT), few preclinical models are currently available for these studies (Schlaak et al., 2020). Among animal models used to study the heart, the mouse (*mus musculus*) is the preferred model due to similarities in the physiology (Laflamme et al., 2012) and pathological responses to radiation (Walls et al., 2022) between mice and humans. Some studies have reported that radiation induces changes in the microvascular density (Seemann et al., 2012), perivascular fibrosis (van der Veen et al., 2015) and cardiac hypertrophy (Monceau et al., 2014). Although abnormalities to the electrical conduction including cases of arrhythmias have been reported in the clinic (Boero et al., 2016; Taunk et al., 2015), mechanisms underlying changes in electrical conductivity of the heart from radiation have not been studied in mouse models (Walls et al., 2022).

According to a recent review of preclinical models for RICT studies by Walls et al., the most commonly used mouse strains for these studies are C57BL/6 and BALB/c mice (Walls et al., 2022). However, these mouse strains are also known to be more “fibrosis-prone” from radiation treatment compared to strains such as SWR, and A/J strains (Franko et al., 1991; Jackson et al., 2010; Sharplin & Franko, 1989). This limits the models utilising C57BL/6 mice in its capacity to more closely mimic late radiation-induced effects (which can include fibrosis) observed in patients. Therefore, there is a need to find a pre-clinical model which more closely mimics human disease and toxicities.

In the Ryan lab, we have used the A/J mouse model to understand normal tissue biology following RT (S. J. Antonia et al., 2017; Gomes et al., 2019; Jiang et al., 2021). These studies have shown that radiation-induced normal tissue events in the A/J mouse model demonstrate similar pathophysiology as seen in the clinic. Radiation-induced normal tissue toxicities in the lung, including pneumonitis and fibrosis (Lourenco, 2017), and oesophagus, including oesophagitis (Martin, 2021), have been studied in the A/J mouse model thus far. However, cardiac tissue toxicity from radiation has not yet been described in this model.

Mechanisms of resolving DNA damage in cardiac tissue – innate immune responses in the heart

In adult mammalian hearts, cardiomyocyte numbers are constant throughout the lifespan with a low turnover rate (< 1% per year in adults) in homeostasis (Bergmann et al., 2015). Endothelial and mesenchymal cell types within the cardiac tissue have higher turnover and increase into adulthood (Bergmann et al., 2015).

Adult mammalian hearts lack regenerative potential and resort to scarring mechanisms rather than regeneration during tissue damage or injury (Hashimoto et al., 2018; Porrello & Olson, 2014; Uygur & Lee, 2016). These cardiac regenerative/ reparative properties are more similar between rodents and humans compared to other animal models like zebrafish models whose hearts have high regenerative capacity (Hashimoto et al., 2018).

During ischaemic heart injuries such as myocardial infarction, toll-like receptor signalling is activated and reactive oxygen species (ROS) can induce cytokine and chemokine upregulation (Frangogiannis, 2014). Leukocytes are then recruited to the area of injury and remove dead cells by phagocytosis and by simulating signalling for scar formation, in some cases resulting in fibrosis (Frangogiannis, 2019; Frantz & Nahrendorf, 2014)

In contrast, immune responses in the heart following sub-cellular/ molecular damage (as compared to large areas of tissue damage) are generally poorly understood. A study by Higo et al. (2017) showed that the accumulation of unrepaired single-strand breaks (SSBs) observed in cardiomyocytes in a failing heart leads to cytokine release through NF-κB signalling. Additionally, Oka et al. (2012) demonstrated that the lack of mitophagy and leakage of mitochondrial DNA can lead to a Toll-like receptor 9-mediated inflammatory response, resulting in myocarditis and dilated cardiomyopathy. Furthermore, a study by Cao et al. (2018) showed that cyclic GMP-AMP synthase (cGAS) acts as a pattern recognition receptor in the immune response during cardiac ischaemia and suggests that this pathway governs macrophage transformation to a reparative phenotype in the heart. This is supported by evidence presented by King et al. (2017) that demonstrates the involvement of the

innate immune response (through interferon signalling) after myocardial infarction. These studies interestingly suggest a possible link between DNA damage events/ leakage of nucleic material into the cytosol and immune activation in heart tissue. However, none have described these mechanisms in the context of radiation-induced late cardiac toxicity.

Taken together, we identify a need for a preclinical model for the study of RICT and a lack of understanding of mechanisms, particularly concerning radiation-induced inflammatory events, that play a role in cardiac tissue in late toxicities. Therefore, this chapter will aim to: (1) establish a pre-clinical model in which we can study radiation-induced cardiac disease and I will be exploring the A/J mouse model as a possible model for this purpose; (2) and investigate the mechanisms of response to a genotoxic stressor like radiation in the A/J mouse heart with a particular focus on the DNA damage responses and subsequent immunological events.

6.2 | RESULTS

6.2.1 | Establishing a pre-clinical model to understand radiation-induced cardiac effects

To first evaluate the A/J mouse model for the studies of RICT, A/J mice were treated with whole-heart or whole-thorax RT at a single dose of 13 Gy or 15 Gy. ECG traces were collected 5 to 6 months after RT. Mice were euthanised 6 months after RT at which time hearts were collected for histological, cellular and molecular analyses (**Figure 6.1a**).

Sudden death, pleural effusion, ventricular dilation, arrhythmias, and pericardial fibrosis were observed in the A/J mice that were given a dose of RT to the heart. Specifically, pleural effusion was observed in 33.3% of mice treated with 13 Gy heart RT, 50% of mice treated with 15 Gy heart RT and 100% of mice treated with 13 Gy thorax RT upon necropsy at the experiment endpoint (**Table 6.1**). At the same time, significant drop in body weight loss was observed specifically in the 13 Gy thorax RT setting that was not observed in the heart RT (13 Gy or 15 Gy) settings (**Figure 6.1b**). This suggests that the occurrence of pleural effusions may be more closely associated with the inclusion of the lungs in the field of radiation. Notably, a case of sudden death was observed 17 weeks after 15 Gy heart RT (1 out 6 mice; 16.7% of group), while all mice survived until the experimental endpoint in the 13 Gy heart and thorax RT and mock RT groups (**Figure 6.2a**).

Interestingly, an increase in heart weight ($p < 0.05$) (**Figure 6.2b**) along with increases in ventricular chamber volumes (**Figure 6.2c**) were noted in three mice (50%;

3 of 6). The increase in heart weights and ventricular volumes could be indications of functional dysfunction of the heart. Here, RT could potentially be inducing functional changes, however, other measurements such as ejection fraction (from ultrasound or MR imaging) are required to confirm this.

Table 6.1. Summary of clinical and pathophysiological phenotypes of late radiation-induced cardiac effects in A/J mice.

	No RT	13 Gy (heart)	15 Gy (heart)	13 Gy (thorax)
Sudden death	0% (0/3)	0% (0/3)	16.7% (1/6)	0% (0/6)
Pleural effusion	0% (0/3)	33.3% (1/3)	50% (3/6)	100% (6/6)
Ventricular dilation	0% (0/3)	0% (0/3)	50% (3/6)	No data available
Arrhythmia	0% (0/3)	0% (0/6)	16.7% (1/6)	33.3% (2/6)
Pericardial fibrosis*	0% (0/3)	100% (3/3)	100% (6/6)	100% (6/6)

* > 50% of pericardium with > 5um collagen at the pericardium with Masson's Trichrome stain

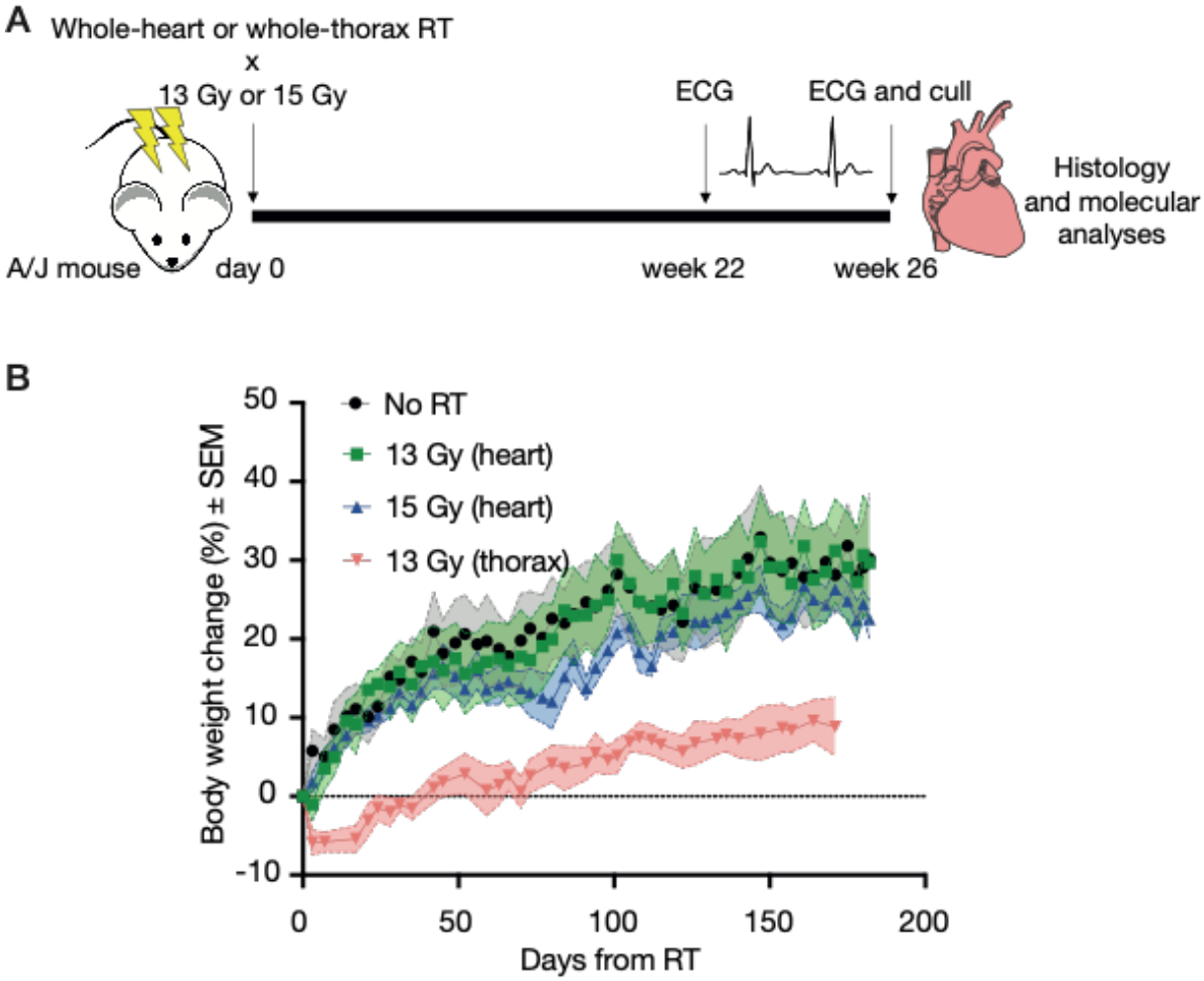


Figure 6.1. Heart and thoracic heart irradiation of A/J mice. (A) Schematic representation of the experimental design for heart and thoracic irradiation of A/J mice and method of ECG, MRI and histology data collection. **(B)** Mean change in body weights of the mice after mock (n = 3), 13 Gy (n = 3) or 15 Gy (n = 6) cardiac or 13 Gy thoracic irradiation (n = 6) tracked until experiment endpoint at 26 weeks after treatment. Body weights were normalised to body weights at day 0 of treatment. Shaded regions indicate the SEM.

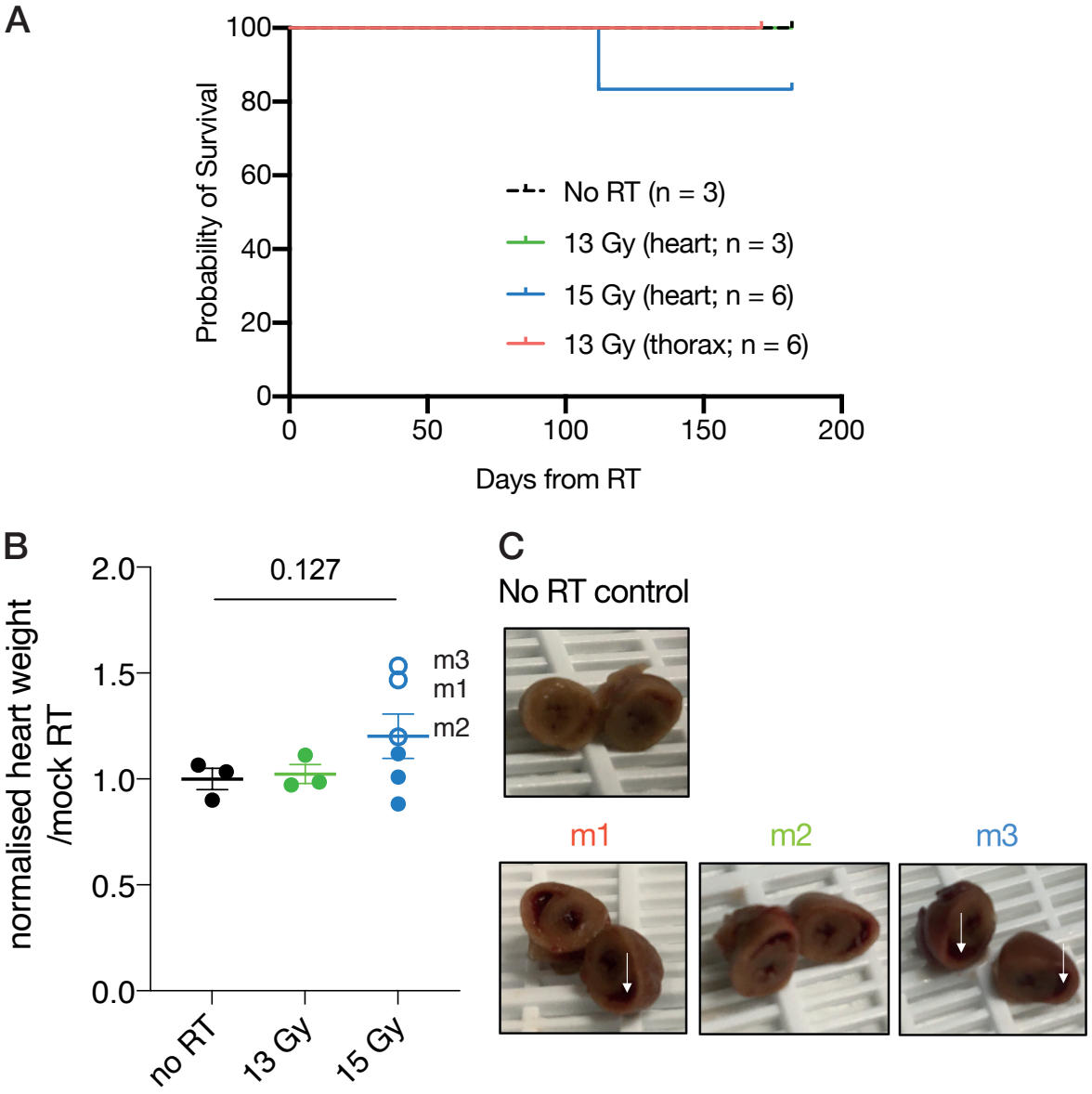


Figure 6.2. Hypertrophic cardiomyopathy and sudden death were observed in radiation-treated A/J mice. (A) Kaplan Meier curve of percent mice that survived after mock (n = 3), 13 Gy (n = 3) or 15 Gy (n = 6) cardiac or 13 Gy thoracic irradiation (n = 6). Day of irradiation is denoted as day 0. **(B)** Heart weights were normalised to the whole-body weights of the mice. Mice treated with 15 Gy RT that had greater heart weights than the average value of the group are highlighted in the plot (mouse 1 in red, mouse 3 in green and mouse 6 in blue). **(C)** Images of transverse cross-sections of formalin-fixed hearts of mouse 1, 3, and 6 in the 15 Gy RT group are shown in the bottom panel and a cross-section of a heart from a mock RT mouse. Enlarged right ventricles are indicated in white arrows.

6.2.2 | Arrhythmia and ECG waveform changes in the heart following radiation treatment

In order to investigate the impact of radiation on the electrical conduction in the heart, electrocardiogram (ECG) data was acquired 22 weeks and 26 weeks after treatment with 13 Gy (heart) or 15 Gy (heart).

Interestingly, arrhythmias were seen in 16.7% of mice (1 out of 6) treated with 15 Gy heart RT and 33.3% of mice (2 out of 6) treated with 13 Gy thorax RT as identified by irregular heartbeats on ECG traces (**Figure 6.3a**). To further investigate the variability between heartbeats, the root mean square of successive differences (RMSSD) were calculated from an analysis of ECG traces. Results confirmed a trending increase in heartrate variability in mice treated with 15 Gy heart RT compared to the mock RT group ($p = 0.347$) (**Figure 6.3b**).

ECG waveforms can reveal information about which part in the propagation of the electrical signalling is failing in the heart and therefore which subsections of the heart are impacted. As such, ECG waveforms of the irradiated and non-irradiated mice were analysed for mean length (milliseconds) of P-waves, length of QRS complex, length of T-waves and height (millivolts) of ST section with a software. Results revealed a significant increase in QTc duration in mice treated with 15 Gy heart RT compared to the mock RT control ($p < 0.05$) (**Figure 6.4b**). Prolonged QTc indicates a delay in ventricular repolarisation and can suggest an increased risk of developing arrhythmias and a higher risk of sudden cardiac death. Additionally, P-waves trended towards an increase with increasing radiation doses (**Figure 6.4b**). A prolonged P wave signifies a conduction delay between the right and left atrium. Changes to QRS complexes, and ST heights were difficult to assess due to variability between the mice. Together,

changes in ECG waveforms indicate that the electrical conduction in both atrial and ventricular compartments is impacted by whole-heart RT. Importantly, conduction abnormalities after radiation treatment for cancer have been reported in clinical studies (with one study in non-Hodgkin's lymphoma patients reporting 74.5% of them having conduction abnormality or arrhythmia on resting ECG (Adams et al., 2004), however few preclinical studies have reported measurable changes to electrical conduction from RT, highlighting the importance of this finding. Of note, electrical equipment was not turned off while acquiring ECG traces at week 22 (but nearby electrical equipment was turned off during data collection at week 26) may have contributed to noise in the ECG data.

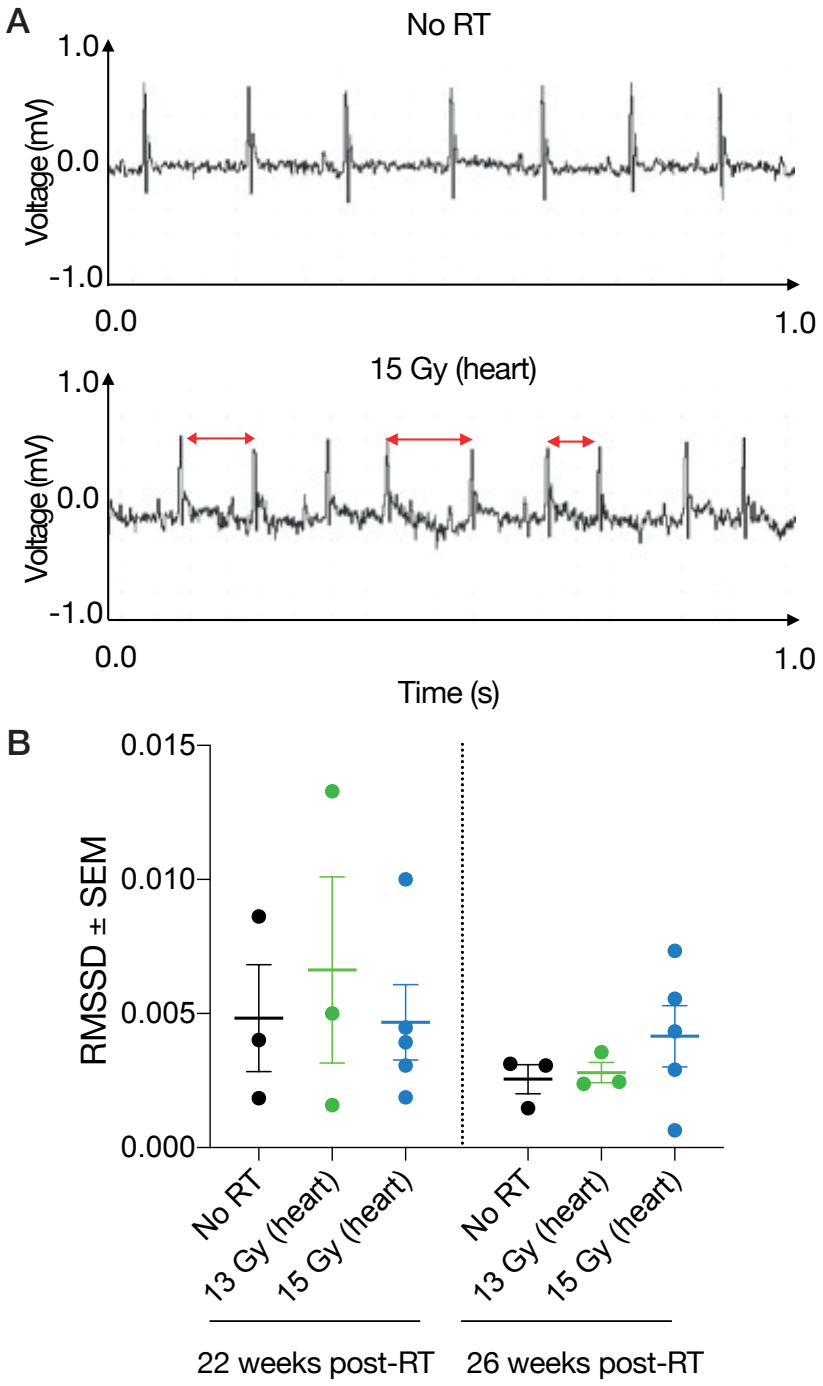


Figure 6.3. Cardiac RT is associated with an increase in heart rate variability. (A) Representative ECG traces were taken from mice 26 weeks after mock RT and 15 Gy (heart) RT. Irregular heartbeats are indicated in red arrows in the 15 Gy (heart) irradiated mouse whilst the ECG trace from the mock irradiated mouse shows a normal sinus rhythm. One of six mice in the 15 Gy cardiac irradiated and two of six mice in the 13 Gy thorax irradiated mice developed arrhythmia six months after RT. **(B)** Heart rate variability was measured by root mean square of successive RR interval differences (RMSSD) of mock, 13 Gy or 15 Gy heart irradiated mice. Each data point represents the mean RMSSD from an analysis of more than 100 successive heartbeats. Error bars indicate SEM. One-way ANOVA test was performed. *p<0.05, **p<0.01, ***p<0.001, ****p<0.0001

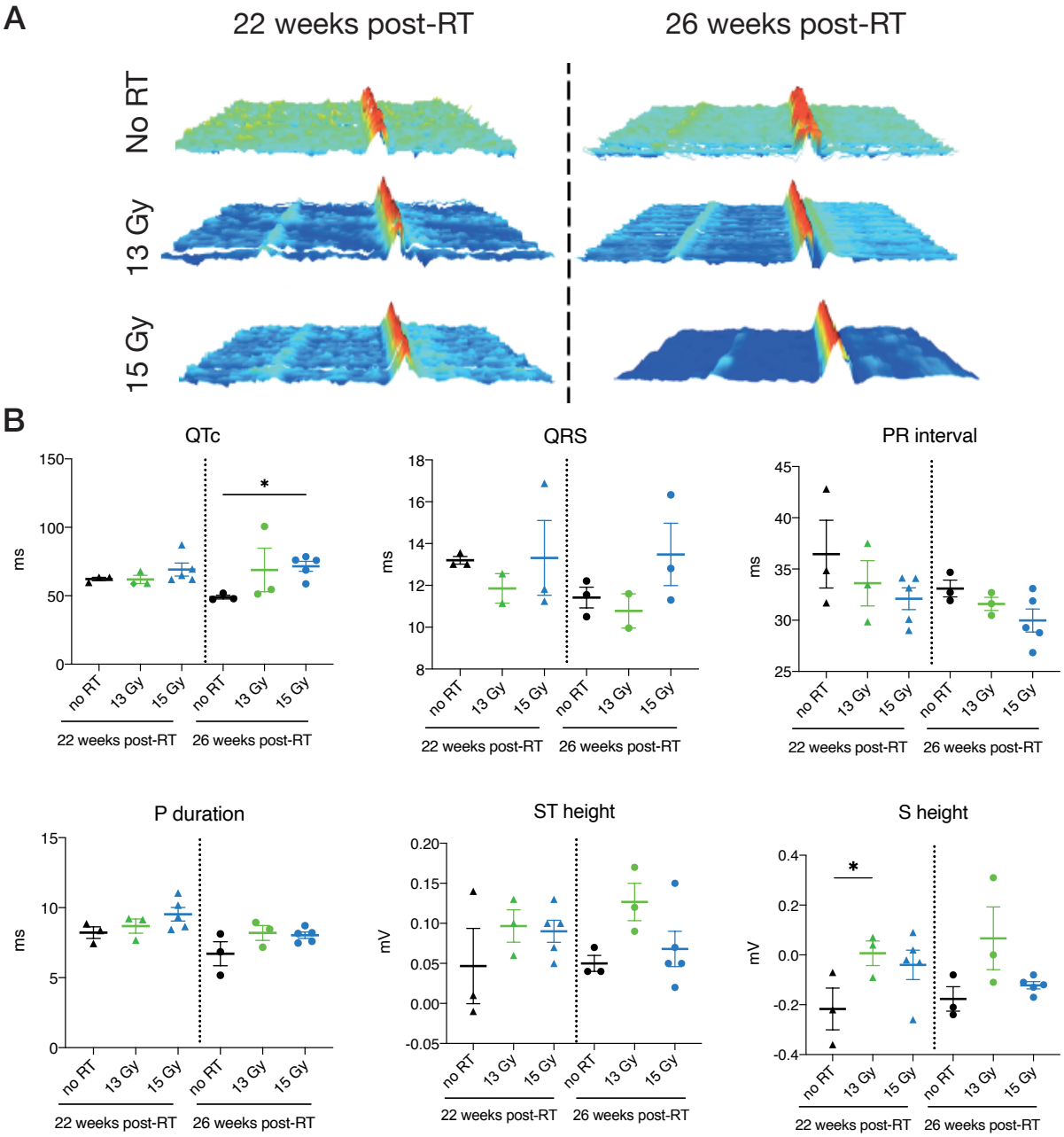


Figure 6.4. Cardiac RT Increases QTc and decreases PR interval. (A) Representative 3D surface plots of stacked ECG waveforms per treatment group. More than 100 stacked ECG waves were stacked in each 3D surface plot. **(B)** Mean QTc, QRS, PR and P-wave lengths and ST and S heights 22 weeks and 26 weeks after mock, 13 Gy or 15 Gy cardiac RT. Each data point is the mean value generated from a waveform analysis of more than 100 heartbeats on an ECG trace per mouse. Error bars indicate SEM. One-way ANOVA test. *p<0.05, **p<0.01, ***p<0.001, ****p<0.0001.

6.2.3 | Radiation induces fibrosis in the pericardium and perivasculature

The late cardiac effects in the heart following RT in the A/J mouse were further characterised for any signs of pathological changes. Hearts of the mice treated with 13 Gy or 15 Gy heart RT were assessed for collagen with Mason's Trichrome staining.

A thickening of collagen around pericardial and perivascular structures of the irradiated hearts were observed on Masson's Trichrome images (which were not observed in mock RT controls) (**Figure 6.5a**). The area of the thickened pericardium (defined as $\geq$ 5um collagen layer in the pericardium) was quantified, which confirmed that there was a significant increase in collagen thickening in mice treated with 13 Gy and 15 Gy heart RT compared to the mock RT control ($p < 0.0001$ in both comparisons) (**Figure 6.5b**). Furthermore, the impact of radiation on perivascular fibrosis were dose-dependent (13 Gy versus 15 Gy, $p < 0.05$) (**Figure 6.5a**). The area of perivascular collagen was quantified using a bespoke machine-learning algorithm on a digital pathology software. Analyses revealed a trending increase in perivascular collagen with increasing doses of radiation ($p = 0.107$) (**Figure 6.5c**).

The observations of cardiac fibrosis here align with findings in other preclinical models of RICT. Indeed, restrictive cardiomyopathy has been reported as the predominant type of radiation-induced myopathic abnormality as a result of fibrosis (Stewart et al., 1995). However, it is also interesting to note that studies have suggested fibrosis to have an impact on cardiac electrical conduction (Adams et al., 2004; Lipshultz & Sallan, 1993).

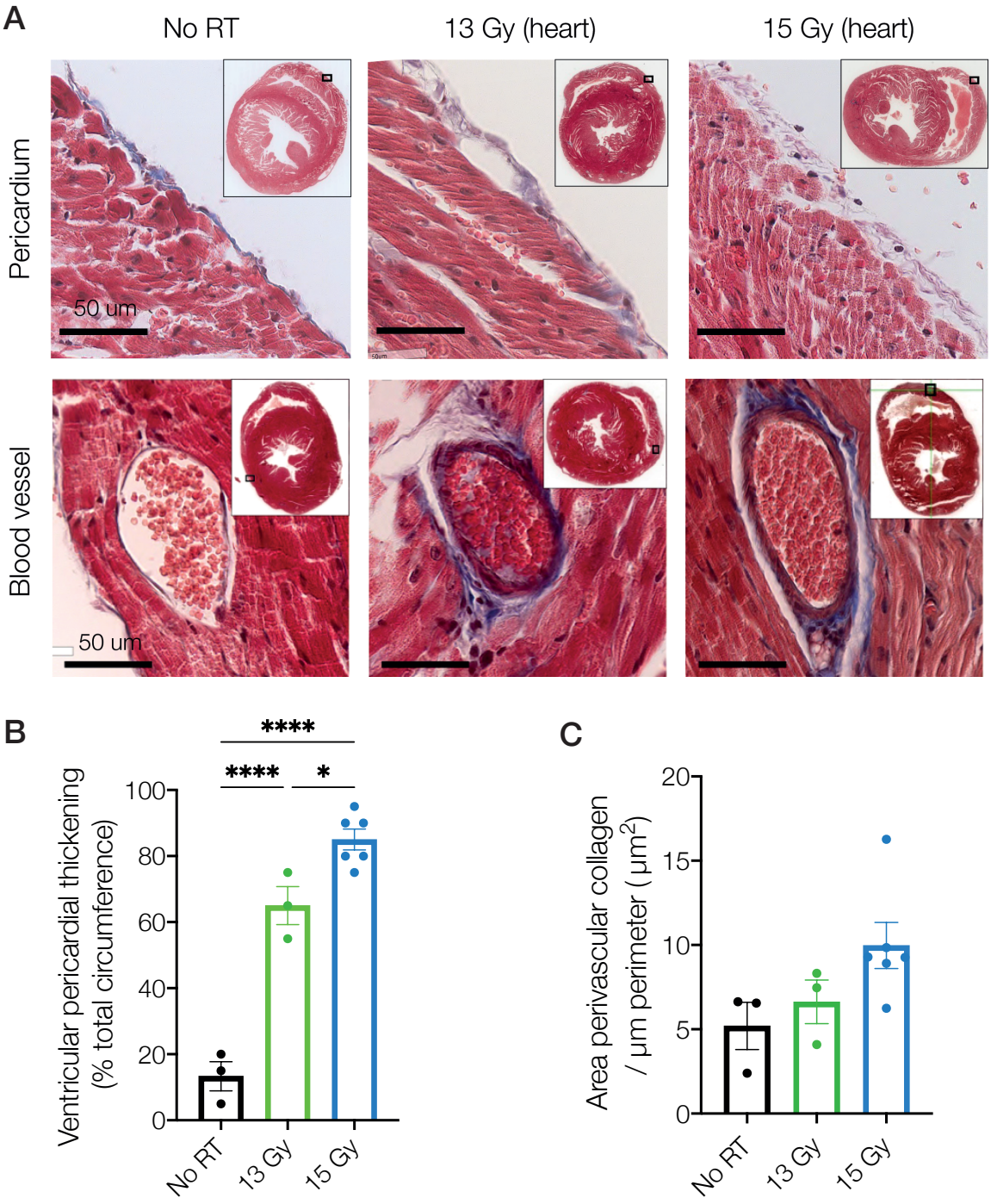


Figure 6.5. Cardiac irradiation above 13 Gy can induce pericardial and perivascular fibrosis 6 months after treatment in an A/J mouse model. (A) Masson's Trichrome stains of transverse cross-sections of mock, 13 Gy and 15 Gy irradiated hearts. Top: representative images of collagen in the pericardium of each treatment group. Bottom: representative images of collagen in the perivasculature of each treatment group. Scale bars: 50 μm. **(B)** Manual pathological quantification of percent area the thickened pericardium (collagen layer ≥ 5μm) occupies of the total ventricular pericardium. **(C)** Quantification of mean area of perivascular collagen per perimeter of the blood vessel using a bespoke machine-learning algorithm on HALO software. Error bars indicate SEM. One-way ANOVA test. *p<0.05, **p<0.01, ***p<0.001, ****p<0.0001.

For a further understanding of collagen organisation, second-harmonic imaging microscopy (SHIM) was performed on sectioned hearts. SHIM on mock and 13 Gy thorax RT hearts showed high intensities of photons in atrial structures in both mock RT and 13 Gy thorax RT groups (indicated in the white dotted circle in **Figure 6.6a**). This is expected, as atria largely consist of supportive structures including collagen. However, interestingly SHIM confirmed differences in photon intensity between mock and 13 Gy RT groups, notably at the pericardium, and potentially across the myocardial region (pericardium indicated in white arrows in **Figure 6.6a**). Furthermore, an analysis of individual collagen fibres was performed using the ct-FIRE software. Results did not reveal any significant differences in length and angles of the collagen fibres. However, showed a trend toward increasing disorganisation of collagen (reflected in reduced straightness and increased width) after RT (**Figure 6.6b**). This is supported by observations elsewhere (Kotova et al., 2018; Xu et al., 2019).

In the following sections in **Chapter 6**, pericardial fibrosis was used as a measurement for radiation-induced or drug-induced cardiac toxicity as it was a consistent and quantifiable phenotype. This approach is supported by our observation that this method of fibrosis quantification is sensitive to dose-dependent differences in the phenotype.

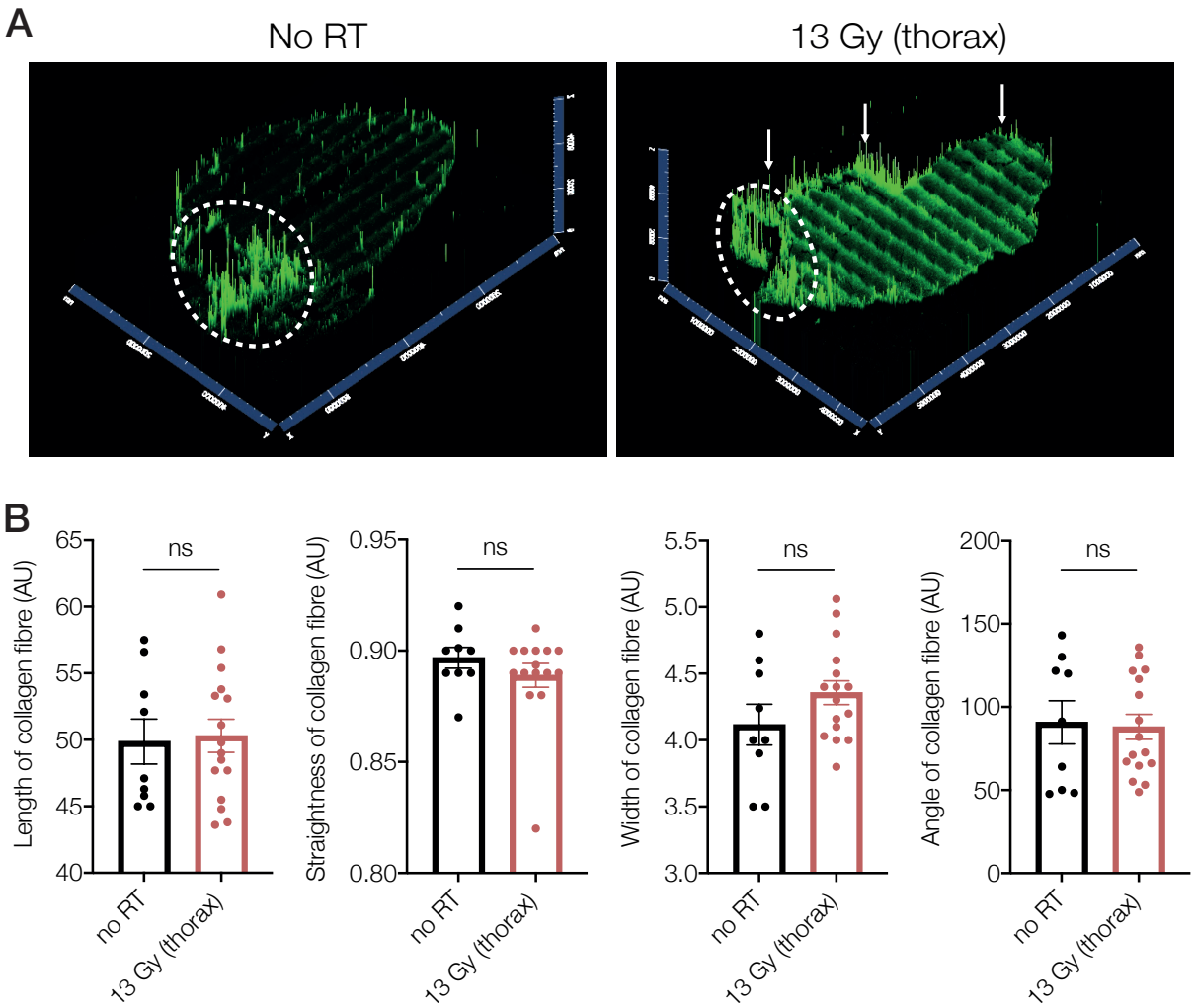


Figure 6.6. SHIM analysis of collagen fibres in the pericardium indicates that radiation does not induce a change in length, width or straightness of collagen fibres. (A) Representative images of longitudinal cross-sections of mock irradiated and 13 Gy irradiated hearts imaged by second-harmonic microscopic imaging (SHMI). Atria are indicated in dotted white circles, and pericardium is indicated in white arrows on the 13 Gy irradiated heart section. **(B)** Quantification of length, width, and straightness of collagen fibres of mock and RT treated heart sections. SHMI of three whole-heart sections were collected per group. Images were deconvoluted and three to five ROIs including the pericardium were selected per section and analysed using the ct-FIRE software. Each data point represents a value generated per ROI. Error bars indicate SEM. Student t-test. *p<0.05, **p<0.01, ***p<0.001, ****p<0.0001.

6.2.4 | Persistent DNA damage in cardiomyocytes is associated with cardiac fibrosis

To investigate the underlying mechanisms that could lead to late cardiac toxicities from radiation, cellular/ molecular and histological analyses were performed on heart tissues collected at 0 hours, 2 hours, 24 hours, and 7 days after 5 Gy thoracic RT.

IHC analysis for markers for DNA damage response (DDR) including γ-H2AX and p-p53 revealed that DDR in the cardiomyocytes lasted up to 7 days after irradiation (**Figure 6.7**). In detail, γ-H2AX foci positive nuclei increased significantly 2 hours after RT ($p < 0.0001$) and persisted at a similar level 7 days after exposure to 5 Gy RT (ns) (**Figure 6.7b**). Similarly, p-p53 positive nuclei also were also significantly higher 2 hours after RT ($p < 0.05$) and did not return to baseline levels 7 days after RT (ns) (**Figure 6.7b**).

The persistent DDR in cardiomyocytes, have not been reported in the literature. Interestingly, studies have shown that adult cardiomyocytes have a limited capacity to re-enter the cell cycle (Lafontant & Field, 2006; Soonpaa & Field, 1998), which may in part, explain the slow resolving of DNA damage/ prolonged activation of repair mechanisms we observe here. Another unique characteristic of cardiomyocytes that may be noteworthy for the interpretation of these results is their multi-nucleated nature. We do not yet know if mammalian cardiomyocytes have a mechanism of resolving DNA damage that is different from other uni-nucleated cells.

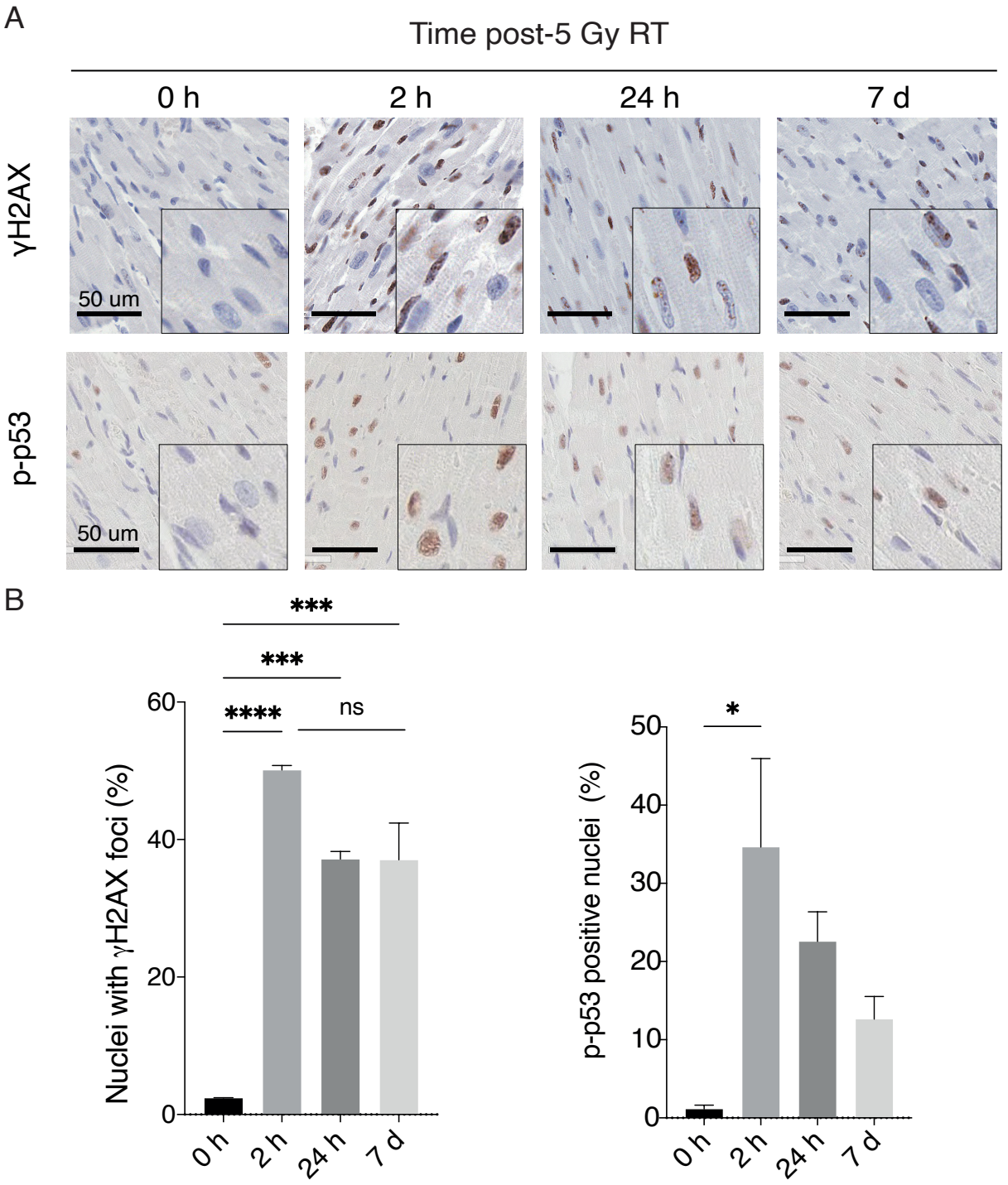


Figure 6.7. Persistent DNA-damage response in the heart. (A) Immunohistochemistry for γH2AX and phospho-p53 on hearts was collected at 0 hours, 2 hours, 24 hours and 7 days after 5 Gy radiation treatment (n = 3 per group). Scale bars: 50 μm. **(B)** Quantification of nuclei positive for γH2AX foci and cells positive for photo-p53 on IHC images. Each data point represents a mean value from an analysis of five ROIs per section (with a minimum of 50 nuclei per ROI). γH2AX foci positive nuclei were manually counted per field, and p-p53 positive nuclei were quantified using a nuclear detection algorithm on the Aperio ImageScope software. Error bars indicate SEM. One-way ANOVA. *p<0.05, **p<0.01, ***p<0.001, ****p<0.0001.

To evaluate the role of DNA damage repair pathways (non-homologous end joining (NHEJ) and homologous recombination (HR)) in cardiac toxicity, we treated A/J mice with a DNA-PK inhibitor (AZ64) and an ATR inhibitor (AZD6738) and examined the histopathology of the heart 5-6 months after the treatments (**Figure 6.8a**). The DNA-PK inhibitor and ATR inhibitor single treatments both increased fibrosis in the pericardium ($p < 0.0001$ for both comparisons) (**Figure 6.8b, c**). These results suggest that a burden on NHEJ or HR repair pathways may be crucial to the pathological cardiac toxicities seen from RT.

To understand the importance of interactions between a radiosensitiser/ inhibition of HR and RT in radiation-induced cardiac toxicity (RICT), RT was combined with an ATM inhibitor (AZ31) (**Figure 6.8c**). ATM inhibition alone caused an increase in cardiac fibrosis ($p < 0.001$). However, when combined with RT, treatment with ATM inhibition resulted in a marked increase in fibrosis ($p < 0.0001$) (**Figure 6.8d**). These results could have important implications when considering RT with other therapeutic agents that modulate DNA damage responses in the clinic, as this study indicates a potential increase in normal tissue toxicity using these combination approaches.

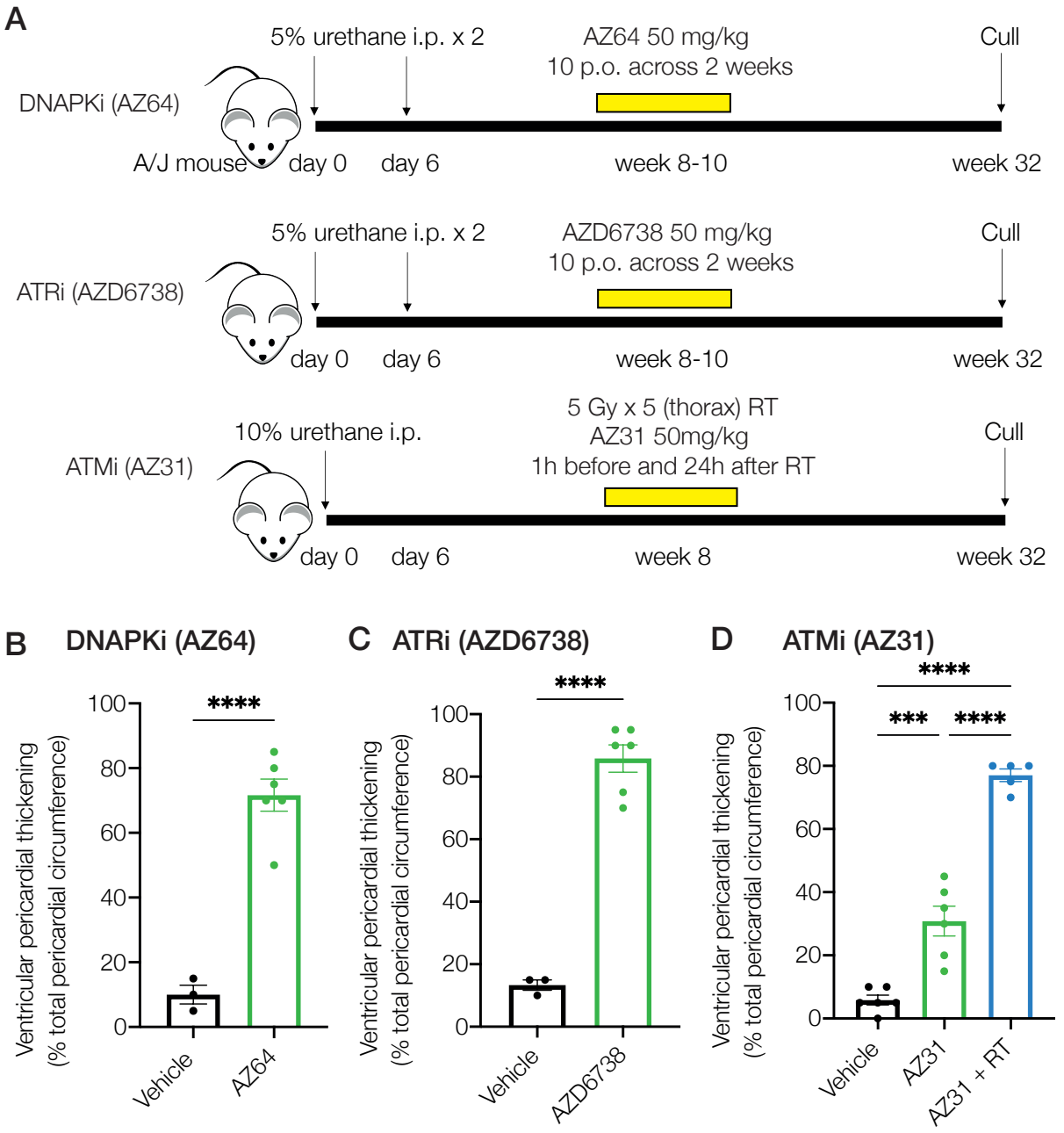


Figure 6.8. Treatment with DDR modulators increases pericardial fibrosis six months after treatment. (A) Schematic representation of the experimental schedule for AZ64 (DNAPKi), AZD6738 (ATRi) and AZ31 (ATMi) treatment of A/J mice. **(B, C, D)** Ventricular pericardial thickening quantified from Masson's Trichrome-stained hearts collected 24 weeks after AZD6738 (ATRi), AZ64 (DNAPKi) and AZ31 (ATMi) or their respective vehicle treatments. Error bars indicate SEM. Student's t-test. *p<0.05, **p<0.01, ***p<0.001, ****p<0.0001.

6.2.5 | Stimulation of IFN increases cardiac fibrosis

Persistent genotoxic stress and the accumulation of DNA damage can result in micronuclei formation (Fenech et al., 2011; Luzhna et al., 2013), which can subsequently lead to the activation of type I IFN and other innate immune pathways. We, therefore, hypothesised that the persistent DNA damage repair response could be leading to micronuclei formation downstream of innate immune pathways through pathways such as the STING pathway.

To investigate if IFN stimulation impacts cardiac fibrosis, we treated A/J mice with a single dose of STING agonist, DMXAA (Vadimezan), intraperitoneally (i.p.) with or without 13 Gy RT to the thorax. Mice were euthanised and assessed for cardiac fibrosis 26 weeks after treatment (**Figure 6.9a**). We demonstrated in **Chapters 3 and 4** that TNF-α and IFN-β levels increase in the peripheral blood 6 hours after a single dose of DMXAA i.p. (**Figure 5.1b**), while on the other hand, thoracic radiation alone does not stimulate a large TNF-α or IFN-β response in the peripheral blood (ns) (**Appendix 11**). DMXAA treatment alone increased cardiac fibrosis ($p < 0.05$), and when combined with RT showed an additive increase in cardiac fibrosis ($p < 0.0001$) (**Figure 6.9b, c**).

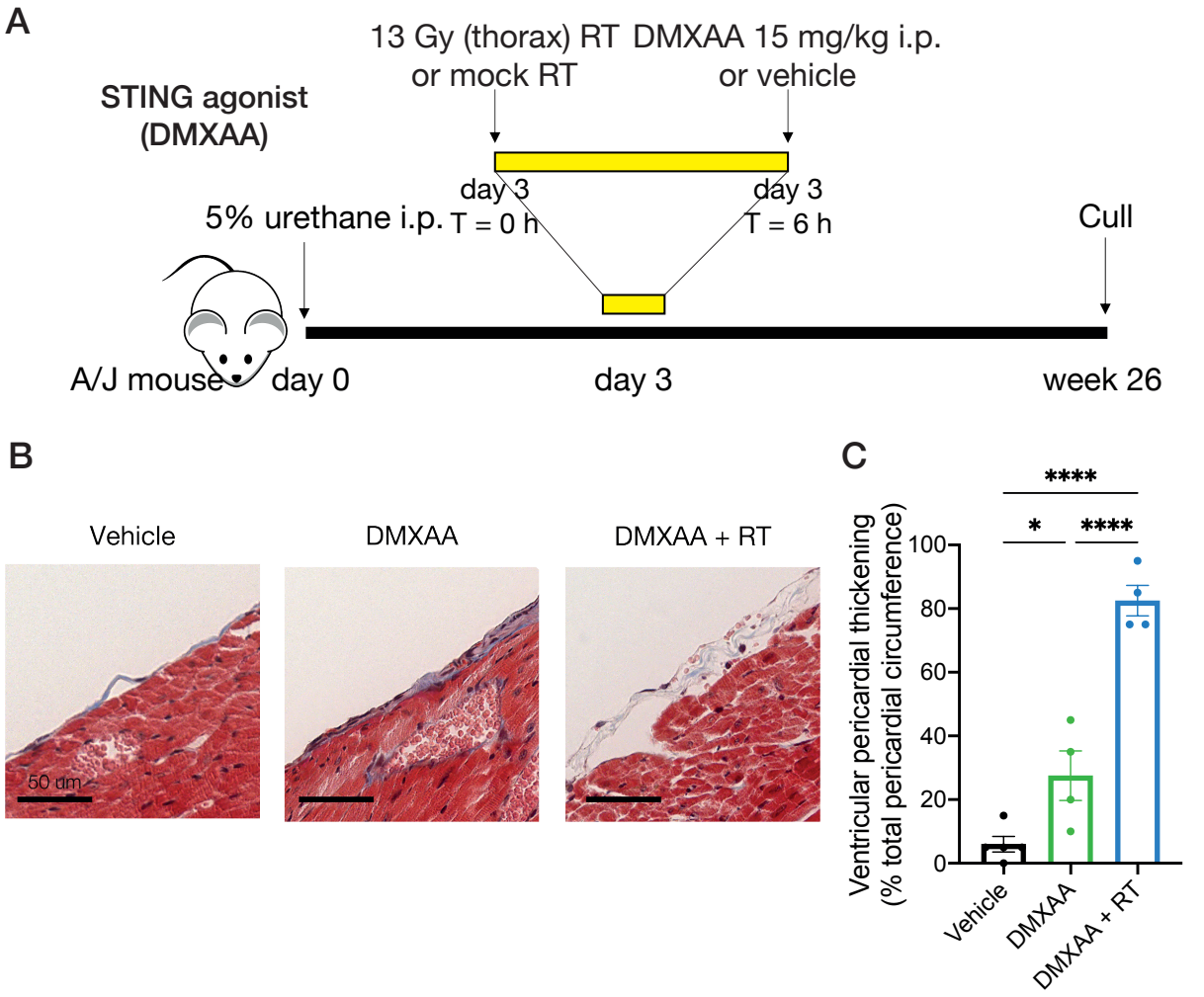


Figure 6.9. Stimulation of IFN increases perivascular fibrosis. (A) Schematic representation of the experimental schedule for DMXAA (STING agonist) and radiation treatment of A/J mice. **(B)** Ventricular pericardial thickening quantified from Masson's Trichrome-stained hearts collected 24 weeks after DMXAA +/- RT and vehicle/ mock RT treatments. Error bars indicate SEM. One-way ANOVA. *p<0.05, **p<0.01, ***p<0.001, ****p<0.0001.

6.2.6 | Macrophage infiltration and M2 macrophage polarisation in cardiac tissue after radiation treatment

To investigate the impact of RT on innate immunity in the heart, we carried out a flow cytometry experiment using single cells isolated from perfused ventricular cardiac tissue from A/J mice collected at 0 hours, 24 hours, and 7 days after 13 Gy thorax RT. We were particularly interested in understanding if M1/ M2 macrophage polarisation plays a role in RICT, as M2-like macrophages are known to be involved in wound healing and tissue repair mechanisms in several tissue types (Orecchioni et al., 2019), and therefore looked for CD45, F4/80, CD11b, CD206 and CD80 markers in our study (**Figure 6.10**).

Flow cytometry data showed that there was an overall decrease in $CD45^+$ lymphocytes 24 hours after irradiation and recovery of the $CD45^+$ population to baseline (0 hours) 7 days after RT ($p < 0.05$) (**Figure 6.11a**). The $F4/80^+$ $CD11b^+$ myeloid population makes up 46.4 ($\pm$ 6.2)% of the $CD45^+$ population at baseline and this population increases significantly 7 days after irradiation ($p < 0.05$) (**Figure 6.11b**). Furthermore, upon analysis of the $F4/80^+$ $CD11b^+$ myeloid population with CD206 mean fluorescence intensity (MFI) and CD80 MFI, revealed an increase in CD206 MFI between 24 hours and 7 days after RT ($p < 0.05$), and a trend toward a decrease in CD80 MFI between 24 hours and 7 days after RT (**Figure 6.11c).** These data suggest that there is a shift away from an M1-like phenotype (identified by CD80 surface marker) and toward an M2-like (identified by CD206 surface marker) phenotype in the macrophage populations in the irradiated heart.

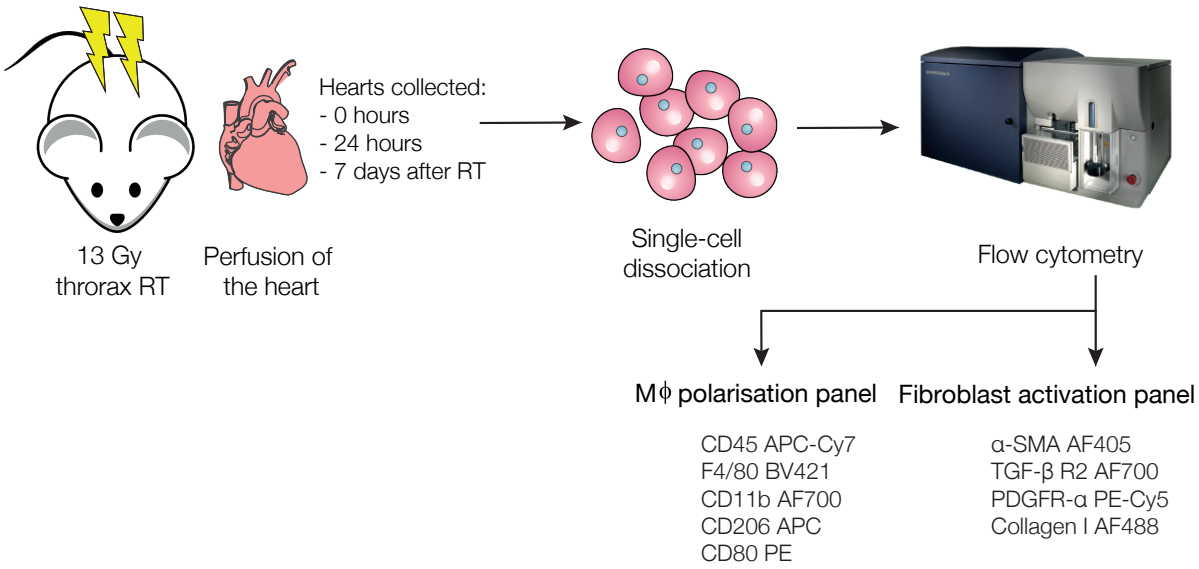


Figure 6.10. Analysis of immune cell infiltration and fibroblast activation with flow cytometry. Schematic representation of the experimental schedule of single-cell isolated cardiac cells from the A/J mice at 0 hours, 24 hours and 7 days after 13 Gy thoracic RT. A flow cytometry panel including CD45, F4/80, CD11b, CD206 and CD80 were used to assess the polarisation of macrophages, and a panel including alpha-SMA, TGF-beta, PDGFR-alpha and collagen I were used to assess cardiac fibroblast activation.

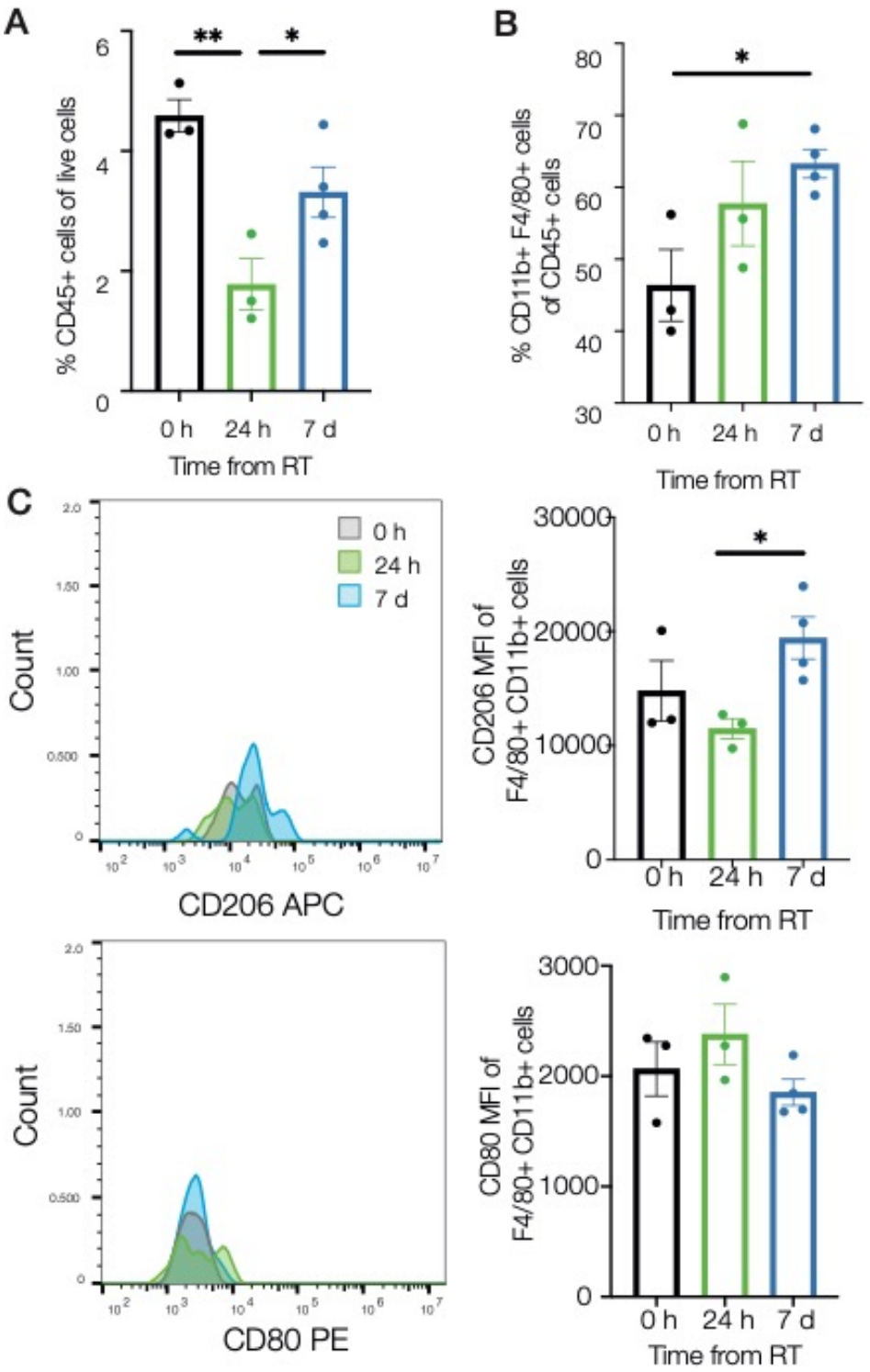


Figure 6.11. Macrophages infiltrate cardiac tissue post-RT and polarise toward an M2-like population. (A) Flow cytometry analysis of macrophage populations 0 hours, 24 hours, and 7 days after 13 Gy thoracic RT. Percent CD45$^+$ cells of live cells 0 hours, 24 hours and 7 days post-RT. **(B)** Percent CD11b$^+$ F4/80$^+$ macrophages of CD45$^+$ cells 0 hours, 24 hours and 7 days post-RT. **(C)** Mean fluorescence intensities (MFI) of CD80$^+$ M1-like and CD206+ M2-like macrophages. Top: histogram of CD206$^+$ M2-like populations in cardiac tissue 0 hours, 24 hours and 7 days after RT, and quantification of MFI. Bottom: histogram of CD80$^+$ M1-like populations in cardiac tissue 0 hours, 24 hours and 7 days after RT, and quantification of MFI. One-way ANOVA. *p<0.05, **p<0.01, ***p<0.001, ****p<0.0001.

6.2.7 | Fibroblast activation in radiation-induced cardiac fibrosis

Another known mechanism which is known to lead to large production of the extracellular matrix is the activation and proliferation of fibroblasts. To investigate if myocardial fibroblasts are activated early after RT, murine cardiac cells were isolated 0 hours, 24 hours, and 7 days after 13 Gy thorax RT (**Figure 6.10**). The panel of antibodies used for the flow cytometry experiment to assess fibroblast activation (α-SMA, collagen I, PDGFR-α and TGF-β II receptor) were selected based on literature review.

Results show a stable expression of in α-SMA, collagen I, PDGFR-α and TGF-β II receptor between 0 hours and 24 hours after RT, and trends toward a decrease in expression of the proteins between 24 hours and 7 days after RT (**Figure 6.12a**). However, IHC for collagens I and III show that there is an increase in both collagen I and III at the pericardium six months after 15 Gy RT (**Figure 6.12b**). This suggests that the activation of fibroblasts could happen late (after 7 days) or over a long period after RT.

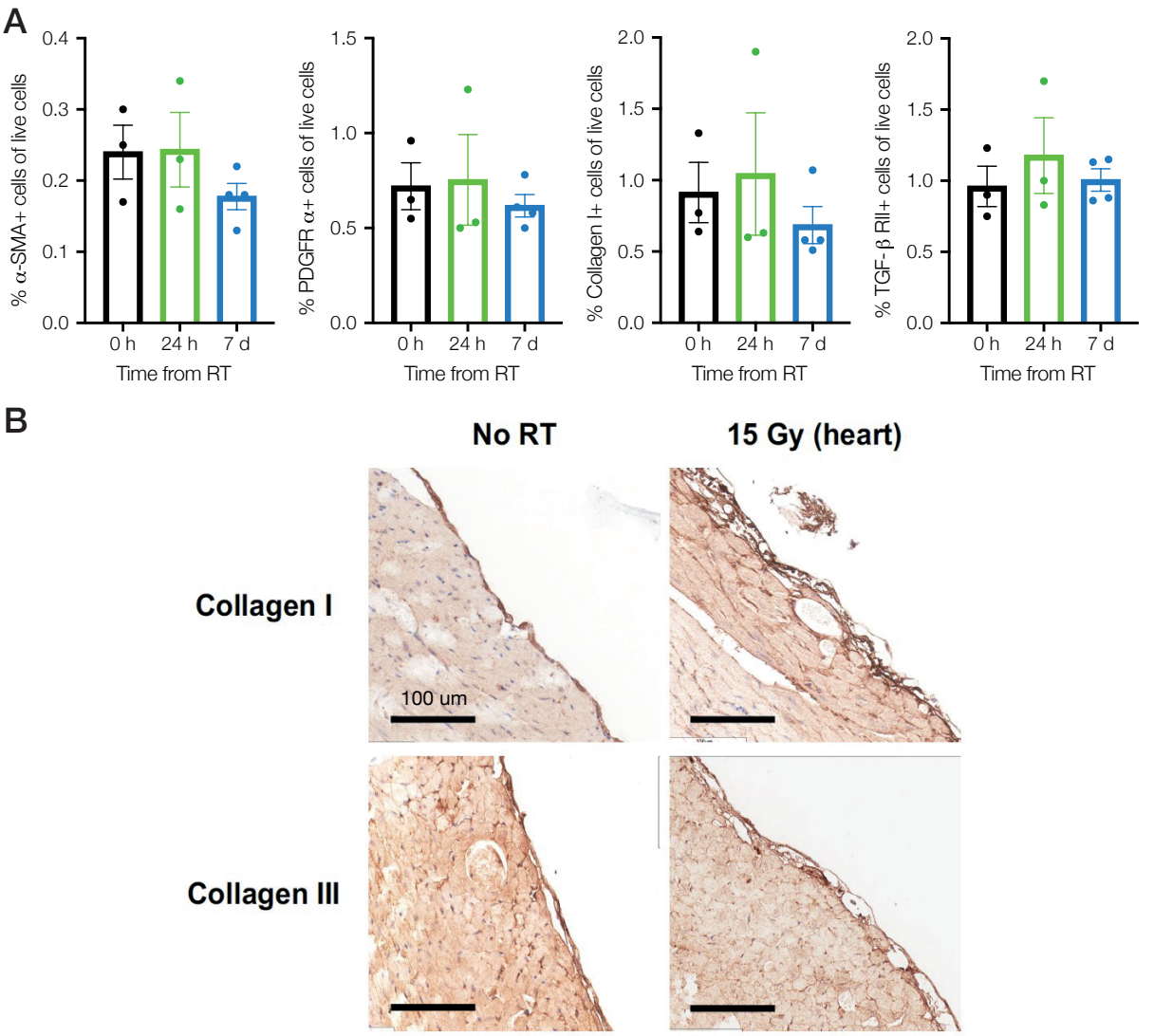


Figure 6.12. Cardiac fibroblasts are not activated 7 days after RT but potentially six months after RT. (A) Flow cytometry analysis of percent alpha-SMA, PDGFR-alpha, collagen I, and TGF-beta receptor II of live cardiac cells 0 hours, 24 hours and 7 days post-RT. One-way ANOVA. *p<0.05, **p<0.01, ***p<0.001, ****p<0.0001. **(B)** Representative images of immunohistochemistry of collagen I and collagen III of mock RT and 15 Gy RT heart sections were collected six months after RT. Scale bars: 100 μm.

6.2.8 | T-cell immunity is an unlikely contributor to cardiac fibrosis in the A/J model

To investigate if T-cell-mediated adaptive immunity contributes to cardiac tissue scarring and fibrosis, we took the approach of (i) investigating if there are changes to T-cell populations in irradiated cardiac tissue with IHC; and (ii) testing if anti-PD-L1 antibody treatment in A/J mice will affect cardiac fibrosis. In our first approach we stained sections of hearts collected 0 hours, 24 hours, 48 hours, 4 days, and 7 days after RT with a T-cell marker, CD3. IHC results showed that there was little to no change in the T-cell population myocardial, endocardial and pericardial tissue types (**Figure 6.13a**).

In our second approach, we treated A/J mice with a single dose of anti-PD-L1 antibody (10 mg/ kg, i.p.) and culled 32 weeks after treatment for assessment of cardiac fibrosis (**Figure 6.13b**). Quantification of cardiac fibrosis from Masson's Trichrome stains showed that the anti-PD-L1 treatment did not increase fibrosis six months after treatment (ns) (**Figure 6.13c**).

These results point toward the possibility that T-cell immunity plays a minimal to no role in late radiation-induced cardiac events.

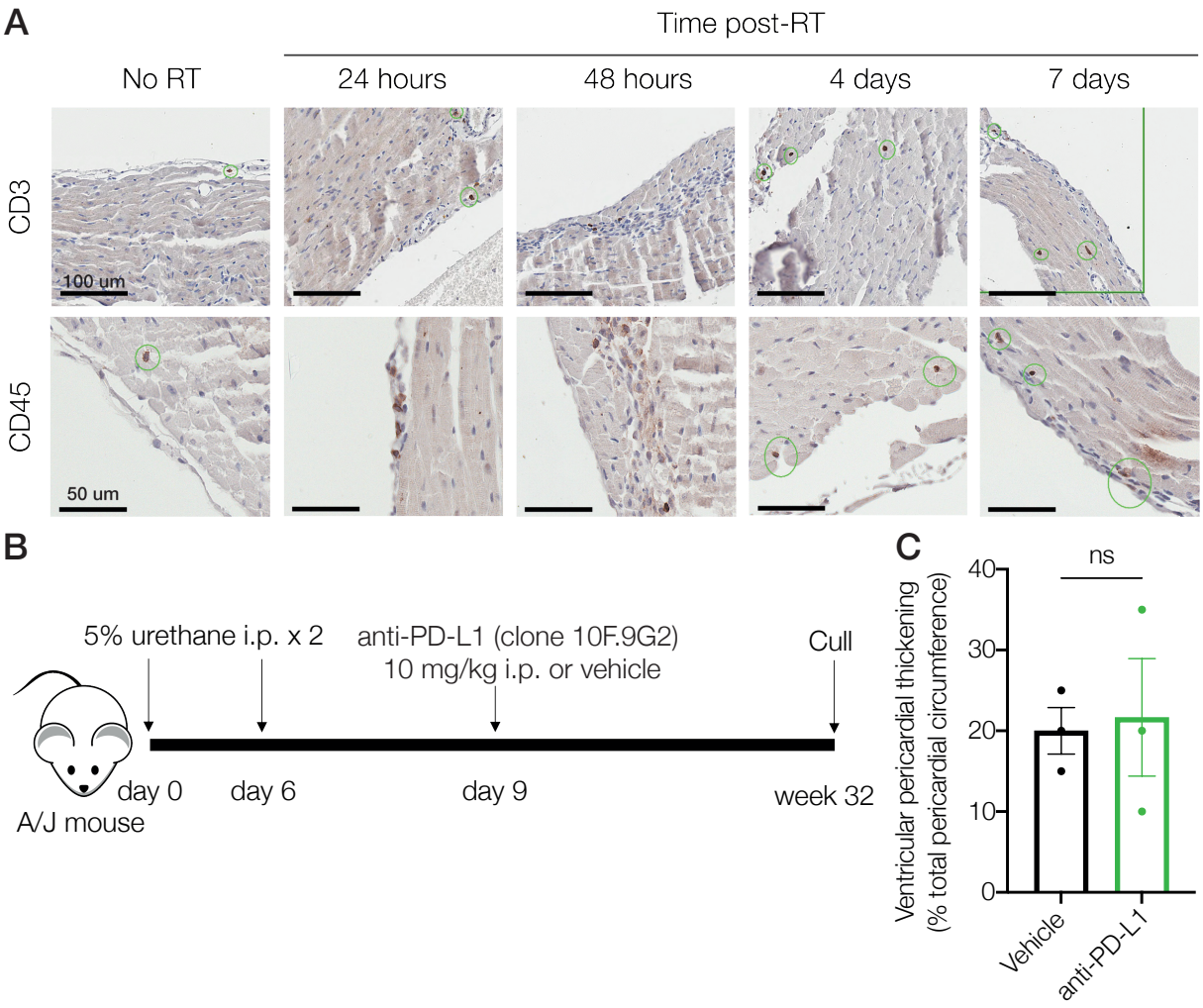


Figure 6.13. No change in CD3+ T-cell populations in cardiac tissue 7 days after RT and no change in cardiac fibrosis after anti-PD-L1 antibody treatment. (A) Immunohistochemistry of cardiac tissue for CD3 and CD45 24 hours, 48 hours, 4 days and 7 days following 13 Gy RT. **(B)** Schematic representation of the experimental schedule for 10F.9G2 (anti-PD-L1) treatment of A/J mice. **(C)** Quantification of Masson's Trichrome images of hearts collected 32 weeks after 10F.9G2 (anti-PD-L1) treatment. One-way ANOVA. *p<0.05, **p<0.01, ***p<0.001, ****p<0.0001.

6.3 | DISCUSSION

We have established the A/J mouse model as a viable and consistent model in which we can study the early molecular and cellular events and the late pathological and physiological events in the heart following RT with or without cancer therapeutic drugs. The late RICT were characterised as (i) fibrosis in the pericardium and perivasculature; (ii) electrophysiological abnormalities; (iii) dilated cardiomyopathy and heart weight increase; (iv) and clinical signs such as pleural effusion and sudden death. Cardiac fibrosis was quantified and used as a measurable output for cardiac toxicity in the A/J model.

We identified several key events occurring hours to days after RT that could be contributing to RICT in the A/J mice. These are: (i) persistent DNA-damage response as shown by sustained γ-H2AX foci and p-p53 expression beyond hours after RT; (ii) stimulation of IFN; and (iii) macrophage polarization toward an M2-like phenotype. On the other hand, we have found that T-cell-mediated adaptive immune responses may not play a role in late cardiac toxicity. We were unable to confirm if cardiac fibroblast activation occurred in our model or contributed to the late cardiac fibrosis; this area requires further investigation. These results taken together, begin to paint a picture of the mechanisms that contribute to RICT in the A/J mouse model.

We hypothesise that some of the immunological changes that we see happening (e.g., M2 macrophage or STING activation) could be contributing to the accumulation of collagen around damaged/ repairing tissue. However, we have not been able to prove a direct link between macrophage polarization and the increase in collagen structures. Separately, we have also observed that STING agonist treatment

led to an accumulation of collagen in the heart. It is yet to be confirmed, however, whether IFN stimulation is the mechanism that is leading to late radiation-induced cardiotoxicity. Interestingly, a recent study by Shamseddine et al. (2021, pre-print) shows that treatment with a STING antagonist suppresses IFN responses induced by DNA-damaging agents (including doxorubicin and RT) and reduces cardiotoxicity in cGAS and STING KO mouse models (Shamseddine et al., 2021). We are seeing persistent DDR in the myocardial cells, which we hypothesise could be leading to an accumulation of unresolved DNA damage/ genotoxic stress and micronuclei formation which could subsequently be activating the IFN pathways in our mouse model. This is an area that has potential for exploration in future studies. Additionally, the location in which fibrosis is most pronounced months after RT – pericardium and perivasculature – suggests the possibility that structures that are closer to blood vessels where immune cells can infiltrate are more vulnerable to fibrotic events than the myocardium that are further away from these structures, for instance.

Radiation-induced abnormalities in electrical conduction are currently an area of interest, and although epidemiological studies have suggested the correlation (Taunk et al., 2015; Wang et al., 2017; Yegya-Raman et al., 2018), has not been described in or studied extensively in mouse models in RICT studies. Our study, which looks to understand the direct impact of heart RT intervention on ECG outputs is important as it shows that RT is associated with increased variability in the heart beats and induces waveform changes, particularly in QTc and P-waves. Biologically, abnormalities in the electrical conduction system from RT can be interesting, especially as recent studies are beginning to unpack the roles that resident cardiac macrophages are playing in the propagation of electrical conduction in the heart (Hulsmans et al.,

2017). Additionally, studies have shown a correlation between cardiac fibrosis and arrhythmia (de Jong et al., 2011; Kazbanov et al., 2016), the two RICT phenotypes are related in the A/J model. Abnormalities in the electrical conduction (including higher frequencies of arrhythmias) are associated with increased risk of cardiac event-induced sudden deaths (Brouillette et al., 2019). Interestingly, the same individual in which sudden death was observed 17 weeks after 15 Gy RT, also had particularly irregular conduction as seen from ECG traces (greater heart rate variability and QTc/ P-wave changes).

Interestingly, the locations in the heat in which we observe late radiation-induced cardiac effects - the pericardium, perivasculature and electrical conduction – are all made up of layers that are made of connective tissues (which highly consist of collagenous structures). The pericardium is a fibrous double-layered structure, one of which is the epicardium – a mesothelium derivative which consists of adipocytes and neurovascular tissue. Tunica intima of blood vessels and the endocardium (thicker in areas including the atria and other tissues in the heart that contains nerves and Purkinje fibres) are also made of a network of connective tissue and a layer of elastic fibres. All these structures lined with collagen appear to be vulnerable to radiation-induced late effects. Valvular abnormalities have been described as a RICT in the clinic (Cutter et al., 2015), but have not been studied extensively in preclinical models. There is a possibility, that heart valves too, which are also largely comprised of collagen and other supportive structures, could be impacted by radiation in the A/J mouse and even lead to physiological phenotypes such as dilated cardiomyopathy.

In this chapter, a new robust and consistent pre-clinical model in which we can study RICT with cardiac fibrosis and electrophysiological data as measurable

outcomes (in addition to the characterised clinical outcomes such as dilated cardiomyopathy, pleural effusion, and sudden deaths) was established. Additionally, the association between persistent DDR and RICT and the involvement of the innate immune pathways (including activation of the STING pathway and M2 macrophage polarisation) in RICT has also been studied here. We have also arrived at some interesting hypotheses that could be explored in future studies.

CHAPTER 7. CONCLUSIONS AND DISCUSSION

Throughout this work, we have utilised the urethane-induced lung adenocarcinoma model in A/J mouse as an experimental system for the evaluation of anti-tumour and normal tissue toxicities of cancer therapies. Furthermore, we have studied the important mechanisms underlying lung carcinogenesis by perturbation of biological processes in the preneoplastic lung with radiation and a STING agonist. Finally, we have studied the late-radiation-induced toxic events in normal tissues in the heart and lung.

This is the first known study to identify the induction of TLSs by radiation. Furthermore, we have found a correlation between radiation-induced TLS with a cancer preventative effect. Investigation of the early events following carcinogen treatment revealed that the carcinogen treatment initiated lasting immune events in the preneoplastic lung, suggesting chronic inflammatory activity. Upon treatment with radiation during this preneoplastic state, sequestering of cell division and cell cycle events including E2F targets and G2/M checkpoints, and upregulation of immune events including IFN-α and IFN-γ signalling were observed. We further confirmed the immune events upregulated with RT to consist of adaptive immune responses, with a notable increase in T-cells in the lung. Further investigation by perturbation of the preneoplastic state with a STING agonist (DMXAA) resulted in a long-term increase in immune cells in the lung (however lacking aggregate structures that resembled TLSs) and no evidence of tumour prevention. However, in the setting of RT and DMXAA combination treatment, a synergistic effect was observed (though not reaching statistical significance), whereby higher frequencies in TLSs and more pronounced tumour preventative effects compared to single treatment were seen. We, therefore,

present a suggested mechanism of carcinogen-induced lung tumourigenesis in this mouse model illustrated in **Figure 7.1**.

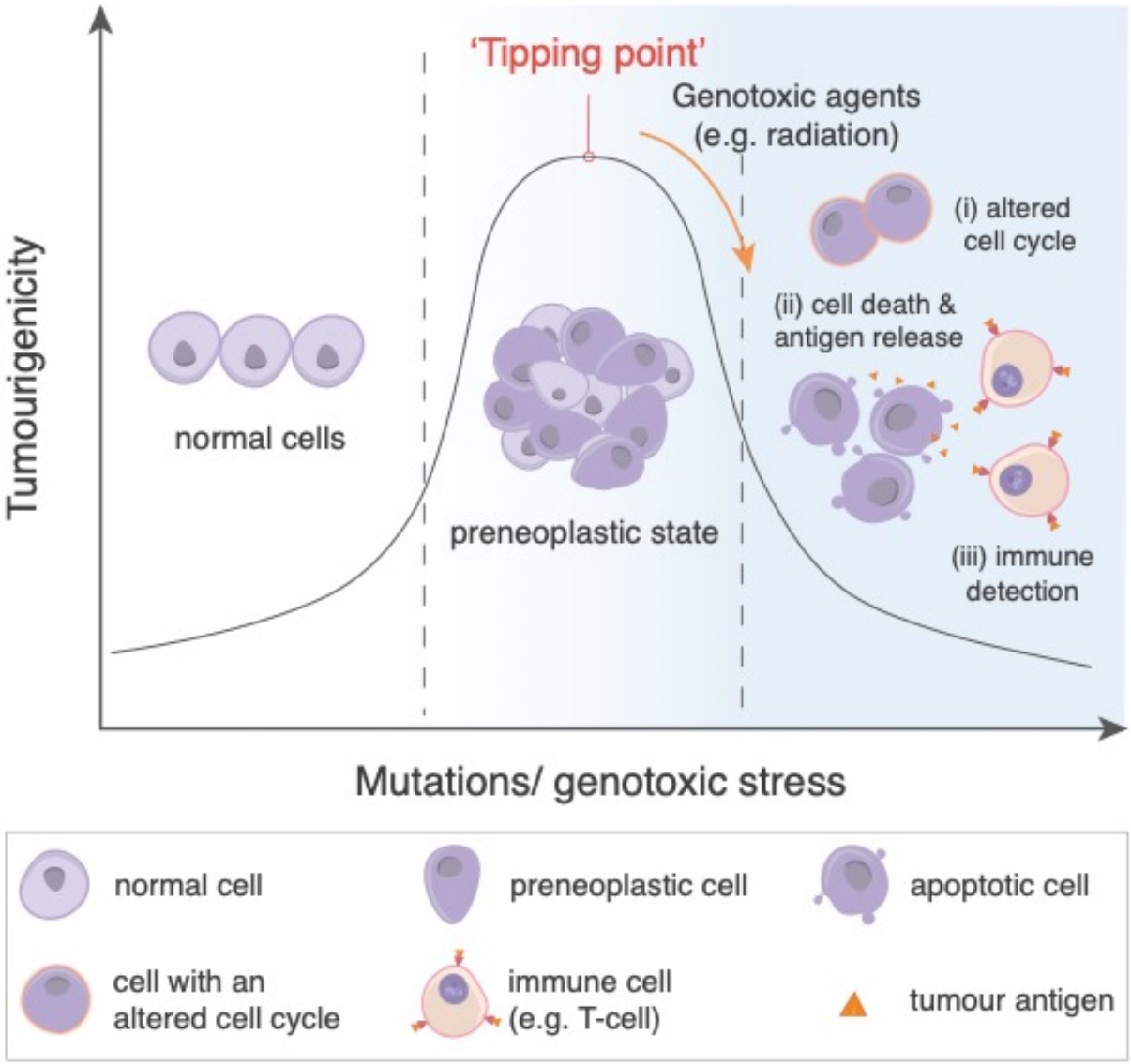


Figure 7.1. The 'vulnerable state' of preneoplastic pulmonary cells. Summary schematic of the suggested biological mechanisms related to the tumorigenicity of cells undergoing mutations and genotoxic stress. We suggest that there is a critical 'tipping point' (i.e. a threshold) at which the accumulation of mutations leads to the elimination of or curb in cell growth through the activation of cell senescence/ cell death or increase in detectability by immune cells.

Previously, induction of TLS in cancer therapeutic settings has largely been reported in patients administered with cancer vaccines (Lutz et al., 2014; Maldonado et al., 2014). Given our findings, the observation that cancer vaccines may induce the formation of TLS in the target organ is noteworthy for two reasons: (i) it could imply similarities between vaccine induction and radiation treatment in the mechanisms underlying TLS formation; and (ii) the stage in cancer development at which vaccine or radiation interventions resulted in TLSs was in the early stages of tumourigenesis or pre-tumour formation when the subjects have a functioning immune system that has not undergone the processes of cancer immunoediting. We hypothesise that radiation may generate an immune response through increased (neo)antigen release. This hypothesis was based on evidence from past studies that have reported that radiation can induce neoantigen presentation and that carcinogen-induced cancers such as lung adenocarcinoma in smoker patients can have a high mutation burden and a tendency to present more tumour antigens. If radiation and cancer vaccines share similarities in their biological mechanisms such as the presentation of tumour-specific peptides, this can have wider implications for cancer intervention strategies in the future.

To our knowledge, our work in radiation-induced cardiotoxic events in the A/J mouse is the first preclinical study that describes a number of phenotypes indicating cardiotoxicity from radiation, including fibrosis (in the pericardium and perivasculature), abnormalities in the electrical conduction and possible ventricular dilation. Additionally, no other studies have reported persistent DDR responses in cardiomyocytes as a potential mechanism that may initiate late toxic effects in the heart. Further investigation of the immune mechanisms stimulated by radiation revealed a

polarisation of macrophages toward an M2-like phenotype in cardiac tissue. We hypothesised that a lasting DDR could give rise to a chronic inflammatory state in the heart, leading to subsequent late cardiac-induced events. Furthermore, we noted that the fibrotic events were occurring more frequently in structures with high collagenous content (e.g. pericardium, perivasculature, and potentially the conduction system). We summarise the proposed mechanisms for radiation-induced cardiac toxicity illustrated in **Figure 7.2**.

Interestingly, findings from other studies support the suggested link between persistent DDR, chronic inflammation and subsequent cardiotoxic events. A study by Shamseddine and colleagues identified cytosolic cGAS+ foci in irradiated hearts and demonstrated that STING antagonism suppressed IFN responses by DNA-damaging agents (Shamseddine et al., 2021). Additionally, Oka and colleagues established that the presence of mitochondrial DNA in cardiac tissue can lead to the activation of Toll-like receptor 9 (TLR9)-mediated inflammatory responses, and associated these events with myocarditis and dilated cardiomyopathy (Oka et al., 2012). Investigating the significance of the persistent DDR in myocardial cells and if these play a role in chronic inflammation for lasting cardiac damage is important as it can provide insights into the potential risks of cancer therapies and ways in which to avoid or minimise cardiac toxicities in patients.

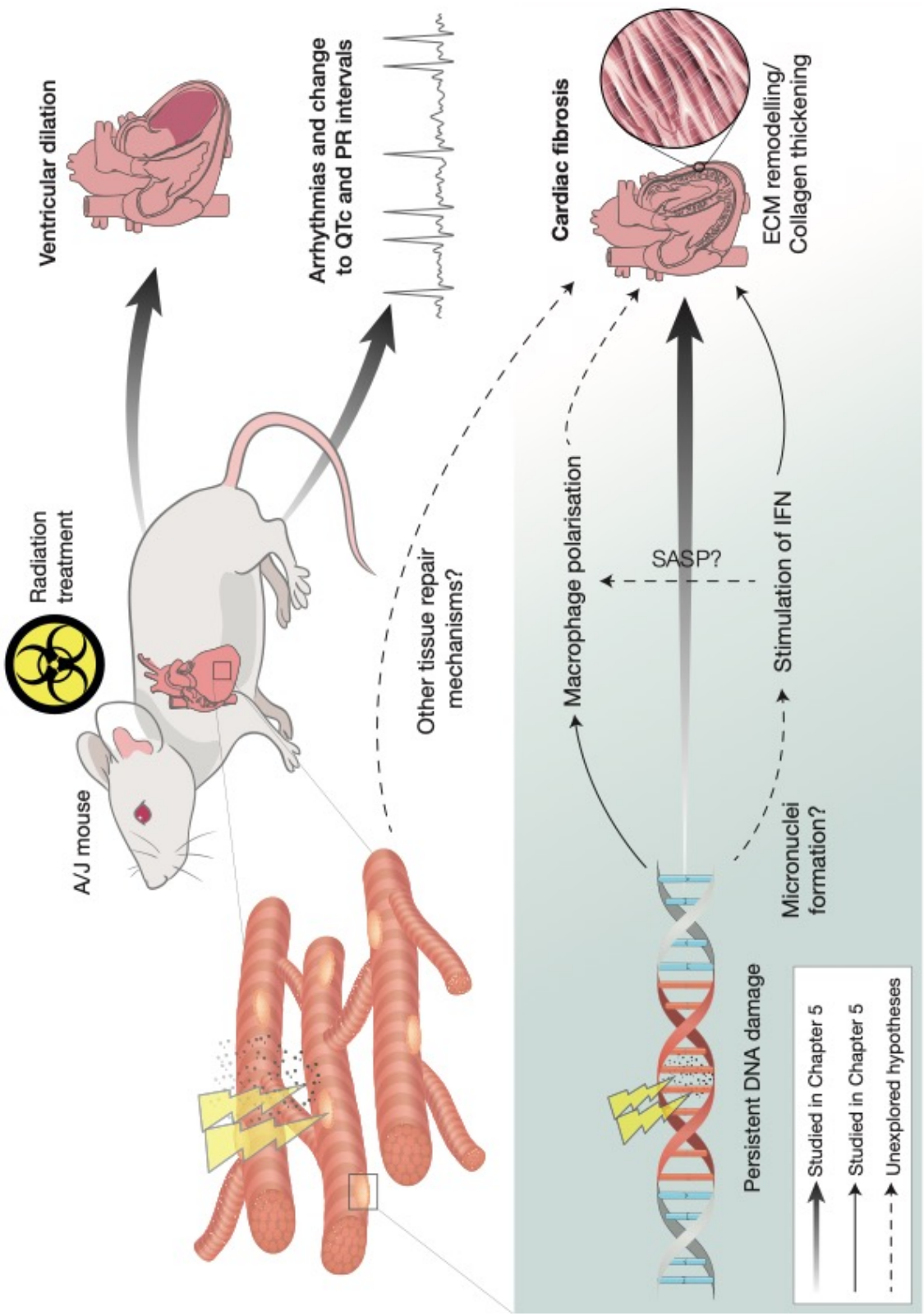


Figure 7.2. Radiation-induced cardiac toxicity in the A/J mouse model. Summary schematic of radiation-induced cardiac toxicity. Increased cardiac fibrosis, changes to electrical conduction and possible ventricular dilation were observed months after cardiac irradiation. Persistent DNA damage in myocardial cells and macrophage polarisation were observed hours to days after irradiation. In addition, a stimulation of IFN leads to increased cardiac fibrosis.

Taken together, future work should prioritise the investigation of (neo)antigen presentation following RT of preneoplastic lesions in the A/J mouse with TCR-sequencing for the understanding of the important radiation-induced immunological events in tumour prevention and TLS induction. Furthermore, identifying key peptides generated from irradiation during early cancer development may provide insight for future vaccines for cancers that do not yet have known antigens. In addition to TCR-sequencing, a study on TLSs in tumour biopsies from lung cancer patients taken prior to treatment and after radiation treatment will allow further understanding of radiation-induced TLSs.

For the investigation of radiation-induced cardiac events, future work in this area would benefit from a more granular understanding of radiation-induced events occurring in different cell types that make up the heart (particularly cardiomyocytes, immune cells and fibroblasts and collagen structures). Specifically, single-cell sequencing of cardiac tissues following radiation would allow for a greater understanding of cells that are more vulnerable to radiation. Additionally, spatial transcriptomic methods may provide an understanding of the dynamic interactions of cells in the heart following exposure to DNA-damaging agents such as radiation.

Experiments in this work were limited by the lack of available GEMM models (specifically KO models for specific genes) in the A/J background. In the tumourigenesis study, the use of a STING KO model could have contributed greatly to our understanding of STING in tumourigenesis in **Chapter 5**. For the cardiac study, a KO model for DNA repair pathways such as ATM could have provided additional insight into the importance of persistent DDR in late cardiotoxic effects. Additionally, in the tumourigenesis study, we were limited in our ability to identify normal cells that were

not impacted by carcinogen exposure and those that were undergoing neoplastic cell transformation. There is currently a lack of available methods that allow for the labelling and tracking of cells that undergo high levels of mutagenic events, genotoxic stress or chromosomal instability from chemical carcinogen treatment.

In summary, our data introduce the carcinogen-induced lung adenocarcinoma A/J mouse as a novel model for the co-evaluation of tumour and normal tissues following treatment with cancer therapies including radiation. We have also suggested a potential vulnerable state in the preneoplastic cells that have undergone carcinogen treatment and that this vulnerability may lie in altered cell division processes or immune responses that are affected by irradiation. Results from STING agonist treatment indicate that STING activation at tumour initiation might apply a selection pressure, potentially resulting in the survival and growth of immune-resilient clones. Furthermore, a study of radiation-induced toxic events in the heart revealed persistent DDR from radiation as a potential initiating event for late pathological and electrophysiological abnormalities. These findings may have important implications for strategies for the treatment of lung cancers, both in early cancer interventions and for avoiding normal tissue toxicities, and further suggest the different aspects of radiation-induced immunological responses that can play key roles in different tissue settings.

BIBLIOGRAPHY

Chapter 1 General Introduction

Agostinetto, E., Eiger, D., Lambertini, M., Ceppi, M., Bruzzone, M., Ponde, N., Plummer, C., Awada, A. H., Santoro, A., Piccart-Gebhart, M., & de Azambuja, E. (2021). Cardiotoxicity of immune checkpoint inhibitors: A systematic review and meta-analysis of randomised clinical trials. *Eur J Cancer*, *148*, 76-91. https://doi.org/10.1016/j.ejca.2021.01.043

American Cancer Society. Cancer Facts and Figures 2015. http://www.cancer.org/acs/groups/content/@editorial/documents/document/acspc-044552.pdf

Anagnostou, V., Smith, K. N., Forde, P. M., Niknafs, N., Bhattacharya, R., White, J., Zhang, T., Adleff, V., Phallen, J., Wali, N., Hruban, C., Guthrie, V. B., Rodgers, K., Naidoo, J., Kang, H., Sharfman, W., Georgiades, C., Verde, F., Illei, P., . . . Velculescu, V. E. (2017). Evolution of Neoantigen Landscape during Immune Checkpoint Blockade in Non-Small Cell Lung Cancer. *Cancer Discov*, *7*(3), 264-276. https://doi.org/10.1158/2159-8290.Cd-16-0828

Antonia, S. J., Villegas, A., Daniel, D., Vicente, D., Murakami, S., Hui, R., Kurata, T., Chiappori, A., Lee, K. H., De Wit, M., Cho, B. C., Bourhaba, M., Quantin, X., Tokito, T., Mekhail, T., Planchard, D., Kim, Y.-C., Karapetis, C. S., Hiret, S., . . . Özgüroğlu, M. (2018). Overall Survival with Durvalumab after Chemoradiotherapy in Stage III NSCLC. *New England Journal of Medicine*, *379*(24), 2342-2350. https://doi.org/10.1056/nejmoa1809697

Antonia, S. J., Villegas, A., Daniel, D., Vicente, D., Murakami, S., Hui, R., Yokoi, T., Chiappori, A., Lee, K. H., De Wit, M., Cho, B. C., Bourhaba, M., Quantin, X., Tokito, T., Mekhail, T., Planchard, D., Kim, Y.-C., Karapetis, C. S., Hiret, S., . . . Özgüroğlu, M. (2017). Durvalumab after Chemoradiotherapy in Stage III Non–Small-Cell Lung Cancer. *New England Journal of Medicine*, *377*(20), 1919-1929. https://doi.org/10.1056/nejmoa1709937

Asrir, A., Tardiveau, C., Coudert, J., Laffont, R., Blanchard, L., Bellard, E., Veerman, K., Bettini, S., Lafouresse, F., Vina, E., Tarroux, D., Roy, S., Girault, I., Molinaro, I., Martins, F., Scoazec, J.-Y., Ortega, N., Robert, C., & Girard, J.-P. (2022). Tumor-associated high endothelial venules mediate lymphocyte entry into

tumors and predict response to PD-1 plus CTLA-4 combination immunotherapy. *Cancer Cell*, *40*(3), 318-334.e319. https://doi.org/10.1016/j.ccell.2022.01.002

Bailey, C., Black, J. R. M., Reading, J. L., Litchfield, K., Turajlic, S., McGranahan, N., Jamal-Hanjani, M., & Swanton, C. (2021). Tracking Cancer Evolution through the Disease Course. *Cancer Discovery*, *11*(4), 916-932. https://doi.org/10.1158/2159-8290.cd-20-1559

Barker, H. E., Paget, J. T. E., Khan, A. A., & Harrington, K. J. (2015). The tumour microenvironment after radiotherapy: mechanisms of resistance and recurrence. *Nature Reviews Cancer*, *15*(7), 409-425. https://doi.org/10.1038/nrc3958

Bates, G. J., Fox, S. B., Han, C., Leek, R. D., Garcia, J. F., Harris, A. L., & Banham, A. H. (2006). Quantification of regulatory T cells enables the identification of high-risk breast cancer patients and those at risk of late relapse. *J Clin Oncol*, *24*(34), 5373-5380. https://doi.org/10.1200/jco.2006.05.9584

Berraondo, P., Teijeira, A., & Melero, I. (2016). Cancer Immunosurveillance Caught in the Act. *Immunity*, *44*(3), 525-526. https://doi.org/10.1016/j.immuni.2016.03.004

Boero, I. J., Paravati, A. J., Triplett, D. P., Hwang, L., Matsuno, R. K., Gillespie, E. F., Yashar, C. M., Moiseenko, V., Einck, J. P., Mell, L. K., Parikh, S. A., & Murphy, J. D. (2016). Modern Radiation Therapy and Cardiac Outcomes in Breast Cancer. *Int J Radiat Oncol Biol Phys*, *94*(4), 700-708. https://doi.org/10.1016/j.ijrobp.2015.12.018

Burnet, F. M. (1970). The concept of immunological surveillance. *Prog Exp Tumor Res*, *13*, 1-27. https://doi.org/10.1159/000386035

Centers for Disease, C., Prevention, National Center for Chronic Disease, P., Health, P., Office on, S., & Health. (2010). Publications and Reports of the Surgeon General. In *How Tobacco Smoke Causes Disease: The Biology and Behavioral Basis for Smoking-Attributable Disease: A Report of the Surgeon General*. Centers for Disease Control and Prevention (US).

Chabanon, R. M., Rouanne, M., Lord, C. J., Soria, J.-C., Pasero, P., & Postel-Vinay, S. (2021). Targeting the DNA damage response in immuno-oncology: developments and opportunities. *Nature Reviews Cancer*, *21*(11), 701-717. https://doi.org/10.1038/s41568-021-00386-6

Clarke, M., Collins, R., Darby, S., Davies, C., Elphinstone, P., Evans, V., Godwin, J., Gray, R., Hicks, C., James, S., MacKinnon, E., McGale, P., McHugh, T., Peto, R., Taylor, C., Wang, Y., & Early Breast Cancer Trialists' Collaborative, G. (2005). Effects of radiotherapy and of differences in the extent of surgery for early breast cancer on local recurrence and 15-year survival: an overview of the randomised trials. *Lancet*, *366*(9503), 2087-2106. https://doi.org/10.1016/S0140-6736(05)67887-7

Clemente, C. G., Mihm, M. C., Jr., Bufalino, R., Zurrida, S., Collini, P., & Cascinelli, N. (1996). Prognostic value of tumor infiltrating lymphocytes in the vertical growth phase of primary cutaneous melanoma. *Cancer*, *77*(7), 1303-1310. https://doi.org/10.1002/(sici)1097-0142(19960401)77:7<1303::Aid-cncr12>3.0.Co;2-5

Comprehensive molecular profiling of lung adenocarcinoma. (2014). *Nature*, *511*(7511), 543-550. https://doi.org/10.1038/nature13385

Coté, M. L., Liu, M., Bonassi, S., Neri, M., Schwartz, A. G., Christiani, D. C., Spitz, M. R., Muscat, J. E., Rennert, G., Aben, K. K., Andrew, A. S., Bencko, V., Bickeböller, H., Boffetta, P., Brennan, P., Brenner, H., Duell, E. J., Fabianova, E., Field, J. K., . . . Hung, R. J. (2012). Increased risk of lung cancer in individuals with a family history of the disease: A pooled analysis from the International Lung Cancer Consortium. *European Journal of Cancer*, *48*(13), 1957-1968. https://doi.org/10.1016/j.ejca.2012.01.038

Cutter, D. J., Schaapveld, M., Darby, S. C., Hauptmann, M., van Nimwegen, F. A., Krol, A. D., Janus, C. P., van Leeuwen, F. E., & Aleman, B. M. (2015). Risk of valvular heart disease after treatment for Hodgkin lymphoma. *J Natl Cancer Inst*, *107*(4). https://doi.org/10.1093/jnci/djv008

Darby, S., Hill, D., Auvinen, A., Barros-Dios, J. M., Baysson, H., Bochicchio, F., Deo, H., Falk, R., Forastiere, F., Hakama, M., Heid, I., Kreienbrock, L., Kreuzer, M., Lagarde, F., Mäkeläinen, I., Muirhead, C., Oberaigner, W., Pershagen, G., Ruano-Ravina, A., . . . Doll, R. (2005). Radon in homes and risk of lung cancer: collaborative analysis of individual data from 13 European case-control studies. *BMJ*, *330*(7485), 223. https://doi.org/10.1136/bmj.38308.477650.63

Darby, S., McGale, P., Peto, R., Granath, F., Hall, P., & Ekbom, A. (2003). Mortality from cardiovascular disease more than 10 years after radiotherapy for breast cancer: nationwide cohort study of 90 000 Swedish women. *BMJ*, *326*(7383), 256-257. https://doi.org/10.1136/bmj.326.7383.256

Darby, S. C., Ewertz, M., McGale, P., Bennet, A. M., Blom-Goldman, U., Bronnum, D., Correa, C., Cutter, D., Gagliardi, G., Gigante, B., Jensen, M. B., Nisbet, A., Peto, R., Rahimi, K., Taylor, C., & Hall, P. (2013). Risk of ischemic heart disease in women after radiotherapy for breast cancer. *N Engl J Med*, *368*(11), 987-998. https://doi.org/10.1056/NEJMoa1209825

Darby, S. C., McGale, P., Taylor, C. W., & Peto, R. (2005). Long-term mortality from heart disease and lung cancer after radiotherapy for early breast cancer: prospective cohort study of about 300,000 women in US SEER cancer registries. *Lancet Oncol*, *6*(8), 557-565. https://doi.org/10.1016/S1470-2045(05)70251-5

Day, C.-P., Merlino, G., & Terry. (2015). Preclinical Mouse Cancer Models: A Maze of Opportunities and Challenges. *Cell*, *163*(1), 39-53. https://doi.org/10.1016/j.cell.2015.08.068

De Ruysscher, D., Niedermann, G., Burnet, N. G., Siva, S., Lee, A. W. M., & Hegi-Johnson, F. (2019b). Radiotherapy toxicity. *Nature Reviews Disease Primers*, *5*(1), 13. https://doi.org/10.1038/s41572-019-0064-5

Deng, L., Liang, H., Xu, M., Yang, X., Burnette, B., Arina, A., Li, X. D., Mauceri, H., Beckett, M., Darga, T., Huang, X., Gajewski, T. F., Chen, Z. J., Fu, Y. X., & Weichselbaum, R. R. (2014). STING-Dependent Cytosolic DNA Sensing Promotes Radiation-Induced Type I Interferon-Dependent Antitumor Immunity in Immunogenic Tumors. *Immunity*, *41*(5), 843-852. https://doi.org/10.1016/j.immuni.2014.10.019

Dieu-Nosjean, M.-C., Goc, J., Giraldo, N. A., Sautès-Fridman, C., & Fridman, W. H. (2014). Tertiary lymphoid structures in cancer and beyond. *Trends in Immunology*, *35*(11), 571-580. https://doi.org/https://doi.org/10.1016/j.it.2014.09.006

Dillon, M. T., Bergerhoff, K. F., Pedersen, M., Whittock, H., Crespo-Rodriguez, E., Patin, E. C., Pearson, A., Smith, H. G., Paget, J. T. E., Patel, R. R., Foo, S., Bozhanova, G., Ragulan, C., Fontana, E., Desai, K., Wilkins, A. C., Sadanandam, A., Melcher, A., McLaughlin, M., & Harrington, K. J. (2019). ATR Inhibition Potentiates the Radiation-induced Inflammatory Tumor Microenvironment. *Clinical Cancer Research*, *25*(11), 3392-3403. https://doi.org/10.1158/1078-0432.ccr-18-1821

Ding, N. H., Li, J. J., & Sun, L. Q. (2013). Molecular mechanisms and treatment of radiation-induced lung fibrosis. *Curr Drug Targets*, *14*(11), 1347-1356. https://doi.org/10.2174/13894501113149990198

Doll, R., & Hill, A. B. (1950). Smoking and Carcinoma of the Lung. *BMJ*, *2*(4682), 739-748. https://doi.org/10.1136/bmj.2.4682.739

Dovedi, S. J., Cheadle, E. J., Popple, A. L., Poon, E., Morrow, M., Stewart, R., Yusko, E. C., Sanders, C. M., Vignali, M., Emerson, R. O., Robins, H. S., Wilkinson, R. W., Honeychurch, J., & Illidge, T. M. (2017). Fractionated Radiation Therapy Stimulates Antitumor Immunity Mediated by Both Resident and Infiltrating Polyclonal T-cell Populations when Combined with PD-1 Blockade. *Clin Cancer Res*, *23*(18), 5514-5526. https://doi.org/10.1158/1078-0432.Ccr-16-1673

Drake, C. G., Jaffee, E., & Pardoll, D. M. (2006). Mechanisms of immune evasion by tumors. *Adv Immunol*, *90*, 51-81. https://doi.org/10.1016/s0065-2776(06)90002-9

Dranoff, G. (2012). Experimental mouse tumour models: what can be learnt about human cancer immunology? *Nature Reviews Immunology*, *12*(1), 61-66. https://doi.org/10.1038/nri3129

Drapkin, B. J., & Minna, J. D. (2020). Studying Lineage Plasticity One Cell at a Time. *Cancer Cell*, *38*(2), 150-152. https://doi.org/10.1016/j.ccell.2020.07.001

Drayton, D. L., Liao, S., Mounzer, R. H., & Ruddle, N. H. (2006). Lymphoid organ development: from ontogeny to neogenesis. *Nature Immunology*, *7*(4), 344-353. https://doi.org/10.1038/ni1330

Dunn, G. P., Old, L. J., & Schreiber, R. D. (2004). The Immunobiology of Cancer Immunosurveillance and Immunoediting. *Immunity*, *21*(2), 137-148. https://doi.org/10.1016/j.immuni.2004.07.017

Durante, M., & Formenti, S. C. (2018). Radiation-Induced Chromosomal Aberrations and Immunotherapy: Micronuclei, Cytosolic DNA, and Interferon-Production Pathway. *Front Oncol*, *8*, 192. https://doi.org/10.3389/fonc.2018.00192

Ebert, P. J. R., Cheung, J., Yang, Y., McNamara, E., Hong, R., Moskalenko, M., Gould, S. E., Maecker, H., Irving, B. A., Kim, J. M., Belvin, M., & Mellman, I. (2016). MAP Kinase Inhibition Promotes T Cell and Anti-tumor Activity in Combination with PD-L1 Checkpoint Blockade. *Immunity*, *44*(3), 609-621. https://doi.org/10.1016/j.immuni.2016.01.024

Formenti, S. C., Rudqvist, N.-P., Golden, E., Cooper, B., Wennerberg, E., Lhuillier, C., Vanpouille-Box, C., Friedman, K., Ferrari De Andrade, L., Wucherpfennig, K. W., Heguy, A., Imai, N., Gnjatic, S., Emerson, R. O., Zhou, X. K., Zhang, T., Chachoua, A., & Demaria, S. (2018). Radiotherapy induces responses of lung cancer to CTLA-4 blockade. *Nature Medicine*, *24*(12), 1845-1851. https://doi.org/10.1038/s41591-018-0232-2

Fridman, W. H., Pagès, F., Sautès-Fridman, C., & Galon, J. (2012). The immune contexture in human tumours: impact on clinical outcome. *Nat Rev Cancer*, *12*(4), 298-306. https://doi.org/10.1038/nrc3245

Galon, J., Costes, A., Sanchez-Cabo, F., Kirilovsky, A., Mlecnik, B., Lagorce-Pagès, C., Tosolini, M., Camus, M., Berger, A., Wind, P., Zinzindohoué, F., Bruneval, P., Cugnenc, P.-H., Trajanoski, Z., Fridman, W.-H., & Pagès, F. (2006). Type, Density, and Location of Immune Cells Within Human Colorectal Tumors Predict Clinical Outcome. *Science*, *313*(5795), 1960-1964. https://doi.org/10.1126/science.1129139

Garg, A. D., Nowis, D., Golab, J., Vandenabeele, P., Krysko, D. V., & Agostinis, P. (2010). Immunogenic cell death, DAMPs and anticancer therapeutics: an emerging amalgamation. *Biochim Biophys Acta*, *1805*(1), 53-71. https://doi.org/10.1016/j.bbcan.2009.08.003

Garnett, C. T., Palena, C., Chakraborty, M., Tsang, K. Y., Schlom, J., & Hodge, J. W. (2004). Sublethal irradiation of human tumor cells modulates phenotype resulting in enhanced killing by cytotoxic T lymphocytes. *Cancer Res*, *64*(21), 7985-7994. https://doi.org/10.1158/0008-5472.Can-04-1525

Garrido, F., Perea, F., Bernal, M., Sánchez-Palencia, A., Aptsiauri, N., & Ruiz-Cabello, F. (2017). The Escape of Cancer from T Cell-Mediated Immune Surveillance: HLA Class I Loss and Tumor Tissue Architecture. *Vaccines (Basel)*, *5*(1). https://doi.org/10.3390/vaccines5010007

Gazdar, A., Robinson, L., Oliver, D., Xing, C., Travis, W. D., Soh, J., Toyooka, S., Watumull, L., Xie, Y., Kernstine, K., & Schiller, J. H. (2014). Hereditary Lung Cancer Syndrome Targets Never Smokers with Germline EGFR Gene T790M Mutations. *Journal of Thoracic Oncology*, *9*(4), 456-463. https://doi.org/10.1097/jto.0000000000000130

Global Cancer Observatory: cancer today. International Agency for Research on Cancer, World Health Organization. Retrieved September from https://gco.iarc.fr/today

Golden, E. B., Chhabra, A., Chachoua, A., Adams, S., Donach, M., Fenton-Kerimian, M., Friedman, K., Ponzo, F., Babb, J. S., Goldberg, J., Demaria, S., & Formenti, S. C. (2015). Local radiotherapy and granulocyte-macrophage colony-stimulating factor to generate abscopal responses in patients with metastatic solid tumours: a proof-of-principle trial. *Lancet Oncol*, *16*(7), 795-803. https://doi.org/10.1016/s1470-2045(15)00054-6

Golden, E. B., Demaria, S., Schiff, P. B., Chachoua, A., & Formenti, S. C. (2013). An abscopal response to radiation and ipilimumab in a patient with metastatic non-small cell lung cancer. *Cancer Immunol Res*, *1*(6), 365-372. https://doi.org/10.1158/2326-6066.Cir-13-0115

Goldstraw, P., Chansky, K., Crowley, J., Rami-Porta, R., Asamura, H., Eberhardt, W. E. E., Nicholson, A. G., Groome, P., Mitchell, A., Bolejack, V., Goldstraw, P., Rami-Porta, R., Asamura, H., Ball, D., Beer, D. G., Beyruti, R., Bolejack, V., Chansky, K., Crowley, J., . . . Yokoi, K. (2016). The IASLC Lung Cancer Staging Project: Proposals for Revision of the TNM Stage Groupings in the Forthcoming (Eighth) Edition of the TNM Classification for Lung Cancer. *Journal of Thoracic Oncology*, *11*(1), 39-51. https://doi.org/10.1016/j.jtho.2015.09.009

Gould, S. E., Junttila, M. R., & de Sauvage, F. J. (2015). Translational value of mouse models in oncology drug development. *Nat Med*, *21*(5), 431-439. https://doi.org/10.1038/nm.3853

Hanahan, D. (2022). Hallmarks of Cancer: New Dimensions. *Cancer Discovery*, *12*(1), 31-46. https://doi.org/10.1158/2159-8290.cd-21-1059

Hanahan, D., & Coussens, L. M. (2012). Accessories to the Crime: Functions of Cells Recruited to the Tumor Microenvironment. *Cancer Cell*, *21*(3), 309-322. https://doi.org/10.1016/j.ccr.2012.02.022

Hanahan, D., & Robert. (2011). Hallmarks of Cancer: The Next Generation. *Cell*, *144*(5), 646-674. https://doi.org/10.1016/j.cell.2011.02.013

Hanahan, D., & Weinberg, R. A. (2000). The Hallmarks of Cancer. *Cell*, *100*(1), 57-70. https://doi.org/10.1016/s0092-8674(00)81683-9

Haque, W., Verma, V., Fakhreddine, M., Butler, E. B., Teh, B. S., & Simone, C. B., 2nd. (2018). Trends in Cardiac Mortality in Patients With Locally Advanced Non-Small Cell Lung Cancer. *Int J Radiat Oncol Biol Phys*, *100*(2), 470-477. https://doi.org/10.1016/j.ijrobp.2017.10.031

Harding, S. M., Benci, J. L., Irianto, J., Discher, D. E., Minn, A. J., & Greenberg, R. A. (2017). Mitotic progression following DNA damage enables pattern recognition within micronuclei. *Nature*, *548*(7668), 466-470. https://doi.org/10.1038/nature23470

Harris, E. E., Correa, C., Hwang, W. T., Liao, J., Litt, H. I., Ferrari, V. A., & Solin, L. J. (2006). Late cardiac mortality and morbidity in early-stage breast cancer patients after breast-conservation treatment. *J Clin Oncol*, *24*(25), 4100-4106. https://doi.org/10.1200/JCO.2005.05.1037

Hecht, S. S. (2003). Tobacco carcinogens, their biomarkers and tobacco-induced cancer. *Nature Reviews Cancer*, *3*(10), 733-744. https://doi.org/10.1038/nrc1190

Hegde, P. S., & Chen, D. S. (2020). Top 10 Challenges in Cancer Immunotherapy. *Immunity*, *52*(1), 17-35. https://doi.org/https://doi.org/10.1016/j.immuni.2019.12.011

Herbst, R. S., Morgensztern, D., & Boshoff, C. (2018). The biology and management of non-small cell lung cancer. *Nature*, *553*(7689), 446-454. https://doi.org/10.1038/nature25183

Hwang, S. J., Cheng, L. S., Lozano, G., Amos, C. I., Gu, X., & Strong, L. C. (2003). Lung cancer risk in germline p53 mutation carriers: association between an inherited cancer predisposition, cigarette smoking, and cancer risk. *Hum Genet*, *113*(3), 238-243. https://doi.org/10.1007/s00439-003-0968-7

Hynds, R. E., Frese, K. K., Pearce, D. R., Grönroos, E., Dive, C., & Swanton, C. (2021). Progress towards non-small-cell lung cancer models that represent clinical evolutionary trajectories. *Open Biology*, *11*(1), 200247. https://doi.org/10.1098/rsob.200247

Jackson, E. L., Willis, N., Mercer, K., Bronson, R. T., Crowley, D., Montoya, R., Jacks, T., & Tuveson, D. A. (2001). Analysis of lung tumor initiation and progression using conditional expression of oncogenic K-ras. *Genes Dev*, *15*(24), 3243-3248. https://doi.org/10.1101/gad.943001

Jackson, S. P., & Bartek, J. (2009). The DNA-damage response in human biology and disease. *Nature*, *461*(7267), 1071-1078. https://doi.org/10.1038/nature08467

Jacobse, J. N., Duane, F. K., Boekel, N. B., Schaapveld, M., Hauptmann, M., Hooning, M. J., Seynaeve, C. M., Baaijens, M. H. A., Gietema, J. A., Darby, S. C., van Leeuwen, F. E., Aleman, B. M. P., & Taylor, C. W. (2019). Radiation Dose-Response for Risk of Myocardial Infarction in Breast Cancer Survivors. *Int J Radiat Oncol Biol Phys*, *103*(3), 595-604. https://doi.org/10.1016/j.ijrobp.2018.10.025

Jamal-Hanjani, M., Wilson, G. A., McGranahan, N., Birkbak, N. J., Watkins, T. B. K., Veeriah, S., Shafi, S., Johnson, D. H., Mitter, R., Rosenthal, R., Salm, M., Horswell, S., Escudero, M., Matthews, N., Rowan, A., Chambers, T., Moore, D. A., Turajlic, S., Xu, H., . . . Consortium, T. R. (2017). Tracking the Evolution of Non-Small-Cell Lung Cancer. *N Engl J Med*, *376*(22), 2109-2121. https://doi.org/10.1056/NEJMoa1616288

Jiang, W., Chan, C. K., Weissman, I. L., Kim, B. Y. S., & Hahn, S. M. (2016). Immune Priming of the Tumor Microenvironment by Radiation. *Trends Cancer*, *2*(11), 638-645. https://doi.org/10.1016/j.trecan.2016.09.007

Johnson, S. K., Kerr, K. M., Chapman, A. D., Kennedy, M. M., King, G., Cockburn, J. S., & Jeffrey, R. R. (2000). Immune cell infiltrates and prognosis in primary carcinoma of the lung. *Lung Cancer*, *27*(1), 27-35. https://doi.org/10.1016/s0169-5002(99)00095-1

Kang, W., Feng, Z., Luo, J., He, Z., Liu, J., Wu, J., & Rong, P. (2021). Tertiary Lymphoid Structures in Cancer: The Double-Edged Sword Role in Antitumor Immunity and Potential Therapeutic Induction Strategies. *Front Immunol*, *12*, 689270. https://doi.org/10.3389/fimmu.2021.689270

Kwon, J., & Bakhoum, S. F. (2020). The Cytosolic DNA-Sensing cGAS-STING Pathway in Cancer. *Cancer Discov*, *10*(1), 26-39. https://doi.org/10.1158/2159-8290.CD-19-0761

Loechler, E. L., Green, C. L., & Essigmann, J. M. (1984). In vivo mutagenesis by O6-methylguanine built into a unique site in a viral genome. *Proc Natl Acad Sci U S A*, *81*(20), 6271-6275. https://doi.org/10.1073/pnas.81.20.6271

Lomax, M. E., Folkes, L. K., & O'Neill, P. (2013). Biological Consequences of Radiation-induced DNA Damage: Relevance to Radiotherapy. *Clinical Oncology*, *25*(10), 578-585. https://doi.org/10.1016/j.clon.2013.06.007

Lopez de Rodas, M., Nagineni, V., Ravi, A., Datar, I. J., Mino-Kenudson, M., Corredor, G., Barrera, C., Behlman, L., Rimm, D. L., Herbst, R. S., Madabhushi, A., Riess,

J. W., Velcheti, V., Hellmann, M. D., Gainor, J., & Schalper, K. A. (2022). Role of tumor infiltrating lymphocytes and spatial immune heterogeneity in sensitivity to PD-1 axis blockers in non-small cell lung cancer. *Journal for ImmunoTherapy of Cancer*, *10*(6), e004440. https://doi.org/10.1136/jitc-2021-004440

Mackenzie, K. J., Carroll, P., Martin, C.-A., Murina, O., Fluteau, A., Simpson, D. J., Olova, N., Sutcliffe, H., Rainger, J. K., Leitch, A., Osborn, R. T., Wheeler, A. P., Nowotny, M., Gilbert, N., Chandra, T., Reijns, M. A. M., & Jackson, A. P. (2017). cGAS surveillance of micronuclei links genome instability to innate immunity. *Nature*, *548*(7668), 461-465. https://doi.org/10.1038/nature23449

Marjanovic, N. D., Hofree, M., Chan, J. E., Canner, D., Wu, K., Trakala, M., Hartmann, G. G., Smith, O. C., Kim, J. Y., Evans, K. V., Hudson, A., Ashenberg, O., Porter, C. B. M., Bejnood, A., Subramanian, A., Pitter, K., Yan, Y., Delorey, T., Phillips, D. R., . . . Tammela, T. (2020). Emergence of a High-Plasticity Cell State during Lung Cancer Evolution. *Cancer Cell*, *38*(2), 229-246.e213. https://doi.org/10.1016/j.ccell.2020.06.012

Martin, M. D., & Badovinac, V. P. (2018). Defining Memory CD8 T Cell [Mini Review]. *Frontiers in Immunology*, *9*. https://doi.org/10.3389/fimmu.2018.02692

Martinek, J., Wu, T. C., Cadena, D., Banchereau, J., & Palucka, K. (2019). Interplay between dendritic cells and cancer cells. *Int Rev Cell Mol Biol*, *348*, 179-215. https://doi.org/10.1016/bs.ircmb.2019.07.008

Matakidou, A., Eisen, T., & Houlston, R. S. (2005). Systematic review of the relationship between family history and lung cancer risk. *Br J Cancer*, *93*(7), 825-833. https://doi.org/10.1038/sj.bjc.6602769

McGale, P., Darby, S. C., Hall, P., Adolfsson, J., Bengtsson, N. O., Bennet, A. M., Fornander, T., Gigante, B., Jensen, M. B., Peto, R., Rahimi, K., Taylor, C. W., & Ewertz, M. (2011). Incidence of heart disease in 35,000 women treated with radiotherapy for breast cancer in Denmark and Sweden. *Radiother Oncol*, *100*(2), 167-175. https://doi.org/10.1016/j.radonc.2011.06.016

McGranahan, N., Rosenthal, R., Hiley, C. T., Rowan, A. J., Watkins, T. B. K., Wilson, G. A., Birkbak, N. J., Veeriah, S., Van Loo, P., Herrero, J., Swanton, C., Swanton, C., Jamal-Hanjani, M., Veeriah, S., Shafi, S., Czyzewska-Khan, J., Johnson, D., Laycock, J., Bosshard-Carter, L., . . . Dessimoz, C. (2017). Allele-Specific HLA Loss and Immune Escape in Lung Cancer Evolution. *Cell*, *171*(6), 1259-1271.e1211. https://doi.org/10.1016/j.cell.2017.10.001

McGranahan, N., & Swanton, C. (2017). Clonal Heterogeneity and Tumor Evolution: Past, Present, and the Future. *Cell*, *168*(4), 613-628. https://doi.org/10.1016/j.cell.2017.01.018

McLaughlin, M., Patin, E. C., Pedersen, M., Wilkins, A., Dillon, M. T., Melcher, A. A., & Harrington, K. J. (2020). Inflammatory microenvironment remodelling by tumour cells after radiotherapy. *Nature Reviews Cancer*, *20*(4), 203-217. https://doi.org/10.1038/s41568-020-0246-1

Mendes, N., Dias Carvalho, P., Martins, F., Mendonça, S., Malheiro, A. R., Ribeiro, A., Carvalho, J., & Velho, S. (2020). Animal Models to Study Cancer and Its

Microenvironment. In (pp. 389-401). Springer International Publishing. https://doi.org/10.1007/978-3-030-34025-4_20

Menon, H., Ramapriyan, R., Cushman, T. R., Verma, V., Kim, H. H., Schoenhals, J. E., Atalar, C., Selek, U., Chun, S. G., Chang, J. Y., Barsoumian, H. B., Nguyen, Q. N., Altan, M., Cortez, M. A., Hahn, S. M., & Welsh, J. W. (2019). Role of Radiation Therapy in Modulation of the Tumor Stroma and Microenvironment. *Front Immunol*, *10*, 193. https://doi.org/10.3389/fimmu.2019.00193

Myers, C. J., & Lu, B. (2017). Decreased Survival After Combining Thoracic Irradiation and an Anti-PD-1 Antibody Correlated With Increased T-cell Infiltration Into Cardiac and Lung Tissues. *Int J Radiat Oncol Biol Phys*, *99*(5), 1129-1136. https://doi.org/10.1016/j.ijrobp.2017.06.2452

Najafi, M., Majidpoor, J., Toolee, H., & Mortezaee, K. (2021). The current knowledge concerning solid cancer and therapy. *J Biochem Mol Toxicol*, *35*(11), e22900. https://doi.org/10.1002/jbt.22900

National Cancer Institute. SEER Cancer Statistics Review, 2012-2018. https://seer.cancer.gov/statfacts/html/lungb.html

National Center for Chronic Disease, P., Health Promotion Office on, S., & Health. (2014). Reports of the Surgeon General. In *The Health Consequences of Smoking—50 Years of Progress: A Report of the Surgeon General*. Centers for Disease Control and Prevention (US).

Noguchi, M., Morikawa, A., Kawasaki, M., Matsuno, Y., Yamada, T., Hirohashi, S., Kondo, H., & Shimosato, Y. (1995). Small adenocarcinoma of the lung. Histologic characteristics and prognosis. *Cancer*, *75*(12), 2844-2852. https://doi.org/10.1002/1097-0142(19950615)75:12<2844::aid-cncr2820751209>3.0.co;2-#

Non-Small Cell Lung Cancer Treatment. (2002).

Pitzalis, C., Jones, G. W., Bombardieri, M., & Jones, S. A. (2014). Ectopic lymphoid-like structures in infection, cancer and autoimmunity. *Nature Reviews Immunology*, *14*(7), 447-462. https://doi.org/10.1038/nri3700

Pope Iii, C. A. (2002). Lung Cancer, Cardiopulmonary Mortality, and Long-term Exposure to Fine Particulate Air Pollution. *JAMA*, *287*(9), 1132. https://doi.org/10.1001/jama.287.9.1132

Postow, M. A., Callahan, M. K., Barker, C. A., Yamada, Y., Yuan, J., Kitano, S., Mu, Z., Rasalan, T., Adamow, M., Ritter, E., Sedrak, C., Jungbluth, A. A., Chua, R., Yang, A. S., Roman, R.-A., Rosner, S., Benson, B., Allison, J. P., Lesokhin, A. M., . . . Wolchok, J. D. (2012). Immunologic Correlates of the Abscopal Effect in a Patient with Melanoma. *New England Journal of Medicine*, *366*(10), 925-931. https://doi.org/10.1056/nejmoa1112824

Pribluda, A., De La Cruz, C. C., & Jackson, E. L. (2015). Intratumoral Heterogeneity: From Diversity Comes Resistance. *Clinical Cancer Research*, *21*(13), 2916-2923. https://doi.org/10.1158/1078-0432.ccr-14-1213

Raaschou-Nielsen, O., Andersen, Z. J., Beelen, R., Samoli, E., Stafoggia, M., Weinmayr, G., Hoffmann, B., Fischer, P., Nieuwenhuijsen, M. J., Brunekreef, B., Xun, W. W., Katsouyanni, K., Dimakopoulou, K., Sommar, J., Forsberg, B.,

Modig, L., Oudin, A., Oftedal, B., Schwarze, P. E., . . . Hoek, G. (2013). Air pollution and lung cancer incidence in 17 European cohorts: prospective analyses from the European Study of Cohorts for Air Pollution Effects (ESCAPE). *The Lancet Oncology*, *14*(9), 813-822. https://doi.org/10.1016/s1470-2045(13)70279-1

Radiation Therapy to Treat Cancer. (January 8, 2019). National Cancer Institute, National Institutes of Health. Retrieved 12 September from https://www.cancer.gov/about-cancer/treatment/types/radiation-therapy

Reits, E. A., Hodge, J. W., Herberts, C. A., Groothuis, T. A., Chakraborty, M., Wansley, E. K., Camphausen, K., Luiten, R. M., de Ru, A. H., Neijssen, J., Griekspoor, A., Mesman, E., Verreck, F. A., Spits, H., Schlom, J., van Veelen, P., & Neefjes, J. J. (2006). Radiation modulates the peptide repertoire, enhances MHC class I expression, and induces successful antitumor immunotherapy. *J Exp Med*, *203*(5), 1259-1271. https://doi.org/10.1084/jem.20052494

Rodrigues, J., Heinrich, M. A., Teixeira, L. M., & Prakash, J. (2021). 3D In Vitro Model (R)evolution: Unveiling Tumor–Stroma Interactions. *Trends in Cancer*, *7*(3), 249-264. https://doi.org/10.1016/j.trecan.2020.10.009

Rosenthal, R., Swanton, C., & McGranahan, N. (2021). Understanding the impact of immune-mediated selection on lung cancer evolution. *British Journal of Cancer*, *124*(10), 1615-1617. https://doi.org/10.1038/s41416-020-01232-6

Rudqvist, N. P., Pilones, K. A., Lhuillier, C., Wennerberg, E., Sidhom, J. W., Emerson, R. O., Robins, H. S., Schneck, J., Formenti, S. C., & Demaria, S. (2018). Radiotherapy and CTLA-4 Blockade Shape the TCR Repertoire of Tumor-Infiltrating T Cells. *Cancer Immunol Res*, *6*(2), 139-150. https://doi.org/10.1158/2326-6066.Cir-17-0134

Saiki, H., Petersen, I. A., Scott, C. G., Bailey, K. R., Dunlay, S. M., Finley, R. R., Ruddy, K. J., Yan, E., & Redfield, M. M. (2017). Risk of Heart Failure With Preserved Ejection Fraction in Older Women After Contemporary Radiotherapy for Breast Cancer. *Circulation*, *135*(15), 1388-1396. https://doi.org/10.1161/CIRCULATIONAHA.116.025434

Salem, J. E., Manouchehri, A., Moey, M., Lebrun-Vignes, B., Bastarache, L., Pariente, A., Gobert, A., Spano, J. P., Balko, J. M., Bonaca, M. P., Roden, D. M., Johnson, D. B., & Moslehi, J. J. (2018). Cardiovascular toxicities associated with immune checkpoint inhibitors: an observational, retrospective, pharmacovigilance study. *Lancet Oncol*, *19*(12), 1579-1589. https://doi.org/10.1016/S1470-2045(18)30608-9

Schaue, D., Comin-Anduix, B., Ribas, A., Zhang, L., Goodglick, L., Sayre, J. W., Debucquoy, A., Haustermans, K., & McBride, W. H. (2008). T-cell responses to survivin in cancer patients undergoing radiation therapy. *Clin Cancer Res*, *14*(15), 4883-4890. https://doi.org/10.1158/1078-0432.Ccr-07-4462

Schlaak, R. A., SenthilKumar, G., Boerma, M., & Bergom, C. (2020). Advances in Preclinical Research Models of Radiation-Induced Cardiac Toxicity. *Cancers (Basel)*, *12*(2). https://doi.org/10.3390/cancers12020415

Schreiber, R. D., Old, L. J., & Smyth, M. J. (2011). Cancer Immunoediting: Integrating Immunity's Roles in Cancer Suppression and Promotion. *Science*, *331*(6024), 1565-1570. https://doi.org/10.1126/science.1203486

Schumacher, T. N., & Thommen, D. S. (2022). Tertiary lymphoid structures in cancer. *Science*, *375*(6576), eabf9419. https://doi.org/10.1126/science.abf9419

Seo, K. Y., Jelinsky, S. A., & Loechler, E. L. (2000). Factors that influence the mutagenic patterns of DNA adducts from chemical carcinogens. *Mutat Res*, *463*(3), 215-246. https://doi.org/10.1016/s1383-5742(00)00047-8

Sharabi, A. B., Nirschl, C. J., Kochel, C. M., Nirschl, T. R., Francica, B. J., Velarde, E., Deweese, T. L., & Drake, C. G. (2015). Stereotactic Radiation Therapy Augments Antigen-Specific PD-1-Mediated Antitumor Immune Responses via Cross-Presentation of Tumor Antigen. *Cancer Immunol Res*, *3*(4), 345-355. https://doi.org/10.1158/2326-6066.Cir-14-0196

Sharma, A., Bode, B., Wenger, R. H., Lehmann, K., Sartori, A. A., Moch, H., Knuth, A., Von Boehmer, L., & Van Den Broek, M. (2011). γ-Radiation Promotes Immunological Recognition of Cancer Cells through Increased Expression of Cancer-Testis Antigens In Vitro and In Vivo. *PLoS One*, *6*(11), e28217. https://doi.org/10.1371/journal.pone.0028217

Sharma, R., Lewis, S., & Wlodarski, M. W. (2020). DNA Repair Syndromes and Cancer: Insights Into Genetics and Phenotype Patterns. *Front Pediatr*, *8*, 570084. https://doi.org/10.3389/fped.2020.570084

Shrimali, R. K., Ahmad, S., Verma, V., Zeng, P., Ananth, S., Gaur, P., Gittelman, R. M., Yusko, E., Sanders, C., Robins, H., Hammond, S. A., Janik, J. E., Mkrtichyan, M., Gupta, S., & Khleif, S. N. (2017). Concurrent PD-1 Blockade Negates the Effects of OX40 Agonist Antibody in Combination Immunotherapy through Inducing T-cell Apoptosis. *Cancer Immunol Res*, *5*(9), 755-766. https://doi.org/10.1158/2326-6066.Cir-17-0292

Simone, C. B., 2nd. (2017). Thoracic Radiation Normal Tissue Injury. *Semin Radiat Oncol*, *27*(4), 370-377. https://doi.org/10.1016/j.semradonc.2017.04.009

Singer, B., & Essigmann, J. M. (1991). Site-specific mutagenesis: retrospective and prospective. *Carcinogenesis*, *12*(6), 949-955. https://doi.org/10.1093/carcin/12.6.949

Spyratos, D., Zarogoulidis, P., Porpodis, K., Tsakiridis, K., Machairiotis, N., Katsikogiannis, N., Kougioumtzi, I., Dryllis, G., Kallianos, A., Rapti, A., Li, C., & Zarogoulidis, K. (2013). Occupational exposure and lung cancer. *J Thorac Dis*, *5 Suppl 4*(Suppl 4), S440-445. https://doi.org/10.3978/j.issn.2072-1439.2013.07.09

Stein-Merlob, A. F., Rothberg, M. V., Holman, P., & Yang, E. H. (2021). Immunotherapy-Associated Cardiotoxicity of Immune Checkpoint Inhibitors and Chimeric Antigen Receptor T Cell Therapy: Diagnostic and Management Challenges and Strategies. *Curr Cardiol Rep*, *23*(3), 11. https://doi.org/10.1007/s11886-021-01440-3

Swanton, C., Hill, W., Lim, E., Lee, C., Weeden, C. E., Augustine, M., Chen, K., Kuan, F., Marongiu, F., Rodrigues, F., Cha, H., Jacks, T., Luchtenborg, M., Malanchi,

I., Downward, J., Carlsten, C., Hackshaw, A., Litchfield, K. R., DeGregori, J., & Jamal-Hanjani, M. (2022, 10 Sep 2022). *Mechanism of action and an actionable inflammatory axis for air pollution induced non-small cell lung cancer in never smokers* ESMO Congress, Paris Auditorium. https://oncologypro.esmo.org/meeting-resources/esmo-congress/mechanism-of-action-and-an-actionable-inflammatory-axis-for-air-pollution-induced-non-small-cell-lung-cancer-towards-molecular-cancer-prevention

Taunk, N. K., Haffty, B. G., Kostis, J. B., & Goyal, S. (2015). Radiation-induced heart disease: pathologic abnormalities and putative mechanisms. *Front Oncol*, *5*, 39. https://doi.org/10.3389/fonc.2015.00039

Taylor, C., Correa, C., Duane, F. K., Aznar, M. C., Anderson, S. J., Bergh, J., Dodwell, D., Ewertz, M., Gray, R., Jagsi, R., Pierce, L., Pritchard, K. I., Swain, S., Wang, Z., Wang, Y., Whelan, T., Peto, R., McGale, P., & Early Breast Cancer Trialists' Collaborative, G. (2017). Estimating the Risks of Breast Cancer Radiotherapy: Evidence From Modern Radiation Doses to the Lungs and Heart and From Previous Randomized Trials. *J Clin Oncol*, *35*(15), 1641-1649. https://doi.org/10.1200/JCO.2016.72.0722

Thai, A. A., Solomon, B. J., Sequist, L. V., Gainor, J. F., & Heist, R. S. (2021). Lung cancer. *The Lancet*, *398*(10299), 535-554. https://doi.org/10.1016/s0140-6736(21)00312-3

Townsend, E. C., Murakami, M. A., Christodoulou, A., Christie, A. L., Köster, J., DeSouza, T. A., Morgan, E. A., Kallgren, S. P., Liu, H., Wu, S. C., Plana, O., Montero, J., Stevenson, K. E., Rao, P., Vadhi, R., Andreeff, M., Armand, P., Ballen, K. K., Barzaghi-Rinaudo, P., . . . Weinstock, D. M. (2016). The Public Repository of Xenografts Enables Discovery and Randomized Phase II-like Trials in Mice. *Cancer Cell*, *29*(4), 574-586. https://doi.org/10.1016/j.ccell.2016.03.008

Tran, E., Robbins, P. F., Lu, Y.-C., Prickett, T. D., Gartner, J. J., Jia, L., Pasetto, A., Zheng, Z., Ray, S., Groh, E. M., Kriley, I. R., & Rosenberg, S. A. (2016). T-Cell Transfer Therapy Targeting Mutant KRAS in Cancer. *New England Journal of Medicine*, *375*(23), 2255-2262. https://doi.org/10.1056/nejmoa1609279

Travis, W. D., Brambilla, E., Nicholson, A. G., Yatabe, Y., Austin, J. H. M., Beasley, M. B., Chirieac, L. R., Dacic, S., Duhig, E., Flieder, D. B., Geisinger, K., Hirsch, F. R., Ishikawa, Y., Kerr, K. M., Noguchi, M., Pelosi, G., Powell, C. A., Tsao, M. S., & Wistuba, I. (2015). The 2015 World Health Organization Classification of Lung Tumors. *Journal of Thoracic Oncology*, *10*(9), 1243-1260. https://doi.org/10.1097/jto.0000000000000630

Tsakiroglou, A. M., Fergie, M., Oguejiofor, K., Linton, K., Thomson, D., Stern, P. L., Astley, S., Byers, R., & West, C. M. L. (2020). Spatial proximity between T and PD-L1 expressing cells as a prognostic biomarker for oropharyngeal squamous cell carcinoma. *British Journal of Cancer*, *122*(4), 539-544. https://doi.org/10.1038/s41416-019-0634-z

Tseng, Y. D., Nguyen, M. H., Baker, K., Cook, M., Redman, M., Lachance, K., Bhatia, S., Liao, J. J., Apisarnthanarax, S., Nghiem, P. T., & Parvathaneni, U. (2018). Effect of Patient Immune Status on the Efficacy of Radiation Therapy and

Recurrence-Free Survival Among 805 Patients With Merkel Cell Carcinoma. *Int J Radiat Oncol Biol Phys*, *102*(2), 330-339. https://doi.org/10.1016/j.ijrobp.2018.05.075

Tukenova, M., Guibout, C., Oberlin, O., Doyon, F., Mousannif, A., Haddy, N., Guerin, S., Pacquement, H., Aouba, A., Hawkins, M., Winter, D., Bourhis, J., Lefkopoulos, D., Diallo, I., & de Vathaire, F. (2010). Role of cancer treatment in long-term overall and cardiovascular mortality after childhood cancer. *J Clin Oncol*, *28*(8), 1308-1315. https://doi.org/10.1200/JCO.2008.20.2267

Twyman-Saint Victor, C., Rech, A. J., Maity, A., Rengan, R., Pauken, K. E., Stelekati, E., Benci, J. L., Xu, B., Dada, H., Odorizzi, P. M., Herati, R. S., Mansfield, K. D., Patsch, D., Amaravadi, R. K., Schuchter, L. M., Ishwaran, H., Mick, R., Pryma, D. A., Xu, X., . . . Minn, A. J. (2015). Radiation and dual checkpoint blockade activate non-redundant immune mechanisms in cancer. *Nature*, *520*(7547), 373-377. https://doi.org/10.1038/nature14292

van de Pavert, S. A., & Mebius, R. E. (2010). New insights into the development of lymphoid tissues. *Nature Reviews Immunology*, *10*(9), 664-674. https://doi.org/10.1038/nri2832

van Nimwegen, F. A., Schaapveld, M., Cutter, D. J., Janus, C. P., Krol, A. D., Hauptmann, M., Kooijman, K., Roesink, J., van der Maazen, R., Darby, S. C., Aleman, B. M., & van Leeuwen, F. E. (2016). Radiation Dose-Response Relationship for Risk of Coronary Heart Disease in Survivors of Hodgkin Lymphoma. *J Clin Oncol*, *34*(3), 235-243. https://doi.org/10.1200/JCO.2015.63.4444

Vendramin, R., Litchfield, K., & Swanton, C. (2021). Cancer evolution: Darwin and beyond. *The EMBO Journal*, *40*(18). https://doi.org/10.15252/embj.2021108389

Vivekanandan, S., Landau, D. B., Counsell, N., Warren, D. R., Khwanda, A., Rosen, S. D., Parsons, E., Ngai, Y., Farrelly, L., Hughes, L., Hawkins, M. A., & Fenwick, J. D. (2017). The Impact of Cardiac Radiation Dosimetry on Survival After Radiation Therapy for Non-Small Cell Lung Cancer. *Int J Radiat Oncol Biol Phys*, *99*(1), 51-60. https://doi.org/10.1016/j.ijrobp.2017.04.026

Walls, G. M., O'Kane, R., Ghita, M., Kuburas, R., McGarry, C. K., Cole, A. J., Jain, S., & Butterworth, K. T. (2022). Murine models of radiation cardiotoxicity: A systematic review and recommendations for future studies. *Radiother Oncol*, *173*, 19-31. https://doi.org/10.1016/j.radonc.2022.04.030

Weichselbaum, R. R., Liang, H., Deng, L., & Fu, Y.-X. (2017). Radiotherapy and immunotherapy: a beneficial liaison? *Nature Reviews Clinical Oncology*, *14*(6), 365-379. https://doi.org/10.1038/nrclinonc.2016.211

Westcott, P. M., Halliwill, K. D., To, M. D., Rashid, M., Rust, A. G., Keane, T. M., Delrosario, R., Jen, K. Y., Gurley, K. E., Kemp, C. J., Fredlund, E., Quigley, D. A., Adams, D. J., & Balmain, A. (2015). The mutational landscapes of genetic and chemical models of Kras-driven lung cancer. *Nature*, *517*(7535), 489-492. https://doi.org/10.1038/nature13898

Wilkins, A. C., Patin, E. C., Harrington, K. J., & Melcher, A. A. (2019). The immunological consequences of radiation-induced DNA damage. *The Journal of Pathology*, *247*(5), 606-614. https://doi.org/10.1002/path.5232

Yamamoto, H., Higasa, K., Sakaguchi, M., Shien, K., Soh, J., Ichimura, K., Furukawa, M., Hashida, S., Tsukuda, K., Takigawa, N., Matsuo, K., Kiura, K., Miyoshi, S., Matsuda, F., & Toyooka, S. (2014). Novel Germline Mutation in the Transmembrane Domain of HER2 in Familial Lung Adenocarcinomas. *JNCI: Journal of the National Cancer Institute*, *106*(1), djt338-djt338. https://doi.org/10.1093/jnci/djt338

Yatim, N., Cullen, S., & Albert, M. L. (2017). Dying cells actively regulate adaptive immune responses. *Nat Rev Immunol*, *17*(4), 262-275. https://doi.org/10.1038/nri.2017.9

Yegya-Raman, N., Wang, K., Kim, S., Reyhan, M., Deek, M. P., Sayan, M., Li, D., Patel, M., Malhotra, J., Aisner, J., Marks, L. B., & Jabbour, S. K. (2018). Dosimetric Predictors of Symptomatic Cardiac Events After Conventional-Dose Chemoradiation Therapy for Inoperable NSCLC. *J Thorac Oncol*, *13*(10), 1508-1518. https://doi.org/10.1016/j.jtho.2018.05.028

Yoshida, K., Gowers, K. H. C., Lee-Six, H., Chandrasekharan, D. P., Coorens, T., Maughan, E. F., Beal, K., Menzies, A., Millar, F. R., Anderson, E., Clarke, S. E., Pennycuick, A., Thakrar, R. M., Butler, C. R., Kakiuchi, N., Hirano, T., Hynds, R. E., Stratton, M. R., Martincorena, I., . . . Campbell, P. J. (2020). Tobacco smoking and somatic mutations in human bronchial epithelium. *Nature*, *578*(7794), 266-272. https://doi.org/10.1038/s41586-020-1961-1

Chapter 2 Materials and Methods

Aronoff, L., Epelman, S., & Clemente-Casares, X. (2018). Isolation and Identification of Extravascular Immune Cells of the Heart. *J Vis Exp*(138). https://doi.org/10.3791/58114

Ashburner, M., Ball, C. A., Blake, J. A., Botstein, D., Butler, H., Cherry, J. M., Davis, A. P., Dolinski, K., Dwight, S. S., Eppig, J. T., Harris, M. A., Hill, D. P., Issel-Tarver, L., Kasarskis, A., Lewis, S., Matese, J. C., Richardson, J. E., Ringwald, M., Rubin, G. M., & Sherlock, G. (2000). Gene Ontology: tool for the unification of biology. *Nature genetics*, *25*(1), 25-29. https://doi.org/10.1038/75556

Gomes, A. L., Kinchesh, P., Gilchrist, S., Allen, P. D., Lourenco, L. M., Ryan, A. J., & Smart, S. C. (2019). Cardio-Respiratory synchronized bSSFP MRI for high throughput in vivo lung tumour quantification. *PLoS One*, *14*(2), e0212172. https://doi.org/10.1371/journal.pone.0212172

Hübner, R.-H., Gitter, W., Eddine El Mokhtari, N., Mathiak, M., Both, M., Bolte, H., Freitag-Wolf, S., & Bewig, B. (2008). Standardized quantification of pulmonary fibrosis in histological samples. *BioTechniques*, *44*(4), 507-517. https://doi.org/10.2144/000112729

Liberzon, A., Birger, C., Thorvaldsdóttir, H., Ghandi, M., Jill, & Tamayo, P. (2015). The Molecular Signatures Database Hallmark Gene Set Collection. *Cell Systems*, *1*(6), 417-425. https://doi.org/10.1016/j.cels.2015.12.004

Love, M. I., Huber, W., & Anders, S. (2014). Moderated estimation of fold change and dispersion for RNA-seq data with DESeq2. *Genome Biology*, *15*(12). https://doi.org/10.1186/s13059-014-0550-8

Mootha, V. K., Lindgren, C. M., Eriksson, K.-F., Subramanian, A., Sihag, S., Lehar, J., Puigserver, P., Carlsson, E., Ridderstråle, M., Laurila, E., Houstis, N., Daly, M. J., Patterson, N., Mesirov, J. P., Golub, T. R., Tamayo, P., Spiegelman, B., Lander, E. S., Hirschhorn, J. N., . . . Groop, L. C. (2003). PGC-1alpha-responsive genes involved in oxidative phosphorylation are coordinately downregulated in human diabetes. *Nature genetics*, *34*(3), 267-273. https://doi.org/10.1038/ng1180

Patro, R., Duggal, G., Love, M. I., Irizarry, R. A., & Kingsford, C. (2017). Salmon provides fast and bias-aware quantification of transcript expression. *Nature Methods*, *14*(4), 417-419. https://doi.org/10.1038/nmeth.4197

Pinto, A. R., Chandran, A., Rosenthal, N. A., & Godwin, J. W. (2013). Isolation and analysis of single cells from the mouse heart. *J Immunol Methods*, *393*(1-2), 74-80. https://doi.org/10.1016/j.jim.2013.03.012

Raudvere, U., Kolberg, L., Kuzmin, I., Arak, T., Adler, P., Peterson, H., & Vilo, J. (2019). g:Profiler: a web server for functional enrichment analysis and conversions of gene lists (2019 update). *Nucleic Acids Research*, *47*(W1), W191-W198. https://doi.org/10.1093/nar/gkz369

Soneson, C., Love, M. I., & Robinson, M. D. (2016). Differential analyses for RNA-seq: transcript-level estimates improve gene-level inferences. *F1000Research*, *4*, 1521. https://doi.org/10.12688/f1000research.7563.2

Subramanian, A., Tamayo, P., Mootha, V. K., Mukherjee, S., Ebert, B. L., Gillette, M. A., Paulovich, A., Pomeroy, S. L., Golub, T. R., Lander, E. S., & Mesirov, J. P. (2005). Gene set enrichment analysis: A knowledge-based approach for interpreting genome-wide expression profiles. *Proceedings of the National Academy of Sciences*, *102*(43), 15545-15550. https://doi.org/10.1073/pnas.0506580102

Supek, F., Bošnjak, M., Škunca, N., & Šmuc, T. (2011). REVIGO Summarizes and Visualizes Long Lists of Gene Ontology Terms. *PLoS One*, *6*(7), e21800. https://doi.org/10.1371/journal.pone.0021800

Wu, T., Hu, E., Xu, S., Chen, M., Guo, P., Dai, Z., Feng, T., Zhou, L., Tang, W., Zhan, L., Fu, X., Liu, S., Bo, X., & Yu, G. (2021). clusterProfiler 4.0: A universal enrichment tool for interpreting omics data. *The Innovation*, *2*(3), 100141. https://doi.org/10.1016/j.xinn.2021.100141

Yushkevich, P. A., Piven, J., Hazlett, H. C., Smith, R. G., Ho, S., Gee, J. C., & Gerig, G. (2006). User-guided 3D active contour segmentation of anatomical structures: Significantly improved efficiency and reliability. *NeuroImage*, *31*(3), 1116-1128. https://doi.org/10.1016/j.neuroimage.2006.01.015

Chapter 3

20034-20037 (2012). https://www.fda.gov/tobacco-products/rules-regulationsand-guidance/harmful-and-potentially-harmful-constituents-tobacco-productsand-tobacco-smoke-established-list

Auerbach, C. (1967). The Chemical Production of Mutations. *Science*, *158*(3805), 1141-1147. https://doi.org/doi:10.1126/science.158.3805.1141

Balermpas, P., Michel, Y., Wagenblast, J., Seitz, O., Weiss, C., Rödel, F., Rödel, C., & Fokas, E. (2014). Tumour-infiltrating lymphocytes predict response to definitive chemoradiotherapy in head and neck cancer. *British Journal of Cancer*, *110*(2), 501-509. https://doi.org/10.1038/bjc.2013.640

Barbazan, J., & Matic Vignjevic, D. (2019). Cancer associated fibroblasts: is the force the path to the dark side? *Curr Opin Cell Biol*, *56*, 71-79. https://doi.org/10.1016/j.ceb.2018.09.002

Bayne, L. J., Beatty, G. L., Jhala, N., Clark, C. E., Rhim, A. D., Stanger, B. Z., & Vonderheide, R. H. (2012). Tumor-derived granulocyte-macrophage colony-stimulating factor regulates myeloid inflammation and T cell immunity in pancreatic cancer. *Cancer Cell*, *21*(6), 822-835. https://doi.org/10.1016/j.ccr.2012.04.025

Borrego, A., Cabrera, W. H. K., Jensen, J. R., Correa, M., Ribeiro, O. G., Starobinas, N., De Franco, M., Pettinicchio, A., Dragani, T. A., Ibañez, O. C. M., & Manenti, G. (2018). Germline control of somatic Kras mutations in mouse lung tumors. *Mol Carcinog*, *57*(6), 745-751. https://doi.org/10.1002/mc.22796

Chen, B., Johanson, L., Wiest, J. S., Anderson, M. W., & You, M. (1994). The second intron of the K-ras gene contains regulatory elements associated with mouse lung tumor susceptibility. *Proc Natl Acad Sci U S A*, *91*(4), 1589-1593. https://doi.org/10.1073/pnas.91.4.1589

Cotroneo, C. E., Dassano, A., Colombo, F., Pettinicchio, A., Lecis, D., Dugo, M., De Cecco, L., Dragani, T. A., & Manenti, G. (2016). Expression quantitative trait analysis reveals fine germline transcript regulation in mouse lung tumors. *Cancer Lett*, *375*(2), 221-230. https://doi.org/10.1016/j.canlet.2016.02.054

Curiel, T. J., Coukos, G., Zou, L., Alvarez, X., Cheng, P., Mottram, P., Evdemon-Hogan, M., Conejo-Garcia, J. R., Zhang, L., Burow, M., Zhu, Y., Wei, S., Kryczek, I., Daniel, B., Gordon, A., Myers, L., Lackner, A., Disis, M. L., Knutson, K. L., . . . Zou, W. (2004). Specific recruitment of regulatory T cells in ovarian carcinoma fosters immune privilege and predicts reduced survival. *Nat Med*, *10*(9), 942-949. https://doi.org/10.1038/nm1093

Dahl, G. A., Miller, J. A., & Miller, E. C. (1978). Vinyl carbamate as a promutagen and a more carcinogenic analog of ethyl carbamate. *Cancer Res*, *38*(11 Pt 1), 3793-3804.

Dassano, A., Colombo, F., Trincucci, G., Frullanti, E., Galvan, A., Pettinicchio, A., De Cecco, L., Borrego, A., Martinez Ibañez, O. C., Dragani, T. A., & Manenti, G. (2014). Mouse Pulmonary Adenoma Susceptibility 1 Locus Is an Expression QTL Modulating Kras-4A. *PLoS Genetics*, *10*(4), e1004307. https://doi.org/10.1371/journal.pgen.1004307

Demaria, S., & Formenti, S. (2012). Role of T lymphocytes in tumor response to radiotherapy [Review]. *Frontiers in Oncology*, *2*. https://doi.org/10.3389/fonc.2012.00095

Deng, L., Liang, H., Burnette, B., Beckett, M., Darga, T., Weichselbaum, R. R., & Fu, Y. X. (2014). Irradiation and anti-PD-L1 treatment synergistically promote antitumor immunity in mice. *J Clin Invest*, *124*(2), 687-695. https://doi.org/10.1172/jci67313

Feig, C., Jones, J. O., Kraman, M., Wells, R. J., Deonarine, A., Chan, D. S., Connell, C. M., Roberts, E. W., Zhao, Q., Caballero, O. L., Teichmann, S. A., Janowitz, T., Jodrell, D. I., Tuveson, D. A., & Fearon, D. T. (2013). Targeting CXCL12 from FAP-expressing carcinoma-associated fibroblasts synergizes with anti-PD-L1 immunotherapy in pancreatic cancer. *Proc Natl Acad Sci U S A*, *110*(50), 20212-20217. https://doi.org/10.1073/pnas.1320318110

Field, K. J., & Lang, C. M. (1988). Hazards of urethane (ethyl carbamate): a review of the literature. *Laboratory Animals*, *22*(3), 255-262. https://doi.org/10.1258/002367788780746331

Forkert, P. G. (2010). Mechanisms of lung tumorigenesis by ethyl carbamate and vinyl carbamate. *Drug Metab Rev*, *42*(2), 355-378. https://doi.org/10.3109/03602531003611915

Formenti, S. C., & Demaria, S. (2013). Combining radiotherapy and cancer immunotherapy: a paradigm shift. *J Natl Cancer Inst*, *105*(4), 256-265. https://doi.org/10.1093/jnci/djs629

Frey, B., Rubner, Y., Wunderlich, R., Weiss, E. M., Pockley, A. G., Fietkau, R., & Gaipl, U. S. (2012). Induction of abscopal anti-tumor immunity and immunogenic tumor cell death by ionizing irradiation - implications for cancer therapies. *Curr Med Chem*, *19*(12), 1751-1764. https://doi.org/10.2174/092986712800099811

Galon, J., & Bruni, D. (2019). Approaches to treat immune hot, altered and cold tumours with combination immunotherapies. *Nature Reviews Drug Discovery*, *18*(3), 197-218. https://doi.org/10.1038/s41573-018-0007-y

Garcia, A. J., Ruscetti, M., Arenzana, T. L., Tran, L. M., Bianci-Frias, D., Sybert, E., Priceman, S. J., Wu, L., Nelson, P. S., Smale, S. T., & Wu, H. (2014). Pten null prostate epithelium promotes localized myeloid-derived suppressor cell expansion and immune suppression during tumor initiation and progression. *Mol Cell Biol*, *34*(11), 2017-2028. https://doi.org/10.1128/mcb.00090-14

Gariboldi, M., Manenti, G., Canzian, F., Falvella, F. S., Radice, M. T., Pierotti, M. A., Della Porta, G., Binelli, G., & Dragani, T. A. (1993). A major susceptibility locus to murine lung carcinogenesis maps on chromosome 6. *Nature genetics*, *3*(2), 132-136. https://doi.org/10.1038/ng0293-132

Giraldo, N. A., Sanchez-Salas, R., Peske, J. D., Vano, Y., Becht, E., Petitprez, F., Validire, P., Ingels, A., Cathelineau, X., Fridman, W. H., & Sautès-Fridman, C. (2019). The clinical role of the TME in solid cancer. *British Journal of Cancer*, *120*(1), 45-53. https://doi.org/10.1038/s41416-018-0327-z

Gooden, M. J., de Bock, G. H., Leffers, N., Daemen, T., & Nijman, H. W. (2011). The prognostic influence of tumour-infiltrating lymphocytes in cancer: a systematic

review with meta-analysis. *Br J Cancer*, *105*(1), 93-103. https://doi.org/10.1038/bjc.2011.189

Gunning, W. T., Castonguay, A., Goldblatt, P. J., & Stoner, G. D. (1991). Strain A/J mouse lung adenoma growth patterns vary when induced by different carcinogens. *Toxicol Pathol*, *19*(2), 168-175. https://doi.org/10.1177/019262339101900212

Hendry, S., Salgado, R., Gevaert, T., Russell, P. A., John, T., Thapa, B., Christie, M., Van De Vijver, K., Estrada, M. V., Gonzalez-Ericsson, P. I., Sanders, M., Solomon, B., Solinas, C., Van Den Eynden, G. G. G. M., Allory, Y., Preusser, M., Hainfellner, J., Pruneri, G., Vingiani, A., . . . Fox, S. B. (2017). Assessing Tumor-infiltrating Lymphocytes in Solid Tumors: A Practical Review for Pathologists and Proposal for a Standardized Method From the International Immunooncology Biomarkers Working Group: Part 1: Assessing the Host Immune Response, TILs in Invasi. *Advances in Anatomic Pathology*, *24*(5), 235-251. https://doi.org/10.1097/pap.0000000000000162

Hernandez, L. G., & Forkert, P.-G. (2007). In vivomutagenicity of vinyl carbamate and ethyl carbamate in lung and small intestine of F1(Big Blue® × A/J) transgenic mice. *International Journal of Cancer*, *120*(7), 1426-1433. https://doi.org/10.1002/ijc.22502

Horio, Y., Chen, A., Rice, P., Roth, J. A., Malkinson, A. M., & Schrump, D. S. (1996). Ki-ras and p53 mutations are early and late events, respectively, in urethane-induced pulmonary carcinogenesis in A/J mice. *Mol Carcinog*, *17*(4), 217-223. https://doi.org/10.1002/(sici)1098-2744(199612)17:4<217::Aid-mc5>3.0.Co;2-a

Jackson, I. L., Vujaskovic, Z., & Down, J. D. (2011). A further comparison of pathologies after thoracic irradiation among different mouse strains: finding the best preclinical model for evaluating therapies directed against radiation-induced lung damage. *Radiat Res*, *175*(4), 510-518. https://doi.org/10.1667/rr2421.1

Janeway, C. A. (2001). How the immune system works to protect the host from infection: A personal view. *Proceedings of the National Academy of Sciences*, *98*(13), 7461-7468. https://doi.org/10.1073/pnas.131202998

Jiang, Y., Martin, J., Alkadhimi, M., Shigemori, K., Kinchesh, P., Gilchrist, S., Kersemans, V., Smart, S., Thompson, J. M., Hill, M. A., O'Connor, M. J., Davies, B. R., & Ryan, A. J. (2021). Olaparib increases the therapeutic index of hemithoracic irradiation compared with hemithoracic irradiation alone in a mouse lung cancer model. *Br J Cancer*, *124*(11), 1809-1819. https://doi.org/10.1038/s41416-021-01296-y

Joyce, J. A., & Fearon, D. T. (2015). T cell exclusion, immune privilege, and the tumor microenvironment. *Science*, *348*(6230), 74-80. https://doi.org/10.1126/science.aaa6204

Koppensteiner, L., Mathieson, L., O'Connor, R. A., & Akram, A. R. (2022). Cancer Associated Fibroblasts - An Impediment to Effective Anti-Cancer T Cell Immunity. *Front Immunol*, *13*, 887380. https://doi.org/10.3389/fimmu.2022.887380

Lesokhin, A. M., Hohl, T. M., Kitano, S., Cortez, C., Hirschhorn-Cymerman, D., Avogadri, F., Rizzuto, G. A., Lazarus, J. J., Pamer, E. G., Houghton, A. N., Merghoub, T., & Wolchok, J. D. (2012). Monocytic CCR2(+) myeloid-derived suppressor cells promote immune escape by limiting activated CD8 T-cell infiltration into the tumor microenvironment. *Cancer Res*, *72*(4), 876-886. https://doi.org/10.1158/0008-5472.Can-11-1792

Li, Y., & Hecht, S. S. (2022). Carcinogenic components of tobacco and tobacco smoke: A 2022 update. *Food Chem Toxicol*, *165*, 113179. https://doi.org/10.1016/j.fct.2022.113179

Lourenco, L. H. M. (2017). *The old and the new: mouse models for evaluating the therapeutic margin of radiation in lung cancer* University of Oxford]. Oxford.

Malkinson, A. M. (1992). Primary lung tumors in mice: an experimentally manipulable model of human adenocarcinoma. *Cancer Res*, *52*(9 Suppl), 2670s-2676s. https://www.ncbi.nlm.nih.gov/pubmed/1562998

Martin, J. C. (2020). *The impact of DNA damage repair inhibitors on the therapeutic window of thoracic radiation* University of Oxford]. Oxford.

McBride, W. H., Chiang, C. S., Olson, J. L., Wang, C. C., Hong, J. H., Pajonk, F., Dougherty, G. J., Iwamoto, K. S., Pervan, M., & Liao, Y. P. (2004). A sense of danger from radiation. *Radiat Res*, *162*(1), 1-19. https://doi.org/10.1667/rr3196

Medrek, C., Pontén, F., Jirström, K., & Leandersson, K. (2012). The presence of tumor associated macrophages in tumor stroma as a prognostic marker for breast cancer patients. *BMC Cancer*, *12*, 306. https://doi.org/10.1186/1471-2407-12-306

Meng, Y., Beckett, M. A., Liang, H., Mauceri, H. J., van Rooijen, N., Cohen, K. S., & Weichselbaum, R. R. (2010). Blockade of tumor necrosis factor alpha signaling in tumor-associated macrophages as a radiosensitizing strategy. *Cancer Res*, *70*(4), 1534-1543. https://doi.org/10.1158/0008-5472.Can-09-2995

Molon, B., Ugel, S., Del Pozzo, F., Soldani, C., Zilio, S., Avella, D., De Palma, A., Mauri, P., Monegal, A., Rescigno, M., Savino, B., Colombo, P., Jonjic, N., Pecanic, S., Lazzarato, L., Fruttero, R., Gasco, A., Bronte, V., & Viola, A. (2011). Chemokine nitration prevents intratumoral infiltration of antigen-specific T cells. *Journal of Experimental Medicine*, *208*(10), 1949-1962. https://doi.org/10.1084/jem.20101956

Monteran, L., & Erez, N. (2019). The Dark Side of Fibroblasts: Cancer-Associated Fibroblasts as Mediators of Immunosuppression in the Tumor Microenvironment. *Front Immunol*, *10*, 1835. https://doi.org/10.3389/fimmu.2019.01835

Mostofi, F. K., & Larsen, C. D. (1951). The Histopathogenesis of Pulmonary Tumors Induced in Strain a Mice by Urethan2. *JNCI: Journal of the National Cancer Institute*, *11*(6), 1187-1221. https://doi.org/10.1093/jnci/11.6.1187

Motz, G. T., Santoro, S. P., Wang, L. P., Garrabrant, T., Lastra, R. R., Hagemann, I. S., Lal, P., Feldman, M. D., Benencia, F., & Coukos, G. (2014). Tumor endothelium FasL establishes a selective immune barrier promoting tolerance in tumors. *Nat Med*, *20*(6), 607-615. https://doi.org/10.1038/nm.3541

Paolo, Cuevas, C., Amy, Vikas, Daniel, & Sunil. (2012). Enzymatic Targeting of the Stroma Ablates Physical Barriers to Treatment of Pancreatic Ductal Adenocarcinoma. *Cancer Cell*, *21*(3), 418-429. https://doi.org/10.1016/j.ccr.2012.01.007

Paun, A., Bergeron, M.-E., & Haston, C. K. (2017). The Th1/Th17 balance dictates the fibrosis response in murine radiation-induced lung disease. *Scientific reports*, *7*(1), 11586. Retrieved 2017/09//, from http://europepmc.org/abstract/MED/28912510

https://doi.org/10.1038/s41598-017-11656-5

https://europepmc.org/articles/PMC5599556

https://europepmc.org/articles/PMC5599556?pdf=render

Provenzano, P. P., Eliceiri, K. W., Campbell, J. M., Inman, D. R., White, J. G., & Keely, P. J. (2006). Collagen reorganization at the tumor-stromal interface facilitates local invasion. *BMC Med*, *4*(1), 38. https://doi.org/10.1186/1741-7015-4-38

Sahai, E., Astsaturov, I., Cukierman, E., Denardo, D. G., Egeblad, M., Evans, R. M., Fearon, D., Greten, F. R., Hingorani, S. R., Hunter, T., Hynes, R. O., Jain, R. K., Janowitz, T., Jorgensen, C., Kimmelman, A. C., Kolonin, M. G., Maki, R. G., Powers, R. S., Puré, E., . . . Werb, Z. (2020). A framework for advancing our understanding of cancer-associated fibroblasts. *Nature Reviews Cancer*, *20*(3), 174-186. https://doi.org/10.1038/s41568-019-0238-1

Salmon, H., & Donnadieu, E. (2012). Within tumors, interactions between T cells and tumor cells are impeded by the extracellular matrix. *Oncoimmunology*, *1*(6), 992-994. https://doi.org/10.4161/onci.20239

Schaue, D., Kachikwu, E. L., & McBride, W. H. (2012). Cytokines in radiobiological responses: a review. *Radiat Res*, *178*(6), 505-523. https://doi.org/10.1667/rr3031.1

Strachan, D. C., Ruffell, B., Oei, Y., Bissell, M. J., Coussens, L. M., Pryer, N., & Daniel, D. (2013). CSF1R inhibition delays cervical and mammary tumor growth in murine models by attenuating the turnover of tumor-associated macrophages and enhancing infiltration by CD8(+) T cells. *Oncoimmunology*, *2*(12), e26968. https://doi.org/10.4161/onci.26968

Titis, A. P., & Forkert, P. G. (2001). Strain-related differences in bioactivation of vinyl carbamate and formation of DNA adducts in lungs of A/J, CD-1, and C57BL/6 mice. *Toxicological sciences : an official journal of the Society of Toxicology*, *59 1*, 82-91.

To, M. D., Perez-Losada, J., Mao, J.-H., Hsu, J., Jacks, T., & Balmain, A. (2006). A functional switch from lung cancer resistance to susceptibility at the Pas1 locus in Kras2LA2 mice. *Nature genetics*, *38*(8), 926-930. https://doi.org/10.1038/ng1836

Weichselbaum, R., Fu, Y.-X., & Burnette, B. (2012). The confluence of radiotherapy and immunotherapy [Review]. *Frontiers in Oncology*, *2*. https://doi.org/10.3389/fonc.2012.00143

White, M. R., Grendon, A., & Jones, H. B. (1970). Tumor incidence and cellularity in lungs of mice given various dose schedules of urethan. *Cancer Res*, *30*(4), 1030-1036.

Zappa, C., & Mousa, S. A. (2016). Non-small cell lung cancer: current treatment and future advances. *Translational Lung Cancer Research*, *5*(3), 288-300. https://doi.org/10.21037/tlcr.2016.06.07

Chapter 4

Altorki, N. K., Markowitz, G. J., Gao, D., Port, J. L., Saxena, A., Stiles, B., McGraw, T., & Mittal, V. (2019). The lung microenvironment: an important regulator of tumour growth and metastasis. *Nat Rev Cancer*, *19*(1), 9-31. https://doi.org/10.1038/s41568-018-0081-9

Boivin, G., Kalambaden, P., Faget, J., Rusakiewicz, S., Montay-Gruel, P., Meylan, E., Bourhis, J., Lesec, G., & Vozenin, M. C. (2018). Cellular Composition and Contribution of Tertiary Lymphoid Structures to Tumor Immune Infiltration and Modulation by Radiation Therapy. *Front Oncol*, *8*, 256. https://doi.org/10.3389/fonc.2018.00256

Cabrita, R., Lauss, M., Sanna, A., Donia, M., Skaarup Larsen, M., Mitra, S., Johansson, I., Phung, B., Harbst, K., Vallon-Christersson, J., van Schoiack, A., Lövgren, K., Warren, S., Jirström, K., Olsson, H., Pietras, K., Ingvar, C., Isaksson, K., Schadendorf, D., . . . Jönsson, G. (2020). Tertiary lymphoid structures improve immunotherapy and survival in melanoma. *Nature*, *577*(7791), 561-565. https://doi.org/10.1038/s41586-019-1914-8

Colbeck, E. J., Ager, A., Gallimore, A., & Jones, G. W. (2017). Tertiary Lymphoid Structures in Cancer: Drivers of Antitumor Immunity, Immunosuppression, or Bystander Sentinels in Disease? *Front Immunol*, *8*, 1830. https://doi.org/10.3389/fimmu.2017.01830

Dieu-Nosjean, M. C., Giraldo, N. A., Kaplon, H., Germain, C., Fridman, W. H., & Sautès-Fridman, C. (2016). Tertiary lymphoid structures, drivers of the anti-tumor responses in human cancers. *Immunol Rev*, *271*(1), 260-275. https://doi.org/10.1111/imr.12405

Gan, Y., Li, X., Han, S., Liang, Q., Ma, X., Rong, P., Wang, W., & Li, W. (2022). The cGAS/STING Pathway: A Novel Target for Cancer Therapy [Review]. *Frontiers in Immunology*, *12*. https://doi.org/10.3389/fimmu.2021.795401

Helmink, B. A., Reddy, S. M., Gao, J., Zhang, S., Basar, R., Thakur, R., Yizhak, K., Sade-Feldman, M., Blando, J., Han, G., Gopalakrishnan, V., Xi, Y., Zhao, H., Amaria, R. N., Tawbi, H. A., Cogdill, A. P., Liu, W., Lebleu, V. S., Kugeratski, F. G., . . . Wargo, J. A. (2020). B cells and tertiary lymphoid structures promote immunotherapy response. *Nature*, *577*(7791), 549-555. https://doi.org/10.1038/s41586-019-1922-8

Ingulli, E. (2010). Mechanism of cellular rejection in transplantation. *Pediatr Nephrol*, *25*(1), 61-74. https://doi.org/10.1007/s00467-008-1020-x

Lauss, M., Donia, M., Svane, I. M., & Jonsson, G. (2022). B Cells and Tertiary Lymphoid Structures: Friends or Foes in Cancer Immunotherapy? *Clin Cancer Res*, *28*(9), 1751-1758. https://doi.org/10.1158/1078-0432.CCR-21-1130

Lhuillier, C., Rudqvist, N. P., Elemento, O., Formenti, S. C., & Demaria, S. (2019). Radiation therapy and anti-tumor immunity: exposing immunogenic mutations to the immune system. *Genome Med*, *11*(1), 40. https://doi.org/10.1186/s13073-019-0653-7

Little, J. B. (2000). Radiation carcinogenesis. *Carcinogenesis*, *21*(3), 397-404. https://doi.org/10.1093/carcin/21.3.397

Lutz, E. R., Wu, A. A., Bigelow, E., Sharma, R., Mo, G., Soares, K., Solt, S., Dorman, A., Wamwea, A., Yager, A., Laheru, D., Wolfgang, C. L., Wang, J., Hruban, R. H., Anders, R. A., Jaffee, E. M., & Zheng, L. (2014). Immunotherapy converts nonimmunogenic pancreatic tumors into immunogenic foci of immune regulation. *Cancer Immunol Res*, *2*(7), 616-631. https://doi.org/10.1158/2326-6066.Cir-14-0027

Maldonado, L., Teague, J. E., Morrow, M. P., Jotova, I., Wu, T. C., Wang, C., Desmarais, C., Boyer, J. D., Tycko, B., Robins, H. S., Clark, R. A., & Trimble, C. L. (2014). Intramuscular therapeutic vaccination targeting HPV16 induces T cell responses that localize in mucosal lesions. *Sci Transl Med*, *6*(221), 221ra213. https://doi.org/10.1126/scitranslmed.3007323

Ozasa, K., Shimizu, Y., Suyama, A., Kasagi, F., Soda, M., Grant, E. J., Sakata, R., Sugiyama, H., & Kodama, K. (2012). Studies of the mortality of atomic bomb survivors, Report 14, 1950-2003: an overview of cancer and noncancer diseases. *Radiat Res*, *177*(3), 229-243. https://doi.org/10.1667/rr2629.1

Petitprez, F., de Reyniès, A., Keung, E. Z., Chen, T. W., Sun, C. M., Calderaro, J., Jeng, Y. M., Hsiao, L. P., Lacroix, L., Bougoüin, A., Moreira, M., Lacroix, G., Natario, I., Adam, J., Lucchesi, C., Laizet, Y. H., Toulmonde, M., Burgess, M. A., Bolejack, V., . . . Fridman, W. H. (2020). B cells are associated with survival and immunotherapy response in sarcoma. *Nature*, *577*(7791), 556-560. https://doi.org/10.1038/s41586-019-1906-8

Qin, M., Hamanishi, J., Ukita, M., Yamanoi, K., Takamatsu, S., Abiko, K., Murakami, R., Miyamoto, T., Suzuki, H., Ueda, A., Hosoe, Y., Horie, A., Yamaguchi, K., & Mandai, M. (2022). Tertiary lymphoid structures are associated with favorable survival outcomes in patients with endometrial cancer. *Cancer Immunol Immunother*, *71*(6), 1431-1442. https://doi.org/10.1007/s00262-021-03093-1

Raaby Gammelgaard, K., Sandfeld-Paulsen, B., Godsk, S. H., Demuth, C., Meldgaard, P., Sorensen, B. S., & Jakobsen, M. R. (2020). cGAS-STING pathway expression as a prognostic tool in NSCLC. *Translational Lung Cancer Research*, *10*(1), 340-354. https://tlcr.amegroups.com/article/view/46144

Rosenthal, R., Cadieux, E. L., Salgado, R., Bakir, M. A., Moore, D. A., Hiley, C. T., Lund, T., Tanic, M., Reading, J. L., Joshi, K., Henry, J. Y., Ghorani, E., Wilson, G. A., Birkbak, N. J., Jamal-Hanjani, M., Veeriah, S., Szallasi, Z., Loi, S., Hellmann, M. D., . . . consortium, T. R. (2019). Neoantigen-directed immune escape in lung cancer evolution. *Nature*, *567*(7749), 479-485. https://doi.org/10.1038/s41586-019-1032-7

Ruffin, A. T., Cillo, A. R., Tabib, T., Liu, A., Onkar, S., Kunning, S. R., Lampenfeld, C., Atiya, H. I., Abecassis, I., Kurten, C. H. L., Qi, Z., Soose, R., Duvvuri, U., Kim, S., Oesterrich, S., Lafyatis, R., Coffman, L. G., Ferris, R. L., Vignali, D. A. A., & Bruno, T. C. (2021). B cell signatures and tertiary lymphoid structures contribute to outcome in head and neck squamous cell carcinoma. *Nat Commun*, *12*(1), 3349. https://doi.org/10.1038/s41467-021-23355-x

Sautès-Fridman, C., Lawand, M., Giraldo, N. A., Kaplon, H., Germain, C., Fridman, W. H., & Dieu-Nosjean, M. C. (2016). Tertiary Lymphoid Structures in Cancers: Prognostic Value, Regulation, and Manipulation for Therapeutic Intervention. *Front Immunol*, *7*, 407. https://doi.org/10.3389/fimmu.2016.00407

Sautes-Fridman, C., Petitprez, F., Calderaro, J., & Fridman, W. H. (2019). Tertiary lymphoid structures in the era of cancer immunotherapy. *Nat Rev Cancer*, *19*(6), 307-325. https://doi.org/10.1038/s41568-019-0144-6

Teijaro, J. R., Ng, C., Lee, A. M., Sullivan, B. M., Sheehan, K. C. F., Welch, M., Schreiber, R. D., Carlos de la Torre, J., & Oldstone, M. B. A. (2013). Persistent LCMV Infection Is Controlled by Blockade of Type I Interferon Signaling. *Science*, *340*(6129), 207-211. https://doi.org/10.1126/science.1235214

Tian, Y., Zhai, X., Yan, W., Zhu, H., & Yu, J. (2021). Clinical outcomes of immune checkpoint blockades and the underlying immune escape mechanisms in squamous and adenocarcinoma NSCLC. *Cancer Med*, *10*(1), 3-14. https://doi.org/10.1002/cam4.3590

Wang, S.-S., Liu, W., Ly, D., Xu, H., Qu, L., & Zhang, L. (2019). Tumor-infiltrating B cells: their role and application in anti-tumor immunity in lung cancer. *Cellular & Molecular Immunology*, *16*(1), 6-18. https://doi.org/10.1038/s41423-018-0027-x

Wennhold, K., Thelen, M., Lehmann, J., Schran, S., Preugszat, E., Garcia-Marquez, M., Lechner, A., Shimabukuro-Vornhagen, A., Ercanoglu, M. S., Klein, F., Thangarajah, F., Eidt, S., Loser, H., Bruns, C., Quaas, A., von Bergwelt-Baildon, M., & Schlosser, H. A. (2021). CD86(+) Antigen-Presenting B Cells Are Increased in Cancer, Localize in Tertiary Lymphoid Structures, and Induce Specific T-cell Responses. *Cancer Immunol Res*, *9*(9), 1098-1108. https://doi.org/10.1158/2326-6066.CIR-20-0949

Williams, D. (2008). Radiation carcinogenesis: lessons from Chernobyl. *Oncogene*, *27*(2), S9-S18. https://doi.org/10.1038/onc.2009.349

Wilson, E. B., Yamada, D. H., Elsaesser, H., Herskovitz, J., Deng, J., Cheng, G., Aronow, B. J., Karp, C. L., & Brooks, D. G. (2013). Blockade of Chronic Type I Interferon Signaling to Control Persistent LCMV Infection. *Science*, *340*(6129), 202-207. https://doi.org/10.1126/science.1235208

Chapter 5

Ahn, J., Xia, T., Konno, H., Konno, K., Ruiz, P., & Barber, G. N. (2014). Inflammation-driven carcinogenesis is mediated through STING. *Nat Commun*, *5*, 5166. https://doi.org/10.1038/ncomms6166

Bakhoum, S. F. (2022). cGAS–STING and the deadly CIN: how chronic inflammation represents a therapeutic vulnerability in chromosomally unstable cancers. *Trends in Cancer*. https://doi.org/10.1016/j.trecan.2022.07.006

Barbie, D. A., Tamayo, P., Boehm, J. S., Kim, S. Y., Moody, S. E., Dunn, I. F., Schinzel, A. C., Sandy, P., Meylan, E., Scholl, C., Fröhling, S., Chan, E. M., Sos, M. L., Michel, K., Mermel, C., Silver, S. J., Weir, B. A., Reiling, J. H., Sheng, Q., . . . Hahn, W. C. (2009). Systematic RNA interference reveals that oncogenic KRAS-driven cancers require TBK1. *Nature*, *462*(7269), 108-112. https://doi.org/10.1038/nature08460

Coppé, J. P., Patil, C. K., Rodier, F., Sun, Y., Muñoz, D. P., Goldstein, J., Nelson, P. S., Desprez, P. Y., & Campisi, J. (2008). Senescence-associated secretory phenotypes reveal cell-nonautonomous functions of oncogenic RAS and the p53 tumor suppressor. *PLoS Biol*, *6*(12), 2853-2868. https://doi.org/10.1371/journal.pbio.0060301

Diamond, M. S., Kinder, M., Matsushita, H., Mashayekhi, M., Dunn, G. P., Archambault, J. M., Lee, H., Arthur, C. D., White, J. M., Kalinke, U., Murphy, K. M., & Schreiber, R. D. (2011). Type I interferon is selectively required by dendritic cells for immune rejection of tumors. *J Exp Med*, *208*(10), 1989-2003. https://doi.org/10.1084/jem.20101158

Dou, Z., Ghosh, K., Vizioli, M. G., Zhu, J., Sen, P., Wangensteen, K. J., Simithy, J., Lan, Y., Lin, Y., Zhou, Z., Capell, B. C., Xu, C., Xu, M., Kieckhaefer, J. E., Jiang, T., Shoshkes-Carmel, M., Tanim, K., Barber, G. N., Seykora, J. T., . . . Berger, S. L. (2017). Cytoplasmic chromatin triggers inflammation in senescence and cancer. *Nature*, *550*(7676), 402-406. https://doi.org/10.1038/nature24050

Feldman, C., & Anderson, R. (2013). Cigarette smoking and mechanisms of susceptibility to infections of the respiratory tract and other organ systems. *J Infect*, *67*(3), 169-184. https://doi.org/10.1016/j.jinf.2013.05.004

Glück, S., Guey, B., Gulen, M. F., Wolter, K., Kang, T. W., Schmacke, N. A., Bridgeman, A., Rehwinkel, J., Zender, L., & Ablasser, A. (2017). Innate immune sensing of cytosolic chromatin fragments through cGAS promotes senescence. *Nat Cell Biol*, *19*(9), 1061-1070. https://doi.org/10.1038/ncb3586

Harlin, H., Meng, Y., Peterson, A. C., Zha, Y., Tretiakova, M., Slingluff, C., McKee, M., & Gajewski, T. F. (2009). Chemokine expression in melanoma metastases associated with CD8+ T-cell recruitment. *Cancer Res*, *69*(7), 3077-3085. https://doi.org/10.1158/0008-5472.Can-08-2281

Konno, H., Yamauchi, S., Berglund, A., Putney, R. M., Mulé, J. J., & Barber, G. N. (2018). Suppression of STING signaling through epigenetic silencing and missense mutation impedes DNA damage mediated cytokine production. *Oncogene*, *37*(15), 2037-2051. https://doi.org/10.1038/s41388-017-0120-0

Liang, D., Xiao-Feng, H., Guan-Jun, D., Er-Ling, H., Sheng, C., Ting-Ting, W., Qin-Gang, H., Yan-Hong, N., & Ya-Yi, H. (2015). Activated STING enhances Tregs infiltration in the HPV-related carcinogenesis of tongue squamous cells via the c-jun/CCL22 signal. *Biochim Biophys Acta*, *1852*(11), 2494-2503. https://doi.org/10.1016/j.bbadis.2015.08.011

Liang, H., Deng, L., Hou, Y., Meng, X., Huang, X., Rao, E., Zheng, W., Mauceri, H., Mack, M., Xu, M., Fu, Y. X., & Weichselbaum, R. R. (2017). Host STING-dependent MDSC mobilization drives extrinsic radiation resistance. *Nat Commun*, *8*(1), 1736. https://doi.org/10.1038/s41467-017-01566-5

Marcus, A., Mao, A. J., Lensink-Vasan, M., Wang, L., Vance, R. E., & Raulet, D. H. (2018). Tumor-Derived cGAMP Triggers a STING-Mediated Interferon Response in Non-tumor Cells to Activate the NK Cell Response. *Immunity*, *49*(4), 754-763.e754. https://doi.org/10.1016/j.immuni.2018.09.016

Mehta, H., Nazzal, K., & Sadikot, R. T. (2008). Cigarette smoking and innate immunity. *Inflamm Res*, *57*(11), 497-503. https://doi.org/10.1007/s00011-008-8078-6

Qiu, F., Liang, C. L., Liu, H., Zeng, Y. Q., Hou, S., Huang, S., Lai, X., & Dai, Z. (2017). Impacts of cigarette smoking on immune responsiveness: Up and down or upside down? *Oncotarget*, *8*(1), 268-284. https://doi.org/10.18632/oncotarget.13613

Ranoa, D. R. E., Widau, R. C., Mallon, S., Parekh, A. D., Nicolae, C. M., Huang, X., Bolt, M. J., Arina, A., Parry, R., Kron, S. J., Moldovan, G. L., Khodarev, N. N., & Weichselbaum, R. R. (2019). STING Promotes Homeostasis via Regulation of Cell Proliferation and Chromosomal Stability. *Cancer Res*, *79*(7), 1465-1479. https://doi.org/10.1158/0008-5472.Can-18-1972

Ritchie, C., Cordova, A. F., Hess, G. T., Bassik, M. C., & Li, L. (2019). SLC19A1 Is an Importer of the Immunotransmitter cGAMP. *Mol Cell*, *75*(2), 372-381.e375. https://doi.org/10.1016/j.molcel.2019.05.006

Song, S., Peng, P., Tang, Z., Zhao, J., Wu, W., Li, H., Shao, M., Li, L., Yang, C., Duan, F., Zhang, M., Zhang, J., Wu, H., Li, C., Wang, X., Wang, H., Ruan, Y., & Gu, J. (2017). Decreased expression of STING predicts poor prognosis in patients with gastric cancer. *Scientific reports*, *7*, 39858. https://doi.org/10.1038/srep39858

Woo, S. R., Fuertes, M. B., Corrales, L., Spranger, S., Furdyna, M. J., Leung, M. Y., Duggan, R., Wang, Y., Barber, G. N., Fitzgerald, K. A., Alegre, M. L., & Gajewski, T. F. (2014). STING-dependent cytosolic DNA sensing mediates innate immune recognition of immunogenic tumors. *Immunity*, *41*(5), 830-842. https://doi.org/10.1016/j.immuni.2014.10.017

Xia, T., Konno, H., Ahn, J., & Barber, G. N. (2016). Deregulation of STING Signaling in Colorectal Carcinoma Constrains DNA Damage Responses and Correlates With Tumorigenesis. *Cell Rep*, *14*(2), 282-297. https://doi.org/10.1016/j.celrep.2015.12.029

Xia, T., Konno, H., & Barber, G. N. (2016). Recurrent Loss of STING Signaling in Melanoma Correlates with Susceptibility to Viral Oncolysis. *Cancer Res*, *76*(22), 6747-6759. https://doi.org/10.1158/0008-5472.Can-16-1404

Yang, H., Wang, H., Ren, J., Chen, Q., & Chen, Z. J. (2017). cGAS is essential for cellular senescence. *Proc Natl Acad Sci U S A*, *114*(23), E4612-e4620. https://doi.org/10.1073/pnas.1705499114

Chapter 6

Antonia, S. J., Villegas, A., Daniel, D., Vicente, D., Murakami, S., Hui, R., Yokoi, T., Chiappori, A., Lee, K. H., de Wit, M., Cho, B. C., Bourhaba, M., Quantin, X., Tokito, T., Mekhail, T., Planchard, D., Kim, Y. C., Karapetis, C. S., Hiret, S., . . . Investigators, P. (2017). Durvalumab after Chemoradiotherapy in Stage III Non-Small-Cell Lung Cancer. *N Engl J Med*, *377*(20), 1919-1929. https://doi.org/10.1056/NEJMoa1709937

Bergmann, O., Zdunek, S., Felker, A., Salehpour, M., Alkass, K., Bernard, S., Sjostrom, S. L., Szewczykowska, M., Jackowska, T., Dos Remedios, C., Malm, T., Andra, M., Jashari, R., Nyengaard, J. R., Possnert, G., Jovinge, S., Druid, H., & Frisen, J. (2015). Dynamics of Cell Generation and Turnover in the Human Heart. *Cell*, *161*(7), 1566-1575. https://doi.org/10.1016/j.cell.2015.05.026

Brouillette, J., Cyr, S., & Fiset, C. (2019). Mechanisms of Arrhythmia and Sudden Cardiac Death in Patients With HIV Infection. *Can J Cardiol*, *35*(3), 310-319. https://doi.org/10.1016/j.cjca.2018.12.015

Cao, D. J., Schiattarella, G. G., Villalobos, E., Jiang, N., May, H. I., Li, T., Chen, Z. J., Gillette, T. G., & Hill, J. A. (2018). Cytosolic DNA Sensing Promotes Macrophage Transformation and Governs Myocardial Ischemic Injury. *Circulation*, *137*(24), 2613-2634. https://doi.org/10.1161/CIRCULATIONAHA.117.031046

de Jong, S., van Veen, T. A., van Rijen, H. V., & de Bakker, J. M. (2011). Fibrosis and cardiac arrhythmias. *J Cardiovasc Pharmacol*, *57*(6), 630-638. https://doi.org/10.1097/FJC.0b013e318207a35f

Fenech, M., Kirsch-Volders, M., Natarajan, A. T., Surralles, J., Crott, J. W., Parry, J., Norppa, H., Eastmond, D. A., Tucker, J. D., & Thomas, P. (2011). Molecular mechanisms of micronucleus, nucleoplasmic bridge and nuclear bud formation in mammalian and human cells. *Mutagenesis*, *26*(1), 125-132. https://doi.org/10.1093/mutage/geq052

Frangogiannis, N. G. (2014). The inflammatory response in myocardial injury, repair, and remodelling. *Nat Rev Cardiol*, *11*(5), 255-265. https://doi.org/10.1038/nrcardio.2014.28

Frangogiannis, N. G. (2019). Cardiac fibrosis: Cell biological mechanisms, molecular pathways and therapeutic opportunities. *Mol Aspects Med*, *65*, 70-99. https://doi.org/10.1016/j.mam.2018.07.001

Franko, A. J., Sharplin, J., Ward, W. F., & Hinz, J. M. (1991). The genetic basis of strain-dependent differences in the early phase of radiation injury in mouse lung. *Radiat Res*, *126*(3), 349-356. https://www.ncbi.nlm.nih.gov/pubmed/1852022

Frantz, S., & Nahrendorf, M. (2014). Cardiac macrophages and their role in ischaemic heart disease. *Cardiovasc Res*, *102*(2), 240-248. https://doi.org/10.1093/cvr/cvu025

Hashimoto, H., Olson, E. N., & Bassel-Duby, R. (2018). Therapeutic approaches for cardiac regeneration and repair. *Nat Rev Cardiol*, *15*(10), 585-600. https://doi.org/10.1038/s41569-018-0036-6

Higo, T., Naito, A. T., Sumida, T., Shibamoto, M., Okada, K., Nomura, S., Nakagawa, A., Yamaguchi, T., Sakai, T., Hashimoto, A., Kuramoto, Y., Ito, M., Hikoso, S.,

Akazawa, H., Lee, J.-K., Shiojima, I., McKinnon, P. J., Sakata, Y., & Komuro, I. (2017). DNA single-strand break-induced DNA damage response causes heart failure. *Nature Communications*, *8*(1), 15104. https://doi.org/10.1038/ncomms15104

Hulsmans, M., Clauss, S., Xiao, L., Aguirre, A. D., King, K. R., Hanley, A., Hucker, W. J., Wulfers, E. M., Seemann, G., Courties, G., Iwamoto, Y., Sun, Y., Savol, A. J., Sager, H. B., Lavine, K. J., Fishbein, G. A., Capen, D. E., Da Silva, N., Miquerol, L., . . . Nahrendorf, M. (2017). Macrophages Facilitate Electrical Conduction in the Heart. *Cell*, *169*(3), 510-522 e520. https://doi.org/10.1016/j.cell.2017.03.050

Jackson, I. L., Vujaskovic, Z., & Down, J. D. (2010). Revisiting strain-related differences in radiation sensitivity of the mouse lung: recognizing and avoiding the confounding effects of pleural effusions. *Radiat Res*, *173*(1), 10-20. https://doi.org/10.1667/RR1911.1

Kazbanov, I. V., ten Tusscher, K. H., & Panfilov, A. V. (2016). Effects of Heterogeneous Diffuse Fibrosis on Arrhythmia Dynamics and Mechanism. *Scientific reports*, *6*, 20835. https://doi.org/10.1038/srep20835

King, K. R., Aguirre, A. D., Ye, Y. X., Sun, Y., Roh, J. D., Ng, R. P., Jr., Kohler, R. H., Arlauckas, S. P., Iwamoto, Y., Savol, A., Sadreyev, R. I., Kelly, M., Fitzgibbons, T. P., Fitzgerald, K. A., Mitchison, T., Libby, P., Nahrendorf, M., & Weissleder, R. (2017). IRF3 and type I interferons fuel a fatal response to myocardial infarction. *Nat Med*, *23*(12), 1481-1487. https://doi.org/10.1038/nm.4428

Kotova, S. L., Timashev, P. S., Belkova, G. V., Kochueva, M. V., Babak, K. V., Timofeeva, V. A., Kiseleva, E. B., Vasilieva, O. O., Maslennikova, A. V., & Solovieva, A. B. (2018). Early Effects of Ionizing Radiation on the Collagen Hierarchical Structure of Bladder and Rectum Visualized by Atomic Force Microscopy. *Microscopy and Microanalysis*, *24*(1), 38-48. https://doi.org/10.1017/S1431927618000065

Laflamme, M. A., Sebastian, M. M., & Buetow, B. S. (2012). 10 - Cardiovascular. In P. M. Treuting & S. M. Dintzis (Eds.), *Comparative Anatomy and Histology* (pp. 135-153). Academic Press. https://doi.org/https://doi.org/10.1016/B978-0-12-381361-9.00010-X

Lafontant, P. J., & Field, L. J. (2006). The cardiomyocyte cell cycle. *Novartis Found Symp*, *274*, 196-207; discussion 208-113, 272-196. https://doi.org/10.1002/0470029331.ch12

Luzhna, L., Kathiria, P., & Kovalchuk, O. (2013). Micronuclei in genotoxicity assessment: from genetics to epigenetics and beyond. *Front Genet*, *4*, 131. https://doi.org/10.3389/fgene.2013.00131

Martin, J. C. (2021). University of Oxford]. Oxford.

Monceau, V., Llach, A., Azria, D., Bridier, A., Petit, B., Mazevet, M., Strup-Perrot, C., To, T. H., Calmels, L., Germaini, M. M., Gourgou, S., Fenoglietto, P., Bourgier, C., Gomez, A. M., Escoubet, B., Dörr, W., Haagen, J., Deutsch, E., Morel, E., & Vozenin, M. C. (2014). Epac contributes to cardiac hypertrophy and amyloidosis

induced by radiotherapy but not fibrosis. *Radiother Oncol*, *111*(1), 63-71. https://doi.org/10.1016/j.radonc.2014.01.025

Oka, T., Hikoso, S., Yamaguchi, O., Taneike, M., Takeda, T., Tamai, T., Oyabu, J., Murakawa, T., Nakayama, H., Nishida, K., Akira, S., Yamamoto, A., Komuro, I., & Otsu, K. (2012). Mitochondrial DNA that escapes from autophagy causes inflammation and heart failure. *Nature*, *485*(7397), 251-255. https://doi.org/10.1038/nature10992

Orecchioni, M., Ghosheh, Y., Pramod, A. B., & Ley, K. (2019). Macrophage Polarization: Different Gene Signatures in M1(LPS+) vs. Classically and M2(LPS-) vs. Alternatively Activated Macrophages. *Front Immunol*, *10*, 1084. https://doi.org/10.3389/fimmu.2019.01084

Porrello, E. R., & Olson, E. N. (2014). A neonatal blueprint for cardiac regeneration. *Stem Cell Res*, *13*(3 Pt B), 556-570. https://doi.org/10.1016/j.scr.2014.06.003

Seemann, I., Gabriels, K., Visser, N. L., Hoving, S., te Poele, J. A., Pol, J. F., Gijbels, M. J., Janssen, B. J., van Leeuwen, F. W., Daemen, M. J., Heeneman, S., & Stewart, F. A. (2012). Irradiation induced modest changes in murine cardiac function despite progressive structural damage to the myocardium and microvasculature. *Radiother Oncol*, *103*(2), 143-150. https://doi.org/10.1016/j.radonc.2011.10.011

Shamseddine, A., Patel, S. H., Chavez, V., Adnan, M., Bona, M. D., Li, J., Dang, C. T., Ramanathan, L. V., Oeffinger, K. C., Liu, J. E., Steingart, R. M., Piersigilli, A., Socci, N. D., Chan, A. T., Yu, A. F., Bakhoum, S. F., & Schmitt, A. M. (2021). *Innate immune signaling drives late cardiac toxicity following DNA damaging cancer therapies*. bioRxiv. https://dx.doi.org/10.1101/2021.09.26.461865

Sharplin, J., & Franko, A. J. (1989). A quantitative histological study of strain-dependent differences in the effects of irradiation on mouse lung during the early phase. *Radiat Res*, *119*(1), 1-14. https://www.ncbi.nlm.nih.gov/pubmed/2756101

Soonpaa, M. H., & Field, L. J. (1998). Survey of studies examining mammalian cardiomyocyte DNA synthesis. *Circ Res*, *83*(1), 15-26. https://doi.org/10.1161/01.res.83.1.15

Uygur, A., & Lee, R. T. (2016). Mechanisms of Cardiac Regeneration. *Dev Cell*, *36*(4), 362-374. https://doi.org/10.1016/j.devcel.2016.01.018

van der Veen, S. J., Ghobadi, G., de Boer, R. A., Faber, H., Cannon, M. V., Nagle, P. W., Brandenburg, S., Langendijk, J. A., van Luijk, P., & Coppes, R. P. (2015). ACE inhibition attenuates radiation-induced cardiopulmonary damage. *Radiother Oncol*, *114*(1), 96-103. https://doi.org/10.1016/j.radonc.2014.11.017

Wang, K., Pearlstein, K. A., Patchett, N. D., Deal, A. M., Mavroidis, P., Jensen, B. C., Lipner, M. B., Zagar, T. M., Wang, Y., Lee, C. B., Eblan, M. J., Rosenman, J. G., Socinski, M. A., Stinchcombe, T. E., & Marks, L. B. (2017). Heart dosimetric analysis of three types of cardiac toxicity in patients treated on dose-escalation trials for Stage III non-small-cell lung cancer. *Radiother Oncol*, *125*(2), 293-300. https://doi.org/10.1016/j.radonc.2017.10.001

Xu, S., Xu, H., Wang, W., Li, S., Li, H., Li, T., Zhang, W., Yu, X., & Liu, L. (2019). The role of collagen in cancer: from bench to bedside. *J Transl Med*, *17*(1), 309. https://doi.org/10.1186/s12967-019-2058-1

Uncategorized References

Adams, M. J., Lipsitz, S. R., Colan, S. D., Tarbell, N. J., Treves, S. T., Diller, L., Greenbaum, N., Mauch, P., & Lipshultz, S. E. (2004). Cardiovascular Status in Long-Term Survivors of Hodgkin's Disease Treated With Chest Radiotherapy. *Journal of Clinical Oncology*, *22*(15), 3139-3148. https://doi.org/10.1200/JCO.2004.09.109

Biswas, S. K., & Mantovani, A. (2010). Macrophage plasticity and interaction with lymphocyte subsets: cancer as a paradigm. *Nature Immunology*, *11*(10), 889-896. https://doi.org/10.1038/ni.1937

Bourhis, J., Sire, C., Tao, Y., Martin, L., Alfonsi, M., Prevost, J. B., Rives, M., Lafond, C., Tourani, J. M., Biau, J., Geoffrois, L., Coutte, A., Liem, X., Vauleon, E., Drouet, F., Pechery, A., Guigay, J., Wanneveich, M., Aupérin, A., & Sun, X. (2020). LBA38 Pembrolizumab versus cetuximab, concomitant with radiotherapy (RT) in locally advanced head and neck squamous cell carcinoma (LA-HNSCC): Results of the GORTEC 2015-01 “PembroRad” randomized trial. *Annals of Oncology*, *31*, S1168. https://doi.org/10.1016/j.annonc.2020.08.2268

De Ruysscher, D., Niedermann, G., Burnet, N. G., Siva, S., Lee, A. W. M., & Hegi-Johnson, F. (2019a). Radiotherapy toxicity. *Nature Reviews Disease Primers*, *5*(1). https://doi.org/10.1038/s41572-019-0064-5

Helmink, B. A., Reddy, S. M., Gao, J., Zhang, S., Basar, R., Thakur, R., Yizhak, K., Sade-Feldman, M., Blando, J., Han, G., Gopalakrishnan, V., Xi, Y., Zhao, H., Amaria, R. N., Tawbi, H. A., Cogdill, A. P., Liu, W., LeBleu, V. S., Kugeratski, F. G., . . . Wargo, J. A. (2020). B cells and tertiary lymphoid structures promote immunotherapy response. *Nature*, *577*(7791), 549-555. https://doi.org/10.1038/s41586-019-1922-8

Jayasingam, S. D., Citartan, M., Thang, T. H., Mat Zin, A. A., Ang, K. C., & Ch'ng, E. S. (2020). Evaluating the Polarization of Tumor-Associated Macrophages Into M1 and M2 Phenotypes in Human Cancer Tissue: Technicalities and Challenges in Routine Clinical Practice [Mini Review]. *Frontiers in Oncology*, *9*. https://www.frontiersin.org/articles/10.3389/fonc.2019.01512

Lipshultz, S. E., & Sallan, S. E. (1993). Cardiovascular abnormalities in long-term survivors of childhood malignancy. *Journal of Clinical Oncology*, *11*(7), 1199-1203. https://doi.org/10.1200/JCO.1993.11.7.1199

Noy, R., & Pollard, Jeffrey W. (2014). Tumor-Associated Macrophages: From Mechanisms to Therapy. *Immunity*, *41*(1), 49-61. https://doi.org/https://doi.org/10.1016/j.immuni.2014.06.010

Pan, Y., Yu, Y., Wang, X., & Zhang, T. (2020). Tumor-Associated Macrophages in Tumor Immunity [Review]. *Frontiers in Immunology*, *11*. https://doi.org/10.3389/fimmu.2020.583084

Stewart, J. R., Fajardo, L. F., Gillette, S. M., & Constine, L. S. (1995). Radiation injury to the heart. *International Journal of Radiation Oncology*Biology*Physics*, *31*(5), 1205-1211. https://doi.org/https://doi.org/10.1016/0360-3016(94)00656-6

Tao, Y., Biau, J., Sun, X. S., Sire, C., Martin, L., Alfonsi, M., Prevost, J. B., Modesto, A., Lafond, C., Tourani, J. M., Miroir, J., Kaminsky, M. C., Coutte, A., Liem, X., Chautard, E., Vauleon, E., Drouet, F., Ruffier, A., Ramee, J. F., . . . Bourhis, J. (2023). Pembrolizumab versus cetuximab concurrent with radiotherapy in patients with locally advanced squamous cell carcinoma of head and neck unfit for cisplatin (GORTEC 2015-01 PembroRad): a multicenter, randomized, phase II trial. *Annals of Oncology*, *34*(1), 101-110. https://doi.org/10.1016/j.annonc.2022.10.006

APPENDIX

Appendix 1. Equipment, machines and their manufacturers.

REAGENT or RESOURCE	SOURCE	IDENTIFIER
Chemicals, peptides and recombinant proteins		
Acetic acid (glacial)	BDH Chemicals (UAE)	100012K
Antibody diluent	Abcam (UK)	ab64211
Aquatex®	Sigma-Aldrich (USA)	108562
Bouin's solution	Sigma-Aldrich	HT10132
5-Bromo-2′-deoxyuridine (BrdU)	Sigma-Aldrich	B9285
Citrate Buffer, pH 6.0, 10X	Sigma-Aldrich	C9999
Citroclear	TCS Biosciences (UK)	HC5005
Dako Dual Endogenous Enzyme Block	Agilent (USA)	S2003
Dako EnVision+ System-HRP Labelled Polymer Anti-Rabbit	Agilent	K400311
Dako EnVision+ System-HRP Labelled Polymer Anti-mouse	Agilent	K4000
Dako Liquid DAB+ Substrate Chromogen System	Agilent	K3468
Dimethyl sulfoxide (DMSO)	Thermo Fisher Scientific	85190
DPX mountant	Merck (Germany)	44581
Dulbecco's Modified Eagle Medium/Ham's F-12	Thermo Fisher Scientific	12634-010
Ethylenediaminetetraacetic acid (EDTA)	BDH Chemicals	4438882G
Elite ABC Rat IgG	Vector Laboratories	PK-6104
Ethanol	Thermo Fisher Scientific	E/0665DF/17
Eosin	Sigma-Aldrich	HT110132
Foetal bovine serum	Sigma-Aldrich	F7524
Formalin (10% neutral buffered)	Sigma-Aldrich	HT501128
GlutaMAX	Thermo Fisher Scientific	35050-038
Haematoxylin (Harris's)	Sigma-Aldrich	351945S
Haematoxylin (Gill's)	Sigma-Aldrich	GHS132
Hydrochloric acid (HCl)	Sigma-Aldrich	320331
Hydrogen peroxide 30%	Thermo Fisher Scientific	H/1750/15
Hydroxypropyl methyl cellulose	Merck	9004-65-3
Lithium carbonate	Scientific Laboratory Supplies	CHE2354
Magnesium Sulfate	Sigma-Aldrich	M7506
Mouse on Mouse Blocking Reagent	Vector Laboratories	MKB-2213-1
Paraffin (Histoplast)	Thermo Scientific	6774060
Pentobarbitone sodium (Pentoject®)	Animalcare Ltd. (UK)	-
Penicillin-Streptomycin (5,000 U/mL)	Thermo Fisher Scientific	15070063
Phosphate-buffered saline (PBS)	Sigma-Aldrich	94417
Pimonidazole HCl	Hypoxyprobe, Inc. (USA)	HP1-1000Kit
Poly(ethylene glycol)	Sigma-Aldrich	91893
Sodium bicarbonate	Corning	61-065-RO
Trizma® base (Tris Base)	Sigma-Aldrich	T1503
TWEEN 20	Sigma-Aldrich	P1379
TWEEN 80	Merck	8.17061.1000

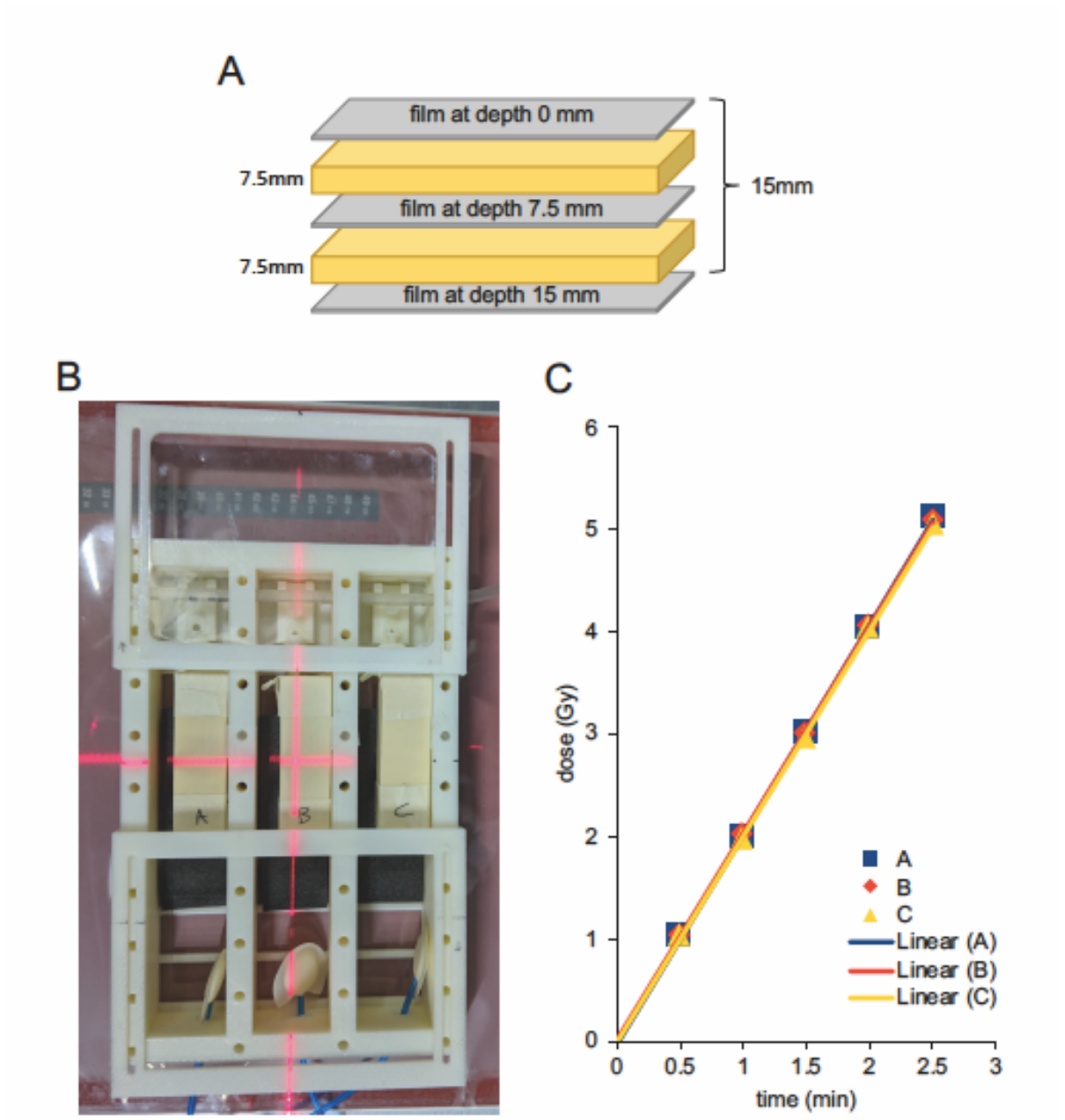
Urethane	Sigma-Aldrich	U2857
Weigert's iron hematoxylin	Sigma-Aldrich	HT1079
Xylene	Sigma-Aldrich	534056
DMXAA (Vadimesan)	Selleckchem	S1537
H-151	Selleckchem	S6652
anti-PD-L1 (clone 10F.9G2)	BioXCell	BE0101
Hanks Balanced Salt Solution	Gibco	14025092
Red blood cell lysis buffer	Roche	11814389001
RNAlater	Qiagen	76104
DNAse I	Roche	10104159001
Collagenase D	Roche	11088882001
Nitrocellulose membrane (0.45 µm pores)	Bio-Rad	162-0115
Methanol	Sigma-Aldrich	32213
Running buffer (10x)	Bio-Rad	1610732
Transfer buffer (10x)	Bio-Rad	1610734
Sodium dodecylsulphate (SDS)	Applichem	A0676,0500
Sodium hydroxide (NaOH)	BDH Chemicals	28244.262
Sodium orthovanadate (Na3VO4)	Sigma-Aldrich	450243-10G
Protease inhibitor	Roche	11697498001
Sample buffer, Laemmli 2x concentrated	Sigma-Aldrich	S3401
Sodium bicarbonate	Corning	61-065-RO
Penicillin-streptomycin	Life Technologies	15070-063
Criterion™ TGX gels	Bio-Rad	5671085
Trypsin-EDTA (0.25%)	Life Technologies	25200-056
Hanks' Balanced Salt Solution (HBSS) with Ca2+, Mg2+	Gibco	11550456
DAPI	Akoya Biosciences	FP1490
Antibodies		
Unconjugated CD45	Abcam (UK)	ab10558
Unconjugated CD3 (SP7)	Abcam (UK)	ab16669
Unconjugated CD8	Abcam (UK)	ab209775
Unoconjugated Ly6G / GR-1	Invitrogen	RM3000
Unconjugated F4/80	Proteintech	18705-1-AP
Unconjugated CD68 (KP1)	Abcam	ab955
Unconjugated γH2AX (Ser139)	Cell Signalling Technologies	9718
Unconjugated 53BP1	Cell Signalling Technologies	4937
Phospho-TBK1/NAK (Ser172) (D52C2) Rabbit	Cell Signalling Technologies	5483
Phospho-IRF-3 (Ser396) (D6O1M) Rabbit	Cell Signalling Technologies	29047
TBK1/NAK (D1B4) Rabbit	Cell Signalling Technologies	3504
IRF-3 (D83B9) Rabbit	Cell Signalling Technologies	4302
STING (D1V5L) Rabbit mAb	Cell Signalling Technologies	50494

CD4	Abcam (UK)	ab183685
CD19	Cell Signalling Technologies	90176T
FoxP3 (D608R)	Cell Signalling Technologies	12653S
PNAd (Meca-79)	Biolegend	120802
CD103	eBioscience	14-1031-81
CXCL13/ BCA1	Bioss	bs-2553R
CD45R/ B220	Biolegend	103201
CD83	Biolegend	121503
CD31	Abcam (UK)	ab28364
Phospho-p53 (Ser15) Antibody	Cell Signalling Technologies	9284
MHC class II (Y-Ae)	Santa Cruz Biotechnology	Sc-32247
Anti-CD163 antibody [EPR19518]	Abcam (UK)	ab182422
Alexa Fluor 488 anti-rabbit goat IgG (H+L)	Life Technologies	A11008
Alexa Fluor 488 anti-mouse goat IgG (H+L)	Life Technologies	A11001
CD69	Invitrogen	PA5-11489
FACS antibodies		
Purified Rat Anti-Mouse CD16/CD32	BD Biosciences	553141
PE-Cyanine7 anti-mouse CD11b (M1/70)	eBioscience	25-0112-82
APC anti-mouse Ly-6G	Biolegend	127613
APC/Cy7 anti-mouse Ly-6C	Biolegend	128025
PerCP/Cy5.5 anti-mouse CD206 (MMR)	Biolegend	141716
Brilliant Violet 510 anti-mouse Ly-6G/Ly-6C (Gr-1)	Biolegend	108437
Brilliant Violet 421 anti-mouse F4/80	Biolegend	123137
Brilliant Violet 605 anti-mouse CD11c	Biolegend	117333
Brilliant Violet 711 anti-mouse I-A/I-E	Biolegend	107643
PE anti-mouse CD45 (30-F11)	eBioscience	12-0451-82
PE/Cy7 anti-mouse CD8a	Biolegend	100722
PerCP/Cy5.5 anti-mouse NK-1.1	Biolegend	108727
APC anti-mouse CD4	Biolegend	100516
APC/Cy7 anti-mouse CD3	Biolegend	100221
Brilliant Violet 421 anti-mouse CD279 (PD-1)	Biolegend	135217
Brilliant Violet 605 anti-mouse CD25	Biolegend	102035
APC/Cy7 anti-mouse CD45	Biolegend	103116
PE FOXP3 (NRRF-30)	eBioscience	12-4771-80
PE iNOS (CXNFT)	eBioscience	12-5920-82
Commercial assays		
Fixation/Permeabilization Diluent	eBioscience	00-5223-56
Fixation/Permeabilization Concentrate	eBioscience	00-5123-43
Permeabilization Buffer (10X)	eBioscience	00-8333-56
Trichrome Stain (Masson) Kit	Sigma-Aldrich	HT15
Mouse TNF-alpha Quantikine ELISA Kit	R&D Systems	MTA00B

Mouse IFN-beta Quantikine ELISA Kit	R&D Systems	MIFNB0
LIVE/DEAD Fixable Green Dead Cell Stain Kit, for 488 nm excitation	Invitrogen	L23101
SureSelectXT Mouse All Exon, 16 sample enrichment kit	Agilent	5190-4641
BOND™ Polymer Refine Detection System	Leica Biosystems	DS9800
Software		
FlowJo (version 10.7)	BD Bioscience	
ImageJ	NIH	
Adobe Illustrator (25.4.1)	Adobe	
HALO Image Analysis Platform Software	IndicaLabs	
ITK-SNAP (version 3.6.0)	Open source	http://itksnap.org
Aperio Scanner	Leica	
ImageScope (version 12.3.3)	Leica	
QuPath (version 0.3.2)	Open source	https://qupath.readthedocs.io/en/stable/
ct-FIRE	Open source	https://loci.wisc.edu/software/ctfire
R (version 4.0.5)	R Studios	
Prism (version 9.0)	GraphPad	
LabChart8 (version 8.1.21)	ADInstruments	
ImageStudio (version 5.2.5)	LI-COR Biosciences	

Appendix 2. Specifications for MR image acquisition settings.

Machine	7.0 T, 310mm horizontal bore Varian Nuclear Magnetic Resonance Spectrometer (VNMRS)
Coil	310mm horizontal bore
Frames	8 frames per R-R interval
Repetition time (TR)	2.684 ms
echo time (TE)	1.342 ms
Flip angle (FA)	20°
Field of view (FOV)	48×24×24 mm3
Matrix	256×96×96
RF hard pulse duration	16 μs



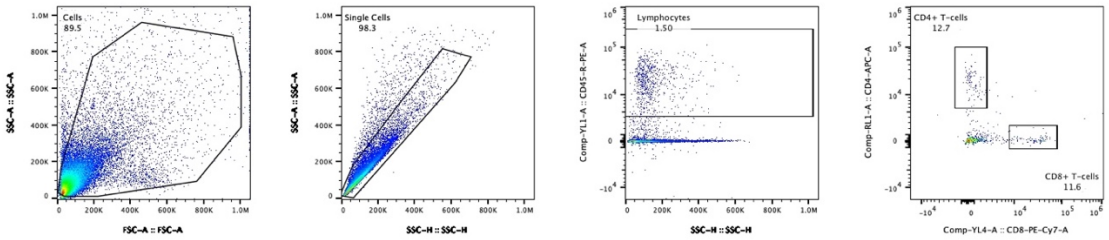
Appendix 3. Physical set-up of irradiation rigs. (A) Phantom mice were created with Gafchromic EBT3 films stacked with 7.5 mm thick solid water slabs. **(B)** Dosimetry was performed at 3 levels of depths and 3 positions in the irradiation rigs (labelled A, B, and C). **(C)** The dose rates in positions A, B and C were calculated as 2.02 Gy/min. Figure adapted from Martin (DPhil Thesis, 2021).

Appendix 4. Variation in radiation dose received in positions A-B on mouse rig and depth. Radiation dosimetry calculated in positions A-B and depth of 0mm-15mm on a phantom mouse. Reproduced from Martin (DPhil Thesis, 2021)

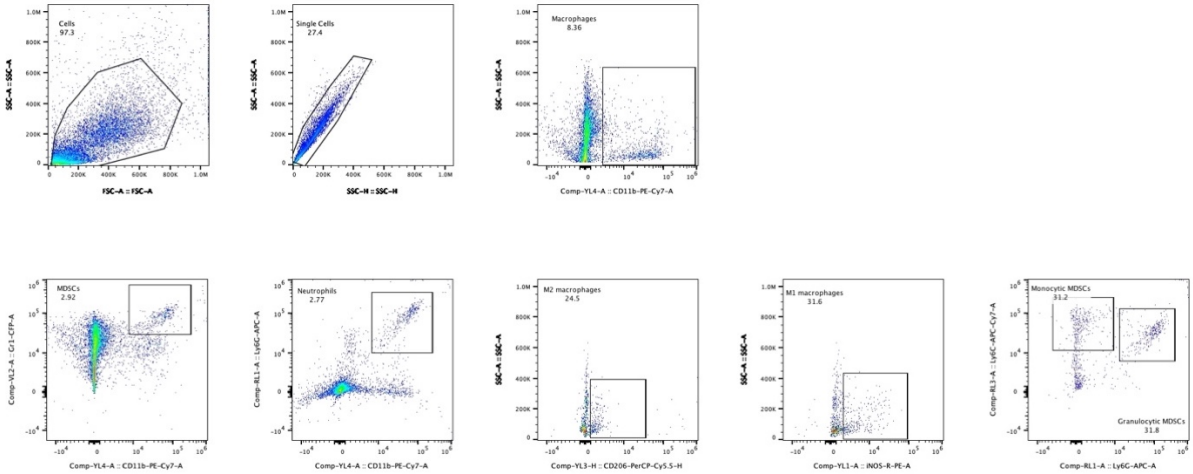
Variation in dose received in positions		Variation in dose with depth	
A	101.10%	0 mm	112.40%
B	99.80%	7.5 mm	100%
C	99.10%	15 mm	84.90%

Appendix 5. Flow cytometry gating strategies. Gating strategies for FlowJo analyses on lymphoid, myeloid and fibroblast panels shown.

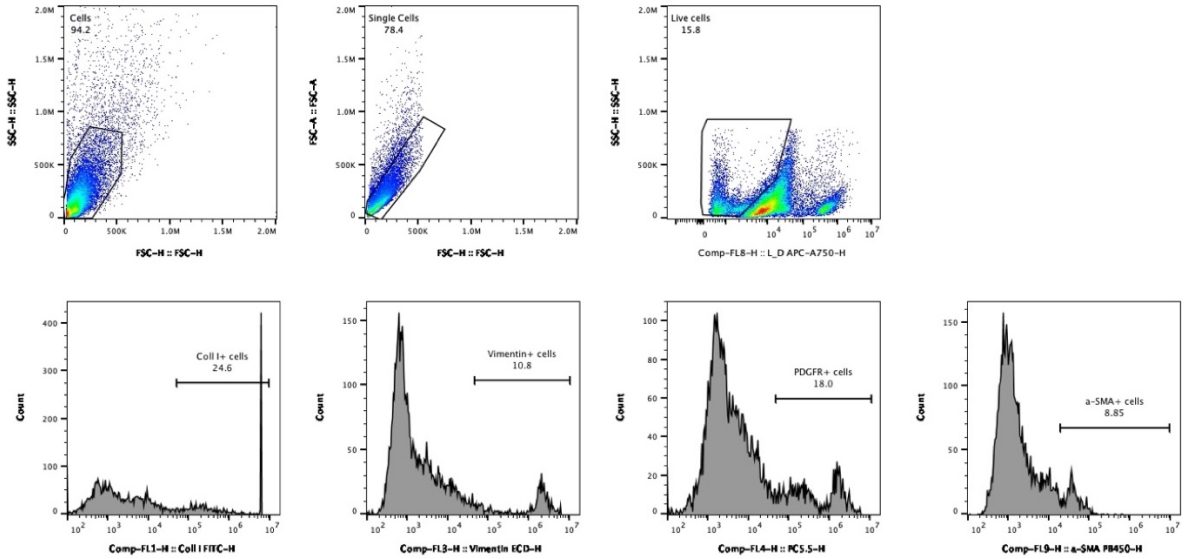
Lymphoid panel (lung cells)



Myeloid panel (lung cells)



Fibroblast activation panel (cardiac cells)



Appendix 6. Script for *DESeq2* for differential gene expression analysis.

```
### DESeq2 normalisation and differential expression analysis

library(DESeq2)
# Create a table (i.e. "sampleTable") mapping sample IDs to
treatment group identifiers (A, B, C, ...)
sampleTable <- data.frame(Sample = names(files))

library(dplyr)
sampleTable <- sampleTable %>%
  mutate(Condition = case_when(
    grepl("Control", sampleTable$Sample) ~ "A",
    grepl("Sample_1_", sampleTable$Sample) | grepl("Sample_2_",
sampleTable$Sample) | grepl("Sample_3_", sampleTable$Sample) ~ "B",
    grepl("Sample_4_", sampleTable$Sample) | grepl("Sample_5_",
sampleTable$Sample) | grepl("Sample_6_", sampleTable$Sample) ~ "C",
    grepl("Sample_7_", sampleTable$Sample) | grepl("Sample_8_",
sampleTable$Sample) | grepl("Sample_9_", sampleTable$Sample) ~ "D",
    grepl("Sample_10_", sampleTable$Sample) | grepl("Sample_11_",
sampleTable$Sample) ~ "E",
    grepl("Sample_12_", sampleTable$Sample) | grepl("Sample_13_",
sampleTable$Sample) ~ "F",
    grepl("Sample_14_", sampleTable$Sample) | grepl("Sample_15_",
sampleTable$Sample) ~ "G",
    grepl("Sample_16_", sampleTable$Sample) | grepl("Sample_17_",
sampleTable$Sample) ~ "H",
    grepl("Sample_18_", sampleTable$Sample) | grepl("Sample_19_",
sampleTable$Sample) ~ "I"

  ))


sampleTable$Condition <- factor(sampleTable$Condition)
sampleTable <- data.frame(sampleTable[,"Condition"])
rownames(sampleTable) <- colnames(txi$counts)
colnames(sampleTable) <- "Condition"

# Set control condition (A; untreated) as reference condition for
your comparisons
# (Set the ref condition to your reference condition of interest for
specific comparisons (e.g. set it to "C" if you want to retrieve the
F versus C comparison))
sampleTable$Condition <- relevel(sampleTable$Condition, ref = "A")


### Perform DESeq2 differential expression analysis

# Perform DESeq2 normalisation and differential expression analysis
dds <- DESeqDataSetFromTximport(txi, colData=sampleTable, ~
Condition)

# Filter out rows (genes) with fewer than 10 transcripts across all
samples (very non-stringent filtering)
keep <- rowSums(counts(dds)) >= 10 #& rowSums(counts(dds)> 0) >= 6
```

```
dds <- dds[keep,]
dds <- DESeq(dds)
resultsNames(dds)

# Create a gene expression dataframe of DESeq2-normalised transcript
counts
Counts <- counts(dds, normalized=T)


### Unsupervised learning to chekc sample quality

## Create a correlation matrix of sample-to-sample distances/Pearson
correlations
rld <- rlogTransformation(dds)
rld_heatmap <- assay(rld)
dds_heatmap <- assay(dds)
cor_rld <- cor(rld_heatmap)
cor_rld <- as.data.frame(cor_rld) %>%
  mutate(Condition = case_when(
    grepl("Control", rownames(cor_rld)) ~ "A",
    grepl("Sample_1_", rownames(cor_rld)) | grepl("Sample_2_",
rownames(cor_rld)) | grepl("Sample_3_", rownames(cor_rld)) ~ "B",
    grepl("Sample_4_", rownames(cor_rld)) | grepl("Sample_5_",
rownames(cor_rld)) | grepl("Sample_6_", rownames(cor_rld)) ~ "C",
    grepl("Sample_7_", rownames(cor_rld)) | grepl("Sample_8_",
rownames(cor_rld)) | grepl("Sample_9_", rownames(cor_rld)) ~ "D",
    grepl("Sample_10_", rownames(cor_rld)) | grepl("Sample_11_",
rownames(cor_rld)) ~ "E",
    grepl("Sample_12_", rownames(cor_rld)) | grepl("Sample_13_",
rownames(cor_rld)) ~ "F",
    grepl("Sample_14_", rownames(cor_rld)) | grepl("Sample_15_",
rownames(cor_rld)) ~ "G",
    grepl("Sample_16_", rownames(cor_rld)) | grepl("Sample_17_",
rownames(cor_rld)) ~ "H",
    grepl("Sample_18_", rownames(cor_rld)) | grepl("Sample_19_",
rownames(cor_rld)) ~ "I"))

col_col <- cor_rld
col_col$Sample <- rownames(col_col)
col_col <- col_col[,c("Condition", "Sample")]


## Heatmaps / Hierarchical cluster analysis
library(pheatmap)

# Sample-to-sample distances (Pearson)
pheatmap(cor_rld[,1:22], clustering_distance_rows = "correlation",
annotation_col = col_col, clustering_distance_cols = "correlation",
clustering_method = "average", scale = "none",
         color = colorRampPalette(brewer.pal(9, "YlGnBu"))(100),
labels_row = colnames(cor_rld))

# Gene expression (Euclidean average-linkage; z-scored rows)
```

```
pheatmap(rld_heatmap, clustering_distance_rows = "euclidean", scale
= "row", annotation_col = col_col, clustering_distance_cols =
"euclidean", clustering_method = "average",
         color = colorRampPalette(brewer.pal(9, "RdYlBu"))(100),
labels_row = NULL)

## Principal component analysis
DESeq2::plotPCA(rld, intgroup="Condition") + theme_classic()


# Export differential expression analysis results (all genes,
irrespective of fold-change or significance cut-offs)
# (In this case: export the results of the comparison between
condition A ("untreated") and condition F ("ure, 13 Gy 7d post-RT"))
# (Manually change the condition names in the line of code below to
access the results of your comparison of interest (e.g.
"Condition_I_vs_A"))
res <- results(dds, name="Condition_F_vs_A")
res_DF <- as.data.frame(res)

# Export significantly differentially expressed genes (i.e. DEGs;
log2(fold-change) > 1 and Adjusted P-value <= 0.05))
resDE <- res[which(abs(res$log2FoldChange) > 1 & res$padj <=0.05),]
resDE_DF <- as.data.frame(resDE)

# Map ENSEMBL IDs in results files to Gene Symbols using gene ID
mapping used in the provided quant.sf files
resDE_DF$ENSEMBL <- rownames(resDE_DF)
tx2genetest <- read_excel("/Users/bruno/Documents/University of
Oxford/Collaborations/Kay Shigemori/Source Bioscience RNA-seq/RNA-
seq_Sample_9_S27.xls")
tx2genetest <- tx2genetest[,c("GenName", "GeneId")]
tx2gene <- tx2genetest
tx2gene <- tx2gene[-which(duplicated(tx2gene$GeneId)),]
colnames(tx2gene) <- c("GENENAME", "GENEID")
resDE_DF <- merge(resDE_DF, tx2gene, by.x=0, by.y="GENEID")
res_DF <- merge(res_DF, tx2gene, by.x=0, by.y="GENEID")


### All differentially expressed genes from all comparisons of
interest were retrieved and saved into the excel file titled:
"Salmon-tximport()-DESeq2 - Pairwise comparisons - Differentially
expressed genes (Log2FC cut-off  1, adj.P cut-off 0.05) and commonly
down and upregulated genes.xlsx"

# Read in excel sheet with DEGs (for convenience)

D_G <- read_excel("Salmon-tximport()-DESeq2 - Pairwise comparisons -
Differentially expressed genes (Log2FC cut-off  1, adj.P cut-off
0.05) and commonly down and upregulated genes.xlsx", sheet="D_G")
D_G_up <- D_G[which(D_G$log2FoldChange>0),]
D_G_down <- D_G[which(D_G$log2FoldChange<0),]
```

```
E_H <- read_excel("Salmon-tximport()-DESeq2 - Pairwise comparisons -
Differentially expressed genes (Log2FC cut-off  1, adj.P cut-off
0.05) and commonly down and upregulated genes.xlsx", sheet="E_H")
E_H_up <- E_H[which(E_H$log2FoldChange>0),]
E_H_down <- E_H[which(E_H$log2FoldChange<0),]

F_I <- read_excel("Salmon-tximport()-DESeq2 - Pairwise comparisons -
Differentially expressed genes (Log2FC cut-off  1, adj.P cut-off
0.05) and commonly down and upregulated genes.xlsx", sheet="F_I")
F_I_up <- F_I[which(F_I$log2FoldChange>0),]
F_I_down <- F_I[which(F_I$log2FoldChange<0),]



D_B <- read_excel("Salmon-tximport()-DESeq2 - Pairwise comparisons -
Differentially expressed genes (Log2FC cut-off  1, adj.P cut-off
0.05) and commonly down and upregulated genes.xlsx", sheet="D_B")
D_B_up <- D_B[which(D_B$log2FoldChange>0),]
D_B_down <- D_B[which(D_B$log2FoldChange<0),]

E_B <- read_excel("Salmon-tximport()-DESeq2 - Pairwise comparisons -
Differentially expressed genes (Log2FC cut-off  1, adj.P cut-off
0.05) and commonly down and upregulated genes.xlsx", sheet="E_B")
E_B_up <- E_B[which(E_B$log2FoldChange>0),]
E_B_down <- E_B[which(E_B$log2FoldChange<0),]

F_C <- read_excel("Salmon-tximport()-DESeq2 - Pairwise comparisons -
Differentially expressed genes (Log2FC cut-off  1, adj.P cut-off
0.05) and commonly down and upregulated genes.xlsx", sheet="F_C")
F_C_up <- F_C[which(F_C$log2FoldChange>0),]
F_C_down <- F_C[which(F_C$log2FoldChange<0),]


B_A <- read_excel("Salmon-tximport()-DESeq2 - Pairwise comparisons -
Differentially expressed genes (Log2FC cut-off  1, adj.P cut-off
0.05) and commonly down and upregulated genes.xlsx", sheet="B_A")
B_A_up <- B_A[which(B_A$log2FoldChange>0),]
B_A_down <- B_A[which(B_A$log2FoldChange<0),]

C_A <- read_excel("Salmon-tximport()-DESeq2 - Pairwise comparisons -
Differentially expressed genes (Log2FC cut-off  1, adj.P cut-off
0.05) and commonly down and upregulated genes.xlsx", sheet="C_A")
C_A_up <- C_A[which(C_A$log2FoldChange>0),]
C_A_down <- C_A[which(C_A$log2FoldChange<0),]

G_A <- read_excel("Salmon-tximport()-DESeq2 - Pairwise comparisons -
Differentially expressed genes (Log2FC cut-off  1, adj.P cut-off
0.05) and commonly down and upregulated genes.xlsx", sheet="G_A")
G_A_up <- G_A[which(G_A$log2FoldChange>0),]
G_A_down <- G_A[which(G_A$log2FoldChange<0),]

H_A <- read_excel("Salmon-tximport()-DESeq2 - Pairwise comparisons -
Differentially expressed genes (Log2FC cut-off  1, adj.P cut-off
0.05) and commonly down and upregulated genes.xlsx", sheet="H_A")
```

```
H_A_up <- H_A[which(H_A$log2FoldChange>0),]
H_A_down <- H_A[which(H_A$log2FoldChange<0),]

I_A <- read_excel("Salmon-tximport()-DESeq2 - Pairwise comparisons -
Differentially expressed genes (Log2FC cut-off  1, adj.P cut-off
0.05) and commonly down and upregulated genes.xlsx", sheet="I_A")
I_A_up <- I_A[which(I_A$log2FoldChange>0),]
I_A_down <- I_A[which(I_A$log2FoldChange<0),]

ureRT_upin2 <- read_excel("Salmon-tximport()-DESeq2 - Pairwise
comparisons - Differentially expressed genes (Log2FC cut-off  1,
adj.P cut-off 0.05) and commonly down and upregulated genes.xlsx",
sheet="Up in ≥ 2 ure, RT")



## Rank order plots

# early urethane-induced changes (3d)
# Downregulated
library(ggpubr)
B_A_down$Rank <- rank(B_A_down$padj)
B_A_down$padj <- -log10(B_A_down$padj)
B_A_down$baseMean <- log2(B_A_down$baseMean)

ggscatter(B_A_down, x = "Rank", y = "padj", color =
"log2FoldChange", size = "baseMean", alpha=0.8, label =
ifelse(B_A_down$Rank <= 10, B_A_down$SYMBOL, NA), repel =T)+
  theme_classic()+
  scale_color_gradient2(low="#084594", mid="#6BAED6",
high="#EFF3FF")

# Upregulated
B_A_up$Rank <- rank(B_A_up$padj)
B_A_up$padj <- -log10(B_A_up$padj)
B_A_up$baseMean <- log2(B_A_up$baseMean)

ggscatter(B_A_up, x = "Rank", y = "padj", color = "log2FoldChange",
size = "baseMean", alpha=0.8, label = ifelse(B_A_up$Rank <= 10,
B_A_up$SYMBOL, NA), repel =T)+
  theme_classic()+
  scale_color_gradient2(high="#99000D", mid="#FB6A4A",
low="#FEE5D9")

# Late urethane-induced changes (10d)
# Downregulated
library(ggpubr)
C_A_down$Rank <- rank(C_A_down$padj)
C_A_down$padj <- -log10(C_A_down$padj)
C_A_down$baseMean <- log2(C_A_down$baseMean)

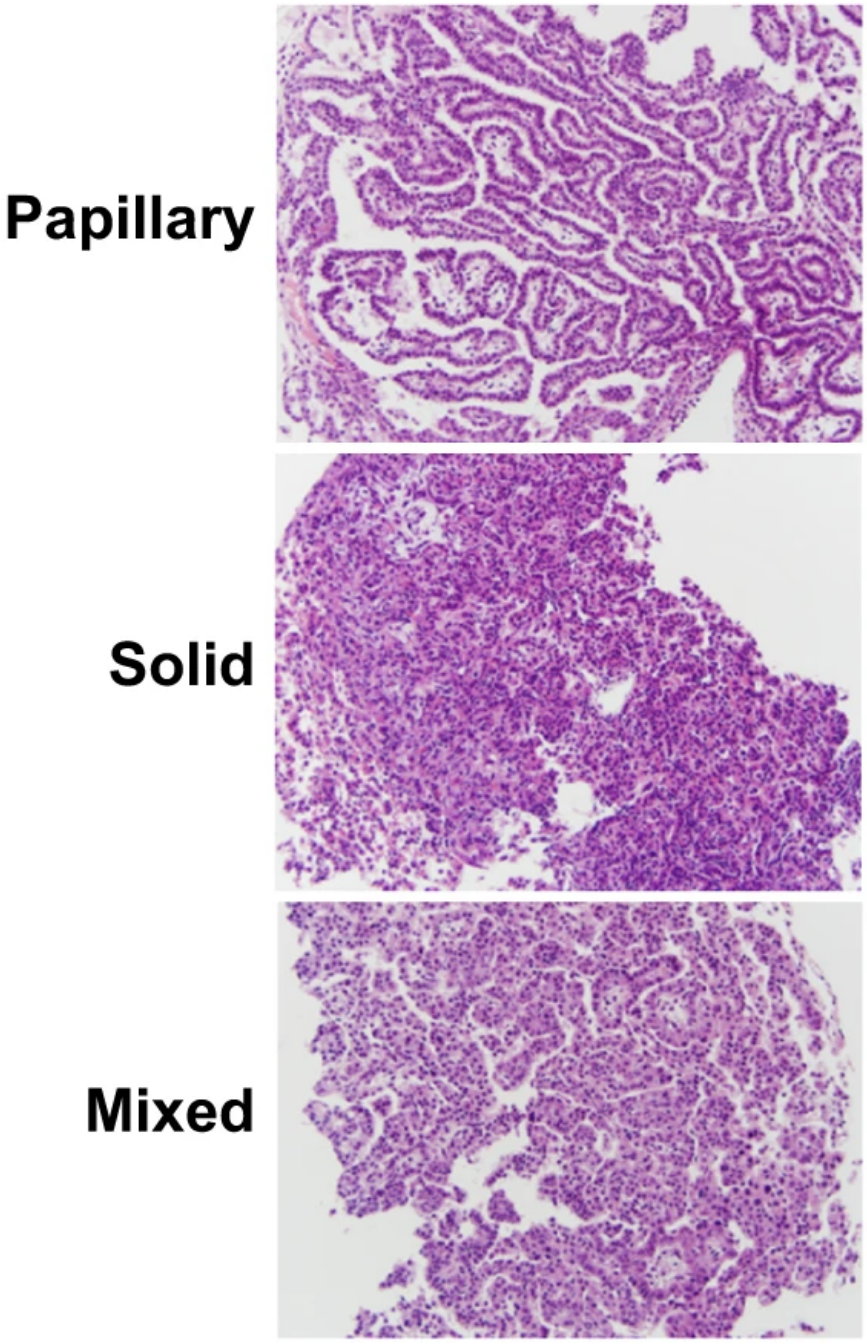
ggscatter(C_A_down, x = "Rank", y = "padj", color =
"log2FoldChange", size = "baseMean", alpha=0.8, label =
ifelse(C_A_down$Rank <= 10, C_A_down$SYMBOL, NA), repel =T)+
```

```
  theme_classic()+
  scale_color_gradient2(low="#084594", mid="#6BAED6",
high="#EFF3FF")

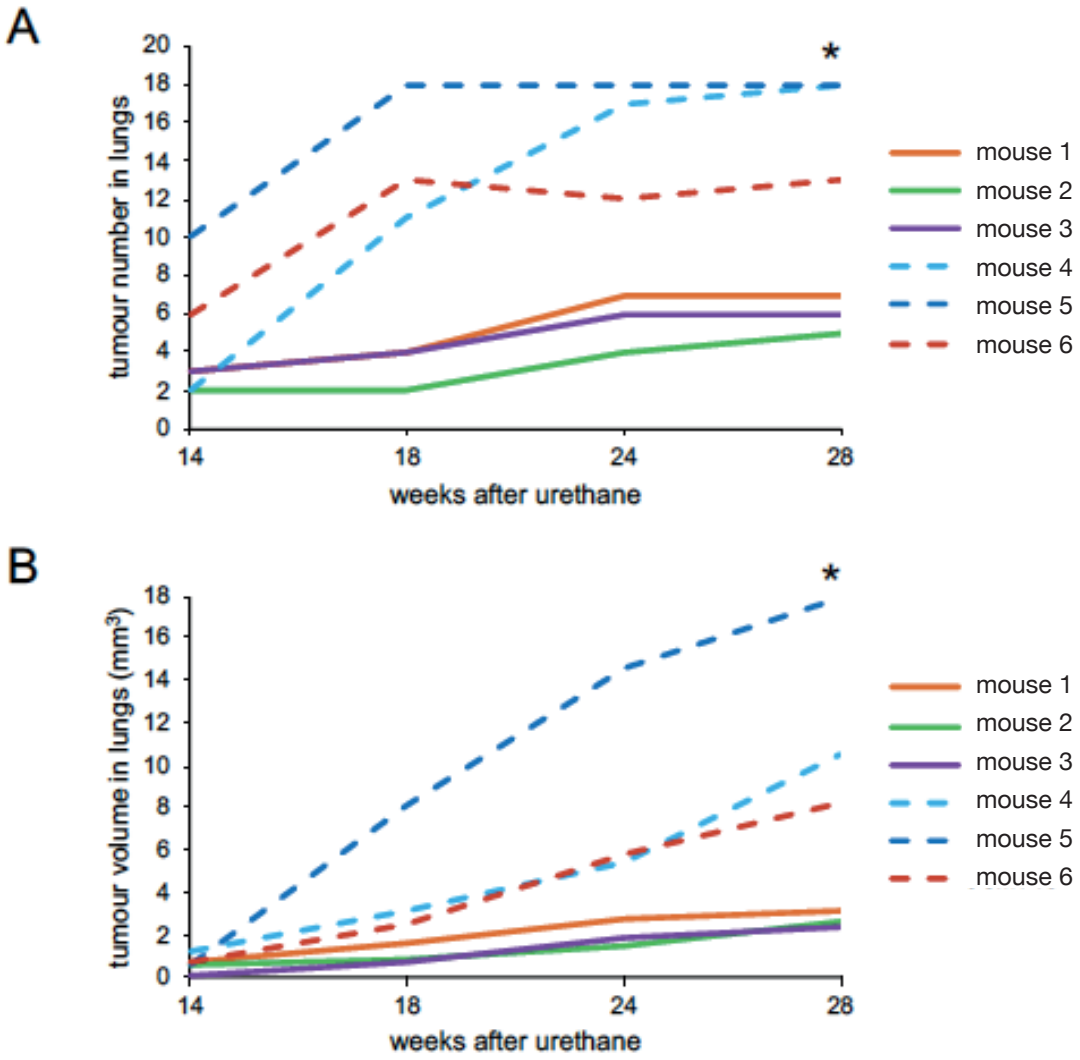
# Upregulated
C_A_up$Rank <- rank(C_A_up$padj)
C_A_up$padj <- -log10(C_A_up$padj)
C_A_up$baseMean <- log2(C_A_up$baseMean)

ggscatter(C_A_up, x = "Rank", y = "padj", color = "log2FoldChange",
size = "baseMean", alpha=0.8, label = ifelse(C_A_up$Rank <= 10,
C_A_up$SYMBOL, NA), repel =T)+
  theme_classic()+
  scale_color_gradient2(high="#99000D", mid="#FB6A4A",
low="#FEE5D9")

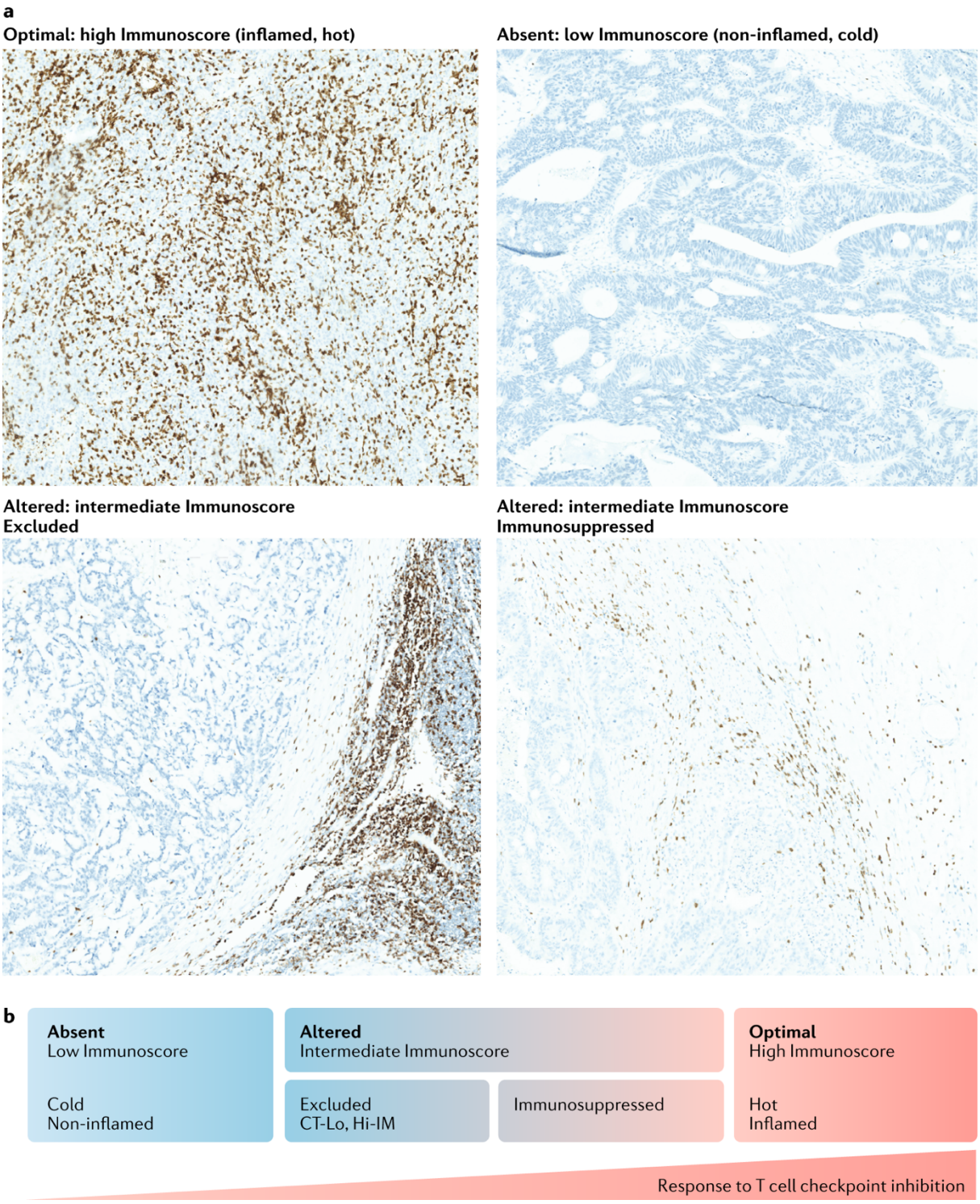

brewer.pal(n=7, "Reds")
display.brewer.all()
```



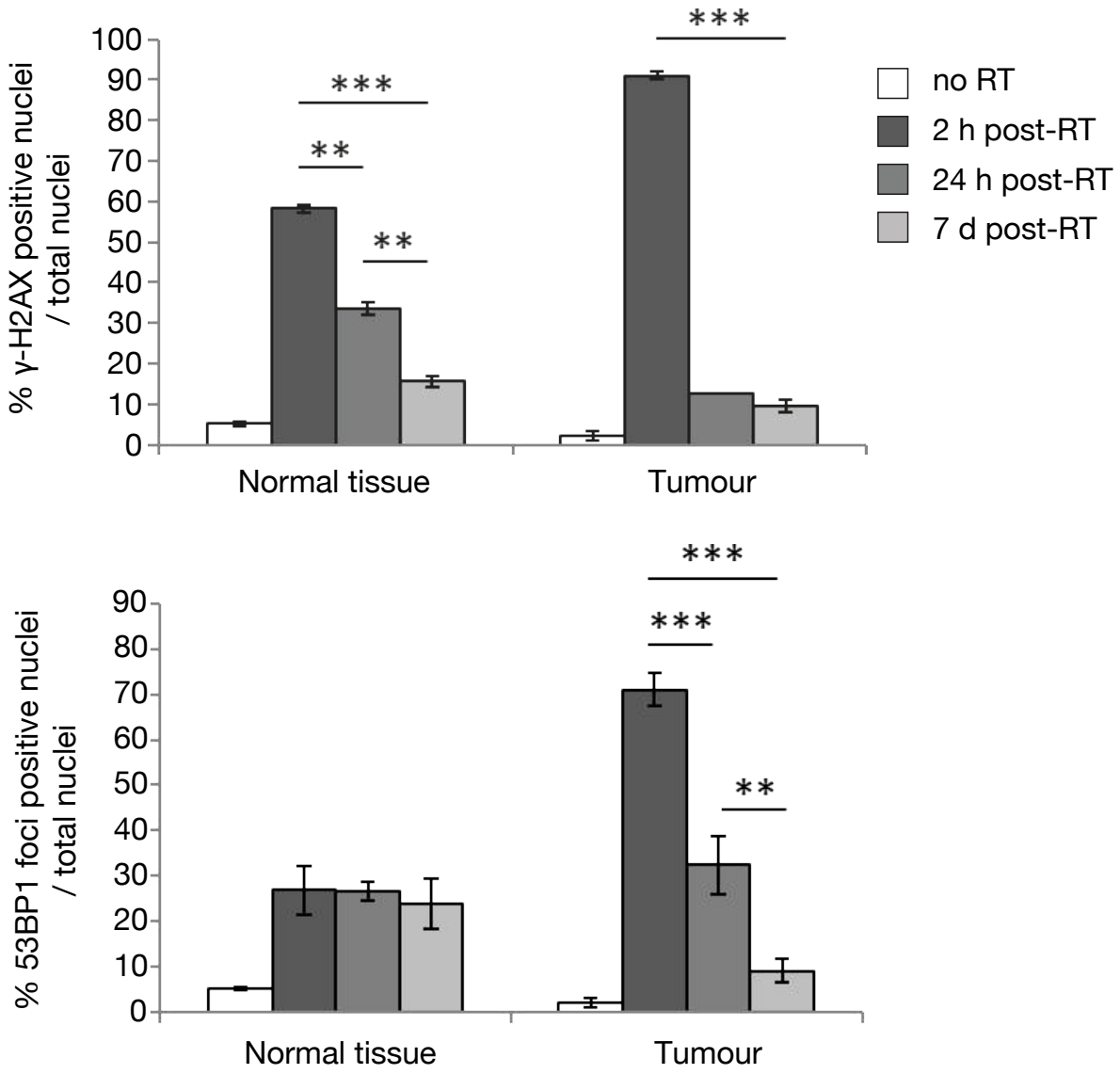
Appendix 7. Representative histology images of papillary, solid, and mixed tumours. Figure adapted from Westcott et al. (2015).



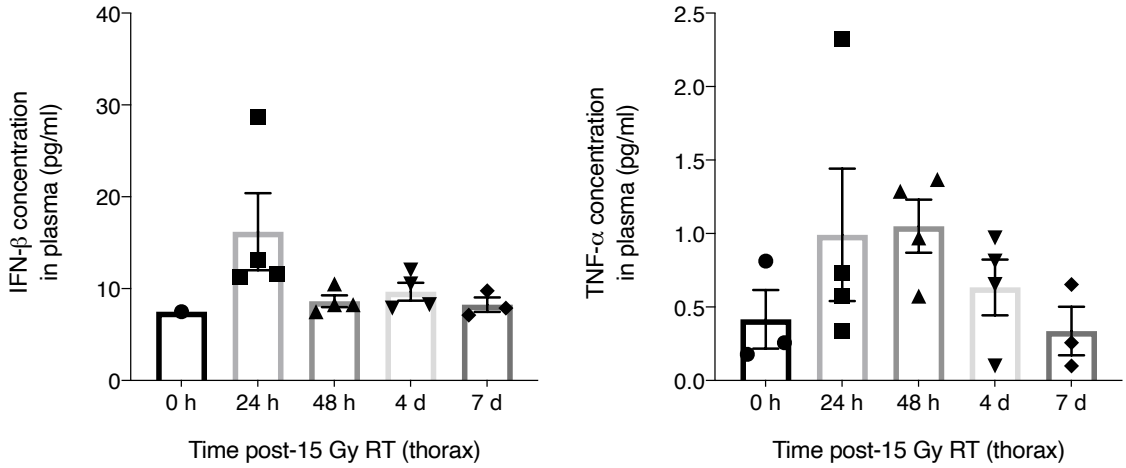
Appendix 8. Tracking lung tumour growth in the A/J mouse with MRI. Figure adapted from Martin DPhil thesis (2021).



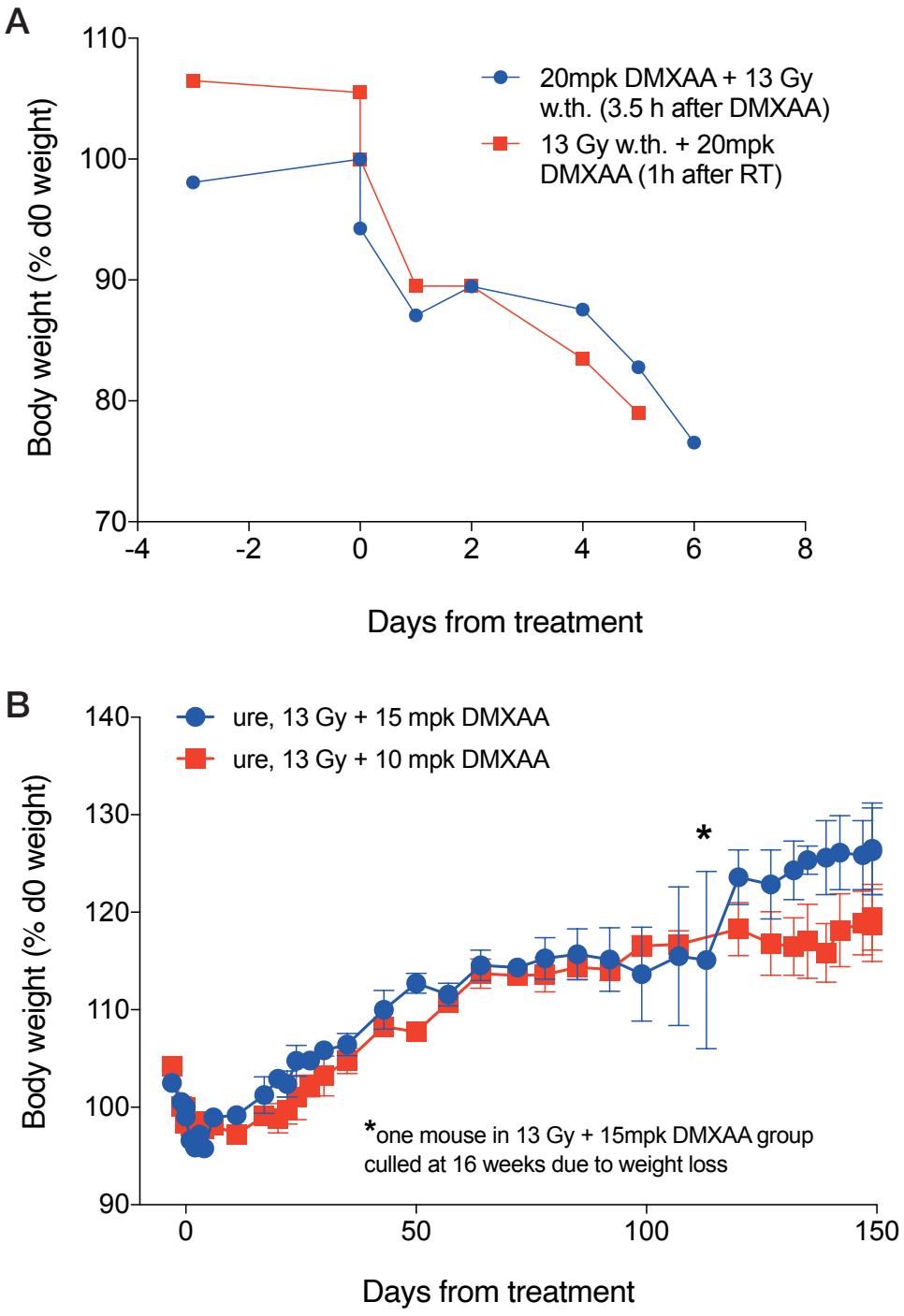
Appendix 9. Categories of immune infiltration based on histological characteristics of tumour-infiltrating T lymphocytes. Figure adapted from Galon and Bruni (2019).



Appendix 10. Lung tumour and normal cells demonstrate different DNA damage response kinetics after RT. Lung samples were collected 2 hours, 24 hours or 7 days post-5 Gy thorax RT and processed for IHC. **(A)** γ-H2AX and **(B)** 53BP1 foci were quantified. 2-6 lung tumour regions, and 3 normal tissue regions were assessed per group. Results represent the mean ± SEM, analysed by a one-tailed student's t-test. $^{ns}p > 0.05$, $*p < 0.05$, $**p < 0.01$, $***p < 0.001$, $****p < 0.0001$. Figure adapted from Lourenco (DPhil thesis, 2017).



Appendix 11. Plasma IFN-β and TNF-α levels 24 hours to 7 days after 15 Gy thorax RT. Plasma were collected from mice 0 hours, 24 hours, 48 hours, 4 days and 7 days after 15 Gy thorax RT. IFN-β and TNF-α concentrations were measured by ELISA. Results represent mean ± SEM.



Appendix 12. 10 mg/ kg and 15 mg/ kg doses of DMXAA were well-tolerated with 13 Gy thorax RT. Body weights from maximum tolerated dose studies of urethane, DMXAA and RT. **(A)** 20 mg/ kg DMXAA i.p. and 13 Gy thorax RT was combined in different orders (blue representing DMXAA followed by RT, and red representing RT followed by DMXAA). n = 1 per group. **(B)** Body weights recorded for 150 days after 15 mg/ kg (blue) and 10 mg/ kg (red) DMXAA i.p. and 13 Gy thorax RT. Results represent mean values ± SEM.